

Cover Page



Universiteit Leiden



The handle <http://hdl.handle.net/1887/28791> holds various files of this Leiden University dissertation.

Author: Rosenberg, Marissa J.F.

Title: Causing a stir : radiative and mechanical feedback in starburst galaxies

Issue Date: 2014-09-18

Causing a Stir
radiative and mechanical feedback in
starburst galaxies
De oorzaak van opschudding

Proefschrift

ter verkrijging van
de graad van Doctor aan de Universiteit Leiden,
op gezag van Rector Magnificus prof. mr. C.J.J.M. Stolker,
volgens besluit van het College voor Promoties
te verdedigen op donderdag 18 september 2014
klokke 15:00 uur

door

Marissa J. F. Rosenberg
geboren te Palo Alto, California, USA
in 1987

Promotiecommissie

Promotors: Prof. dr. Frank Israel
Prof. dr. Paul van der Werf

Overige leden: Prof. dr. Suzanne Aalto (Chalmers University of Technology)
Dr. Axel Weiß (Max-Planck-Institut für Radioastronomie)
Prof. dr. Huub Röttgering
Dr. Jarle Brinchmann

ISBN: 978-94-6259-298-8

Cover: Sub-mm spectrum of NGC 253.

Designed by Mart van de Wiel and Marissa Rosenberg.

Created by Mart van de Wiel.

The most exciting phrase to hear in science, the one that heralds new discoveries, is not 'Eureka!' but 'That's funny...'
-- *Issac Asimov*

Dedicated to my parents,
who taught me to always
embrace change.

Contents

1	Introduction	1
1.1	The Extreme Environments of Galaxy Centers	2
1.1.1	Starbursts and (U)LIRGs	2
1.1.2	Structure of the ISM	3
1.2	Diagnostics of heating mechanisms	5
1.2.1	Modeling Molecular Emission	5
1.2.2	UV Heating	6
1.2.3	X-ray and Cosmic Ray Heating	7
1.2.4	Mechanical Heating	8
1.3	In this Thesis	10
1.3.1	NGC 253 - An archetypal starburst (Chapter 2, 3)	10
1.3.2	Arp 299 - A case study of gas excitation (Chapter 4) . . .	11
1.3.3	Tracing shock excitation in star forming galaxies (Chapter 5)	11
1.3.4	Gas cooling in (U)LIRGs (Chapter 6)	12
2	The excitation of near-infrared H₂ emission in NGC 253	13
2.1	Introduction	14
2.2	Observations	16
2.2.1	SINFONI Observations	16
2.2.2	ISAAC Observations	16
2.3	Results	17
2.4	The Kinematic Center of NGC 253	20
2.5	Gas Excitation Mechanisms in NGC 253	23
2.5.1	Shocks vs Fluorescence	26
2.5.2	Tracers of Fluorescence	28
2.6	PDR and Shock Models	31
2.7	Conclusion	34

3	Radiative and mechanical feedback into the molecular gas of NGC 253	37
3.1	Introduction	38
3.2	Observations and Data Reduction	39
3.3	Results	41
3.4	Dissecting the CO Excitation Ladder	41
3.4.1	LVG Analysis	44
3.4.2	PDR Analysis	47
3.5	Dominant Molecular Excitation Mechanisms	51
3.5.1	Excitation Mechanisms	51
3.5.2	Application to NGC 253	53
3.6	Discussion	58
3.6.1	Case 1	58
3.6.2	Case 2	60
3.6.3	Case 3	60
3.7	Conclusions	62
4	Molecular gas heating in Arp 299	65
4.1	Introduction	66
4.2	Observations and data reduction	67
4.2.1	Observations	67
4.2.2	Data reduction	69
4.3	Results	71
4.3.1	SPIRE FTS line fluxes	71
4.3.2	PACS line fluxes	71
4.4	Comparison between Arp 299 A and B+C	74
4.4.1	Basic PDR analysis	75
4.5	A case study: Arp 299 A	78
4.5.1	The low-excitation phase	79
4.5.2	Full PDR analysis	79
4.5.3	Additional heating sources	83
4.5.4	Molecular gas mass	87
4.6	Limitations and usefulness of the ^{12}CO ladder	88
4.7	Conclusions	89
5	[FeII] as a tracer of supernova rate in nearby starburst galaxies	93
5.1	Introduction	94
5.2	Sample	96
5.2.1	NGC 3628	96
5.2.2	NGC 4536	97
5.2.3	NGC 1792	97

5.2.4	NGC 1084	97
5.2.5	NGC 1808	98
5.2.6	NGC 520	98
5.2.7	NGC 7552	98
5.2.8	NGC 7632	99
5.2.9	NGC 1614	99
5.2.10	NGC 6240	99
5.2.11	Arp 220	99
5.3	Observations	100
5.4	Results	101
5.4.1	Spectra	101
5.4.2	Continuum and Linemaps	101
5.5	Methods	107
5.5.1	Extinction correction	107
5.5.2	Calculating SNrate	109
5.6	Analysis	110
5.6.1	Age and SNrate	110
5.6.2	Qualitative correlation	110
5.6.3	Quantitative correlation	113
5.7	Dependency on burst model	114
5.8	Comparison to Radio SNrate	116
5.9	Conclusion	118
6	The Herschel Comprehensive (U)LIRG Emission Survey (HerCULES)	119
6.1	Introduction	120
6.2	Observations	121
6.2.1	The HerCULES sample	121
6.2.2	Herschel/SPIRE observations	123
6.2.3	Herschel/PACS observations	124
6.3	Results	126
6.3.1	Spectra and line fluxes	126
6.3.2	Classification of CO ladders	127
6.4	Analysis	133
6.4.1	Warm gas tracers	134
6.4.2	Cooling budget	135
6.4.3	Heating Mechanisms	141
6.5	Conclusion	146
6.6	Acknowledgments	147

7 Outlook	149
7.1 Heating Mechanisms	150
7.2 Mechanical Heating	153
7.3 Modeling ^{12}CO	154
Bibliography	156
Nederlandse Samenvatting	165
Executive Summary	169
List of Publications	173
Curriculum Vitae	175
Acknowledgements	177

1 | Introduction

Stars arise from regions of cool, dense gas and dust that are called molecular clouds. Molecular clouds represent one phase of the interstellar medium (ISM), which comprises of any gas and dust found between stars within a galaxy. After a stars life, if the star is massive, it violently explodes as a supernova, expelling gas dust and processed materials back into the ISM. If the star is not massive, like our Sun, the star will passively shed its outer layers, also returning gas dust and processed materials back into the ISM.

This cycle of stars forming from gas and dust, processing the material throughout the stars lifetime, and then returning the material back into the ISM is what allows stars to interact so strongly with their environments. The star formation cycle occurs with varying degrees of intensity, which shape the surrounding galaxy environment. The lowest star formation intensity occurs in elliptical galaxies, where there is little remaining star-forming gas and thus very few young stars. Here, only the smallest, oldest, and least influential stars remain. A typical, or normal, intensity of the star formation cycle is what we observe in spiral galaxy disks. This environment is most similar to our local galactic neighborhood.

The most extreme star forming cycle results in a starburst, where stars are formed anywhere from 10-1000 times the 'normal' rate. This high intensity cycle can occur throughout an entire galaxy, or in isolated regions within a galaxy. One unique type of star formation cycle is that which occurs in galaxy centers. There, the star formation cycle is not isolated, but influenced by many additional physical processes, from super massive black holes and powerful shock waves to high densities and intense radiation fields. This thesis aims to understand how the extreme conditions of the ISM in luminous galaxy centers are affected by processes related to star formation.

1.1 The Extreme Environments of Galaxy Centers

The centers of galaxies are extreme environments, in which many physical processes are occurring in the same location. In the most extreme objects, such as ultra luminous infrared galaxies (ULIRGs), these processes are particularly violent, and can even be responsible for turning a healthy blue star-forming galaxy into a red and dead one. The extreme centers play a key role in determining the structure and evolution of their host galaxies by flooding the gas and dust with radiation and injecting it with mechanical energy in the form of winds, outflows, supernovae, shocks, and turbulence. Ultraviolet (UV) radiation, dissipating mechanical energy, and higher energy radiation (from X-rays and cosmic rays) are the main physical processes that affect the gas, dust, and eventually, the star formation in these systems. Analysis of the interplay between the various processes lends insight into the regulation of star formation, which determines the evolution of the most extreme environments in the local universe. These processes are magnified in the most extreme galaxies.

1.1.1 Starbursts and (U)LIRGs

Many extreme galaxies are undergoing starbursts. A starburst is a region, in which a large amount of molecular gas is being rapidly formed into massive stars. Compared to a normal star-forming galaxy with a star formation rate of $1 M_{\odot} \text{ yr}^{-1}$, the corresponding star formation rate in a starburst can be anywhere from 10 to $1000 M_{\odot} \text{ yr}^{-1}$. Such galaxies are often in some stage of interaction (i.e. merging), which is thought to ignite an intense episode of star formation (Tinsley & Larson 1978). As a large mass of gas and dust is transported inward, the gas density in the center of the galaxy increases. The increased density spurs the molecular clouds to collapse and form massive stars (Blitz & Shu 1980). The stellar winds and shocks produced by supernovae further compress and disturb the ISM, which may result in yet more star formation. The excessive amount of mechanical energy in the galaxy nucleus often drives outflows that can extend up to a kiloparsec from the disk. It is possible not only for the ionized and atomic, but also for molecular, star-forming gas to escape through these outflows, as seen in the outflow of M82 (Figure 1.1, Engelbracht et al. 2006). Both the outflows and the limited supply of molecular gas will eventually quench the starburst.

(U)LIRGs are an even more remarkable class of objects exhibiting an extremely high amount of infrared luminosity, $L_{8-1000\mu\text{m}} > 10^{11} L_{\odot}$ for LIRGs and $L_{8-1000\mu\text{m}} > 10^{12} L_{\odot}$ for ULIRGs (Genzel & Cesarsky 2000). These galaxies were first proposed as a class after they were observed with the InfraRed Astronomy Satellite (IRAS), which was launched in 1983 (Houck et al. 1985). They all



Figure 1.1: Left: The starburst galaxy M82, observed in the visible wavelength range by NOAO in Tuscon, AZ. Right: The same galaxy (M82) observed in the infrared at 3.6μ (blue), 4.5μ (green), and 8μ (red) with Spitzer IRAC. We observe the molecular outflow in the 8μ , red image, which traces polycyclic aromatic hydrocarbons (PAHs); molecules known to be associated with star formation.

contain massive amounts of molecular gas and more detailed studies of the spectroscopic cooling lines have been carried out with the *Infrared Space Observatory* (ISO, Malhotra et al. 1997; Luhman et al. 1998). The objects are hosts to intense starbursts, active galactic nuclei (AGN) in the form of a rapidly accreting supermassive black holes, and often are part of a merging galaxy group (Barnes & Hernquist 1992). However, regardless of their various energy sources, the energy output of most (U)LIRGs seems to be driven by nuclear starbursts (Genzel et al. 1998; Downes & Solomon 1998; Veilleux et al. 1999; Gao & Solomon 2004). (U)LIRGs are also thought to represent the transitional phase in evolution from starburst disk galaxies to elliptical/lenticular galaxies (Genzel et al. 2001; Tacconi et al. 2002), and thus must quench their star formation some time during this period. The transitional nature of (U)LIRGs, along with their AGN/starburst duality, make these objects ideal for studies of the interplay of heating mechanisms within the ISM.

1.1.2 Structure of the ISM

The ISM is made up of a number main phases, distinguished by different characteristic temperatures, densities, and sizes. The different phases are distributed around the ISM, and are caused by complex interactions between the ISM and the surrounding physical environment. We can generalize the phases of the ISM into six categories (Draine 2011).

- The *Coronal Gas (HIM)* represents shock-heated gas at very high temperatures ($T \geq 10^{5.5}$ K) and very low densities ($\sim 10^{-3}$ cm $^{-3}$). It is often called the hot ionized medium (HIM) and describes about 50% of the ISM in the Milky Way. The HIM does not cool efficiently.
- The *H II Gas (WIM)* is composed mainly of H II and is only slightly cooler ($T \sim 10^4$ K) than the HIM. Interestingly, the ionized medium can span a large range of densities from 10^{-1} - 10^4 cm $^{-3}$. The high density regions are called H II Regions and are heated by energetic photons from massive (O or B) stars. The lower density regions are referred to as the warm ionized medium (WIM) and contain more mass than their high density counterparts, yet are much harder to observe due to their low luminosities. Compared to the HIM, the WIM cools much more efficiently.
- The *Warm H I (WNM)* is made up of mostly atomic gas at temperatures in the thousands of Kelvin and densities ranging from 0.1-1 cm $^{-3}$. Unlike the WIM, the WNM can be heated by many different processes, including ultraviolet (UV) heating from stars, reprocessed radiation from dust, and cosmic rays.
- The *Cool H I (CNM)* is made up of mostly atomic gas but only has temperatures of hundreds of Kelvin. It is also approximately an order of magnitude more dense than the WNM, with densities in the tens of cubic centimeters.
- The *Diffuse H₂* is the first molecular phase, marked by densities high enough for H₂ self-shielding to come into play and allow molecular hydrogen to become abundant. The temperatures are ~ 50 K and densities are > 100 cm $^{-3}$.
- The *Dense H₂* represents self-gravitating molecular clouds of density 10^3 - 10^6 cm $^{-3}$ and temperatures of 10-50 K. It forms only a small fraction of the ISM in the Milky Way, yet it is also the birthplace of stars, and it is what this thesis will focus on.

Although most phases of the ISM fit into one of the above six categories, it is important to note that in reality, the ISM has a fractal-like structure, and is best thought of as a continuum of these phases (Falgarone & Phillips 1990; Norman & Ferrara 1996).

1.2 Diagnostics of heating mechanisms

We can study the affects of certain heating mechanisms by observing the emission lines of gas in the ISM. Star formation and mechanical energy power various heating mechanisms, while atomic and molecular emission lines as well as the infrared continuum emission from dust re-emit the heat back into the ISM, effectively cooling the gas. By studying which cooling lines are bright, and the relative ratios of these lines, we may attempt to identify which processes are heating the gas. There, we focus mainly on molecular cooling lines for a few key reasons. First, the molecular gas is the gas that will eventually form the stars. Second, most of the molecules in the ISM emit in the submillimeter wavelength range, causing the radiation to be unobscured by dust allowing us to probe the dark centers of star-forming clouds. Finally, molecular line emission from the ISM is sensitive to both excitation and chemistry. We can observe many different excitation levels of the same molecule, indicative of the density, temperature, radiation strength, and column density of the emitting species. We can also observe chemistry of the gas, in terms of relative abundance of different molecules, which gives insight into the heating mechanism directly.

1.2.1 Modeling Molecular Emission

In order to determine the physical properties of the ISM, we observe various emission lines, and then use models to determine which combination of physical parameters fit effectively the observed emission. When molecular lines were first detected in galaxies, observations were limited to the ground state transitions of ^{12}CO and ^{13}CO . In order to estimate the excitation of CO, people assumed that the kinetic and excitation temperatures were identical, the observed clouds were in local thermal equilibrium (LTE). This assumption holds in high density regions and it was used to predict the column densities and optical depths of the lines (e.g. Dickman 1975). It quickly became clear that ^{12}CO is almost always optically thick, and that the LTE approximations do not hold. A new method of modeling lines was developed, the so-called Large Velocity Gradient (LVG) model (Sobolev 1960; de Jong et al. 1975; Goldreich & Scoville 1976). This model was able to account for the radiative transport even with optically thick molecules by solving for the excitation and de-excitation rates for each state in a collapsing sphere. Concurrently, there was a lot of work being done on the chemical networks and the ways in which different excitation sources affected the observed line ratios. Specifically van Dishoeck & Black (1988) and Shull & Hollenbach (1978) calculated how UV photons and shocks, respectively, would affect the molecular abundances of the molecular gas.

It was not until the Photodissociation Region (PDR) model (Tielens & Hollenbach 1985) was created that the radiative transfer and chemistry were combined. The PDR models self-consistently model the chemical and radiative balance for a 1-D cloud that is being illuminated by far-UV photons ($6 \text{ eV} < h\nu < 13.6 \text{ eV}$). Kaufman et al. (1999) published tables and diagrams of PDR models, where observational astronomers could simply look up the density and radiation strength necessary to create the observed line ratios. Most observations at the time were well explained by this new method, as they dealt with Galactic star-forming regions, or extragalactic environments similar to those. However, as more observations became available, problems with the model became apparent. Specifically, in galaxy centers, neutral atomic carbon [C I] is consistently stronger in observations than the PDR models can produce (i.e. Israel & Baas 2002). In addition, the accessibility to higher rotational transitions of ^{12}CO and ^{13}CO suggested that the PDR was not enough to produce the observed emission and that the gas appeared to have an additional heating source. Specifically, much of the circumnuclear gas had kinetic temperatures too high to be explained by a PDR model.

Glassgold & Langer (1973) had already suggested that more energetic photons could also heat the molecular gas. Later, Maloney et al. (1996) studied the physical and chemical state of X-ray dissociation regions. Using these calculations, a grid of models for both X-ray and cosmic-ray heating in addition to UV heating was developed (Meijerink & Spaans 2005; Meijerink et al. 2006, 2007). The additional heating from high energy radiation was then used to explain the phenomenon not understood by the PDR models. For instance, the extremely bright ^{12}CO and ^{13}CO in NGC 253 was initially explained by cosmic rays (Bradford et al. 2003). Yet, the [C I] problem still remained. More recently, the bright emission of NGC 253 has been attributed to mechanical heating; caused by shocks or turbulence (Hailey-Dunsheath et al. 2008; Rosenberg et al. 2014). In addition, Loenen et al. (2008) found that mechanical heating is especially important in starbursts and (U)LIRGs. Very recently, mechanical heating has been incorporated into the PDR models (Kazandjian et al. 2012), but in a naive and simple way. Further improvement in the modeling of mechanical heating is still needed. In the following sections, each heating mechanism and accompanying model, will be discussed in great detail.

1.2.2 UV Heating

Clouds surrounding star-forming regions referred to as Photodissociation Regions (PDRs; Hollenbach & Tielens 1999) have a layered structure due to the absorption of the radiation as the depth of the cloud increases, as seen in Figure 1.2. At the surface, the cloud is being irradiated by UV radiation (6-13 eV), and the gas at the

edge is composed mostly of ionized and atomic species (C^+ , O, and H). As column density increases, temperature decreases, and the ionized gas becomes neutral, and then molecular (i.e. $C^+/C/CO$) transition zones. The deepest PDR layer is the main focus of study in this thesis, since this is the region where the molecules are emitting and star formation can occur.

With their PDR models (also used in this thesis), Meijerink & Spaans (2005) calculate the observed relative intensities of various molecules (eg. CO, HCN, HNC, HCO^+), as a function of density, radiation strength, and column density (depth into the cloud). By comparing the models to observations, they estimate the physical properties.

Another strong diagnostic of UV heating are hydrogen (HI) emission lines. The near-infrared HI emission lines suffer relatively little extinction, and are thus particularly useful for tracing star formation. For example, the $Br\gamma$ and $Pa\alpha$ transitions lie in the K and J bands, respectively, and trace the most massive young stars, predominately the O stars. In order to excite the hydrogen emission lines, a star must emit Lyman continuum photons ($\lambda < 912, 13.6$ eV). Thus, bright hydrogen lines suggest high mass star formation.

Similarly, a strong tracer of UV heating in PDRs are the broad mid-infrared (5-15 μm) features attributed to polycyclic aromatic hydrocarbons (PAHs) (Draine & Li 2007; Tielens 2008a). In PDRs, a PAH molecule becomes highly vibrationally excited from absorbing a single UV photon (Mattioda et al. 2005; Draine & Li 2007). Since PAHs are only fluorescently excited, and easily destroyed by harder radiation, they are ideal tracers of heating via PDRs. In addition, PAHs have a lower excitation energy than HI ($\lambda \sim 4200$ for $N_C > 50$ where $N_C > 50$ is the number of carbon atoms; Bakes & Tielens (1994)) and thus are excited not only by O stars but also by slightly less massive, B-type stars. Therefore, the PAH emission traces the more general fluorescently excited population, including excitation by both O and B stars. Finally, large volumes of molecular hydrogen (H_2) can also be fluorescently excited by UV photons (e.g., Black & van Dishoeck 1987), although it is not as straightforward of a tracer since it can also be excited by shocks (e.g., Shull & Hollenbach 1978).

1.2.3 X-ray and Cosmic Ray Heating

Since (U)LIRGs often have an AGN contribution and high star formation rates that lead to high supernova rates, we must also consider gas heating by more energetic radiation. Clouds of gas around accreting supermassive black holes can experience heating by X-rays (1-100 keV) and are then referred to as X-ray Dominated Regions (XDRs; Lepp & Dalgarno 1996; Maloney et al. 1996). Similarly, gas can be heated by highly energetic cosmic-rays that are most often produced in super-

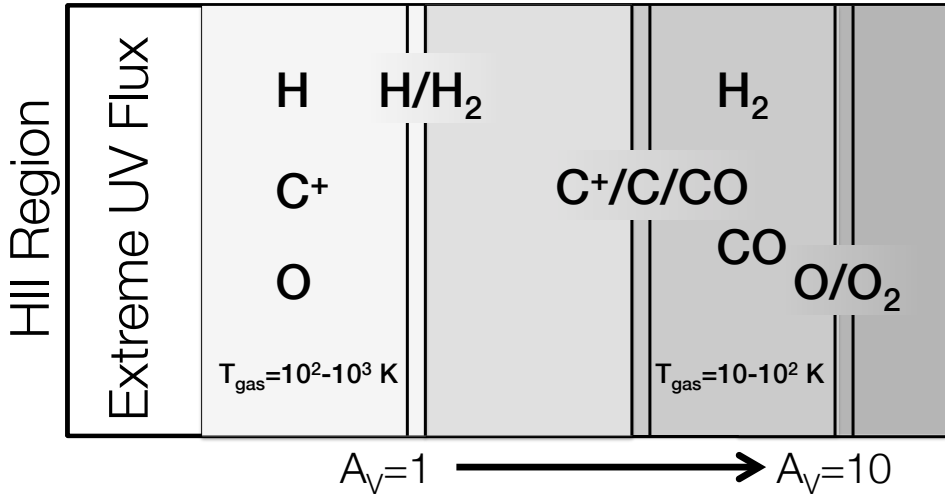


Figure 1.2: Schematic view of a photodissociation region (PDR) as a function of cloud depth. From Hollenbach & Tielens (1999) and Tielens (2005).

novae, and are thus proportional to star formation rate. Unlike UV photons, both X-rays and cosmic rays penetrate deep into clouds ($N_H > 10^{24} \text{ cm}^{-2}$; Meijerink & Spaans 2005; Meijerink et al. 2007). Because of their ability to penetrate deeper than UV photons, XDRs and PDRs with enhanced cosmic-ray ionization conditions (CDRs) lack the layered structure of PDRs and instead show more gradual transitions from ionized to atomic to molecular (Meijerink & Spaans 2005; Meijerink et al. 2006). The cross-section of an XDR is shown in Figure 1.3.

XDRs and CDRs both have a unique chemical signature. Meijerink et al. (2006) show that the ratios of HCN/CO and HCN/HCO⁺ in conjunction with high-J CO lines provide the diagnostic capability to discriminate between the two forms of heating. In addition, Loenen et al. (2008) shows that the HNC/HCN ratio can further discriminate between XDR and PDR heating. Multiwavelength studies of the region can also help determine the feasibility of XDR or CDR heating. X-ray observations between 1-100 keV provide flux estimates, which can be compared to modeling results to determine if the flux is sufficient. Similarly, the cosmic ray ionization rate can be estimated from the star formation rate.

1.2.4 Mechanical Heating

Mechanical heating is a non-radiative heating process that is fueled by various large-scale turbulent motions or shocks. Turbulence is caused by a variety of processes such as massive galactic outflows, merger related shocks, strong stellar winds,

Highly Ionized Region	H	H/H ₂ ~0.01	H ₂
	T~10 ⁴ K	T~2000 K	T<200 K
	C ⁺ ,C	C,C ⁺	CO,C,C ⁺
	O	O	O,OH,O ₂ ,H ² O
	X _e ~10 ⁻² -10 ⁻¹	X _e ~10 ⁻³ -10 ⁻²	X _e <10 ⁻³
	Fe ⁺	Fe ⁺	Fe ⁺ ,Fe

High H_X/n \longrightarrow Low H_X/n

Figure 1.3: Schematic view of a photodissociation region (PDR) as a function of cloud depth. Adapted from Maloney et al. (1996).

rapidly expanding HII regions, or supernova shells. One important result of this thesis is that the chemical signatures observed in the ISM of starburst and (U)LIRGs, cannot be fully explained by any radiative process (Rosenberg et al. 2014) and instead require mechanical heating contribution. The observed temperature of the molecular gas is much higher than expected for clouds heated by a radiative process, so that the only way to effectively heat such large cloud volumes appears to be through mechanical heating processes.

Comparison of PDRs, XDRs (Meijerink & Spaans 2005; Meijerink et al. 2007), CDRs, and mechanically heated PDRs (Kazandjian et al. 2014) to observations of multiple rotational transitions of CO along with a dense gas tracer (i.e. HCN or HNC), provide a strong diagnostic tool. In Chapters 3 and 4, we show that combinations of the rotational transitions of ¹²CO ($1 < J_{\text{upper}} < 13$) with multiple transitions of ¹³CO, HCN, and HNC gives a good means to distinguish between mechanical heating and radiative processes (Rosenberg et al. 2014).

There are other strong diagnostic tracers of mechanical heating at other wavelengths. In particular, the SiO molecule is used to trace shocked material in molecular outflows (Martin-Pintado et al. 1992). In addition, in interstellar space, almost all iron atoms are likewise locked in dust grains, which are destroyed by thermal sputtering in shock fronts from supernovae. This releases the iron into the gas-phase where it is singly ionized by the interstellar radiation field. In the extended post-shock region, [FeII] is excited by electron collisions (Mouri et al. 2000), mak-

ing it also a strong diagnostic shock tracer. H_2 ro-vibrational transitions in the near infrared also show diagnostic capability, although their interpretation is not as straight forward as the [FeII], as emission from fluorescent and shocked gas is sometimes hard to distinguish. In Chapter 2 and 5, we use the near infrared diagnostics to determine the heating source of the star-forming gas.

1.3 In this Thesis

With the launch of the *Herschel Space Observatory*, the molecular universe has been unveiled even more thoroughly than before. The quality and sheer amount of data available is overwhelming and astronomers are just beginning to interpret the data. The high signal-to-noise ratio of the *Herschel* SPIRE and PACS spectra has provided detections of complex molecules not observed before. On the ground, the Atacama Large Millimeter Array (ALMA) has begun science operations. ALMA will provide continued access to molecular observations at unprecedented spatial resolution. Combining the wealth of molecular data with the complex chemical and radiative emission models, astronomers have the opportunity to study the physical properties regulating star formation. In this thesis we use a combination of observations and models to understand the excitation mechanisms acting on the star-forming gas in the extreme environments of galaxy centers.

1.3.1 NGC 253 – An archetypal starburst (Chapter 2, 3)

One of the best nearby laboratories to study extreme star formation is NGC 253, which harbors a starburst in the inner 0.5 kpc Grimm et al. (2003). Employing SINFONI observations of the near infrared H_2 transitions, we determine in Chapter 2 that heating by UV photons, instead of shocks, dominates the overall excitation of hot H_2 in NGC 253 (Rosenberg et al. 2013). Then we identify isolated regions of H_2 bright knots and compare their emission to models of UV and shock heating. We find that in some regions shock excitation can be important and place an upper limit of the emission contributed by shock excited H_2 at 30%. Using PAH emission, we find that not only most H_2 is fluorescently excited, but that it is predominately excited by B-type instead of O-type stars.

In order to distinguish between radiative and shock feedback of cool molecular gas and to achieve a deeper understanding of the star-forming gas in NGC 253, we observe CO and other dense gas tracers using *Herschel*/SPIRE (Chapter 3). We employ a novel and robust fitting routine that takes the observed ^{12}CO , ^{13}CO , HCN, and HNC line emission and compares it to state-of-the-art physical and chemical models. These models, along with observations of CO, HCN, and HNC

fluxes, uniquely discern between UV, X-ray, cosmic ray, or mechanical heating as well as the density and strength of the radiation field. We determine that mechanical heating is necessary to explain the observed emission in NGC 253 and limit the percentage of mechanically heated gas to $\sim 20\%$ by mass (Rosenberg et al. 2014).

1.3.2 Arp 299 – A case study of gas excitation (Chapter 4)

The merging galaxy group Arp 299 is an intriguing case to place boundaries on the usefulness of CO. Arp 299 A (IC 694, NGC 3690) harbors an AGN (Pérez-Torres et al. 2010), Arp 299B is undergoing a starburst (Alonso-Herrero et al. 2000), and Arp 299 C is an extended region of star formation. Using *Herschel*/SPIRE spectra, we extract the CO spectral line fluxes (CO ladders). Simply comparing the general shape of the CO ladders and relative strength of certain emission lines in the spectra of Arp 299 A, B and C, we find that the excitation of the CO in Arp 299 A is very different from that in Arp 299 B and C.

By including PACS observations of high-J CO transitions (up to $J=24-23$) along with ground based observations of HNC and ^{13}CO , we find that once again, mechanical heating is needed to produce the relative intensities of the observed molecular emission, and that the AGN plays a minimal role in heating the gas (Rosenberg et al. in press). We also caution against the use of only ^{12}CO as a tracer of the physical conditions of the molecular ISM.

1.3.3 Tracing shock excitation in star forming galaxies (Chapter 5)

Supernovae are responsible for much of the chemical enrichment of the universe, while simultaneously injecting mechanical energy into the ISM. The supernova rate is usually measured through the non-thermal radio continuum luminosity; however, a correlation between near-infrared [FeII] emission and supernova remnants has also been suggested (Van der Werf et al. 1993; ?).

Using SINFONI NIR observations of a sample of 11 nearby star-forming galaxies spanning a large range of L_{IR} , we determine a quantitative relationship between supernova rate and [FeII] $_{1.26}$ luminosity (Rosenberg et al. 2012). This relation is valid for normal star-forming galaxies but appears to break down for extreme ultra-luminous galaxies.¹

¹A VLT proposal for a follow up study was accepted in order to explore the nature of the correlation in (U)LIRGs, but SINFONI's filter wheel broke and the observations were not obtained. This proposal has been accepted again, and was observed the summer of 2014. Preliminary results show a similar trend for this sample, but an additional follow up proposal will be pursued to improve extinction correction.

1.3.4 Gas cooling in (U)LIRGs (Chapter 6)

Finally, building on our detailed studies of diagnostic excitation tracers in extreme star-forming environments, we perform an observational analysis on a statistically complete sample of (U)LIRGs from the Open Time Key Project *Herschel* Comprehensive (U)LIRG Survey. This sample includes observations with *Herschel*/SPIRE and *Herschel*/PACS, covering all main gas cooling lines, namely [CII] $157\mu\text{m}$, [OI] 63 and $145\mu\text{m}$, [CI] 370 and $609\mu\text{m}$, and CO rotational transitions ($4 < J_{\text{upp}} < 13$). As is in the individual cases of NGC 253 and Arp 299, we find that CO becomes a more efficient coolant when UV heating is weak. This indicates that the CO is more sensitive to alternative heating mechanisms. We present a diagnostic diagram for determining which additional heating mechanism is responsible for the highly excited molecular gas.

2 | The excitation of near-infrared H₂ emission in NGC 253

Because of its large angular size and proximity to the Milky Way, NGC 253, an archetypal starburst galaxy, provides an excellent laboratory to study the intricacies of this intense episode of star formation. We aim to characterize the excitation mechanisms driving the emission in NGC 253. Specifically we aim to distinguish between shock excitation and UV excitation as the dominant driving mechanism, using Br γ , H₂ and [FeII] as diagnostic emission line tracers. Using SINFONI observations, we create linemaps of Br γ , [FeII]_{1.64}, and all detected H₂ transitions. By using symmetry arguments of the gas and stellar gas velocity field, we find a kinematic center in agreement with previous determinations. The ratio of the 2-1 S(1) to 1-0 S(1) H₂ transitions can be used as a diagnostic to discriminate between shock and fluorescent excitation. Using the 1-0 S(1)/2-1 S(1) line ratio as well as several other H₂ line ratios and the morphological comparison between H₂ and Br γ and [FeII], we find that excitation from UV photons is the dominant excitation mechanisms throughout NGC 253. We employ a diagnostic energy level diagram to quantitatively differentiate between mechanisms. We compare the observed energy level diagrams to PDR and shock models and find that in most regions and over the galaxy as a whole, fluorescent excitation is the dominant mechanism exciting the H₂ gas. We also place an upper limit of the percentage of shock excited H₂ at 29%. We find that UV radiation is the dominant excitation mechanism for the H₂ emission. The H₂ emission does not correlate well with Br γ but closely traces the PAH emission, showing that not only is H₂ fluorescently excited, but it is predominately excited by slightly lower mass stars than O stars which excite Br γ , such as B stars.¹

M. J. F. Rosenberg, P. P. van der Werf, and F. P. Israel
A&A 550, A12 (2013)

¹Authors contributed helpful discussion and comments on text and figures.

2.1 Introduction

Understanding the excitation mechanisms and drivers in nearby starburst galaxies is critical to understanding their role in galaxy evolution. One of the best laboratories to study this is NGC 253. This galaxy is a nearby (3.5 Mpc Rekola et al. (2005)), edge-on infrared bright galaxy that is part of the Sculptor group. It is classified as a late-type barred spiral galaxy (SAB(s)c) with star formation confined to the inner 0.5 kpc. The star formation rate of the starburst is $1.4\text{--}9.5 M_{\odot} \text{ yr}^{-1}$ (Grimm et al. 2003). This intense episode of star formation is driven by a 7 kpc bar, which funnels gas into the nucleus (Engelbracht et al. 1998). There is a starburst driven superwind extending perpendicular to the disk (Demoulin & Burbidge 1970; Ulrich 1978; Fabbiano & Trinchieri 1984; McCarthy et al. 1987; Westmoquette et al. 2011).

The inner region of star formation is highly obscured with an A_V of $\sim 5 - 18$ mag (Kornei & McCrady 2009; Fernández-Ontiveros et al. 2009). Many dense, luminous, dust enshrouded young stellar clusters have been found in the nucleus (Forbes et al. 1993, 2000). In addition to the stellar clusters, Alonso-Herrero et al. (2003) and Ulvestad & Antonucci (1997) have observed many compact radio sources in [FeII] and radio respectively, representing young supernova remnants. Turner & Ho (1985) observed over 60 compact radio sources, the brightest of which is named TH2. A high resolution (1"-2") study of the molecular gas in NGC 253 was performed by Sakamoto et al. (2011). They found 5 warm, dense clumps of molecular gas, which are all coincident with radio sources. They suggest that these clumps are natal molecular cloud complexes harboring massive star formation. The K band continuum peak, which was originally defined as the nucleus by Forbes et al. (1991), is the location of a super star cluster. This super star cluster was observed with Hubble Space Telescope by Watson et al. (1996) and is consistent with a single stellar population. In the mid infrared, two bright peaks have been observed in the central regions. The brightest of the two is coincident with the K band continuum peak and super star cluster and has no radio counterpart (Ulvestad & Antonucci 1997). The second, 3.0" to the northeast is coincident to the radio peak TH2. A more recent study by Ulvestad & Antonucci (1997) suggests that TH2 is the true nucleus of NGC 253 and represents either a low-luminosity AGN or a compact supernova remnant.

Although TH2 is generally considered to be the nucleus, a recent study by Müller-Sánchez et al. (2010) provides new estimates for the kinematic center based on the kinematics of the stellar component. Using SINFONI on the VLT, they were able to achieve very high angular resolution and derive the stellar velocity field. They found the kinematic center to be offset from TH2 only by $\Delta x = 0''.6$

and $\Delta y = 0''.4$ (i.e. by 12 pc) in the southwest direction. They propose an alternative position for the kinematic center as the X-ray source X-1 (Weaver et al. 2002). Although NGC 253 has been the target for many detailed kinematic studies, there is still much uncertainty about the precise location of the true kinematic center.

The subject of excitation mechanisms has been extensively studied in NGC 253. Martín et al. (2006) finds that the chemistry and heating of NGC 253 is dominated by large scale, low velocity shocks. Presence of shocked molecular material is indeed evident through the presence of widespread SiO emission throughout the nuclear regions (García-Burillo et al. 2000). Martín et al. (2009b) suggest that, although NGC 253 is dominated by shock chemistry, PDRs play a crucial role in the chemistry, since there are very high abundances of PDR tracing molecules, namely HCO^+ , CO^+ . In addition, they find that although NGC 253 was thought to be at an earlier stage of evolution than M 82, a prototypical starburst with strong PDR characteristics, the molecular clouds are larger and have a higher column density, pointing to a later stage of evolution, such as seen in M 82. Martín et al. (2009a) also find that the UV heating in NGC 253 is more similar to M 82 than other starbursts, yet still not the dominant excitation mechanism. Harrison et al. (1998) used the ortho- to para- ratio of H_2 , to argue that most of the H_2 is excited by PDRs instead of shocks. In addition, Israel et al. (1989); Luhman et al. (1994) show in NGC 604 and Orion A respectively that although in small-beam apertures it may seem as if high surface brightness H_2 emission from shocks is dominant, when the beam size increases, it is clear that fluorescent excitation dominates on large scales.

In this paper, we investigate the excitation mechanisms for the molecular gas in the nuclear region of NGC 253. We use the following methods to differentiate between shock dominated and PDR dominated excitation on a 2 pc scale:

- Calculate the 2-1 S(1)/1-0 (S1) line ratio at each pixel position
- Compare morphology of $\text{Br}\gamma$, [FeII], and PAHs to that of the H_2
- Relate observed H_2 excitation diagrams to those generated by shock and PDR models.

In Section 2.2, we will discuss the observations, while in Section 2.3 we present the derived spectra and linemaps. In Section 2.4 we will investigate and define the kinematic center. Then, in Section 2.5, we investigate the nature of the dominant excitation mechanisms throughout the galaxy, focusing on the dense clumps. In Section 2.6, we compare our excitation diagrams to shock and PDR models spanning the parameter space. We summarize our conclusions and their implications in Section 2.7.

2.2 Observations

2.2.1 SINFONI Observations

All observations were made with the Spectrograph for INtegral Field Observations in the Near-Infrared (SINFONI) at the ESO VLT. SINFONI provides spatial and spectral data in the form of data cubes in J, H, and K bands. The SINFONI instrument is mounted at the Cassegrain focus of the Unit Telescope 4 at the Very Large Telescope (VLT).

We observed in the H, and K bands using a spatial pixel scale of 0.25" corresponding to a field of view of 8"×8" per frame and a spectral resolution of 2000, 3000 and 4000 respectively, which corresponds to a velocity resolution of 149.8, 99.9 and 74.9 km/s. All science observations were taken in the ABA' nodding mode (300s of object, 300s of sky, 300s of object), where A' is slightly offset from A. The object exposures are aligned and averaged during the reconstruction of the data cube.

The observations of NGC 253 were made in visitor mode on August 28th, 2005. In order to capture the full extent of the H₂ emission, consecutive frames were taken in the K band moving further away from the center, along the disk until H₂ was no longer detected. This resulted in 6 separate pointings. Since there are also H₂ transitions in the H band, a similar strategy was used, resulting in 4 separate pointings.

We used the standard reduction techniques of the SINFONI pipeline on all observations, including corrections for flat field, dark current, nonlinearity of pixels, distortion, and wavelength calibration. We obtained the flux calibration and atmospheric corrections from observations of a standard star, namely HR 2058 in the H band and HD 20001 in the K band. This is the same dataset Müller-Sánchez et al. (2010) used to determine the kinematic center.

2.2.2 ISAAC Observations

We use the ISAAC observations of NGC253 in the 3.21 and 3.28 μm filters described by Tacconi-Garman et al. (2005). These observations were uncalibrated. We established a flux calibration for these two images using the ISO-SWS spectra by Sturm et al (2000), taking into account the filter profiles of the two ISAAC filters and the precise location and orientations of the ISO-SWS aperture. Inspection of the spectrum by Sturm et al (2000) shows that the 3.21 μm filter contains only continuum emission, while the 3.28 μm filter contains continuum+PAH emission. The peak of the PAH emission is at 3.3 μm , which is fully included in the 3.28 μm filter. The spectral slope is small enough that there is negligible change in con-

tinuum level between 3.21 and 3.28 μm and therefore a PAH emission image was created by subtracting the calibrated 3.21 μm image from the calibrated 3.28 μm image.

2.3 Results

The SINFONI datacubes allow us to construct continuum maps, line maps and velocity maps of emission lines detected in these bands. The K band continuum map and H₂ 1-0 S(1) emission line map are shown in Figure 2.1 and the Br γ and [FeII]_{1.64} emission line maps are shown in Figure 2.2. All line maps are centered on the kinematic center proposed by Müller-Sánchez et al. (2010). We have chosen 8 regions defined by the most dominant H₂ peaks and these regions are overplotted by white rectangles in each map. There is an additional region centered on the kinematic center. All regions are 12 \times 12 pixels or 1.5 \times 1.5 arcseconds. These regions were selected based on H₂ flux. There is a relatively bright H₂ emission clump to the north west of Region 1, which was not selected for analysis since it shows similar emission features to Region 1.

The K band continuum map reveals the inclined disk of the galaxy, tracing the older stellar population. The disk appears irregular with clear clumps of high luminosity. The kinematic center (Region 3) shows a very high level of continuum emission. In addition, superimposed on the bright continuum emission around the kinematic center, there is a bright flux peak at the location of the super star cluster (Region 2) studied by Watson et al. (1996).

On the other hand, the H₂ 1-0 S(1) map shows a completely different morphology. The H₂ extends along the entire disk with its brightest clump located several arcseconds east of the kinematic center (Region 3). However, the H₂ is even more inhomogeneous than the K band continuum. There are clear H₂ bright clumps ranging out into the furthest regions. The white rectangles highlight the brightest emission clumps. There is also significant H₂ emission originating from the super star cluster (Region 2), but not from the center.

Similarly, comparison of the H₂ and the Br γ map reveals little correlation. The Br γ flux peak is coincident with the super star cluster, but shows no clear flux increase near Region 4, where H₂ is brightest, nor at the center. The Br γ is also generally less extended than the H₂, with most of the emission in the southwestern portion of the galaxy, centered on the super star cluster.

The [FeII]_{1.64} map also reveals emission peaking near, but not coincident with, Region 4. In the northeastern regions, the [FeII] emission is also quite clumpy, with some of the clumps coinciding with the H₂, such as Regions 5, 7 and 8. Comparing the [FeII] to the Br γ emission, we see in both cases, as well as in the

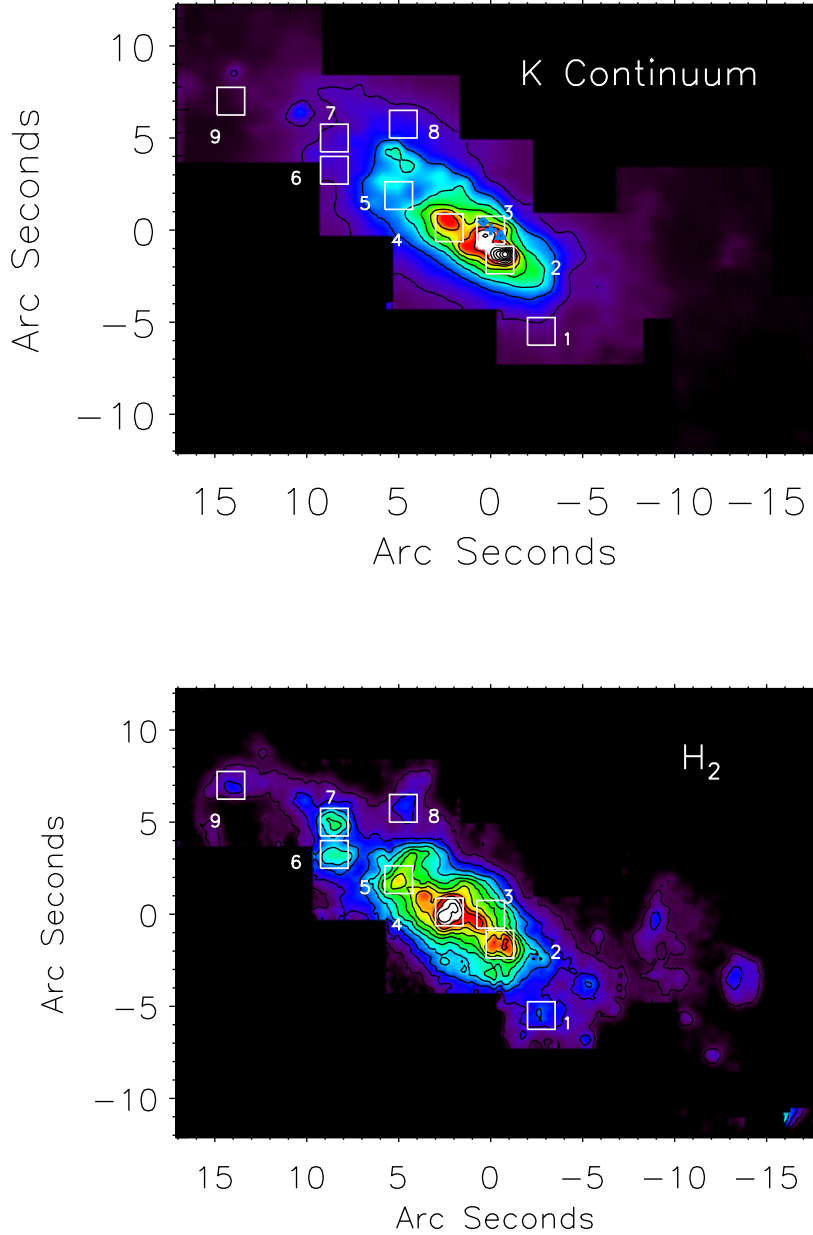


Figure 2.1: K band continuum map and H₂ 1-0 S(1) line map of NGC 253. The offset from the kinematic center at position $(\alpha, \delta)_{2000} = (00^h 47^m 33^s.14, -25^\circ 17' 17''.52)$ is given on each axis. The contours represent 13 equally spaced levels with a maximum flux of $1.3 \times 10^{-11} \text{ erg s}^{-1} \text{ cm}^{-2} \mu\text{m}^{-1} \text{ arcsec}^{-2}$ and $5.4 \times 10^{-15} \text{ erg s}^{-1} \text{ cm}^{-2} \text{ arcsec}^{-2}$, for the K band continuum and H₂ respectively. The white rectangular regions are H₂ flux peaks, with the exception of Region 3, which is centered on the kinematic center. The blue '+' represents the kinematic center, the blue triangle represents X-1 and the blue diamond represents TH2.

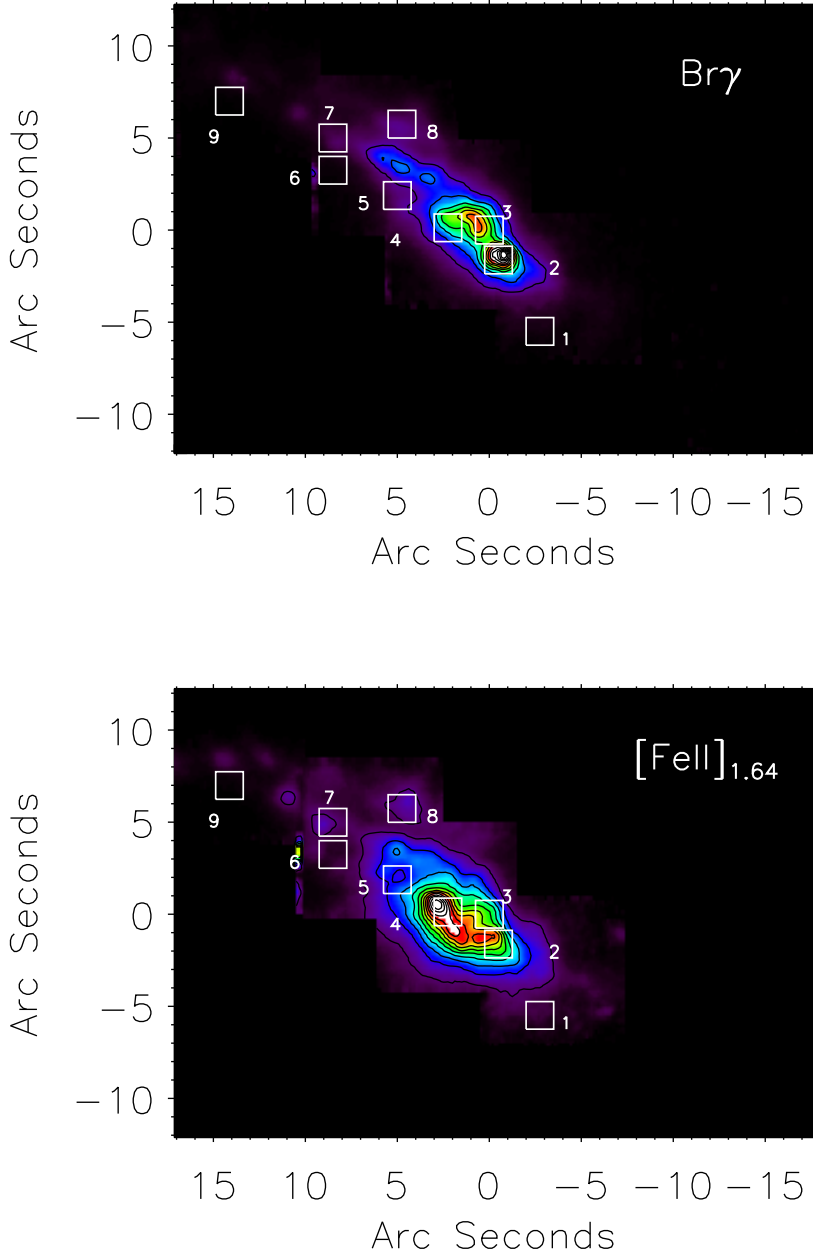


Figure 2.2: $\text{Br}\gamma$ and $[\text{FeII}]_{1.64}$ emission line map of NGC 253. The offset from the kinematic center at position $(\alpha, \delta)_{2000} = (00^{\text{h}}47^{\text{m}}33^{\text{s}}.14, -25^{\circ}17'17''.52)$ is given on each axis. The contours represent 13 equally spaced levels with a maximum flux of 4.5×10^{-14} and 2.8×10^{-14} $\text{erg s}^{-1} \text{cm}^{-2} \text{arcsec}^{-2}$ for $\text{Br}\gamma$ and $[\text{FeII}]$ respectively. The white rectangular regions are areas of concentrated H_2 flux, with the exception of Region 3, which is centered on the kinematic center.

K continuum, an elongated arm-like feature coming from the center, curving out towards the northeast corner along the disk, bordering on the northern edge of Region 5. However the [FeII] feature is spatially offset towards the south with respect to the Br γ feature, as noted originally by Forbes et al. (1993). The H₂ and continuum emission in this region traces neither Br γ or [FeII].

Figure 2.3 displays the rest-frame K band spectra, integrated over the regions shown on the H₂ map (Figure 2.1). The main emission lines are highlighted. Specifically, we see many H₂ transitions as well as Br γ and HeI. The highest energy H₂ transition detected is the 3-2 S(3) transition. This is located at 2.2008 μm and only marginally visible in Region 8 of Figure 2.3, although we have 2σ detections of it in Regions 1, 2, and 3. This is an important detection since this transition can only be excited by high energy photons, and therefore points towards fluorescent excitation. In Table 2.1 we present the integrated fluxes and fluxes in each region of all detected H₂ lines with error bars. These error bars were derived by calculating the flux for a range of different continuum baselines and finding the standard deviation of these values. We also attempted to extract H₂ line fluxes from transitions in the H band, yet the stellar absorption features overpowered the emission lines and we were unable to get reliable flux measurements.

Using the SINFONI data cubes, we can extract both a gas and stellar velocity map. Figure 2.4 displays the stellar velocity field with the H₂ molecular gas velocity field in contours. The stellar velocity field was calculated by fitting the three stellar CO photospheric absorption features. Fitting with a set of 6 template stars (K3V, M0III, M0V, M4V, M5III and M5II), we used the Cappellari & Emsellem (2004) Penalized Pixel Fitting (PPXF) package. All the template stars were observed with SINFONI on the same settings as the NGC 253 observations. In addition, the pixels were binned using a Voronoi tessellation (Cappellari & Copin 2003), with a signal-to-noise of 50 per bin. These binned spectra were then fit with the best combination of the 6 template stellar spectra varying velocity and dispersion. Then, the systemic velocity of the galaxy, 243 km/s, was subtracted from the velocity field.

2.4 The Kinematic Center of NGC 253

The stellar velocity field and the H₂ velocity field show many general similarities, especially in the central region. Specifically, both the stellar and gas velocity fields show an 'S'-shaped morphology in the velocity contours in the 0 km/s range. This morphology is typical of galaxies with a bar potential, and supports the claim of a bar potential in NGC 253.

Since the H₂ velocity field is much cleaner than the stellar velocity field and

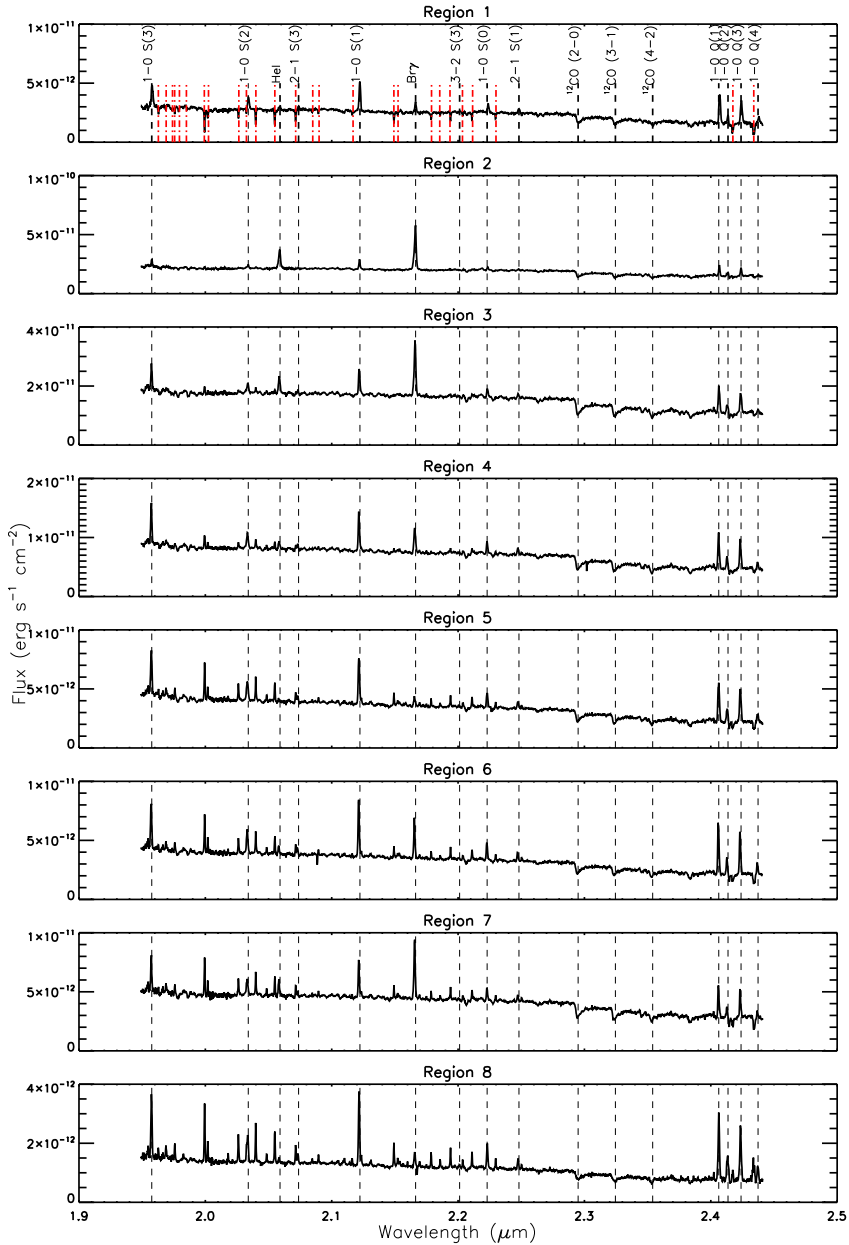


Figure 2.3: K band spectra of H_2 bright clumps. The integrated K band spectra, in the rest frame, integrated over the regions shown in Figure 2.1. Vertical dotted lines are used to show dominant emission lines. The strongest OH lines have been marked in the spectrum of Region 1 with the red dot-dash line. The ^{12}CO absorption bands are also visible at 2.294, 2.323, and 2.353 μm respectively. Region 2 is the K Continuum peak and hot spot, Region 3 is the kinematic nucleus, and Region 4 is the H_2 emission peak.

Table 2.1: Integrated fluxes for selected regions and over the full map of all detected H₂ transitions. For the regions the units of flux are 10⁻¹⁵ erg s⁻¹cm⁻². Only detections above 3σ are reported with the exception of 1-0 Q(4), where we report all fluxes over 2σ. The errors on the integrated fluxes represent 1 standard deviation. Each region is 12×12 pixels, or 1.5×1.5 arcseconds.

	1-0 S(0)	1-0 S(1)	1-0 S(2)	1-0 S(3)	2-1 S(1)	2-1 S(3)	3-2 S(3)	1-0 Q(1)	1-0 Q(2)	1-0 Q(3)	1-0 (Q4)
Region 1	0.7±0.03	2.8±0.07	1.0±0.08	2.6±0.3	0.5±0.1	0.2±0.04	0.1±0.01	2.8±0.3	0.7±0.1	2.6±0.4	--
Region 2	2.8±0.1	10.2±0.3	4.9±0.9	5.3±1.2	1.3±0.4	1.0±0.05	0.4±0.1	10.7±1.2	5.3±1.1	11.2±1.3	3.4±1.3
Region 3	2.6±0.2	8.3±0.2	4.3±0.9	4.0±1.1	1.4±0.1	0.9±0.04	0.4±0.1	9.3±1.0	4.5±1.2	10.2±1.3	2.6±0.9
Region 4	3.8±0.2	12.3±0.2	6.0±0.8	7.5±0.9	2.0±0.09	0.9±0.05	0.3±0.1	12.8±1.1	4.8±1.3	13.2±1.3	3.2±1.0
Region 5	2.6±0.08	8.5±0.2	4.2±0.3	6.7±0.5	1.3±0.04	--	--	8.2±0.5	2.5±0.7	8.0±0.7	1.7±0.7
Region 6	1.3±0.1	4.3±0.8	2.2±0.1	3.1±0.5	0.6±0.01	--	--	4.0±0.2	1.0±0.3	3.8±0.3	--
Region 7	1.7±0.07	5.1±0.1	2.5±0.1	3.3±0.5	0.7±0.02	--	--	4.8±0.4	--	4.6±0.4	--
Region 8	0.5±0.03	1.6±0.03	0.9±0.07	0.8±0.3	0.2±0.01	--	--	1.5±0.1	--	1.4±0.2	--
Region 9	0.3±0.009	0.8±0.009	0.4±0.02	0.5±0.1	0.07±0.003	0.03±0.003	--	0.8±0.08	0.4±0.05	0.7±0.06	0.3±0.1
Integrated	100±50	380±50	140±30	250±40	50±20	30±9	6±4	370±20	140±20	320±40	120±40

they share a similar morphology, we will use the H₂ velocity to estimate the kinematic center of NGC 253. In order to estimate this position, we create a mirrored reflection around a set of central points that could be the center. By subtracting this mirrored map from the original map, we can find which pixel provides the most symmetric profile. Using this method, we can determine the center pixel, or the pixel with the most symmetry. To determine the absolute coordinates of this pixel, we employ the 2MASS K band image of NGC 253. We anchor the SINFONI observations to the 2MASS observations by finding the position of the K-band peak. We then use the offset of the kinematic center to the K band center to determine the absolute coordinates, $(\alpha, \delta)_{2000} = (00^h 47^m 33^s.084, -25^\circ 17' 18''.42)$. Müller-Sánchez et al. (2010) find the kinematic center at $(\alpha, \delta)_{2000} = (00^h 47^m 33^s.14, -25^\circ 17' 17''.52)$ with a mean 3σ error of $r=1.2''$. Thus, our center is within this error and in good agreement with their result. The difference between the two results is due to the method. Muller-Sanchez used an inclined disk model to find their kinematic center, however the symmetry argument focuses on finding the point of highest symmetry. This method is compromised due to two symmetric circular regions in the velocity field, the top circle is located within the red error circle and the symmetric counterpart is just below it and appears green. Our method finds the center to be just between these two circles, at the radius of the Muller-Sanchez error radius, represented as a square. Due to this symmetric point, we consider the Muller-Sanchez center to be the true kinematic center, which is also clear from the inflection point of the bar profile 'S' shape seen in the H₂ velocity field. Since the H₂ inflection point coincides perfectly with the Muller-Sanchez center, it proves that there is no true offset between the H₂ and CO measured centers. We therefore independently confirm the kinematic center proposed by Müller-Sánchez et al. (2010). In Figure 2.4, the H₂ 1-0 S(1) velocity map is presented with the Müller-Sánchez et al. (2010) 3σ center circled in red and their proposed kinematic center

overlaid with a white plus sign. For completeness, the radio peak TH2 and the x-ray peak X-1 are both overplotted as a diamond and triangle respectively.

2.5 Gas Excitation Mechanisms in NGC 253

In general, the morphologies of the K band continuum, H_2 , $Br\gamma$, and $[FeII]_{1.64}$ emission are dissimilar. None of the peaks are coincident with each other with the exception of the K band and $Br\gamma$ peaks at the super star cluster. There are certain regions where the H_2 matches the $Br\gamma$, while some H_2 clumps match the $[FeII]_{1.64}$ emission. This suggests that the H_2 , $Br\gamma$ and $[FeII]$ are being excited through different physical processes.

The $Br\gamma$ peak, tracing massive, young star formation, is coincident with the K band continuum peak, at the location of the super star cluster. In general, the K band continuum traces the older medium and low mass populations of stars in contrast to the youngest, most massive stars powering the $Br\gamma$ emission. There is extended emission in the northeastern direction of the $Br\gamma$ peak, but no other strong emission regions.

$[FeII]$ is another strong NIR diagnostic line, which traces shocks. In interstellar space, iron atoms are typically fully locked into dust grains. Shock fronts associated with supernova remnants (SNRs) may cause very efficient grain destruction through thermal sputtering (Jones et al. 1994). This releases the iron into the gas-phase where it is singly ionized by the interstellar radiation field (Mouri et al. 2000). In the extended post shock region, Fe^+ is excited by electron collisions, rendering it a strong diagnostic shock tracer. The $[FeII]$ peak is located slightly northeast of the H_2 peak (Region 4). It shows diffuse emission consistently along the disk, but does not show any peak at Region 2, the location of the super star cluster. From Rosenberg et al. (2012) we can calculate the supernova rate (SNrate) from the $FeII$ luminosity. In Table 2.2 the calculated SNrates for each region and the whole galaxy is given. The small amount of $[FeII]$ flux and correspondingly low supernova rate suggests that the super star cluster in Region 2 is a young cluster. Fernández-Ontiveros et al. (2009) suggests that Region 2 is a starburst of 6 Myrs, which is also consistent with our age calculations. Our integrated supernova rate in the inner 300 pc of the galaxy, is 0.2 yr^{-1} , which is well matched to previous supernova rate measurement of 0.1-0.3 (Rieke et al. 1980, 1988; Ulvestad & Antonucci 1997).

Unlike $Br\gamma$ and $[FeII]$, the mechanism which excites the H_2 gas is not as clear. The NIR is rich with ro-vibrational H_2 lines, which can either be excited thermally, through shocks, or by fluorescence, through UV photons from O and B stars. In the case of shock excited H_2 emission, the gas is thermalized and the energy levels

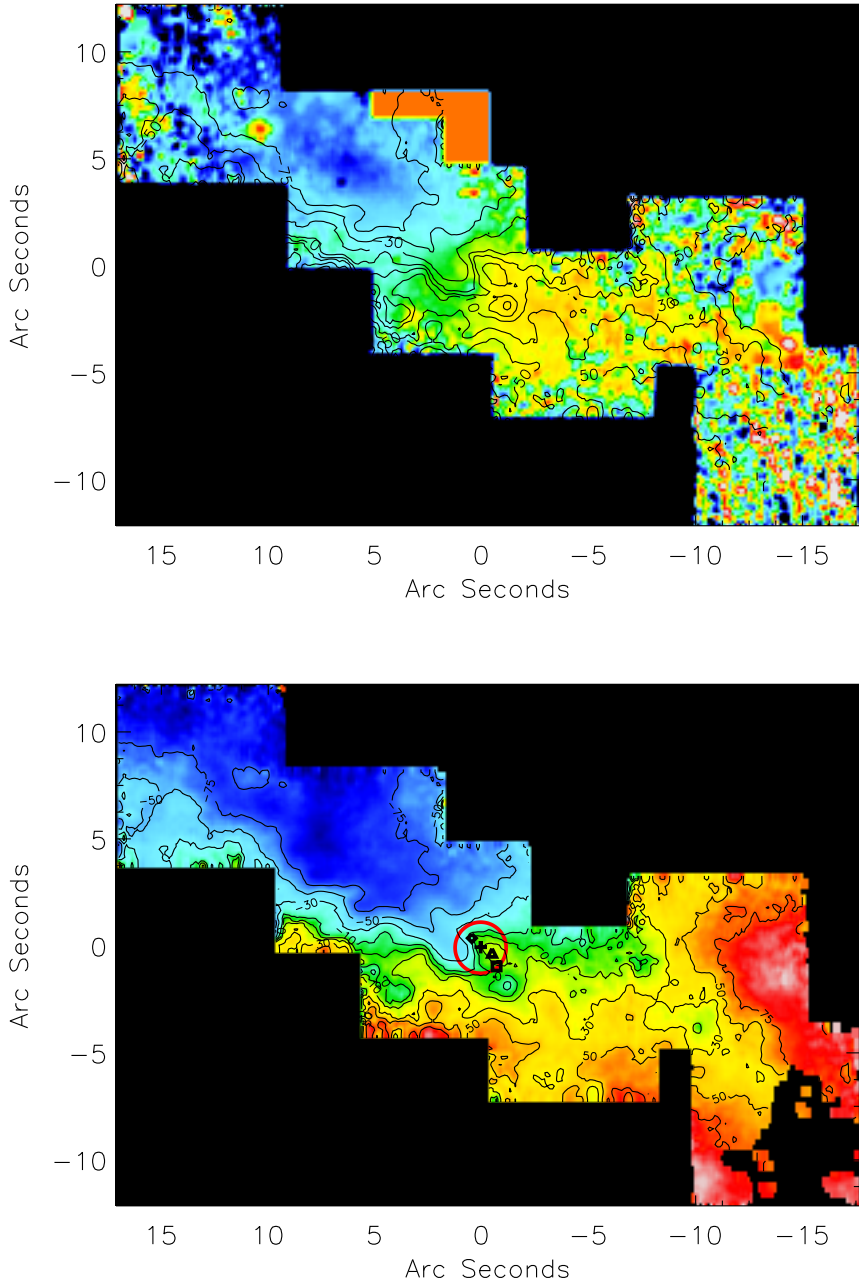


Figure 2.4: Stellar velocity field (left) with H₂ 1-0 S(1) velocity contours and H₂ 1-0 S(1) velocity map with contours (right). The contour levels are -75, -50, -30, -10, 0, 10, 30, 50, 75 km/s. The color bar describes the H₂ and stellar velocity in km/s. On the right panel, the red circle represents the 3σ uncertainty for the center defined by Müller-Sánchez et al. (2010). The plus sign is the center of this circle, and the kinematic center. The diamond is TH2, the radio peak. The triangle is X-1, the X-ray peak. The square is the point of highest symmetry.

are populated in a "bottom-up" manner. The resulting gas temperature is around 1000 K and thus there is little H₂ emission from the $v \geq 3$ states, which have temperatures above 15,000 K. However, in the case of excitation by UV photons, the H₂ molecule absorbs a highly energetic photon and is excited to an upper electronic energy level and then proceeds to cascade downwards. This is considered populating the energy levels from the "top-down", which results in exciting higher H₂ energy levels. In this way, we can use the ratio of certain H₂ lines to discriminate which excitation mechanism is exciting the H₂ emission. However, the case of UV excitation is sometimes degenerate. In the case of high density, the molecules can collide frequently enough to become thermalized in the lower energy levels, which results in line ratios equivalent to the case of shock excitation. For the lines to be thermalized, the density in the region must be comparable to the critical density of the lines, $1.7 \times 10^5 \text{ cm}^{-2}$ for 1-0 S(1) and $1.2 \times 10^5 \text{ cm}^{-2}$ for 2-1 S(1) (Sternberg & Dalgarno 1989).

In order to determine which excitation mechanisms are dominating which regions, we can use the information from the Br γ and [FeII] tracers. Specifically, if the H₂ is undergoing excitation by UV photons in a dense environment, this region should also be bright in Br γ emission if the excitation is by O stars. Conversely, if the H₂ is being excited by shocks, then the [FeII] emission might also be bright in this region.

In Region 2, coincident with the Br γ peak, UV photon excitation is the dominant mechanism and the density of this region is accounting for the lower excitation levels being populated leading to the lower H₂ line ratio. In Region 6, there is little Br γ emission. However, the [FeII] emission shows a bright clump. Therefore, in this region the emission lines suggest that the H₂ is being excited by shocks. However, in the other regions, there is both diffuse [FeII] and diffuse Br γ . In this case, we cannot determine the dominant mechanism by only studying the Br γ and [FeII] emission. Since H₂ can also be excited by slow shocks, too slow to destroy dust grains, or by B stars, which are not energetic enough to excite Br γ , we must use other diagnostics to probe the excitation mechanisms.

One diagnostic is the 2-1 S(1) to 1-0 S(1) transitions at $2.2478 \mu\text{m}$ and $2.1218 \mu\text{m}$ respectively. This line ratio is commonly used because both lines are relatively bright and have similar wavelengths, so they can usually be taken in the same spectrum and suffer identical extinctions. Predictions for the ratio of these two lines due to excitations by shocks range from 0.1 to 0.2 (Shull & Hollenbach 1978), while for photo-excitation it is predicted to be 0.53-0.56 (Black & van Dishoeck 1987).

Table 2.2: Calculated supernova rates for each region and the integrated galaxy based on [FeII] luminosity. The integrated value is integrated over the full map. Supernova rates were calculated with the relation between [FeII] luminosity and SNrate from Rosenberg et al. (2012).

Region	[FeII] Luminosity $10^{37} \text{ erg s}^{-1}$	SNrate 10^{-3} yr^{-1}
Region 1	0.3	0.04
Region 2	0.3	0.04
Region 3	9.8	1.6
Region 4	11.3	1.8
Region 5	17.1	2.8
Region 6	4.1	0.7
Region 7	0.3	0.04
Region 8	0.5	0.08
Region 9	0.4	0.06
Integrated	140.9	23.5

2.5.1 Shocks vs Fluorescence

In Figure 2.5, we present a map of the 2-1 S(1)/1-0 S(1) ratio with the contours of the Br γ line map and the rectangular regions from Figure 2.1 overlaid. The 2-1 S(1) line is significantly weaker than the 1-0 S(1) transition thus this image has less signal-to-noise. We have therefore applied a mask to the map, filtering out values lower than 10% of the maximum flux for both line transitions. The values of the 2-1 S(1)/1-0 S(1) ratio range continuously from 0 to 0.5, showing that we have both thermalized and fluorescently excited gas in the galaxy. Both the mean H₂ ratio for each region and the ratio of the integrated 2-1 S(1) and 1-0 S(1) line fluxes is listed in Table 2.3. The discrepancy in these two values is due to the fact that in the left column, we find the mean value of the H₂ ratio at each pixel for each region, whereas in the right column we first integrate the flux in each region for the two lines, and then divide the fluxes. The latter method is more sensitive to high surface brightness quantities, and shocks excited material has higher surface brightness than that of fluorescent excitation (Shull & Hollenbach 1978). Therefore, the values in the right column are weighted towards shock excitation, and thus show lower ratios for each region. Averaging the ratio on a pixel-by-pixel basis, as done in the left column, does not present such a bias. In regions with very high ratios (≥ 0.3) we can confidently conclude that the molecular hydrogen is being excited by UV photons from O and B stars. Similarly, there are a few regions where the ratio is distinctly lower than the average value of ~ 0.2 . These regions

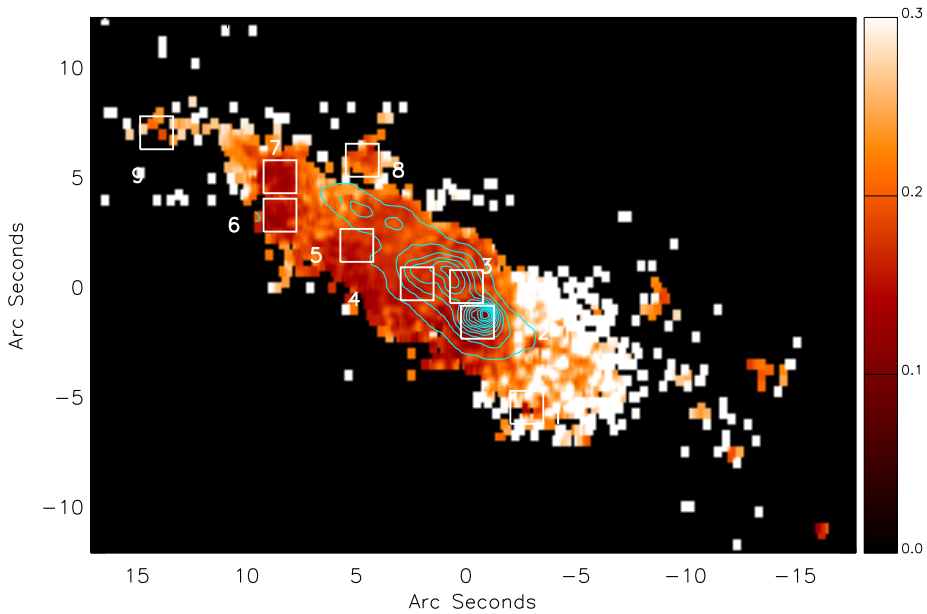


Figure 2.5: The ratio of 2-1 S(1)/1-0 S(1) H₂ lines with the Br γ line map over plotted in contours. The white rectangles are the same regions as defined in Figure 2.1. The color bar values represent the value of the ratio. The offset from the kinematic center at position $(\alpha, \delta)_{2000} = (00^h 47^m 33^s.14, -25^\circ 17' 17''.52)$ is given on each axis. Ratio values where the line flux of either transition is below 10% of the maximum flux of that line are masked.

Table 2.3: Mean H₂ 2-1 S(1)/1-0 S(1) line ratios in each region of Figure 2.8 (left column) and the ratio of the 2-1 S(1) and 1-0 S(1) fluxes (right column). The integrated value is integrated over the whole map.

Region	$\left(\frac{2-1S(1)}{1-0S(0)}\right)$	$\frac{\sum 2-1S(1)}{\sum 1-0S(0)}$
Region 1	0.26±0.01	0.17±0.04
Region 2	0.14±0.02	0.13±0.04
Region 3	0.17±0.03	0.17±0.01
Region 4	0.16±0.02	0.16±0.01
Region 5	0.17±0.02	0.15±0.01
Region 6	0.15±0.02	0.14±0.003
Region 7	0.15±0.04	0.15±0.01
Region 8	0.21±0.02	0.16±0.003
Region 9	0.23±0.01	0.08±0.01
Integrated	0.27±0.06	0.13±0.06

are region 2, 6, and 7 from Figure 2.5. It is interesting to note that these bright regions all correlate with an H₂ clump or luminosity peak. In these regions we cannot determine whether the low H₂ line ratio is indicating excitation by shocks, or a very dense clump being excited by UV photons. However, we can place an upper limit on the amount of shocked gas. Assuming that all gas with a 2-1 S(1)/1-0 S(1) ratio lower than 0.2 is shock excited, we see that 48% of the total 1-0 S(1) H₂ flux may be from "shocked" gas. However, this percentage is including all regions with a ratio lower than 0.2, including regions of high density where the gas is fluorescently excited but thermalized. We can at least partially separate this effect by filtering out the pixels with the highest Br γ flux ($\geq 1 \times 10^{-16}$ erg s⁻¹ cm⁻²), since these regions are dense regions of known fluorescent excitation. As seen in the Br γ contours in Figure 2.5, this affects Regions 2, 3, and 4. Excluding these regions and any pixel with high Br γ flux, no more than 29% of all H₂ is shock excited, and the actual amount may be less.

2.5.2 Tracers of Fluorescence

If strong shocks dominate the excitation of H₂ in NGC 253, we would expect to see a good correlation between H₂ and [FeII], which we do not. If fluorescence is the dominant mechanism, we would expect the Br γ morphology to share more similarities with that of the H₂. We also see no correlation between H₂ and Br γ emission. However, Br γ only traces the most massive and young stars, predominately the O stars. In order to excite Br γ , the star must emitting Lyman continuum

photons ($\lambda < 912, 13.6$ eV), yet H_2 can be excited by lower energy photons as well ($\lambda < 1100, 11.2$ eV).

Similarly to H_2 , polycyclic aromatic hydrocarbons (PAHs) have a lower excitation energy than HI ($\lambda \sim 4200$ for $N_C > 50$ where $N_C > 50$ is the number of carbon atoms; Bakes & Tielens (1994)) and thus are excited not only by O stars but also by slightly less massive, B-type stars. Therefore, the PAH emission traces the more general fluorescently excited population, including excitation by both O and B stars. By comparing the morphology of the H_2 to that of PAH emission, we can determine if it is indeed the B stars that are predominately responsible for exciting the H_2 regions, and why neither the $Br\gamma$, [FeII] or K band continuum matches its morphology.

In Figure 2.6, we present an ISAAC continuum subtracted PAH map at $3.21\mu\text{m}$. The left panel is overlaid with H_2 1-0 S(1) contours, the middle panel is overlaid with $Br\gamma$ contours, and the right panel is overlaid with [FeII] $_{1.64}$ contours. The two maps were centred with respect to one another by matching the K band continuum peak of the SINFONI maps to the 3.21 continuum peak of the ISAAC continuum maps.

From these images, the morphology of the PAH emission matches the H_2 emission, better than both the $Br\gamma$ and [FeII]. The $Br\gamma$ peak is coincident with secondary PAH peak, meaning that in this region, there are many O stars producing photons $E > 13.6\text{eV}$. However, there is little $Br\gamma$ emission coincident with the primary PAH peak, showing that these regions are mainly excited by B stars. The [FeII] peak shows little similarity to the PAH emission. However, the H_2 peaks are coincident with both the primary and secondary PAH peaks and shares a generally similar morphology in the diffuse PAH emission. It is interesting to note that the elongated feature seen in the K Continuum, [FeII] and $Br\gamma$ maps in Figure 2.2, is also present in the PAH map, but not in the H_2 . Since we still have a high amount of diffuse emission in this region, it is most likely that there is H_2 emission originating from this feature, but it is just relatively dimmer than the nearby H_2 peaks, which therefore overshadow it.

In order to test this correlation in a more quantitative sense, we can perform a pixel-pixel analysis of the correlation of our line maps to that of the PAH $3.21\mu\text{m}$ emission. After re-binning the ISAAC PAH map to match the pixel size of SINFONI, we plot the flux of H_2 , $Br\gamma$ and [FeII] as compared to the PAH flux. Figure 2.6 depicts these correlation plots, which show how well H_2 , $Br\gamma$ and [FeII] correlate with the PAH flux. The $Br\gamma$ vs PAH plot shows an interesting morphology, in which the emission seems to be coming from two different areas. First, there is an approximately linear correlation for lower $Br\gamma$ fluxes. This correlation is most likely due to the diffuse $Br\gamma$ emission caused by the same photons excit-

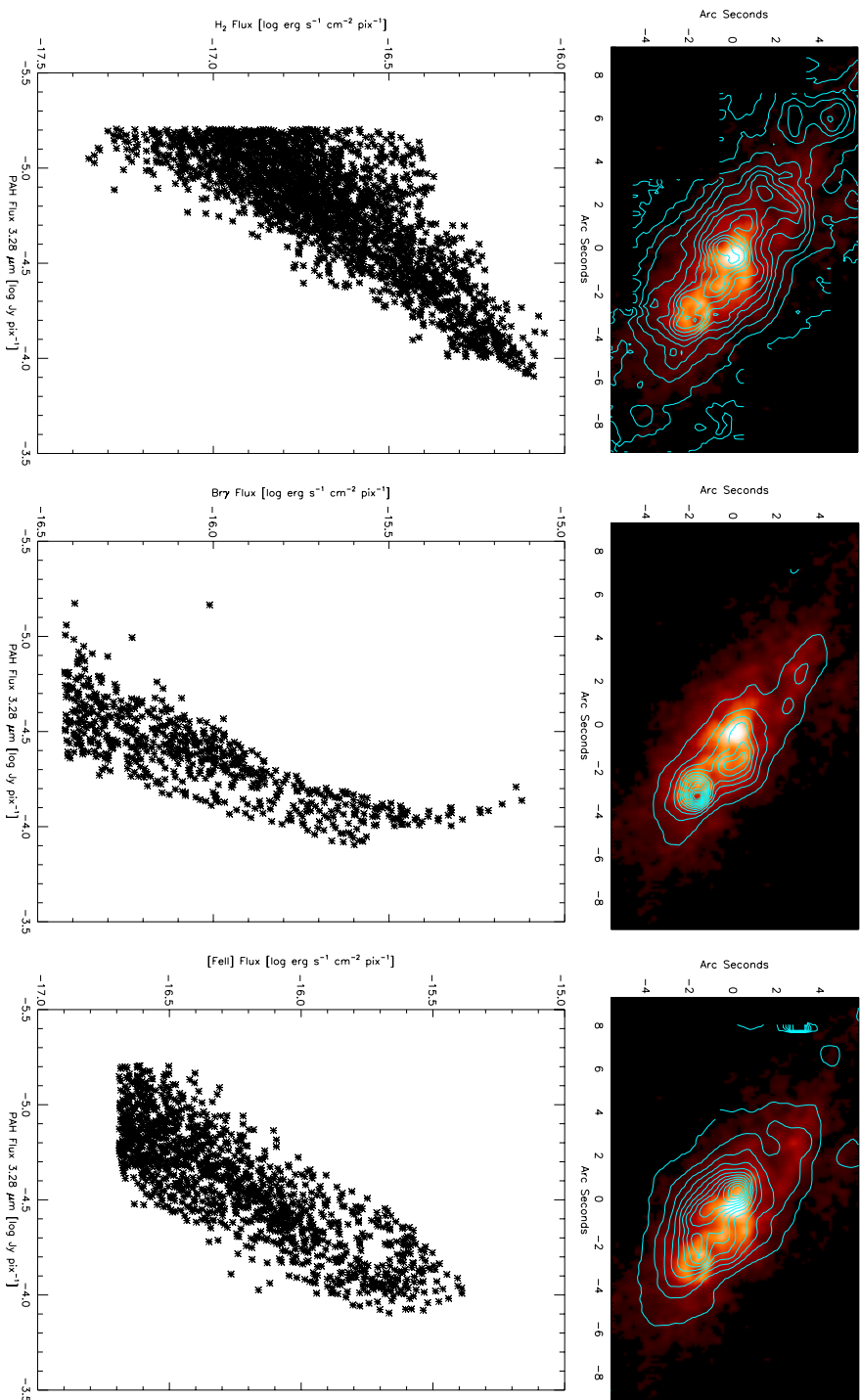


Figure 2.6: Top Panels: PAH 3.28 μm continuum subtracted image from ISAAC. Left panel has H_2 1-0 S(1) contours, middle panel has $Br\gamma$ contours, right panel has $[FeII]_{1.64}$ contours. The offset from the kinematic center at position $(\alpha, \delta)_{2000} = (00^h 47^m 33^s 14, -25^\circ 17' 17''.52)$ is given on each axis. The kinematic center is from Müller-Sánchez et al. (2010). Bottom Panels: Pixel-pixel plots of PAH flux vs H_2 flux (left), $Br\gamma$ flux (center), and $[FeII]$ flux (right). The pixels of the ISAAC PAH observations were rebinned to match those of the SINFONI observations.

ing the PAHs. However, there is a second, non-linear, nearly vertical component of extremely high Br γ flux and medium strength PAH flux. These points correspond to the location of the super star cluster, which is only the secondary flux peak for PAH, but the dominating source of Br γ flux. The [FeII] also seems to correlate with PAH flux with a large, but constant spread, suggesting that these tracers originate in the same general region but without a direct physical correlation, emphasized by the displacement of the [FeII] peak and the PAH peak. The H $_2$ also shows a linear correlation with the PAH flux. However, this correlation has a very large spread at low fluxes and gets continually tighter as both H $_2$ and PAH fluxes increase. We can see this same trend in the morphologies as well. There is a strong correlation, both spatially and numerically for the peaks of the H $_2$ and PAH linemaps, however in the diffuse regions the correlation no longer holds.

The strong, linear correlation between H $_2$ and PAH morphology in the central region of NGC 253 gives added confidence that most of the central emission in NGC 253 (Regions 2, 3, and 4) is fluorescently excited. In addition, the correlation between the PAH morphology and H $_2$ morphology indicates that the H $_2$ in this area, is being excited by the same stars that are exciting the PAHs, mainly B-type stars.

2.6 PDR and Shock Models

Although the morphological correlation of H $_2$ to fluorescently excited PAHs is a strong indicator that this is the dominant mechanism in NGC 253, we can also compare the H $_2$ line ratios in each region to the predicted values from both shock and PDR models for a more quantitative analysis. In Figure 2.5, the ratio is lower than predicted for pure UV excitation, although the correlation to the PAH maps indicates that UV fluorescence is the dominant mechanism. In order to study this further, we present a diagnostic excitation level diagram. This diagram can be seen in Figure 2.8 and plots the upper energy level (E/k) against the column density distribution(N) divided by degeneracy (g) where:

$$\frac{N_{obs}(v, J)}{g_J} = \frac{4\pi\lambda}{hc} \frac{I_{obs}(v, v', J, J')}{A(v, v', J, J')} \quad (2.1)$$

Here, $N_{obs}(v, J)$ is the observed column density of a specific upper electronic energy level (v, J), g_J is the degeneracy of this level, $A(v, v', J, J')$ is the Einstein-A radiative transition probability from Wolniewicz et al. (1998), and I_{obs} is the observed line flux for each transition. The column density is normalized by the 1-0 S(1) column density divided by its degeneracy (g_J). In addition, we can plot the

best fit Maxwell-Boltzmann distribution to the $v = 1$ transitions. The slope of this line tells us the excitation temperature in the region.

In order to directly compare the observed line ratios in NGC 253 to model predictions, we can use predicted line intensities for shock and PDR models and plot them on this diagnostic energy level diagram. Figure 2.7 presents the results from the Shull & Hollenbach (1978) shock models. These models calculate line intensities for shocks moving at 6, 10, and 14 km/s for densities of 10^3 , 10^4 , $3 \cdot 10^5$ cm⁻³. In most of the shock models of Figure 2.7, the $v > 1$ lines (depicted as triangles) lie on or below the thermal distribution indicating subthermal excitation of the higher levels. The exceptions to this case are the higher velocity (10-14 km/s) shocks in very dense environments ($n_H=10^5$). However, the $v > 1$ lines have a shallower slope than the thermal distribution as shown by the dotted red line, indicating a higher excitation temperature for these transitions. In these high velocity, high density shocks, there are two different gas components (temperature slopes).

The bottom 6 panels of Figure 2.7 displays the predicted line intensities from Sternberg & Dalgarno (1989), who model fluorescent excitation of H₂ in environments with $n_H = 10^3 - 10^6$ and $\chi = 10^2$ and Black & van Dishoeck (1987) who model pure fluorescent excitation for a large range of the parameter space. We have chosen models 4, 6, 9, 17,19, and 20 spanning densities of $n_H = 10^2 - 10^4$ cm⁻³ and radiation intensities of $\chi = 10^0 - 10^4$. In contrast to the shock models, the PDR models show the $v > 1$ lines lying high above the thermal distribution in almost all cases, since UV fluorescence populates levels from the top down, the highest energy levels get populated with higher probability compared to the thermalized case. In addition, the lines belonging to the $v = 2$ level share the same excitation temperature (same slope) as the $v = 1$ lines, only offset due to their higher upper energy level, unlike the shock models where there are two distinct excitation temperatures. This is the same for each v level, as shown in Black & van Dishoeck (1987). A general feature of the UV-excited models is that the rotational temperatures (i.e., the excitation temperature determined between different rotational levels within the same vibrational level) are the same in the various vibrational levels. In contrast, the vibrational temperature (i.e., the excitation temperature determined between different vibrational levels) is higher than the rotational temperature. The only exception to this pattern is the top-right panel of Fig. 9, showing a model with low radiation field but very high density. However, this density is only relevant for very dense clumps and the the bulk of the molecular gas in NGC253 is at much lower densities.

Now that we have presented the shock and PDR models, we can compare them to the observational results seen in Figure 2.8. In these plots, only the ($\geq 2\sigma$)

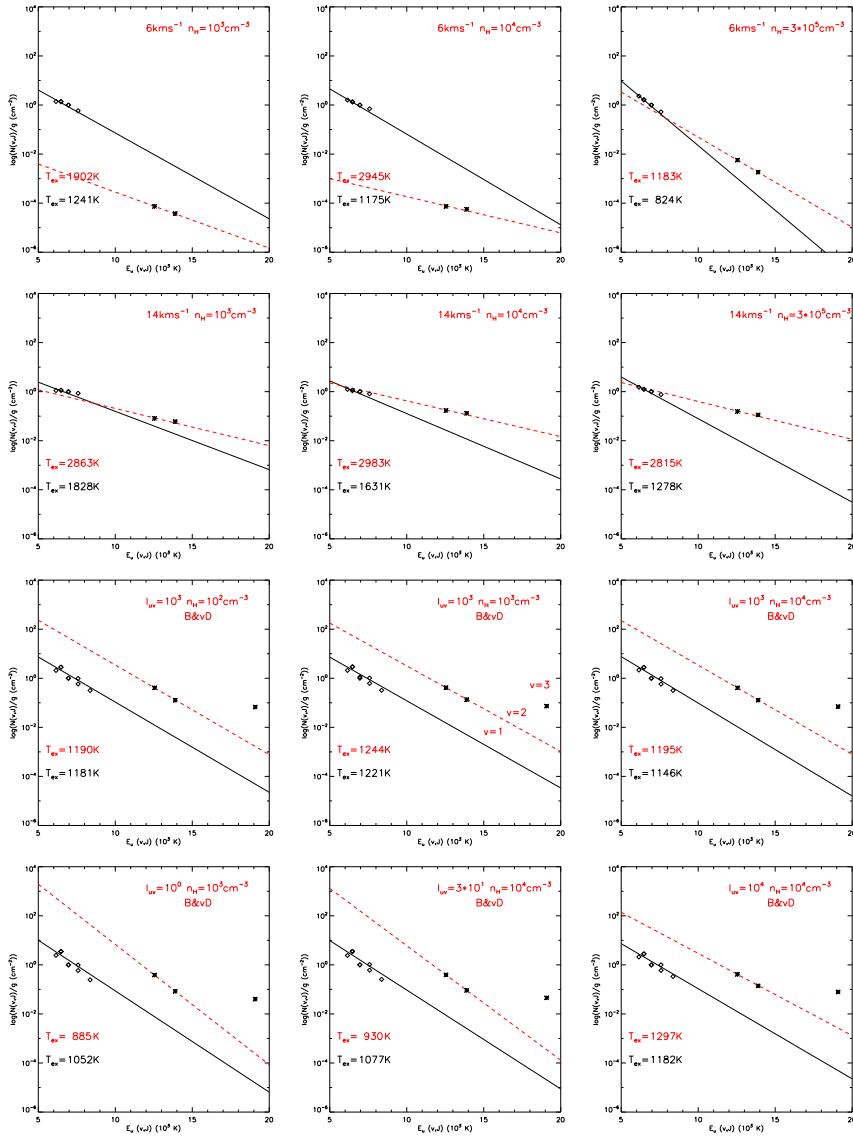


Figure 2.7: Excitation diagrams of shock and PDR model-predicted H_2 line column density distributions as a function of upper energy level. The column density is normalized to the 1-0 S(1) H_2 transition. Diamonds represent lines from $v = 1$ while the asterisks represent points from $v > 1$. The solid line is a best fit of the Boltzmann distribution to the $v = 1$ points, the slope represents the excitation temperature, T_{ex} . Predictions of shock models from Shull & Hollenbach (1978) with shock speeds 6 km/s (top row) and 14 km/s (second row) and densities $n_H = 10^3 \text{ cm}^{-3}$ (left), 10^4 cm^{-3} (middle), and 10^5 cm^{-3} (right). Predictions of PDR models from Black & van Dishoeck (1987) with $l_{uv} = 10^0 - 10^4$ and densities $n_H = 10^3 \text{ cm}^{-3}$, 10^4 cm^{-3} , and 10^5 cm^{-3} , and are labeled with B&vD.

H₂ line detections are included. Each panel of the figure represents the different regions shown in Figure 2.1. In each region, Figure 2.8 reveals the thermalized $v = 1$ lines of varying excitation temperatures. In addition, in all regions where $v > 1$ lines are detected, they lie above the thermal distribution. However, the case becomes ambiguous in regions where we cannot detect $v > 1$ lines, such as Regions 8 and 9. It is possible that in these regions shocks dominate and therefore the higher transitions are not being populated, or that in these regions, we lack the signal to noise to detect the lines above 2σ .

In both Region 1 and Region 3, the kinematic center, we detect two $v = 2$ lines and one $v = 3$ line. Although we only have two $v = 2$ lines, it is clear that they have a similar excitation temperature (slope) to the thermal distribution and do not represent a second hotter gas component. Thus, these lines clearly follow a PDR distribution. In addition, the $v > 2$ lines cannot be excited through shocks, so the presence of the 3-2 S(3) line also suggests fluorescent excitation. Using these criteria and the shock/PDR models as a guide, we can conclude that there is fluorescent excitation in Regions 1, 3, and 4 and most likely in Regions 2, 5 and 6. Since the signal-to-noise is too low in Regions 7 and 8, we cannot determine whether shock excitation or fluorescent excitation is the dominant heating mechanism in these regions. However, based on the integrated spectrum and Regions 1, 2, 3, and 4, it is clear that UV excitation in PDRs is the dominant mechanism for this galaxy, although shocks may dominate in some isolated areas.

2.7 Conclusion

From SINFONI observations, we determine the nature of the excitation of hot H₂ gas in NGC 253 using diagnostic emission lines. Specifically, we use the K band continuum as a tracer of the older stellar population, Br γ as a tracer of high-mass, young (O-type) star formation, [FeII] as a tracer of shocks, and PAHs as a tracer of slightly lower mass (B-type) star formation. Based on the Br γ and [FeII] emission line maps, we can interpret the H₂ excitation. We find that in most regions of NGC 253, excitation by UV photons in PDRs is the dominant mechanism. There are 3 regions where shock excitation may dominate, but these are small relatively isolated regions. Throughout the entire nuclear region of the galaxy, H₂ is being fluorescently excited.

We also present a diagnostic energy level diagram which robustly differentiates between shock and fluorescent excitation. By comparing the observed column densities of each line to the proposed PDR and shock models, it is clear that the NGC 253 H₂ is dominated by fluorescent excitation. A few of the bright H₂ regions may lack the signal-to-noise to resolve the higher energy transitions, or it is

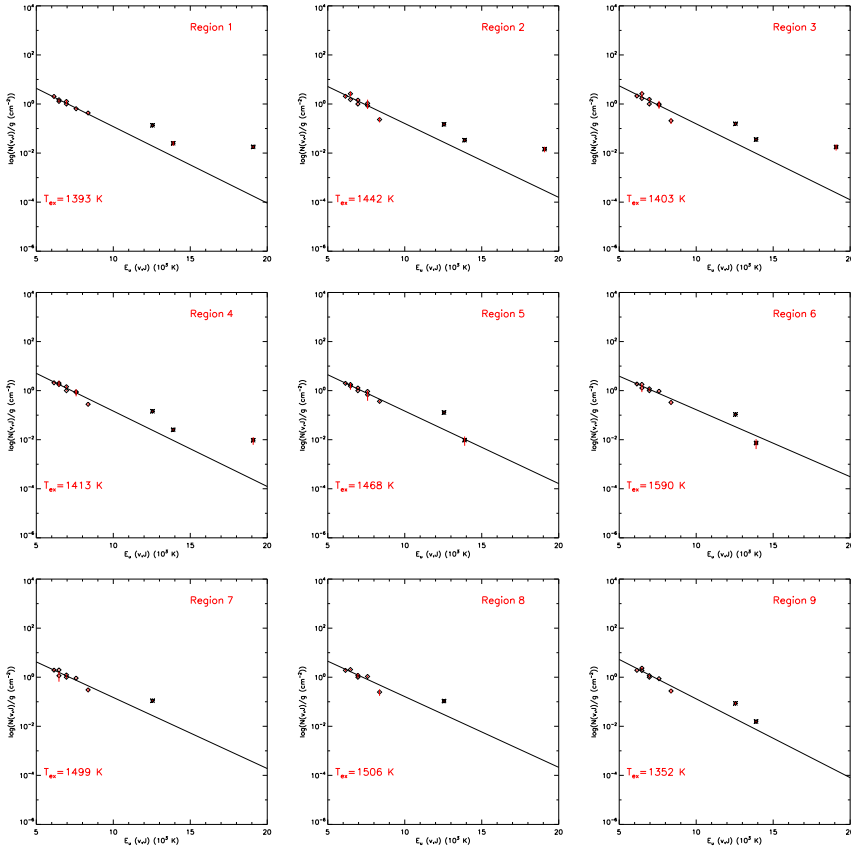


Figure 2.8: Excitation diagrams of observed H_2 line column density distribution as a function of upper energy level. The column density is normalized to the 1-0 $S(1)$ H_2 transition. Diamonds represent lines from $v = 1$ while the asterisks represent points from $v > 1$. The solid line is a best fit of the Boltzmann distribution to the $v = 1$ points, the slope represents the excitation temperature, T_{ex} . Each panel represents a different region, corresponding to the regions in Figure 2.5. The error bars represent a standard deviation from the column density.

possible that in these isolated regions, shocks are the dominant mechanism. In addition, the PAH emission follows the same morphology as the H₂, adding further confidence that through NGC 253, the gas is undergoing fluorescence.

We determine that a maximum of 29% of the hot molecular gas is excited by shocks. Since we are only sensitive to the hottest H₂ gas, we are probing the surfaces of molecular clouds. Within the molecular clouds, where the bulk of the molecular gas is, the gas can have a different excitation mechanism.

Acknowledgements

We thank Lowell Tacconi-Garman for making his ISAAC 3.21 and 3.28 μ images available to us, and Susanne Brown for determining the calibration factors of these images.

3 | Radiative and mechanical feedback into the molecular gas of NGC 253

Starburst galaxies are undergoing intense periods of star formation. Understanding the heating and cooling mechanisms in these galaxies can give us insight to the driving mechanisms that fuel the starburst. Molecular emission lines play a crucial role in the cooling of the excited gas. With SPIRE on the Herschel Space Observatory we have observed the rich molecular spectrum towards the central region of NGC 253. CO transitions from $J=4-3$ to $13-12$ are observed and together with low- J line fluxes from ground based observations, these lines trace the excitation of CO. By studying the CO excitation ladder and comparing the intensities to models, we investigate whether the gas is excited by UV radiation, X-rays, cosmic rays, or turbulent heating. Comparing the ^{12}CO and ^{13}CO observations to large velocity gradient models and PDR models we find three main ISM phases. We estimate the density, temperature, and masses of these ISM phases. By adding ^{13}CO , HCN, and HNC line intensities, we are able to constrain these degeneracies and determine the heating sources. The first ISM phase responsible for the low- J CO lines is excited by PDRs, but the second and third phases, responsible for the mid to high- J CO transitions, require an additional heating source. We find three possible combinations of models that can reproduce our observed molecular emission. Although we cannot determine which of these are preferable, we can conclude that mechanical heating is necessary to reproduce the observed molecular emission and cosmic ray heating is a negligible heating source. We then estimate the mass of each ISM phase; $6 \times 10^7 M_{\odot}$ for phase 1 (low- J CO lines), $3 \times 10^7 M_{\odot}$ for phase 2 (mid- J CO lines), and $9 \times 10^6 M_{\odot}$ for phase 3 (high- J CO lines) for a total system mass of $1 \times 10^8 M_{\odot}$.¹

M. J. F. Rosenberg, M. V. Kazandjian, P. P. van der Werf *et. al*
A&A **564**, A126 (2014)

¹Contributions from coauthors mainly consisted of comments and suggestions to the text. M. V. Kazandjian and R. Meijerink provided their PDR and XDR models and A. Weiß provided beam size corrections for the spectra.

3.1 Introduction

Starburst galaxies are nearby laboratories that allow us to study intense star formation. Studying the heating and cooling mechanisms in these galaxies gives us insight in to which excitation or feedback mechanisms are dominant in fueling starbursts. Molecular emission lines play a crucial role in the cooling of excited gas, and with the Herschel Space Observatory we are able to observe the rich molecular spectrum of the nucleus of NGC 253.

CO is one of the most abundant molecules after H₂, and a good and easily observable tracer of the condition of the molecular gas in the interstellar medium (ISM) of these galaxies. CO in the ISM is mostly located in molecular clouds and photon dominated regions (PDRs), where the radiation can penetrate the cloud and excite the gas. Tielens & Hollenbach (1985) created models of PDRs, which predict the intensities of atoms and molecules in the PDR as a function of density, radiation environment, and column density. These have been expanded to include models for X-ray dominated regions (XDRs)(Meijerink & Spaans 2005; Maloney et al. 1996), PDRs with enhanced cosmic ray ionization rates (Meijerink et al. 2006), and PDRs with additional mechanical heating taken into account (Kazandjian et. al, in press).

NGC 253 is a nearby, $D_L=2.5$ Mpc (Davidge & Pritchett (1990), 12 pc"), edge-on barred spiral galaxy (Scoville et al. 1985). The central kiloparsec of NGC 253 is considered an archetypal starburst nucleus ($L_{IR} \sim 2 \times 10^{10} L_{\odot}$), which is heavily obscured at optical wavelengths by dust lanes (Prada et al. 1996). However, in the far-infrared and submillimeter wavelength regimes, NGC 253 exhibits extremely bright molecular line transitions (Henkel et al. 1991), originating from large molecular clouds in the nuclear region (Israel et al. 1995; Mauersberger et al. 1996; Houghton et al. 1997; Bradford et al. 2003; Martín et al. 2009b). This gas also appears to be highly excited. Observations of HCO⁺ and HCN suggest that at least some of the gas has densities greater than 10^4 cm^{-3} and temperatures over 100 K (Paglione et al. 1995, 1997).

There have been many studies that have attempted to derive the excitation mechanism in NGC 253. The warm, excited molecular gas phase, often associated with PDRs, excites the mid- to high-J CO transitions ($J > 4$). The near infrared H₂ emission lines shows that PDRs are an important excitation mechanism (Rosenberg et al. 2013). However hot H₂ gas only traces the very edges of molecular clouds. In order to study the excitation of the bulk of the molecular gas, we may use CO as a probe. Bradford et al. (2003) have observed ¹²CO up to J=6-5 along with ¹³CO up to J=3-2 and derive a kinetic temperature of 120 K and an H₂ density of $4.5 \times 10^4 \text{ cm}^{-3}$ for the warm phase. However, they suggest that the

CO is excited by cosmic rays, and not only by PDRs. Martín et al. (2006) found that the chemistry and heating of NGC 253 is dominated by large scale, low velocity shocks. Presence of shocked molecular material is indeed evident through the presence of widespread SiO emission throughout the nuclear region (García-Burillo et al. 2000). In addition, Hailey-Dunsheath et al. (2008) detected the first extragalactic ^{13}CO J=6-5 transition, and using this determined that shocks are the dominant excitation mechanism in the nuclear region of NGC 253. Martín et al. (2009b) suggest that, although NGC 253 is dominated by shock chemistry, PDRs also play a crucial role in the chemistry, since there are very high abundances of PDR tracing molecules, namely HCO^+ , CO^+ .

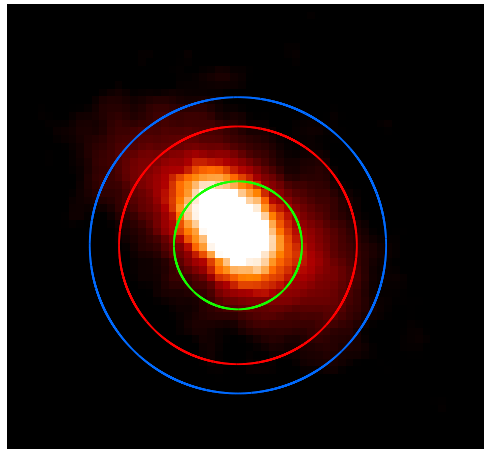
In order to better constrain the dominant excitation mechanism in NGC 253, we present the full ^{12}CO ladder up to J=13-12, the ^{13}CO up to J=6-5 as observed with the Herschel Space Observatory. We combine this with observations of HNC, and HCN transitions and apply these observations to models of PDRs, XDRs, enhanced cosmic ray PDRs, and enhanced mechanical heating PDRs in order to model the excitation directly. These observations were taken as part of the Guaranteed Key Program Herschel EXtra GALactic (HEXGAL, PI: R. Güsten). In Section 3.2, we will describe the observations and data reduction techniques. In Section 3.3, we will present our spectra and line fluxes. Using models of CO emission, in Section 3.4 we will constrain the parameters of the molecular gas phases and introduce a methodology to understand the degeneracies of the models. In order to constrain the densest phase of the ISM, we use the HCO^+ and HCN in Section 3.5 to determine the excitation mechanism. In Section 3.6 we analyze the implication of our results and in Section 3.7 we summarize our main conclusion.

3.2 Observations and Data Reduction

Observations of NGC 253 were taken on December 5th, 2010 with the Herschel Spectral and Photometric Imaging Receiver (SPIRE) in staring mode centered on the nucleus of NGC 253 (Obs ID: 1342210847). SPIRE is an imaging Fourier Transform Spectrometer (FTS) (Griffin et al. 2010a). The high spectral resolution mode was used with a resolution of 1.2 GHz over both observing bands. The low frequency band covers $\nu=447\text{-}989$ GHz ($\lambda=671\text{-}303$ μm) and the high frequency band covers $\nu=958\text{-}1545$ GHz ($\lambda=313\text{-}194$ μm). A reference measurement was used to subtract the emission from the telescope and instrument.

The data were reduced using version 9.0 of the Herschel Interactive Processing Environment (HIPE). Since NGC 253 is an extended source, a beam correction factor is necessary to compensate for the wavelength dependent beam size. Using an archival SCUBA 450 μm map of NGC 253, we convolve the map with a 2-

Figure 3.1: Three SPIRE beam sizes are shown overlotted on a SCUBA 450 μm archival image, 40.5" (blue), 17.5" (green), and 32.5" (red). The SPIRE beam size changes as a function of wavelength, thus the blue circle represents the largest beam size and the green represents the smallest beam size. The red beam size (32.5") represents the beam size of CO J=5-4 transition and all other lines are convolved to this beam size.



D Gaussian with FWHM the same size as our beam sizes. The archival 450 μm SCUBA map of NGC 253 is shown in Figure 3.1 with the largest, smallest, and normalized beam sizes are shown in blue, green, and red respectively. All beam sizes include the brightest part of the nucleus.

The ratio of the flux within each convolved map and the flux within the beam size of the CO J=5-4 transition (beam size=32.5") is the beam correction factor (κ_S) where:

$$F_{corr} = \frac{F_{obs}}{\kappa_S} \quad (3.1)$$

Thus, all fluxes are normalized to a beam size of 32.5" (i.e. 394 pc). In addition, we use the ground based ^{12}CO , ^{13}CO , HCN, HNC fluxes from Israel et al. (1995) and Israel (private communication), all normalized to a beam size of 32.5". We add the 27" aperture integrated ground based observations of HCO^+ 1-0 and 4-3 transitions from Knudsen et al. (2007), also normalized to a beam size of 32.5". Fluxes were first extracted using FTfitter, a program specifically created to extract line fluxes from SPIRE FTS spectra. This is an IDL based GUI, which allows the user to fit lines, choose line profiles, fix any line parameter, and extract the flux. We define a polynomial baseline to fit the continuum and derive the flux from the baseline subtracted spectrum. In order to more accurately determine the amplitude of the line, we fix the FWHM for transitions higher than J=8-7 to the expected line width of ^{12}CO at each source, using the velocity widths measured by Israel et al. (1995).

In the case of very narrow linewidths (~ 780 km/s at $650 \mu\text{m}$), more narrow than the instrumental resolution ($\text{FWHM}_{max}=1000$ km/s at $650 \mu\text{m}$), we do not fix the FWHM but fit the lines as an unresolved profile, which is the case for CO J=4-3 through J=8-7. We use an error of 30% for our fluxes, which encompasses our dominant source of error, specifically the uncertainty of the beam size correction using the $450 \mu\text{m}$ SCUBA map (15%) and line flux extraction (10%). We also have some uncertainty in the SPIRE calibration error of $\sim 5\%$ for extended sources.

3.3 Results

The spectra of NGC 253 are presented in Figure 3.2. The ^{12}CO transitions are visible from J=4-3 to J=13-12 and labeled in red and the two ^{13}CO transitions detected are marked in light blue. There is also a strong detection of [NII] at 1461 GHz and [CI] at 492 GHz and 809 GHz in the rest frame, shown in green. We detect 5 strong water emission lines and $\text{H}_2\text{O } 1_{11} - 0_{00}$ in absorption, marked in blue. We also detect HCO^+ 7-6, also marked in blue. In addition, we also find CH^+ , CH, OH^+ , H_2O^+ , and HF, but do not point them out since they will not be used in our analysis. As seen in Figure 3.2, there is a discontinuity between the high and low frequency bands of the spectrograph, marked with a dotted line. This discontinuity is due to the fact that for the high frequency band, the beam size is much smaller than for the low frequency band. A beam correction factor (κ_S) for each wavelength is calculated using the method described in Section 3.2, and displayed in Table 3.1. Also, the baseline ripple seen in the spectrum, specifically in the inset of Figure 3.2, is due to the sinc profile of the strong CO transitions and does not represent noise.

3.4 Dissecting the CO Excitation Ladder

In order to analyze the excitation conditions in NGC 253, we can create a 'CO ladder' or spectral line energy distribution, which plots the flux of each CO transition as a function of the upper J number. Since we have multiple transitions of both ^{12}CO and ^{13}CO , we can use both in our analysis. Since we take a beam size of $32.5''$ (~ 400 parsec diameter), we get emission from multiple phases of the ISM in one spectrum and cannot spatially separate the distinct ISM environments. Thus, when analyzing the properties of each ISM phase, it is important to realize that these properties are average representative values of the dominant ISM environments that are responsible for the particular emission.

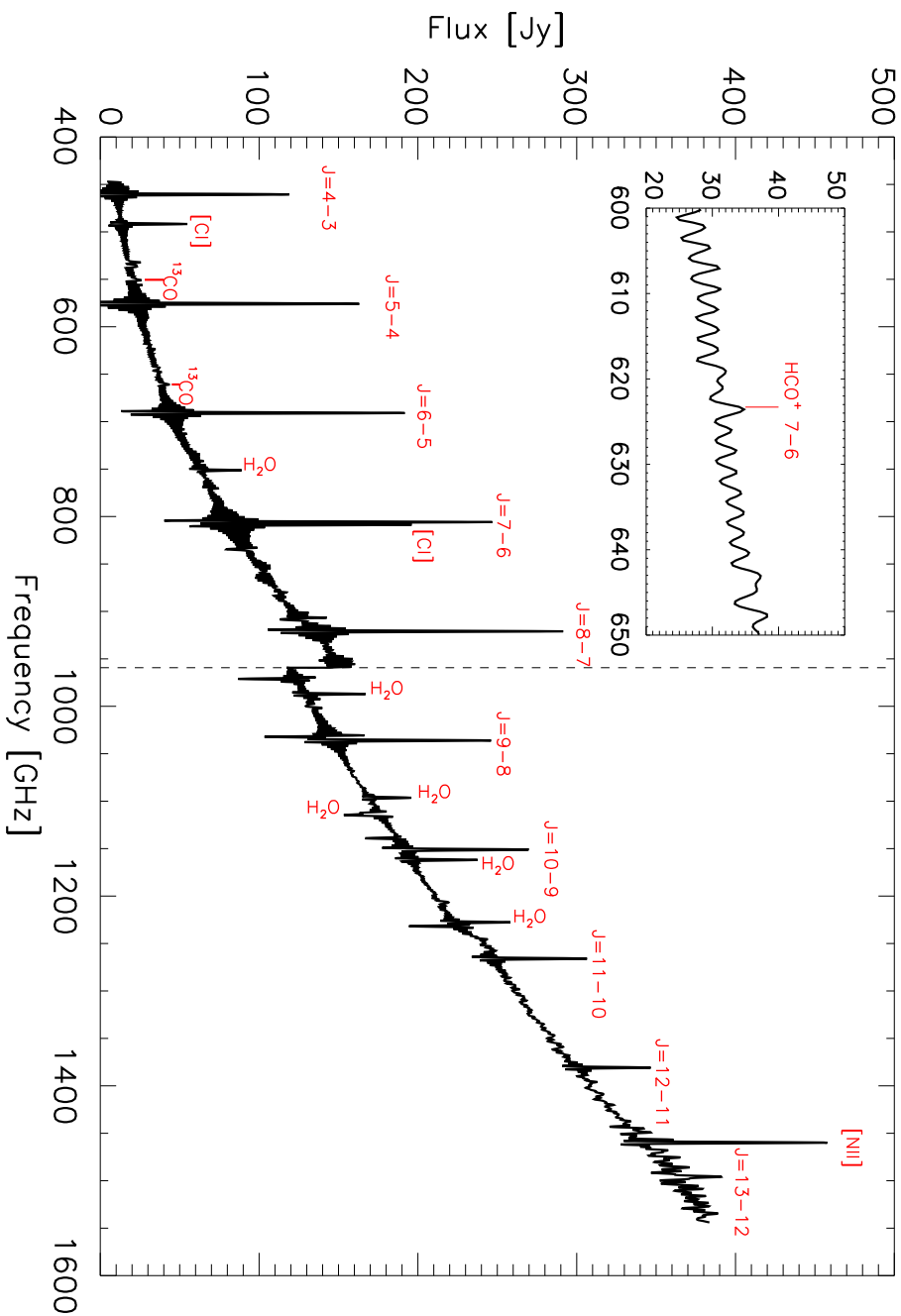


Figure 3.2: SPIRE spectra of NGC 253, short wavelength and long wavelength bands separated by a black dotted line. ^{12}CO transitions, ^{13}CO transitions, atomic transitions, H_2O , and HCO^+ line are marked.

Line	κ_{SA} 32.5"	Line Flux [10^{-16} W m $^{-2}$]
^{12}CO 1-0 ^a	--	0.3
^{12}CO 2-1 ^a	--	2.4
^{12}CO 3-2 ^a	--	7.3
^{12}CO 4-3	1.13	12.8
^{12}CO 5-4	1.00	17.1
^{12}CO 6-5	0.94	17.2
^{12}CO 7-6	1.04	18.2
^{12}CO 8-7	1.07	17.9
^{12}CO 9-8	0.67	12.2
^{12}CO 10-9	0.64	9.3
^{12}CO 11-10	0.62	7.7
^{12}CO 12-11	0.60	5.5
^{12}CO 13-12	0.60	3.9
^{13}CO 1-0 ^a	--	0.02
^{13}CO 2-1 ^a	--	0.2
^{13}CO 3-2 ^a	--	0.8
^{13}CO 5-4	1.00	0.9
^{13}CO 6-5	0.96	0.7
[CI] ³ P ₁ - ³ P ₀	1.09	4.5
[CI] ³ P ₂ - ³ P ₁	1.04	11.4
[NII] ³ P ₁ - ³ P ₀	0.60	29.6
HCO ⁺ 1-0 ^b	0.88	0.006
HCO ⁺ 4-3 ^b	0.88	0.2
HCO ⁺ 7-6	1.00	0.5
HCN 1-0 ^c	0.72	0.009
HCN 3-2 ^c	0.62	0.2
HCN 4-3 ^c	0.47	0.1
HNC 1-0 ^c	0.72	0.008
HNC 3-2 ^c	0.62	0.09
H ₂ O 2 ₁₁ -2 ₀₂	4.73	1.4
H ₂ O 4 ₂₂ -3 ₃₁	1.79	0.5
H ₂ O 2 ₀₂ -1 ₁₁	9.13	2.7
H ₂ O 3 ₁₂ -3 ₀₃	6.24	1.9
H ₂ O 3 ₁₂ -2 ₂₁	2.68	0.8
H ₂ O 3 ₂₁ -3 ₁₂	9.65	2.9
H ₂ O 4 ₂₂ -4 ₁₃	1.08	0.3
H ₂ O 2 ₂₀ -2 ₁₁	7.43	2.2

Table 3.1: Observed (uncorrected) line fluxes and beam size correction factors (κ_S) normalized to 32.5". The errors on all derived fluxes are 30%.

^a From Israel et al. (1995).

^b From Knudsen et al. (2007).

^c From Israel (private communication).

3.4.1 LVG Analysis

To better understand the ISM excitation in the center of NGC 253, we start by modeling the ground-based fluxes, i.e. the first four ^{12}CO and first three ^{13}CO line intensities and ratios with the RADEX large velocity gradient (LVG) radiative transfer models (van der Tak et al. 2007). These codes provide model line intensities as a function of three input parameters per molecular gas phase: molecular gas kinetic temperature T_k , density $n(\text{H}_2)$, and the CO velocity gradient $N(\text{CO})/dV$. By comparing model to observed line *ratios*, we identify the physical parameters best describing the actual conditions.

In the modeling, we assume a constant CO isotopic abundance $^{12}\text{CO}/^{13}\text{CO} = 40$ throughout. This is close to values generally found in starburst galaxy centers (Henkel et al. 1991). We identify acceptable fits by exploring a large grid of model parameter combinations ($T_k = 10 - 150$ K, $n(\text{H}_2) = 10^2 - 10^5 \text{ cm}^{-2}$, and $N(\text{CO})/dV = 6 \times 10^{15} - 3 \times 10^{18} \text{ cm}^{-2} / \text{km s}^{-1}$) for (combined) line ratios matching those observed. No single-phase gas provides a good fit to the observed line intensities. Consequently, we have also modeled the ^{12}CO and ^{13}CO lines simultaneously with *two molecular gas phases*, the relative contribution of the two phases being a free parameter. Lacking a detailed physical model for the distribution of clouds and their sources of excitation, two phases is the most we can fruitfully explore for $J < 5$, especially because only the high signal-to-noise lower J ^{13}CO transitions have observations that allow us to break the inherent $T_k - n(\text{H}_2)$ degeneracy. This degeneracy derives from the fact that the intensity ratios of optically thick ^{12}CO lines exhibit very little change going from hot, low-density gas to cool, high-density gas (*cf* Jansen 1995, Ph.D. Thesis Leiden University, Ch. 2).

No unique solution is obtained. However, in all combinations the parameters of the first molecular gas phase are well-established and narrowly constrained to a low kinetic temperature of about 60 K (± 10), and a density of about $\log(n_H) = 3.5$ (± 0.5). The second phase has in all combinations a reasonably well-determined higher density of typically $\log(n_H) = 5.0$, but the kinetic temperature is not at all constrained by the lower J transitions included, nor is the proportion of molecular gas in either phase.

We now use this result, especially the firmly established parameters of the coldest and least dense gas from phase 1, to optimize a *three-phase* LVG model that includes the higher transitions as well:

$$\text{Model} = \Omega_I \text{LVG}_I + \Omega_{II} \text{LVG}_{II} + \Omega_{III} \text{LVG}_{III} \quad (3.2)$$

where LVG_I , LVG_{II} , and LVG_{III} are three LVG models of specific density, temperature, and column density in units of W m^{-2} . Ω_I , Ω_{II} , and Ω_{III} represent

the respective filling factors of each ISM phase. Filling factors traditionally represent how much of the beam is filled, so they only range from 0 to 1. However, in the case of our filling factors, we model one cloud with a $\delta v = 1 \text{ km s}^{-1}$ and allow for multiple clouds in our line of sight, such that Ω is not only a beam filling factor, but also a volume filling factor, which accounts for it being greater than one. In the case of $\Omega < 1$, only a fraction of the beam is filled by clouds, whereas $\Omega > 1$ represents the number of clouds in our beam volume, each with a slightly different velocity. We also attempted the same procedure for cloud models with $\delta v = 5$ and 10 km s^{-1} without any significant difference. We create a composite model for both ^{12}CO and ^{13}CO where each model ISM phase and filling factor is the same for ^{12}CO and ^{13}CO . Since we already have an idea of the first LVG phase (LVG I), we only vary the second and third LVG phases and all three filling factors.

We perform a modified Pearson's χ^2 minimized fit for ^{12}CO and ^{13}CO simultaneously, where the modified Pearson's χ^2 is:

$$\chi^2 = \frac{\sum_{i=1}^{N_{data}} \left(\frac{obs_i - model_i}{model_i} \right)^2}{N_{data}} \quad (3.3)$$

with obs_i as the observed flux of a particular transition, $model_i$ is the composite model flux (Eq. 3.2) of a particular transition, and N_{data} is the total number of transitions. Thus the χ^2 represents a χ^2 per transition for each molecule. We calculate the χ^2 value as the sum of the χ^2 for ^{12}CO and ^{13}CO for every possible combination of models in our grid. In doing this, we are able to plot the full parameter space for each phase, and show the χ^2 value in gray scale for each combination of density and temperature to see where the degeneracies lie. Figure 3.3 shows these degeneracy plots for the second and third LVG phases (LVG II and LVG III).

Although there is a best fit model, denoted by the black asterisk in Figure 3.3, there are many models for each phase that have similarly low χ^2 values, especially for LVG II. In both LVG phases we see the general diagonal trend displaying the temperature-density degeneracy, trading temperature for density. For LVG II, there is a large range of models that fit well, however the best fits tend to cluster at the low temperature, high density range (lower right corner). On the other hand, LVG III fills a much smaller part of parameter space. The diagonal degeneracy still exists, but this phase requires both high temperature and high density to be fit well. It is also important to note that LVG II and LVG III occupy completely independent diagonal regions of parameter space, and since the diagonal trend trades temperature for density, we can think of these separate regions as unique pressure phases. In Figure 3.3, we only compare the degeneracies of temperature and density, yet we also analyze the degeneracies of $N(\text{CO})/\delta v$ and find that within a

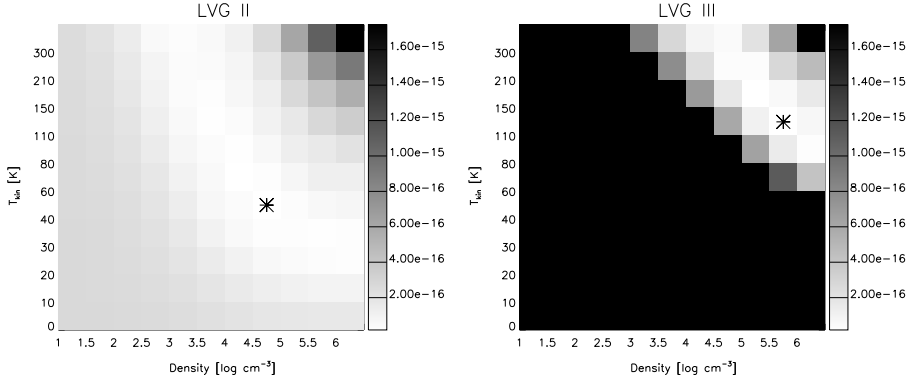


Figure 3.3: Degeneracy plots of LVG II (right) and LVG III (left). Each square represents a model with specific density (x axis) and temperature (y axis) for the best fitting $N(\text{CO})/\delta v$. The color scale represents the χ^2 value of that model fit to the CO data. **Since we use a modified Pearson's χ^2 , the actual values of the grey scale are not meaningful, only their relative differences.** The large black asterisk represents the best fitting model (minimum χ^2).

factor of ± 5 the column density is well constrained.

Although we cannot fully resolve the degeneracies, we will select a range of model parameters with a low χ^2 value to continue our analysis. We will define the density range of LVG II as $4 < \log_{10}(n_H/\text{cm}^{-3}) < 6$ and the range of LVG III as $4.5 < \log_{10}(n_H/\text{cm}^{-3}) < 6$. Figure 3.4 shows our three best fit ISM LVG phases. Here we do not include the dense gas tracers to constrain the density of our LVG models since the abundances may vary between ISM phases, however the densities of our best fit LVG models are consistent with the HCN and HNC ratios shown in Figure 3.7 and Table 3.4.

The model parameters of our best three models (Figure 3.4) are summarized in Table 3.2. The column density stated in this table is the model gradient, $\log(N(\text{CO})/\delta v)$. We show a relative contribution of the emission by summing the flux over all transitions of each model phase and comparing that to the flux of the composite model (red solid line). We compare the total emission (summed flux of CO transitions) to the integrated emission of each ISM phase. We find a relative contribution in terms of emission (luminosity) to the total CO flux from LVG I, LVG II, and LVG III of 0.2 : 0.2 : 0.6 respectively. Next, we compare the relative scaled column densities which take the filling factors into account such that $N_i = \Omega_i \times N_{\text{CO},i}$. We see a relative contribution in terms of column density of 0.6 : 0.4 : 0.02 for LVG I, II and III respectively, which is also proportional to the relative

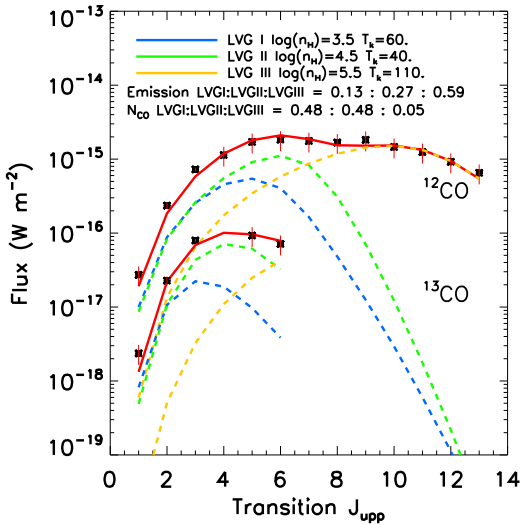


Figure 3.4: ^{12}CO and ^{13}CO excitation ladders of NGC 253 with flux of each transition plotted as black asterisks with red error bars. In blue, green and yellow dotted lines we plot the LVG I, II and III ISM phases with their filling factors. The composite model is plotted with a red solid line. The model density, temperature and column density are shown in the legend along with the relative contribution of each phase in terms of emission and column density.

mass contributions of each phase. Although LVG III is responsible for the bulk of the line emission, and all of the emission for the high J CO lines, it represents a very small fraction ($\sim 2\%$) of the mass. It is also interesting to note that LVG III contributes almost nothing to the ^{13}CO emission. This is due mainly to the low optical depth of LVG III, restricting the $^{12}\text{CO}/^{13}\text{CO}$ to much lower than in LVG I and II. The fact that LVG III has such a high density, but such a low column density implies that the path length is very small or that the CO abundance is very low. The low CO column density combined with a high temperature suggest the physical environment of a PDR where the high UV flux keeps most of the CO dissociated; we explore this further in Section 4.2. We estimate a total gas mass of $3 \times 10^7 M_{\odot}$, which is only a lower limit for the mass since we assume a $[\text{C}]/[\text{H}]$ abundance ratio of 1.4×10^{-4} and that all of the $[\text{C}]$ is in CO. However, in the case of a high-density, high-temperature LVG phase (LVG III), it is likely that the radiation environment is strong, and thus most of the CO would be dissociated, which would suggest a lower H_2 mass than there is in reality. Due to these uncertainties, we will perform a more detailed mass calculation in the following sections.

3.4.2 PDR Analysis

Now that we have constrained the density and temperature ranges of the three dominant molecular ISM phases, we can determine which physical processes are exciting the molecular gas. Since the nucleus of NGC 253 is experiencing high

Component	Density $\log(n_H)$ $\log[\text{cm}^{-3}]$	Kinetic Temp K	$\log \frac{N_{CO}}{\delta v}$ $\log[\text{cm}^{-2} / \text{km s}^{-1}]$	Ω^a	C_{em}^b	C_{NCO}^c
LVG I	3.5	60	17	5.0	0.13	0.48
LVG II	4.5	40	17	5.0	0.27	0.48
LVG III	5.5	110	17	0.5	0.59	0.05

Table 3.2: Model parameters for the three LVG phases.

^a Ω is the beam filling factor for each ISM phase.

^b C_{em} is the fractional contribution of each ISM phase to the emission.

^c C_{NCO} is the fractional contribution of each ISM phase to the column density.

star formation rates, there is an increase in number density of OB stars and thus a high UV energy density. Through photoelectric heating and FUV pumping of H_2 , the FUV photons heat the outer layers ($A_V < 5$) of molecular clouds. This area of the molecular cloud is the PDR, and is responsible for warm molecular gas emission. The thermal state of PDRs is determined by processes such as photo-electric heating, heating by pumping of H_2 , followed by collisional de-excitation, heating by cosmic rays, [OI] and [CII] fine-structure line cooling, and CO, H_2O , H_2 , and OH molecular cooling. The ionization degree of the gas is driven by FUV photo-ionization, and counteracted by recombination and charge transfer reactions with metals and PAHs. The ionization degree is at most $x_e \sim 10^{-4}$ outside of the fully ionized zone. The chemistry exhibits two fundamental transition, H to H_2 , and C^+ to C to CO. Using PDR models from Kazandjian et al. (2012), which solve for chemistry and thermal balance throughout the layers of the PDR, we use the predictions of the ^{12}CO and ^{13}CO emission as a function of density, radiation environment (G , the Habing radiation field), and column density. The density profile is constant, as in the LVG models, and the Habing field is defined as $1 G = G_0 = 1.6 \times 10^{-3} \text{ erg cm}^{-2} \text{ s}^{-1}$ from photons between 6 and 13.6 eV. The fact that these models use G instead of temperature provides a direct diagnostic of the radiation source responsible for the gas excitation. The model is a semi-infinite slab model which is evaluated at $A_V = 3, 4, 5, 10, 20$, and 30 mags, and we calculate the column density from the A_V and density that gives us the best fit emission.

We narrow the PDR model parameter space by allowing only the densities based on Figure 3.3 ($4 < \log_{10}(n_H/\text{cm}^{-3}) < 6$) for the second phase and ($4.5 < \log_{10}(n_H/\text{cm}^{-3}) < 6$) for the third phase. In order to further constrain our fits, we include ^{12}CO , ^{13}CO , HCN, and HNC to our χ^2 calculation. Since HCN and HNC are typically dense gas tracers (both have $n_{crit} > 10^5 \text{ cm}^{-3}$), they provide an important additional constraint on the second and third phases, since according to our LVG analysis both phases are high density. We also have multiple

Component	Density $\log(n_H)$ $\log[\text{cm}^{-3}]$	$\log(G_0)$	$\log(N_{CO})$ $\log[\text{cm}^{-2}]$	$\log(N_{CO})$ $\log[\text{cm}^{-2}]$	Ω^a	C_{em}^b	C_{NCO}^c M_\odot	$\text{Mass}_{N_{H_2}}^d$ M_\odot
PDR I	3.5	2.5	17.1	21.5	10.0	0.04	0.28	9×10^7
PDR II	5.0	2.5	17.5	21.5	10.0	0.34	0.71	9×10^7
PDR III	5.5	5.5	16.0	21.2	1.5	0.62	< 0.01	7×10^6

Table 3.3: Model parameters for the three PDR phases.

^a Ω is the beam filling factor for each ISM phase.

^b C_{em} is the fractional contribution of each ISM phase to the emission.

^c C_{NCO} is the fractional contribution of each ISM phase to the CO column density.

^d $\text{Mass}_{N_{H_2}}$ is the mass of each ISM phase as estimated by the column density using Eq. 3.4.

HCO^+ transition observations but we do not use them in our analysis because of the complicated nature of the emission of HCO^+ . Its abundances are very sensitive to the interplay between heating and ionization rate and the resulting chemical state of the gas (Meijerink et al. 2011) and thus an untrustworthy diagnostic.

The parameters of the best fitting models are listed in Table 3.3. In Figure 3.5 the PDR fit is shown for ^{12}CO , ^{13}CO , HCN, and HNC. Each PDR phase is represented by a blue, green, and yellow dotted line, while the composite model is shown as a red solid line. We can achieve a relatively good fit for all phases, yet it is important to check if this fit makes physical sense.

Using these three model PDR phases, we can estimate the molecular gas mass in each phase by:

$$M_{H_2} = \sum_i^n \frac{\Omega_i N_{H_2,i} A_{beam} m_{H_2}}{M_\odot} \quad (3.4)$$

where N_{H_2} is the H_2 column density in cm^{-2} which is consistently calculated in the PDR models, A_{beam} is the beam area in cm^2 , and m_{H_2} is the mass of a hydrogen molecule. The mass of each PDR phase is shown in Table 3.3 and the total mass of the system is $1.9 \times 10^8 M_\odot$, which is almost equal to the gas mass measured for a beam size of $80''$, $3 \times 10^8 M_\odot$ (Weiß et al. 2008). Harrison et al. (1999) and Bradford et al. (2003) found a gas mass of $\sim 3 \times 10^7 M_\odot$ for a beam size of $15''$, roughly half the size of our beam yet we find a gas mass 6.5 times larger. In addition, our LVG models predict a mass of $\sim 3 \times 10^7 M_\odot$, which is a reasonable (albeit a lower limit) gas mass estimate. The LVG mass is a lower limit since we can see for a PDR with a high radiation field, the CO becomes dissociated. Thus using the standard abundance of CO to H_2 will underestimate the true H_2 column.

To further test the physicality of our PDR models by comparing the atomic gas to the molecular gas. Carral et al. (1994) uses [CII] $158 \mu\text{m}$ to trace the atomic gas mass in the inner $40''$ of NGC 253 and finds an atomic mass of $2.4 \times 10^6 M_\odot$.

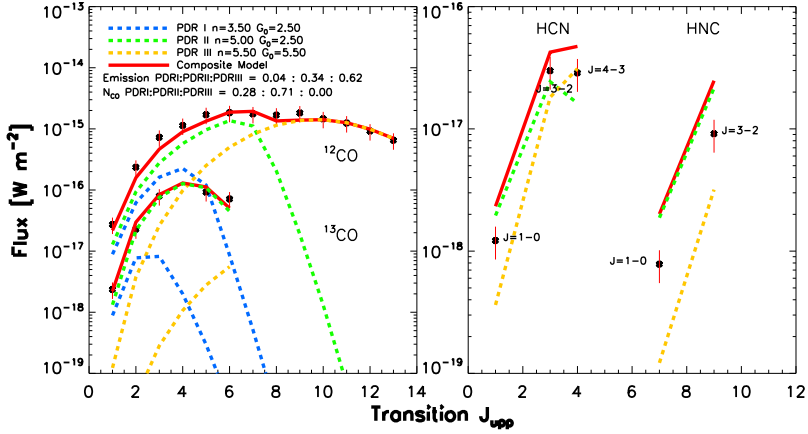


Figure 3.5: Left: ^{12}CO and ^{13}CO excitation ladders, right: HCN and HNC excitation ladders of NGC 253 with flux of each transition plotted as black asterisks with red error bars. In blue, green and yellow dotted lines we plot the PDR I, II and III ISM phases with their filling factors. The composite model is plotted with a red solid line. The model density, G_0 and column density are shown in the legend along with the relative contribution of each phase in terms of emission and column density.

This atomic mass is 30 times smaller than the molecular gas that we observe in our 32.5" beam, which is similar to the findings of Bradford et al. (2003) and Hailey-Dunsheath et al. (2008). Tielens & Hollenbach (1985) predict that in Galactic PDRs, the first $\sim 3 A_V$ s are irradiated and then cooled via atomic lines, whereas the next $3 A_V$ are cooled through molecular lines. From this they estimate that in a PDR, the masses of atomic and molecular mass should be about even. Since our molecular mass is 30 times greater than our atomic mass, we can calculate the A_V where the atomic heating must transition to molecular heating to preserve this ratio and in which conditions this takes place.

First, we assume our PDR is a 2-D finite slab with an (ionized) atomic outer layer and a molecular deeper layer. UV radiation is penetrating the slab from one side and the slab has a constant density and a finite depth. In the case of our PDRs, the depth is $A_V=5$, as shown in Table 3.3. We can measure the mass in each layer, which is proportional to $\text{Volume} \times \text{Density}$, and we assume a constant density and beam area ($V=BA \times r$), where r is the depth into the cloud, so these both drop out. The volume of the first layer is proportional to R_x , where R_x is the radius where the atomic to molecular transition occurs. The volume of the molecular layer is proportional to $R_{A_V=5} - R_x$, where $R_{A_V=5}$ is the distance to the end of the slab. We can then say that the ratio of the molecular to atomic mass is proportional to

$(R_{A_V=5}/R_x) - 1$ and we observe this ratio to be 30. Solving this equation for R_x , we find that in order to observe a molecular to atomic mass ratio of 30, the transition between atomic to molecular must occur at $A_V=0.2$. Although this is a simplified calculation, it demonstrates the difficulty in producing 30 times more molecular mass than atomic. We use our PDR models to test in which environments this very low transition depth occurs. We find the lowest transition depth in our model parameter space is for a PDR with the highest density (10^6 cm^{-3}) and the lowest radiation field ($10^2 G_0$). The transition depth for our three PDR models is $A_V=3.7, 2.2,$ and 4.5 for PDR I, II, and III respectively. Since all of these are much above the necessary $A_V=0.2$, we suggest that an additional heating source is necessary in order to account for the large amount of bright molecular gas.

In order to determine the cause of this discrepancy, we start with our most constrained ISM phase, LVG/PDR I. We have determined that this ISM phase has a density of $10^{3.5} \text{ cm}^{-3}$ and a kinetic temperature of 60 K. We fit this with a PDR with the same density, same column density, and a $G = 10^{2.5} G_0$. From G_0 we can calculate the average temperature of the PDR, which is the dominant factor in determining the emission intensity of the lines. We find that in PDR I, we only have a temperature of 13.5 K, while we need a temperature of 60 K. If we increase the radiation field in order to heat the gas further, we get up to a peak temperature of 18 K and then begin to dissociate the CO. The only way in which we can reproduce a PDR with $n=10^{3.5} \text{ cm}^{-3}$ and $T=60 \text{ K}$ is by including an additional heating term.

3.5 Dominant Molecular Excitation Mechanisms

Since our analysis suggests that a PDR can not be the sole source of the high J CO transitions, we investigate excitation from other sources for comparison.

3.5.1 Excitation Mechanisms

Aside from PDR heating, the three dominant heating mechanism of molecular gas are X-rays, cosmic rays, and mechanical heating. X-rays heat gas in regions (called X-ray Dominated Regions, XDRs) similar to PDRs except that the chemistry is driven by X-ray photons instead of FUV photons, which are able to penetrate further into the cloud without efficiently heating the dust at the same time. These X-rays are mostly produced by active galactic nuclei (AGN) or in areas of extreme massive star formation. The observed X-ray flux between 0.1 and 2.4 keV is $5.72 \pm 0.59 \times 10^{-12} \text{ erg s}^{-1} \text{ cm}^{-2}$, which translates to a luminosity of $L_X = 4 \times 10^{39}$

ergs s^{-1} at a distance of 2.5 Mpc (Pietsch et al. 2000). Since NGC 253 lacks an X-ray bright AGN and has a relatively low X-ray luminosity compared to regions where we see X-ray heating, we exclude this mechanism from further analysis. Cosmic rays can also heat gas in Cosmic Ray Dominated Regions (CDRs). Cosmic rays are able to penetrate into the very centers of molecular clouds, where even X-rays have trouble reaching and are typically produced by supernovae. Similarly, PDRs with additional mechanical heating (mPDRs) are due to turbulence in the ISM, which may be driven by supernovae, strong stellar winds, or jets.

In order to test for mechanical heating, we can add a mechanical heating term to the PDR models (mPDR models). Since turbulence can penetrate a cloud at all scales and depths, as a simple approximation the mechanical heating (Γ_{mech}) is introduced uniformly throughout the 1-D PDR models. We parameterize the strength of Γ_{mech} with α , which represents the fractional contribution of mechanical heating in comparison to the total heating at the surface of a pure PDR (excluding mechanical heating). At the surface the heating budget is dominated by photoelectric heating. When $\alpha=0$, there is only photoelectric heating and cosmic ray heating and when $\alpha=1$, the mechanical heating rate is equal to the photoelectric heating at the edge of the cloud. These rates can be related to supernovae rates, which in turn can be related to star formation rates (as was done in Loenen et al. (2008)). The freedom in the choice of the values of α allow for a flexibility in modeling the source of the absorbed mechanical heating. The surface heating rates for the PDR models can be recovered from Figure 1 in Kazandjian et al. (2012). More details about relating the mechanical heating to the star formation rate can be found in the methods section of that paper and in Loenen et al. (2008). In addition to the mechanical heating, there is a heating rate due to cosmic rays applied throughout the PDR. The heating by cosmic rays is only dependent on H_2 density and ionization rate, in this case the galactic cosmic ray rate ($0.2-3.5 \times 10^{-16} s^{-1}$) (Goldsmith & Langer 1978; van Dishoeck & Black 1986; Indriolo & McCall 2012) and the H_2 density of the selected model.

Since both cosmic rays and mechanical heating derive from supernovae, it is likely that if we have excitation from one mechanism, we should expect excitation from both. Thus, in addition to the mPDR models, we have run mCDR models. These models not only have photoelectric heating from the PDR and mechanical heating, they also have an increased cosmic ray ionization rate of $750 \zeta_{gal}$ or $3.75 \times 10^{-14} s^{-1}$, as suggested by Bradford et al. (2003). The enhanced cosmic ray ionization rate is paired with a varying mechanical heating rate from $\alpha = 0$, or no mechanical heating, up to $\alpha = 1.0$ which translates to a heating rate of $\Gamma_{mech}=1.3 \times 10^{-15} \text{ erg } s^{-1} \text{ cm}^{-3}$. This allows for pure cosmic ray excitation, where $\alpha = 0$ as well as the case where both mechanical heating and cosmic rays play a

role in the gas heating.

3.5.2 Application to NGC 253

In order to determine the alternate heating mechanism, we first start with our most constrained ISM phase, PDR I/LVG I. With only photoelectric heating, we cannot reach the temperature measured in the LVG model (60 K), and thus must include an additional heating source. In order to compare various heating sources, we plot the LVG model (Figure 3.6, left panel) in black and overplot other similar models. Similarly to the pure PDR models, pure CDR with no mechanical heating dissociates the CO before the temperature can get high enough to produce the observed emission. First, we overplot the PDR model that we used in the PDR fit (Section 4.2) in green. The emission from the pure PDR model is approximately a factor of 10 lower than the LVG model of the same density and $T=60$ K. This explains the high filling factors necessary to fit the model emission to our observations, and thus the high mass estimates. We can then use the same parameters as the pure PDR fit, but add additional heating to see if we can reproduce the LVG I emission profile. First we try to fit the emission with an CDR, identical to the PDR except with an enhanced cosmic ray rate of 750 times the galactic CR rate. This curve is overplotted in orange. Not only is the ^{12}CO 10 times less luminous, the $^{12}\text{CO}/^{13}\text{CO}$ ratio is not preserved, the ^{13}CO is underproduced in comparison to the LVG I model, which makes this an unlikely model. We can then test a mechanically heated PDR (mPDR) with an α of only 1%. This matches the emission of LVG I for both ^{12}CO and ^{13}CO and requires only a small amount of mechanical heating. Therefore, we choose mechanical heating as the necessary additional heating mechanism for the first ISM phase.

Next, we must test this first component to see if it is well constrained. In the right panel of Figure 3.6, we have varied radiation strength, column density, and amount of mechanical heating to show that this component is not well constrained. We can match the emission of the LVG model with any model with mechanical heating between 1-25% and radiation between $10^{1.0-2.5} G_0$. However, it is important to note that while these parameters change, so does the column density in a way that preserves mass. Therefore, we cannot determine which of these models represents the true physical conditions, but we can say that mechanical heating is necessary and the mass of the component is around $5 \times 10^7 M_\odot$. In order to proceed with the analysis, we select the model with 1% mechanical heating (blue in Figure 3.6) since it is a slightly better fit to the ^{13}CO .

Now that we have determined the range of models applicable for the first ISM phase, we fit our second and third ISM phases with the mPDR and mCDR models to determine their dominant heating source. We hold the first ISM phase constant

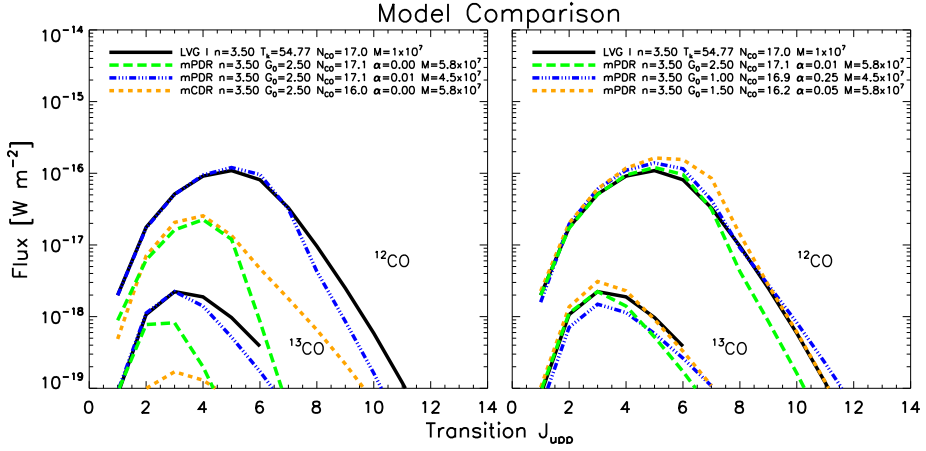


Figure 3.6: Comparison of PDR (green), mPDR (blue), and mCDR (orange) models to LVG I (black) for both ^{12}CO and ^{13}CO .

and equal to that of the 1% mechanical heating mPDR in Figure 3.6 but we allow the filling factor to vary. The second and third phases are held to the same requirements as in the PDR fitting, namely the second phase density is in between 10^4 and 10^6 cm^{-3} and the third phase density is in between $10^{4.5}$ and 10^6 cm^{-3} . The χ^2 for the ^{12}CO , ^{13}CO , HCN, and HNC ladders are summed to find an all around best fit. The best fitting models are shown in Figure 3.7 for:

1. 1 mPDR and 2 mCDRs
2. 2 mPDRs and 1 mCDR
3. 3 mPDRs.

The parameters of the fit for each case are shown in Table 3.4.

Bradford et al. (2003) estimate an ionization rate of $(1.5\text{-}5.3)\times 10^{-14} \text{ s}^{-1}$, which is 750 times larger than the galactic ionization rate. Acero et al. (2009) measured a cosmic ray ionization rate up to 1000 times our galactic ionization rate, which is consistent with the results from Bradford et al. (2003). We consider both of these cosmic ray ionization rates to be upper limits, and suggest that the true cosmic ray ionization rate is somewhere in between galactic and 750 times the galactic value. The difference between a cosmic ray ionization rate of 1000 and 750 times the galactic value is negligible, so we will use the values 750 throughout the rest of the paper. Martín et al. (2006) finds evidence that large scale, low velocity shocks drive the chemistry and heating of NGC 253. In support of this, diffuse SiO emission has been detected throughout the nuclear region (García-Burillo

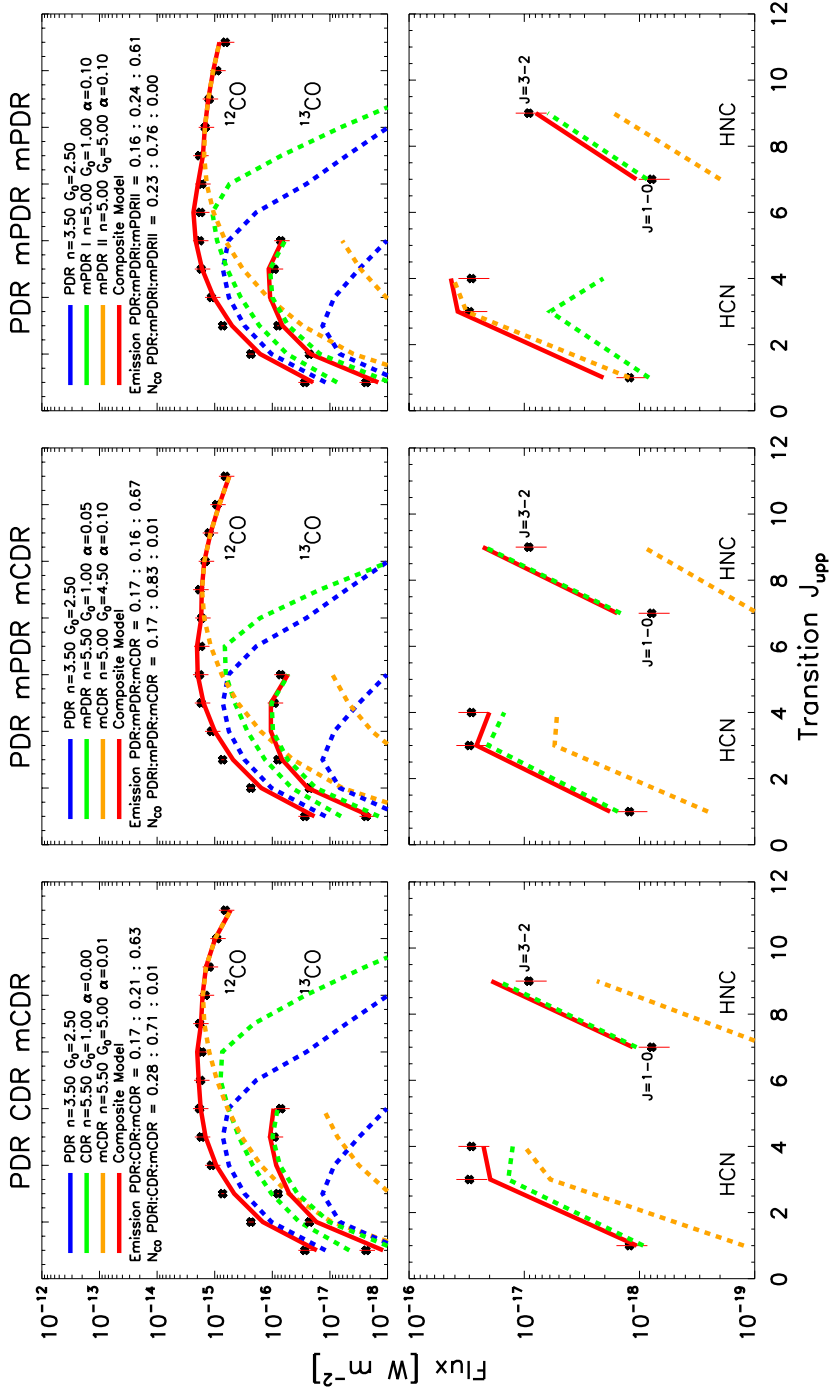


Figure 3.7: ^{12}CO and ^{13}CO (top) with HCN and HNC (bottom) excitation ladders of NGC 253 with flux of each transition plotted as black asterisks with red error bars. In blue, green and yellow dotted lines we plot the PDR/mCDR/mCDR (left), PDR/mPDR/mCDR (center), and PDR/mPDR/mPDR(right) ISM phases with their filling factors. The composite model is plotted with a red solid line. The model H_2 density [$\log \text{cm}^{-3}$], G_0 [$\log \text{Habing flux}$], and percentage mechanical heating (α) are shown in the legend along with the relative contribution of each phase in terms of emission and column density.

Component	Density $\log(n_H)$ $\log[\text{cm}^{-3}]$	$\log(G)$ G_0	$\log(N_{CO})$ $\log[\text{cm}^{-2}]$	$\log(N_{H_2})$ $\log[\text{cm}^{-2}]$	α %	Ω^a	C_{em}^b	C_{NCO}^c	$\text{Mass}_{N_{H_2}}^d$ M_\odot
Case 1 $M_{tot}: 8.4 \times 10^7 M_\odot$									
mPDR	3.5	2.5	17.1	21.5	1	6.0	0.17	0.28	5.7×10^7
CDR	5.5	1.0	17.8	21.4	0	3.0	0.21	0.71	2.3×10^7
mCDR	5.5	5.0	16.8	21.4	1	0.5	0.63	0.01	3.8×10^6
Case 2 $M_{tot}: 1.1 \times 10^8 M_\odot$									
mPDR I	3.5	2.5	17.1	21.5	1	6.0	0.17	0.17	5.7×10^7
mPDR II	5.5	1.0	17.8	21.4	5	5.0	0.16	0.83	4.5×10^7
mCDR	5.0	4.5	16.2	21.2	10	1.5	0.67	< 0.01	7.1×10^6
Case 3 $M_{tot}: 1.1 \times 10^8 M_\odot$									
mPDR I	3.5	2.5	17.1	21.5	1	6.0	0.16	0.23	5.7×10^7
mPDR II	5.0	1.0	17.7	21.4	10	5.0	0.24	0.76	3.8×10^7
mPDR III	5.0	5.0	15.5	21.0	10	5.0	0.61	< 0.01	1.5×10^7

Table 3.4: Model parameters for the three ISM phases for each of the three cases.

^a Ω is the beam filling factor for each ISM phase.

^b C_{em} is the fractional contribution of each ISM phase to the emission.

^c C_{NCO} is the fractional contribution of each ISM phase to the column density.

^d $\text{Mass}_{N_{H_2}}$ is the mass of each ISM phase as estimated by the column density using Eq. 3.4.

et al. 2000). In addition, Martín et al. (2005) have measured an over-abundance of OCS, which is caused by low velocity shocks injecting these molecules into the gas phase. Mechanical heating can also be introduced into the ISM through supernova remnants (Loenen et al. 2008) or strong jets and we test its efficiency at heating molecular gas using the mPDR and mCDR models. Strong molecular outflows have been observed by Bolatto et al. (2013), and they estimate an outflow rate of $9 M_{\odot} \text{ yr}^{-1}$, implying the outflows are a strong source of turbulence in the galactic nucleus.

Since Bradford et al. (2003) suggest that cosmic rays are responsible for most of the molecular gas excitation in NGC 253, we first use case 1, two mCDR models, to fit our observations and see if they are consistent with cosmic ray excitation. We define cosmic ray excitation as ionization by cosmic rays, which produces slow electrons that excite atomic and molecular hydrogen, and in turn produces photons that heat the gas (Glassgold et al. 2012). As seen in the left panel of Figure 3.7, the best fitting model requires no mechanical heating for the second ISM phase, thus it is a pure CDR and requires only 1% mechanical heating for the third ISM phase. The fit of case 1 to CO, HCN, and HNC is very good, yet this begs the question what if the first component also used an enhanced CR rate. We tested a fit with all three ISM phases including an enhanced cosmic ray rate and similarly to Figure 3.6 the ^{13}CO is not fit at all. If we tweak the χ^2 calculation to weight CO more important than HCN and HNC, we can fit ^{12}CO and ^{13}CO but completely destroy the fits of HCN and HNC. However, the fact that we cannot fit three components with a high CR rate does not mean that the fit of case 1 is not possible. Instead, it could represent the physical situation where the diffuse ISM, traced by the first ISM phase, has a diluted cosmic ray rate that can be assumed to be equivalent to the galactic rate.

Since cosmic rays are predominately from supernovae, they may only affect a small percentage of the total gas mass. Therefore, we attempt to recreate our observed line fluxes in case 2 with one PDR, one mPDR, and one mCDR. This scenario represents the case where mechanical heating is present throughout the ISM, and in addition, cosmic rays excite a small amount of gas around supernova remnants. The best fit models for this scenario are shown in the center panel of Figure 3.7. The models fit the ^{12}CO , ^{13}CO , HCN, and HNC reasonably well, if not within the error bars of all transitions. Similarly to case 1, the HNC emission is off by a factor of ~ 2 , yet since our models are not very advanced in their treatment of the chemistry, a factor of 2 is not enough to rule out this case.

Finally, we test the case where mechanical heating is the dominant heating mechanism and cosmic rays are not important to the heating of the molecular gas. The right panel of Figure 3.7 shows the best fit for case 3, three mPDR models,

mPDR II has an $\alpha=0.1$ which translates into a $\Gamma_{mech} = 1 \times 10^{-20} \text{ erg s}^{-1} \text{ cm}^{-3}$ and mPDR III has an $\alpha=0.1$ which is $\Gamma_{mech} = 1.6 \times 10^{-18} \text{ erg s}^{-1} \text{ cm}^{-3}$. This model fits all the ^{12}CO and ^{13}CO transitions within the error bars. In addition, HCN and HNC are better fit than in both case 1 and case 2. Since all three cases reproduce very similar, and very good fits of the molecular transitions, we cannot differentiate between the precise mechanism. Still even in case 1 mechanical heating is needed not only in the first ISM phase but in the third ISM phase needing an $\alpha=0.01$, which is a non-negligible heat rate ($1 \times 10^{-18} \text{ erg s}^{-1} \text{ cm}^{-3}$) as shown in Figure 3.8. Thus it is clear that mechanical heating is necessary to reproduce the observed emission, regardless of the added heating of cosmic rays. This finding is similar to that of Nikola et al. (2011) in NGC 891 and Hailey-Dunsheath et al. (2008) for NGC 253 itself, where they use a combination of shock and PDR models to determine that microturbulence and shocks are responsible for heating the mid-J CO gas.

3.6 Discussion

Since we have concluded that in NGC 253 mechanical heating plays a key role in the gas excitation, we can compare the total mechanical heating with the other heating sources to see which type of heating is dominant. In order to understand the evolution of heating throughout the cloud, we plot the heating rates as a function of A_V , or depth into the cloud. We do this for each ISM phase separately as well as for the total heating of the composite system. We compare all three of our model scenarios: case 1 with two mCDRs, case 2 with one mPDR and one mCDR, and case 3 with two mPDRs. The photoelectric heating includes all related heating mechanisms such as H_2 pumping, CII ionization, viscous heating etc. The heating breakdown is shown in Figure 3.8.

3.6.1 Case 1

For the first ISM phase, the mPDR, the total heating (in black) is produced mostly by photoelectric heating from the PDR since there is only 1% mechanical heating. However, at $A_V=3.5$ the mechanical heating overtakes the photoelectric heating and becomes the dominant heating source. In all cases, the first PDR phase is kept constant, thus for the next sections we will not discuss it further.

For each ISM phase, as well as the integrated heating, at $A_V=0$, or the edge of the cloud, photoelectric heating is the dominant heating source, as expected in a PDR. However, in the second ISM phase, the pure CDR, the cosmic ray heating quickly becomes equally, and slightly more important than photoelectric

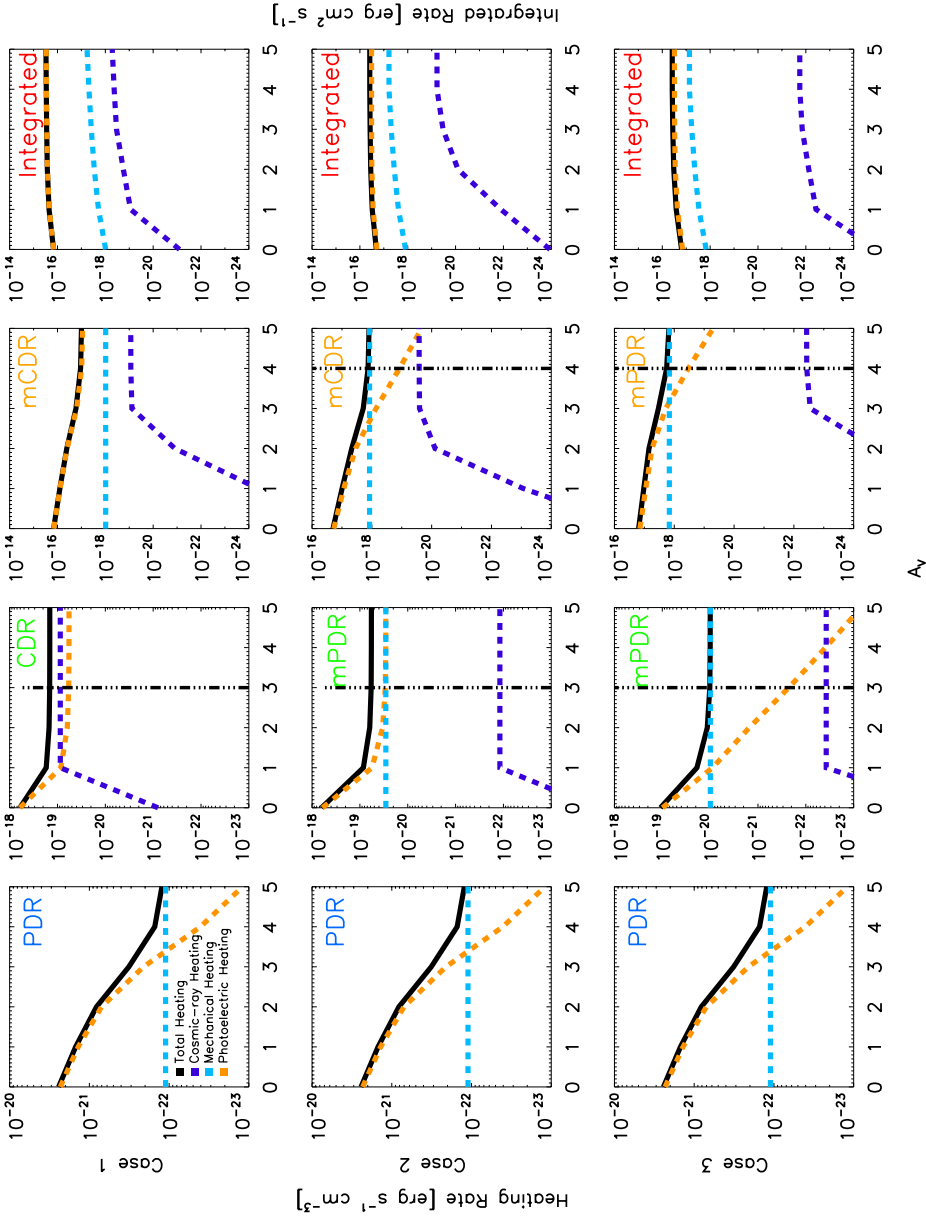


Figure 3.8: Heating rate compared with A_V , or depth into cloud. The total heating is shown in black, the cosmic ray heating is shown in purple, the mechanical heating in blue, and the photoelectric heating in orange. The top row is for case 1 with 1 mPDR, 1 CDR, and 1 mCDR. The middle row is case 2 with 2 mPDRs and 1mCDR and the bottom row is case 3 with 3 mPDRs. The first column is for the first phase for each case, the mPDR, and it is the same in all three cases. The second and third columns represent the second and third ISM phases. Finally, the last column is the integrated heating rates for all ISM phases.

heating at $A_V=1$. The third phase, the mCDR has an $\alpha = 0.01$, and despite a very low mechanical heating rate, the mechanical heating rate is at least 10 times higher than the cosmic ray heating and the photoelectric heating rate dominates the heating through $A_V=5$. Looking at the integrated heating, we see that this case (as well as all cases) is dominated by photoelectric heating. Even though this case includes two ISM phases with an enhanced cosmic ray ionization rate, the CR heating never exceeds that of the mechanical heating.

3.6.2 Case 2

In contrast, the integrated heating for case 2, with two mPDRs and one mCDR, shows although photoelectric heating is the dominant mechanism, mechanical heating still contributes a significant fraction of the heating and CR heating is insignificant. We see that for the second ISM phase, the emission is dominated by photoelectric heating up to $A_V=2$ and then mechanical heating becomes equally as important. Here cosmic rays are relatively unimportant. The mCDR model has an enhanced cosmic ray ionization rate, and is reflected in the heightened CR heating rate. However, in order to reproduce the observed HCN and HNC fluxes, mechanical heating is still necessary and is consistently more important than the cosmic ray heating rate by a factor of at least 50. Thus, in case 2, although we included an enhanced cosmic ray ionization rate in one of the ISM phases, it is unimportant to the total heating of the gas.

3.6.3 Case 3

Finally we study case 3, where there are 3 mPDRs. In this case, both the second and the third phase have an $\alpha = 0.1$ and neither has an enhanced cosmic ray ionization rate. In both mPDR phases, the photoelectric heating drops off sharply, and is replaced by mechanical heating at $A_V=1$ and $A_V=3$ for phase 2 and 3 respectively. Studying the integrated heating, photoelectric heating still dominates, but the mechanical heating is even more important here, and the CR heating is about 5 orders of magnitude less important.

From these plots, we can conclude that in a PDR with any amount of mechanical heating, mechanical heating is more important than the cosmic ray rate, regardless of if it is enhanced. However, mechanical heating being the dominant heating source at the edge of a particular cloud does not mean that it is the overall most efficient source of heating (see the Integrated heating plots). For example, in case 3 with 3 mPDRs, mechanical heating becomes the dominant heating source in each individual PDR by at least $A_V=3.5$, yet if we integrate the heating of the composite model we find that mechanical heating is only responsible for 20% of

the total heating, while photoelectric heating heats 80%. Similarly, if we integrate the contributions from each heating source in the composite model for case 2, we find 84% photoelectric heating at 16% mechanical heating. In both cases 1 and 2, cosmic rays play a negligible role in heating the gas, which may be expected since only the third phase in case 2 has an enhanced cosmic ray ionization rate. However, when we integrate the heating phases of case 1, with two phases with an increased ionization rate, we find 98% of the heating from photoelectric heating and the remaining 2% from mechanical heating. The cosmic ray heating contributes only 0.17% of the total heating. Therefore, we suggest that although we cannot rule out cosmic ray contributions to heating the gas, the dominant heating mechanisms are photoelectric heating and mechanical heating. In addition, although mechanical heating may dominate the heating after $A_V=3$ in individual clouds, it still only contributes a maximum of 20% of the heating in the cloud, in agreement with the upper limit prediction from Rosenberg et al. (2013). This suggests that the source of feedback exciting the high density gas is not directly from star formation, but instead perhaps from the molecular outflows which provide mechanical feedback without the production of cosmic rays Bolatto et al. (2013).

We estimate the mass of each ISM phase and find that regardless of the excitation mechanisms, the mass is relatively well constrained for each case. The first phase, an mPDR with 1% mechanical heating, has a mass of $6 \times 10^7 M_\odot$. The second phase (either CDR or mPDR) has a mass of $2-5 \times 10^7 M_\odot$ and the third phase (either mPDR or mCDR) has a mass of $2-4 \times 10^6 M_\odot$. With the exception of the third phase, the masses of each ISM phase are all approximately the same. In addition, the total mass of each system is well conserved. We find a mass of $8-11 \times 10^7 M_\odot$. This mass is in agreement with $3 \times 10^8 M_\odot$ in an 80" beam (Weiß et al. 2008) since if the gas were evenly distributed, we would expect a mass of $5 \times 10^7 M_\odot$. The gas mass is concentrated in the center of the galaxy, thus it is reasonable to expect a mass a few times higher than the evenly distributed mass. In all cases the third phase contributes at least 60% of the CO emission but represents a maximum of 15% of the mass. Also, in the third ISM phase of all cases, the CO column density is less than 1% of the total CO column. This suggests that the CO is mainly dissociated in this phase, but still responsible for $\sim 60\%$ of the C.

NGC 253 is an ideal case in which we have any observation desired. It is a nearby, well-studied, star-forming galaxy that gives us a representative view of environments undergoing rapid star formation. We have identified that in these galaxies, although mechanical heating is important, heating by UV photons is still the dominant heating source. We have also determined that in this environment, cosmic rays at best play a minor role in heating the molecular gas. In this sense, any star forming galaxy within a similar luminosity class as NGC 253, would have

similar contributions of heating mechanisms. Yet in LIRGs and ULIRGs, there are many other factors in play, including AGN which produce x rays, mergers, and powerful outflows, which increase turbulent heating. It is conceivable that mechanical heating is the dominant source of excitation in such galaxies, or that X-rays are much more important.

For example, studies of Mrk 231 show that the ISM is being processed both by star formation and supernovae (González-Alfonso et al. 2014; Fischer et al. 2010). NGC 6240 on the other hand, shows clear evidence of shocks and mechanical heating (Meijerink et al. 2013). In NGC 1068, Hailey-Dunsheath et al. (2012) find that the gas is either excited by x rays or shocks, but cannot differentiate the two. These galaxies are some examples of (U)LIRGs that show the complexity of disentangling heating mechanisms in these luminous systems. They also demonstrate that in the case of (U)LIRGs it is rarely only UV photons that contribute to heating the molecular gas. Although NGC 253 is not a LIRG, the starburst in the center represents a similar environment, and already demonstrates the need to include an additional heating mechanisms.

3.7 Conclusions

We observe the starburst nucleus of NGC 253 with Herschel SPIRE in order to understand the heating and excitation of the gas.

1. We extract the fluxes of all the lines in our spectra using FT Fitter, and correct them for the changing beam size of SPIRE. We do a basic LVG analysis, using both ^{12}CO and ^{13}CO in order to constrain the parameter space. By mapping the χ^2 values for the full parameter space, we can get a handle on the degeneracies and limit the parameter space further.
2. Using the limits set by the LVG analysis, we perform a PDR analysis. We use not only the 12 and ^{13}CO , but include the HCN and HNC ladders as well, to constrain the dense gas. Although we get a good fit with 3 PDR models, we can see that the solutions are not reasonable and an additional heating source is required. The additional heating source is needed because we cannot reproduce a high enough temperature with just a PDR model to match the observed CO emission.
3. Using PDR models with a constant mechanical heating rate (mPDRs) and PDR models with both a constant mechanical heating rate and a cosmic ray ionization rate equal to 750 times our galactic value (mCDRs), we can fit ^{12}CO , ^{13}CO , HCN, HNC. We fit the four molecular ladders for three

different cases, case 1 is 1 mPDR with 2 mCDRs, case 2 is 2 mPDRs and 1 mCDR, and case 3 is 3 mPDRs.

4. We find that all cases provide a good fit. We cannot fit all four molecules with only enhanced cosmic ray models, we require the first model to be mechanically heated. Although we require mechanical heating to fit the observed transitions, we cannot rule out the existence of cosmic ray heating in addition to the mechanical heating.
5. Taking these three different cases of fits, we study the heating balance as a function of depth into the cloud. We find that in case 1, with an α of just 1% mechanical heating dominates cosmic ray heating at all depths of the cloud. In both cases 2 and 3, mechanical heating quickly becomes the dominant heating mechanism as the cloud depth increases for individual models. In case 3, we see a similar picture with mechanical heating quickly dominating the photoelectric heating in individual models.
6. Regardless of mechanical heating dominating the heating sources, in our most heavily mechanically heated case (case 3), it only contributes about 20% of the total heating, while photoelectric heating is still the dominant overall heating source. In all cases, including case 1 with an enhanced ionization rate for two of the ISM phases, cosmic ray heating is negligible to the total heating of the cloud, as seen in the integrated heating rates of Figure 3.8.
7. We estimate the mass of each ISM phase and regardless of case, the mass is well constrained. The first phase, excited by predominantly photoelectric heating, has a mass of $6 \times 10^7 M_{\odot}$. The second phase has a mass of $3 \times 10^7 M_{\odot}$ and the third phase has a mass of $9 \times 10^6 M_{\odot}$. Although the phases have similar masses, the third phase is responsible for $\sim 60\%$ of the CO emission.

4 | Molecular gas heating in Arp 299

(Ultra) luminous infrared galaxies ((U)LIRGs) are nearby laboratories that allow us to study similar processes to those occurring in high redshift submillimeter galaxies. Understanding the heating and cooling mechanisms in these galaxies gives us insight into the driving mechanisms in their more distant counterparts. Carbon monoxide (CO) is the most abundant and one of the brightest molecules in the Herschel wavelength range. We study Arp 299, a colliding galaxy group, with one component (A) harboring an AGN and two more (B and C) undergoing intense star formation. For Arp 299 A, we present PACS spectrometer observations of high-J CO lines up to J=20-19 and JCMT observations of ^{13}CO and HCN to discern between UV heating and alternative heating mechanisms. There is an immediately noticeable difference in the spectra of Arp 299 A and Arp 299 B+C, with source A having brighter high-J CO transitions. This is reflected in their respective spectral energy line distributions. We find that photon-dominated regions (PDRs, UV heating) are unlikely to heat all the gas since a very extreme PDR is necessary to fit the high-J CO lines. In addition, this extreme PDR does not fit the HCN observations, and the dust spectral energy distribution shows that there is not enough hot dust to match the amount expected from such an extreme PDR. Therefore, we determine that the high-J CO and HCN transitions are heated by an additional mechanism, namely cosmic ray heating, mechanical heating, or X-ray heating. We find that mechanical heating, in combination with UV heating, is the only mechanism that fits all molecular transitions. We also constrain the molecular gas mass of Arp 299 A to $3 \times 10^9 M_{\odot}$ and find that we need 4% of the total heating to be mechanical heating, with the rest UV heating. Finally, we caution against the use of ^{12}CO alone as a probe of physical properties in the interstellar medium.

¹

M. J. F. Rosenberg, R. Meijerink, F. P. Israel *et. al*
A&A, in press (arXiv:1407.2055)

¹Co-authors contributed helpful insight and comments on the main text. The models used, as well as the high-J CO observations are from R. Meijerink, and the ground based observations and corresponding text is from F.P. Israel.

4.1 Introduction

(Ultra) luminous infrared galaxies ((U)LIRGs) are systems or galaxies with very high far-infrared luminosity (ULIRG: $L_{FIR} > 10^{12} L_{\odot}$ and LIRG: $L_{FIR} > 10^{11} L_{\odot}$; Sanders & Mirabel (1996)) owing to a period of intense star formation. Arp 299 (NGC 3690 + IC 694, Mrk 171, VV 118, IRAS 11257+5850, UGC6471/2) is a nearby (42 Mpc Sargent & Scoville (1991)) LIRG ($L_{FIR} = 5 \times 10^{11}$) currently undergoing a major merger event. Arp 299 is dominated by intense, merger-induced star formation and is made up of three main components (Alonso-Herrero et al. 2000). Although the core regions of these components can still be resolved, there is a large overlap in their disks. The separation between Arp 299 A and Arp 299 B and C is 22", or 4.5 kpc in physical distance. Arp 299 B and C are separated by only 6.4", or 1.4 kpc. The largest component is the massive galaxy IC 694 (Arp 299 A), which accounts for about 50% of the galaxies' total infrared luminosity (Alonso-Herrero et al. 2000).

The galaxy NGC 3690 represents the second component (Arp 299 B) that is merging into IC 694 and represents $\sim 27\%$ of the total luminosity (Alonso-Herrero et al. 2000). The third component (Arp 299 C) is an extended region of star formation where the two galaxy disks overlap. Here we use the standard nomenclature, instead of the NED definition. Sargent & Scoville (1991) suggest that an active galactic nucleus (AGN) could be responsible for the large amount of far-infrared luminosity in Arp 299 A, although Alonso-Herrero et al. (2000) find no supporting evidence. Henkel et al. (2005) and Tarchi et al. (2007) suggest that the presence of H₂O masers, along with X-ray imaging and spectroscopy (Della Ceca et al. 2002; Zezas et al. 2003; Ballo et al. 2004) indicate that an AGN must be present in the nuclear region of Arp 299 A. Using milliarcsecond 5.0 GHz resolution images from the VLBI, Pérez-Torres et al. (2010) conclude that there is a low luminosity AGN (LLAGN) at the center of Arp 299 A.

In addition to the AGN, there are intense knots of star formation observed in the infrared and radio (Wynn-Williams et al. 1991). Alonso-Herrero et al. (2000) observe Arp 299 in high-resolution with the Hubble Space Telescope in the near-infrared and also find that over the past 15 Myr, Arp 299 has been undergoing intense merger-related star formation. This star formation is fueled by large amounts of dense molecular gas: $8 \times 10^5 M_{\odot} \text{ pc}^{-2}$ for Arp 299 A, $3 \times 10^4 M_{\odot} \text{ pc}^{-2}$ for Arp 299 B, and $2 \times 10^4 M_{\odot} \text{ pc}^{-2}$ for Arp 299 C (Sargent & Scoville 1991). Most of the star formation responsible for the high far-infrared luminosity is spread over 6-8 kpc (Alonso-Herrero et al. 2009), resulting in most of Arp 299 having typical starburst properties. Only the nucleus of Arp 299 A exhibits true LIRG conditions, with $n_e = 1-5 \times 10^3 \text{ cm}^{-3}$, deep silicate absorption features implying embedded star

formation, and PAH emission (Alonso-Herrero et al. 2009).

In this paper we present observations of the central region of Arp 299 using the Spectral and Photometric Imaging Receiver (SPIRE) on board of the ESA *Herschel* Space Observatory as part of HerCULES (PI: P. P. van der Werf). Due to the large spectral range of SPIRE, we can observe many different line transitions, which enables the study of excitation mechanisms of different phases of the ISM. Specifically, we compare the intensity of different CO transitions to CO emission models to determine the density, temperature, and radiation environment of the phases of the ISM in Arp 299. We directly compare Arp 299 A, which harbors an AGN, to Arp 299 B and C, which are undergoing rapid star formation. Then we add observations from the Photodetector Array Camera and Spectrometer (PACS) (PI: R. Meijerink) and the literature to disentangle the heating mechanisms of the molecular gas. In Section 4.2 we present all of the observations and discuss the data reduction methods. Then in Section 4.3, we present the spectra and line fluxes for both the SPIRE and PACS spectra. A qualitative comparison between Arp 299 A, B, and C is discussed in Section 4.4. Using all available data, in Section 4.5 we explore the heating mechanisms of the highest-J CO transitions and discuss the limitations of using only 12 CO to determine physical parameters in Section 4.6. We state our conclusions in Section 4.7.

4.2 Observations and data reduction

4.2.1 Observations

Herschel SPIRE FTS data: Observations of Arp 299 were taken with the *Herschel* Spectral and Photometric Imaging Receiver and Fourier-Transform Spectrometer (SPIRE-FTS, Griffin et al. 2010a) on board the *Herschel* Space Observatory (Pilbratt et al. 2010a) using three separate pointings centered on Arp 299 A, Arp 299 B, and Arp 299 C (see Table 4.1). The low frequency band covers $\nu=447-989$ GHz ($\lambda=671-303$ μm) and the high frequency band covers $\nu=958-1545$ GHz ($\lambda=313-194$ μm), and these bands include the CO J=4-3 to CO J=13-12 lines. The high spectral resolution mode was used with a resolution of 1.2 GHz over both observing bands. Each source was observed for 4964 seconds (1.4 hours). A reference measurement was used to subtract the emission from the sky, telescope, and instrument. We present the original observed SPIRE spectra in Figure 4.1.

Herschel SPIRE Photometry data: Observations using the SPIRE Photometer were taken as part of the *Herschel* Guaranteed Time Key Program SHINING (PI: E. Sturm). The system was observed on the 6th of January 2010 at 250, 350, and 500 μm (observation ID: 1342199344, 1342199345, 1342199346). The source

Table 4.1: Log of Herschel Observations

Instrument	Transition	Observation ID	Date Y-M-D	Integr. [s]
Arp 299 A $11^{\text{h}}28^{\text{m}}33^{\text{s}}.7 + 58^{\text{d}}33^{\text{m}}46^{\text{s}}$				
PACS	CO $J = 14 - 13$	1342232607	2011-11-21	4759
PACS	CO $J = 16 - 15$	1342232606	2011-11-21	641
PACS	CO $J = 18 - 17$	1342232608	2011-11-22	782
PACS	CO $J = 20 - 19$	1342232603	2011-11-21	1225
PACS	CO $J = 22 - 21$	1342232605	2011-11-21	976
PACS	CO $J = 24 - 23$	1342232603	2011-11-21	1225
PACS	CO $J = 28 - 27$	1342232607	2011-11-21	4759
SPIRE	194 – 671 μm	1342199248	2011-06-27	4964
Arp 299 B $11^{\text{h}}28^{\text{m}}31^{\text{s}} + 58^{\text{d}}33^{\text{m}}41^{\text{s}}$				
SPIRE	194 – 671 μm	1342199249	2011-06-27	4964
Arp 299 C $11^{\text{h}}28^{\text{m}}31^{\text{s}}.13 + 58^{\text{d}}33^{\text{m}}48^{\text{s}}.2$				
SPIRE	194 – 671 μm	1342199250	2011-06-27	4964

was observed 797 seconds in total.

Herschel PACS spectroscopy data: CO $J_{\text{up}} \geq 14$ observations were made with the Photodetector Array Camera and Spectrometer (PACS, Poglitsch et al. 2010a) for Arp 299 A only. The data presented here have been obtained as part of the Herschel program OT1_rmeijeri_1 (PI: Meijerink), complemented by observations from OT1_shaileyd_1 (PI: Hailey-Dunsheath). The observations consisted of deep integrations targeting CO $J = 14 - 13$, CO $J = 16 - 15$, CO $J = 18 - 17$, CO $J = 20 - 19$, CO $J = 22 - 21$, CO $J = 24 - 23$, and CO $J = 28 - 27$. The observation IDs of the targeted CO lines are listed in Table 4.1.

Ground based data: We use the short spacing corrected CO maps from Sliwa et al. (2012) for the $J=1-0$, $2-1$, and $3-2$ transitions for Arp 299 B and C. We integrate the flux corresponding to our largest SPIRE beam ($J=4-3$, $42''$) full-width-half-maximum (FWHM) centered on each of the pointings respectively. We do not use these values for Arp 299 A since the CO $1-0$ map has error bars larger than 50%.

For Arp 299 A, we used dual-polarisation receivers A and B (decommissioned in 2009) on the IRAM 30 m telescope to measure the $J=1-0$ ^{12}CO line towards Arp 299 in November 2005, followed by observations of $J = 2 - 1$ ^{12}CO and both $J=1-0$ and $J=2-1$ ^{13}CO in July 2006. Weather conditions were good to excellent. System temperatures including the sky were 160 K to 240 K for the $J=1-0$ transi-

tions and 400 - 500 K for the $J=2-1$ transitions. Beam sizes are 21"-22" and 11" at 110-115 GHz and 220-230 GHz corresponding to these transitions. Main-beam efficiencies were 0.74, 0.73, 0.48, and 0.45 at these four frequencies, respectively. The $J=2-1$ ^{12}CO and ^{13}CO lines were also observed with the JCMT 15 m telescope in June and July 1995, with overall system temperatures including the sky of 485 and 340 K, respectively. The beam size was 21" - 22", and the main-beam efficiency was 0.69. All spectra were binned to resolutions of 20 km/s. A linear baseline was subtracted, and the line flux was determined by integrating over the velocity range $V(\text{LSR}) = 2800 - 3500$ km/s.

The HCN $J=(3-2)$ observations were made with the JCMT in February 2010 using receiver A3 under good weather conditions with system temperatures of 240 to 310 K; the beam size was 18", and we used a main-beam efficiency of 0.69 at the operating frequency of 265.9 GHz. HCN $J=(4-3)$ was obtained with the HARP array in stare mode on the JCMT in May 2010. Weather was excellent, with $T(\text{sys})$ in the range of 226-240 K. We extracted the line profile from the central pixel. The beam size was about 13" and the main-beam efficiency about 0.6. From the observed spectra, line fluxes were recovered in the same way as for the ^{13}CO observations.

4.2.2 Data reduction

Herschel SPIRE FTS data: The data were reduced using version 9.0 of Herschel Interactive Processing Environment (HIPE). For all extended sources, an aperture correction is necessary to compensate for the wavelength dependent beam size. This requires knowledge of the source distribution at SPIRE wavelength. We approximated the size based on a high spatial resolution SMA CO $J=3-2$ map (Wilson et al. 2008).

Each SMA map was convolved with a 2-D Gaussian to match the FWHM of the SPIRE beam sizes (15-42"). We then determine the flux density at the SPIRE pointing centers as a function of spatial resolution normalized by the flux density in the largest aperture (42"). The resulting dependency between normalized flux density and spatial resolution was then applied to SPIRE's Long Wavelength Spectrometer Array (SLW) and the Short Wavelength Spectrometer Array (SSW) spectra taking the SPIRE beam sizes as a function of wavelength into account. Finally the SLW and SSW spectra were coadded flagging the noisy edge channels in both spectra. This yields a combined spectrum at an effective spatial resolution of 42" for each source.

The quality of the aperture correction can easily be evaluated by comparing the continuum flux densities in the corrected SLW and SSW spectra in their spectral overlap region. Our approach effectively removes the 'jump' visible in the continua

between the SLW and SSW spectra at their original spatial resolution, although we only present the original observed spectra below.

The ratio of the flux between each convolved SMA map and the flux within the largest beam size (42") is the beam correction factor (κ_S) where:

$$F_{corr} = F_{obs} \times \kappa_S \quad (4.1)$$

Thus, all fluxes are normalized to a beam size of 42" (i.e. 9.8 kpc). The beams for pointings B and C significantly overlap, thus it is hard to discern any independent measurements from these pointings. However, pointing A is more isolated. Although the largest beam does include some of B and C, most of the beam sizes are completely independent.

Fluxes were first extracted using FTFFitter, a program specifically created to extract line fluxes from Fourier transform spectrographs. This is an interactive data language (IDL) based graphical user interface that allows the user to fit lines, choose line profiles, fix any line parameter, and extract the flux. We define a polynomial baseline to fit the continuum and derive the flux from the baseline subtracted spectrum. In order to more accurately determine the amplitude of the line, we fix the FWHM to the expected line width of ^{12}CO at each source, using the velocity widths measured by Sliwa et al. (2012). In the case of very narrow linewidths, more narrow than the instrumental resolution (J= 4-3 through 8-7 for Arp 299 C), we do not fix the FWHM but fit the lines as an unresolved profile. We use an error of 30% for our fluxes, which encompasses our dominant sources of error. Specifically, the uncertainty of the beam size correction using SMA CO J=3-2 map is $\sim 20\%$. The error of the absolute calibration uncertainty for staring-mode SPIRE FTS observations is an additional 6% (Swinyard et al. 2014). We also have some uncertainty in the definition of the baseline and flux extractions, since we use an unresolved or Gaussian profile for all emission lines, accumulating to $\sim 5\%$.

Herschel SPIRE photometry data: SPIRE maps were reduced using HIPE 10.3.0 (Ott 2010) and the SPIRE calibration tree v.10.1. A baseline algorithm (Bendo et al. 2010) was applied to every scan of the maps in order to correct for offsets between the detector timelines and remove residual baseline signals. Finally, the maps were created using a naive mapping projection. The global fluxes for Arp 299 are measured to be 21.8, 7.34 and 2.37 Jy for 250, 350 and 500 μm respectively. For the errors in the SPIRE photometry we adopted a 15% calibration uncertainty for extended emission; (SPIRE Observers Manual, v2.4, 2011).

Herschel PACS data: The data were processed and calibrated using HIPE version 10.0 and the pipeline for range spectroscopy. The object was centered on the 9.4" central spaxel of the 5 by 5 PACS array. Little flux is seen outside this central spaxel, and therefore the fluxes are extracted from the central spaxel and referenced to a point source. We use a 3 by 3 spaxel correction for extended sources

and small pointing offsets. We used SPLAT as part of the STARLINK software package to subtract baseline, and determine the peak flux, full-width-half maximum (FWHMs), integrated flux, and its uncertainty for the CO lines. To find the integrated flux and uncertainty, we fit a Gaussian profile to the line and integrate the Gaussian.

Ground Based Data: In the reduction of the line profiles observed with IRAM and JCMT, we used the CLASS package. The JCMT data were retrieved with the SpecX package and turned into FITS files which were subsequently imported into CLASS. The IRAM profiles were immediately available in CLASS format. For all line profiles, second-order baselines were subtracted. Line fluxes were determined both by Gaussian fitting, and by straightforward summing over a sufficiently wide velocity interval. Both methods yielded nearly identical results. We then scaled the ^{13}CO $J=1-0$ and $J=2-1$ up to the 42" beam size using the same method described in Section 4.2.2 for the SPIRE FTS observations.

4.3 Results

Here we present the spectral profiles and line fluxes for the SPIRE FTS spectra and the PACS observations.

4.3.1 SPIRE FTS line fluxes

The ^{12}CO transitions are visible from $J=4-3$ to $J=13-12$. There were also strong detections of [NII] at 1437 GHz and [CI] at 484 GHz and 796 GHz in all three spectra. We detect 7 strong water emission lines, they are most prominent in Source A and become weaker or undetectable in Sources B and C. The lines are labeled in Figure 4.1, ^{12}CO in black, H_2O in blue, and atomic lines in magenta. As seen in this plot there is a discontinuity between the high and low frequency modes of the spectrometer. This discontinuity is due to the different apertures used by the high and low frequency arrays combined with the fact that the object is not a point source. A scaling factor (κ_S) for each wavelength is calculated using the method described in Section 4.2.2, and displayed in Table 4.2.

4.3.2 PACS line fluxes

The PACS CO $J = 14 - 13$, $16 - 15$, $18 - 17$, and $20 - 19$ line detections are shown in Fig. 4.2 and their peak flux, FWHM, and integrated fluxes are listed in Table 4.3. We also would like to note that the CO $J = 20 - 19$ transition is only detected at 2σ . The CO $J = 22 - 21$, $J = 24 - 23$ and $28 - 27$ were not detected, and for these lines we determined an upper limit.

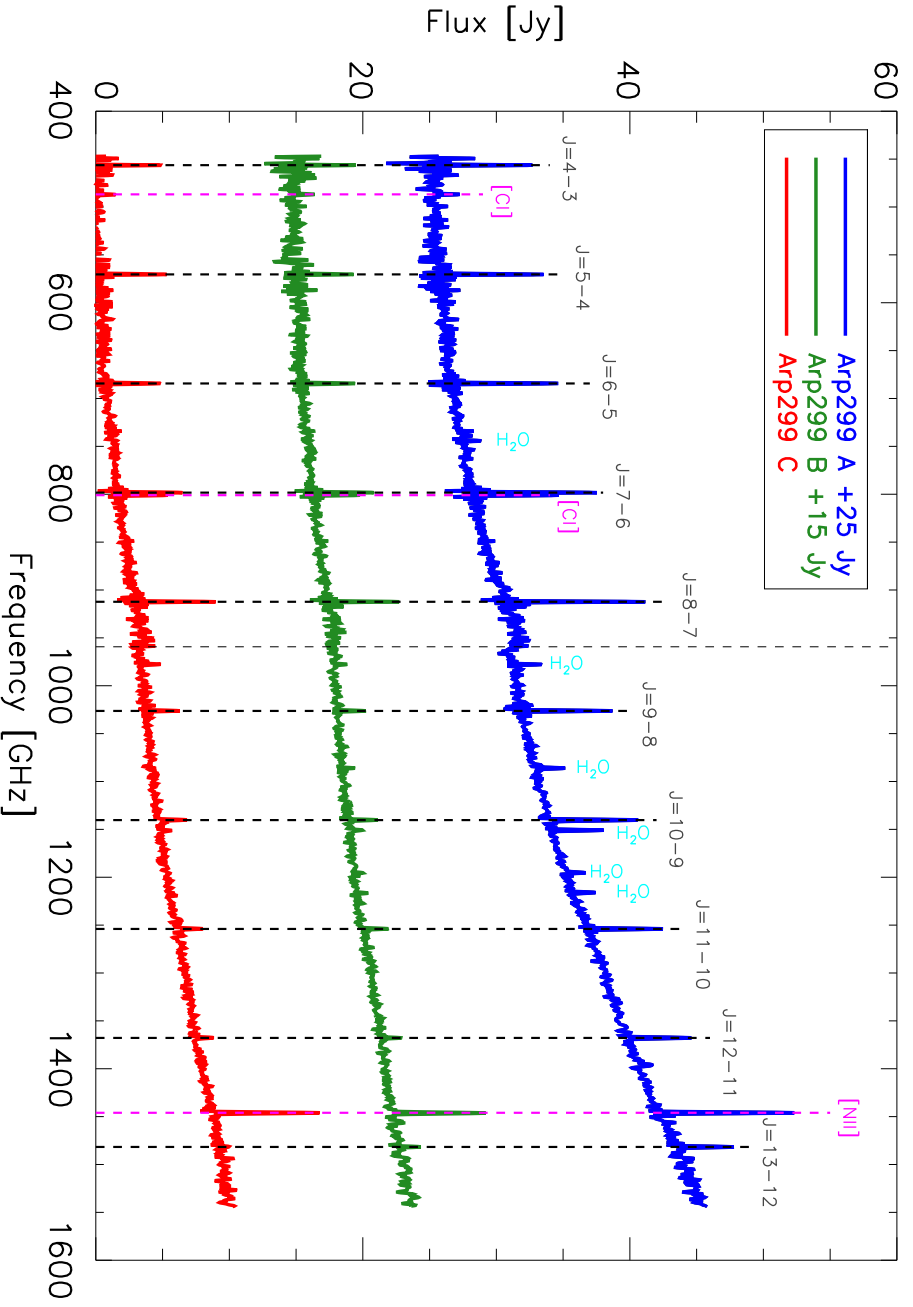


Figure 4.1: SPIRE spectra of Arp 299 A (blue), B (green) and C (red). Source A is offset by 25 Jy, while Source B is offset by 15 Jy. Each bright line is identified, CO lines in black, atomic lines in magenta, and H₂O lines in cyan. The atomic lines and H₂O transitions will be discussed in a different paper.

Line	κ_{S_A} 32.8''	Flux Arp 299 A [10^{-17} W m $^{-2}$]	κ_{S_B} 32.8''	Flux Arp 299 B [10^{-17} W m $^{-2}$]	κ_{S_C} 32.8''	Flux Arp 299 C [10^{-17} W m $^{-2}$]
$^{12}\text{CO } 4-3$	1.01	8.89	1.02	5.28	1.02	5.88
$^{12}\text{CO } 5-4$	1.10	10.8	1.26	6.75	1.24	7.45
$^{12}\text{CO } 6-5$	1.14	12.5	1.40	7.18	1.38	7.02
$^{12}\text{CO } 7-6$	1.07	13.0	1.19	6.39	1.18	6.29
$^{12}\text{CO } 8-7$	1.05	14.2	1.12	6.82	1.12	7.31
$^{12}\text{CO } 9-8$	1.30	13.4	1.39	3.86	1.30	3.97
$^{12}\text{CO } 10-9$	1.33	14.5	1.51	4.80	1.45	3.65
$^{12}\text{CO } 11-10$	1.33	13.2	1.53	3.84	1.47	3.37
$^{12}\text{CO } 12-11$	1.34	11.4	1.57	2.72	1.53	2.29
$^{12}\text{CO } 13-12$	1.35	10.9	1.59	3.45	1.55	1.66
$[\text{CI}]^3 P_1 - ^3 P_0$	1.04	2.56	1.09	2.17	1.08	1.94
$[\text{CI}]^3 P_2 - ^3 P_1$	1.07	8.46	1.19	4.61	1.18	4.49
$[\text{NII}]^3 P_1 - ^3 P_0$	1.35	25.6	1.59	11.1	1.55	5.86
$^{12}\text{CO } 1-0$	--	0.29	--	0.08 ^a	--	0.01 ^a
$^{12}\text{CO } 2-1$	--	1.29	--	0.76 ^a	--	0.73 ^a
$^{12}\text{CO } 3-2^a$	--	5.09	--	2.10	--	3.04
$^{13}\text{CO } 1-0$	--	0.01	--	--	--	--
$^{13}\text{CO } 2-1$	--	0.15	--	--	--	--
HCN 1-0 ^b	--	0.003	--	--	--	--
HCN 3-2	2.52	0.04	--	--	--	--
HCN 4-3	3.77	0.03	--	--	--	--

Table 4.2: Observed line fluxes corrected for beam size using correction factors (κ_S , Section 2.2). Also, the errors on all derived fluxes are 30% as explained in the text. Fluxes from ground-based observations found in the literature are also presented.

^a Determined from the maps presented in Sliwa et al. (2012).

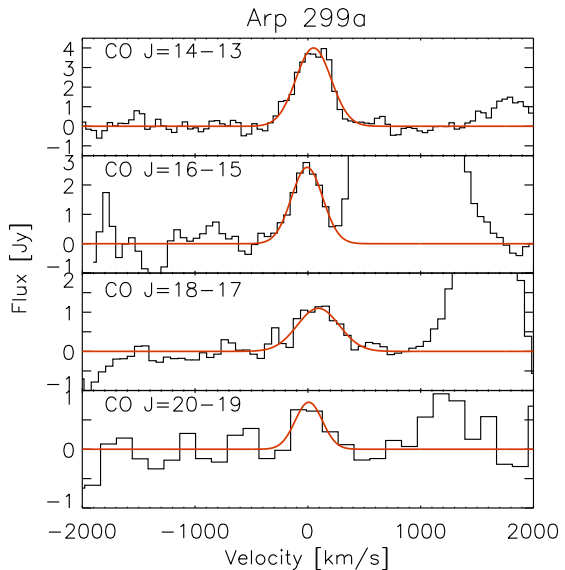
^b From Imanishi & Nakanishi (2006).

Transition	λ_{rest} [μm]	Peak [Jy]	ΔV_c^a [km/s]	FWHM [km/s]	S_{line} [10^{-17} W m $^{-2}$]	$S_{\text{line,corr}}$ [10^{-17} W m $^{-2}$]
Arp 299 A						
CO $J = 14 - 13$	185.999	4.0 ± 0.2	50 ± 7	367 ± 17	8.3 ± 0.5	11.2 ± 0.7
CO $J = 16 - 15$	162.812	2.6 ± 0.1	-7 ± 6	326 ± 16	5.6 ± 0.3	7.5 ± 0.5
CO $J = 18 - 17$	144.784	1.1 ± 0.1	92 ± 21	438 ± 50	3.6 ± 0.5	4.8 ± 0.7
CO $J = 20 - 19$	130.369	0.8 ± 0.2	8 ± 36	285 ± 87	1.8 ± 0.7	2.4 ± 0.9
CO $J = 22 - 21$	118.581				< 2.3	< 3.1
CO $J = 24 - 23$	108.763				< 2.6	< 3.5
CO $J = 28 - 27$	93.3491				< 1.7	< 2.3

Table 4.3: PACS CO observations.

^a ΔV_c is the distance in km/s away from the central wavelength of the line.

Figure 4.2: PACS spectra of Arp 299 A, showing the detections for CO $J = 14 - 13$, $16 - 15$, $18 - 17$, and $20 - 19$. The $J = 20 - 19$ transition is only a 2σ detection. The line to the right of the $J = 16 - 15$ transition, around 1000 km/s is the OH doublet ($\Pi_{1/2} - \Pi_{1/2}$ $3/2 - 1/2$ $163.124 - 163.397 \mu\text{m}$), and the line to the right of the $J = 18 - 17$ transition is the [O I] $145 \mu\text{m}$ line. The velocity scale is calculated for a redshift of $z = 0.01030$ and the channel spacings are 47 , 57 , 64 , and 140 km/s for the $J = 14 - 13$, $16 - 15$, $18 - 17$, and $20 - 19$ respectively.



4.4 Comparison between Arp 299 A and B+C

In this section, we perform a comparison of Arp 299 A, B, and C using only the SPIRE FTS fluxes to determine what differences are observed from ^{12}CO alone. The most notable aspect of the spectra presented in Figure 4.1 is that the high- J CO lines of Arp 299 A are distinctly brighter than those of Arp 299 B and C. It is clear simply from inspecting the spectra that the molecular gas in Arp 299 A is more excited than that of Arp 299 B and C.

For each spectrum (A, B, and C) we can create a spectral line energy distribution or 'CO ladder', which plots the intensity of each CO transition as a function of the upper J number. This type of diagram is predicted to be a powerful diagnostic tool as shown by Meijerink & Spaans (2005) and Meijerink et al. (2007), where models show that these CO ladders have very different shapes depending on the type of excitation (i.e. photon dominated region, PDR or X-ray dominated region, XDR) as well as density and radiation environment. The three CO ladders for Source A, B, and C are plotted on top of each other in Figure 4.3. For context, their smallest and largest beam sizes are plotted over a SCUBA $450 \mu\text{m}$ image, showing the overlap between the Arp 299 B and C pointings. This overlap is also apparent in the CO ladders, the two ladders follow the same shape and intensity, meaning they are essentially an averaged observation of both Arp 299 B and C. Because of this, we only use the averaged values for Arp 299 B and C from here on. Although we cannot discern anything independent about Arp 299 B and C, it

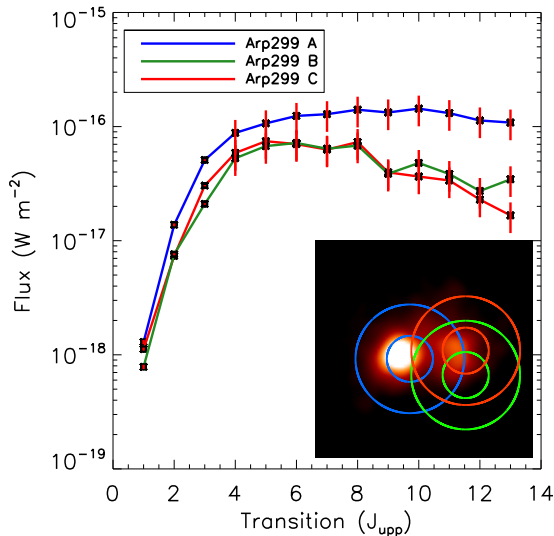


Figure 4.3: CO excitation ladders of Arp 299 A (blue), B (green), and C (red). Intensities are in W m^{-2} . The inset in the bottom right corner shows the three SPIRE beam FWHMs for Arp 299 A, B, and C overplotted on a SCUBA $450 \mu\text{m}$ archival image. The smaller circle represents the smallest beam FWHM ($\sim 17''$) and the larger circle represents the largest beam FWHM ($\sim 42''$).

is immediately apparent that Arp 299 A has a very different CO ladder. Arp 299 A flattens in intensity with increasing transitions, while Arp 299 B and C both show a turnover in their ladders at $J_{\text{upp}}=5$. This indicates clearly that there is more warm CO in Arp 299 A than in B+C and we expect to see this reflected in the following PDR analysis.

4.4.1 Basic PDR analysis

Since Arp 299 is a LIRG with a high star formation rate, there must be a high density of OB stars and thus a high UV energy density. Through photoelectric heating and FUV pumping of H_2 , the FUV photons heat the outer layers ($A_V < 5$) of molecular clouds. This area of the molecular cloud is the PDR, and is responsible for warm molecular gas emission. The thermal state of PDRs is determined by processes such as photo-electric heating; heating by pumping of H_2 followed by collisional de-excitation; heating by cosmic rays; [OI] and [CII] fine-structure line cooling; and CO, H_2O , H_2 , and OH molecular cooling. The ionization degree of the gas is driven by FUV photo-ionization, and counteracted by recombination and charge transfer reactions with metals and PAHs. The ionization degree is at most $x_e \sim 10^{-4}$ outside of the fully ionized zone. The chemistry exhibits two fundamental transitions, H to H_2 and C^+ to C to CO. Using PDR models (Meijerink & Spaans 2005; Kazandjian et al. 2012) that solve for chemistry and thermal balance throughout the layers of the PDR, we use the predictions of the

^{12}CO emission as a function of density, radiation environment (G , in units of the Habing radiation field $G_0=1.6\times 10^{-3}$ erg cm $^{-2}$ s $^{-1}$), and column density. We use an isotopic abundance ratio of 80 for $^{12}\text{CO}/^{13}\text{CO}$, since our observed $^{12}\text{CO}/^{13}\text{CO}$ J=1-0 intensity ratio is ~ 24 , which is common in (U)LIRGs (Aalto et al. 1997). González-Alfonso et al. (2012) find an isotope ratio around 100 for the prominent starburst Arp 220, which is similar to that of Mrk 231 (Henkel et al. 2014). However, for a less powerful starburst, such as NGC 253, the isotope ratio was measured to be 40 (Henkel et al. 2014). Since Arp 299 is a moderate starburst, an estimate of 80 is reasonable. The density profile is constant and the Habing field is parameterized in units of G_0 from photons between 6 eV and 13.6 eV. We perform an unbiased fitting of the models to the CO ladder, employing an automated χ^2 fitting routine, described in detail in Rosenberg et al. (2014). This routine allows for up to 3 different ISM phases where we define the total model as:

$$Model = \Omega_I PDR_I + \Omega_{II} PDR_{II} + \Omega_{III} PDR_{III} \quad (4.2)$$

where PDR_I , PDR_{II} , and PDR_{III} are the distinct contributions of the three PDR models. Ω_I , Ω_{II} , and Ω_{III} represent the respective filling factors of each ISM phase. Filling factors traditionally represent how much of the beam is filled, so they only range from 0 to 1. However, this assumes that these clouds do not overlap in velocity, which we allow for. Thus, Ω is not only a beam filling factor, but also allows for an overlap in velocity, which accounts for it being slightly greater than one.

We perform a modified Pearson's χ^2 minimized fit for ^{12}CO and ^{13}CO simultaneously, where the modified Pearson's χ^2 is:

$$\chi_{mol}^2 = \frac{\sum_{i=1}^{N_{data}} \frac{(obs_i - model_i)^2}{model_i}}{N_{data}} \quad (4.3)$$

We define χ_{mol}^2 as the modified Pearson's χ^2 for a specific molecule. The total χ^2 is the sum of the χ_{mol}^2 terms for each molecule. The numerator of this equation is the traditional Pearson's χ^2 , then in the denominator we divide by the total number of transitions in each respective molecule, essentially yielding an average χ^2 for ^{12}CO and ^{13}CO separately. In Section 5, we refer to the total χ^2 as being the sum of Eq. 4.3 for all molecules; ^{12}CO , ^{13}CO , and HCN.

Using this equation, we calculate the χ^2 for every combination of 3 models and filling factors. In this way, we cannot only see which models make the best fit, but we can also see the χ^2 values for all the other model combinations. This allows us to understand the level of degeneracy inherent to the models and understand the limitations of this method. In Figure 4.4, we show the best fitting models for

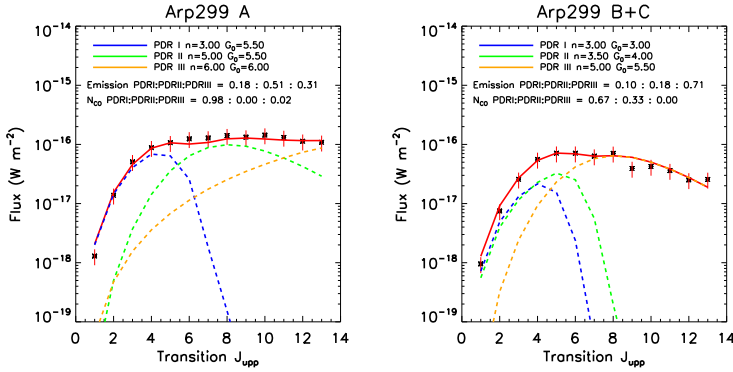


Figure 4.4: Best fit (χ^2 minimized) PDR models simulating the ^{12}CO emission for Arp 299 A (left) and B+C (right) using three ISM phases.

The red line is the sum of the three phase models, the black asterisks are the data points with error bars, and the blue, green, and orange lines represent the independent PDR models for each phase. The model density, temperature and column density are shown in the legend along with the relative contribution of each phase in terms of emission and column density.

Arp 299 A and Arp 299 B+C. We also calculate the relative contribution of each independent model to the overall CO ladder intensity in terms of emission and CO column density.

One aspect of these fits is that each of the CO ladders needs a minimum of three ISM phases to be fit well. In addition, the lowest J transitions are fit with a relatively low density and low G PDR, the middle phase is a medium density and medium G PDR, and finally the highest J transitions can only be fit by extreme PDRs, which makes up a negligible percent of the CO column density, but over 30% of the total CO emission in the case of Arp 299 A and over 60% of the total CO emission in Arp 299 B+C. In Figure 4.5, we display the degeneracy plots for Arp 299 B+C. These plots are only a slice of the full degeneracy cube, held at the best fit column densities. They are a representative example of the degeneracy plots of the other fits and share similar characteristics. In the left panel, we show the degeneracy plot for the first ISM phase (PDR I). Each small square represents a different model with a particular density and radiation. The color represents the χ^2 value, white being the lowest and black being the highest.

As seen in Figure 4.5, the fits are degenerate. We do have a 'best fit', designated with an asterisk, but especially in the case of PDR I, there are a wide range of models that would fit almost as well as the selected model. We can only constrain density to $n = 10^{2.5} - 10^{5.5} \text{ cm}^{-3}$ and the radiation field is unconstrained. Even

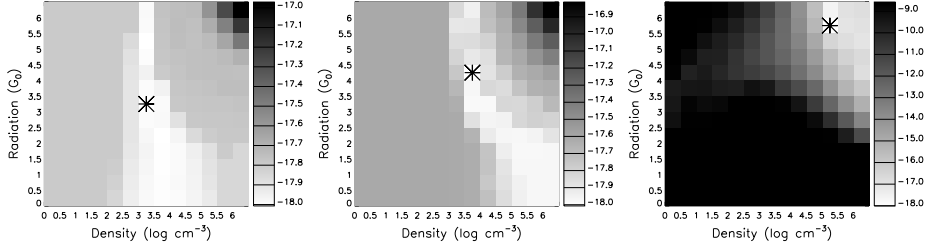


Figure 4.5: Degeneracy plots for Arp 299 B+C. Each plot represents the full grid of models for each phase in Figure 4.4, PDR I (left), PDR II (center), PDR III(right). The asterisk represents the model with the lowest χ^2 , which are also plotted in Figure 4.4. The gray scale of each small square indicates the associated $\log(\chi^2)$ value for that particular model, white being the best fits and black being the worst. The χ^2 value is defined in Equation 4.3 and shown in log gray scale.

though the fits are degenerate, it is clear that each phase has a specific and independent range of parameter space for which there is a good fit. Each ISM phase has a trade off between radiation and density, but each cover a different range of values. For instance, PDR I ranges in density from $n = 10^{2.5} - 10^{5.5} \text{ cm}^{-3}$, while PDR II ranges from $n = 10^3 - 10^6 \text{ cm}^{-3}$ and PDR III ranges from $n = 10^{5.0} - 10^6 \text{ cm}^{-3}$. The radiation field strength is not as well constrained and varies inversely to the density. However without more information, we cannot break the observed degeneracies.

Since we have ancillary data for Arp 299 A, and since we cannot separate the contributions from Arp 299 B and C, the following discussion will focus on Arp 299 A.

4.5 A case study: Arp 299 A

Using the PACS high-J ^{12}CO as well as the JCMT ^{13}CO , and HCN observations, we determine if Arp 299 A can be heated purely through UV heating or if additional heating sources are necessary. We can use the PACS observations presented in Section 4.3.2 to extend the SPIRE CO ladder from $J_{\text{upp}}=13$ to $J_{\text{up}} = 20$. We then add the observations of ^{13}CO J=1-0 and J=2-1 to constrain column density and observations of HCN J=1-0, J=3-2, and J=4-3 to constrain the high density components. In addition, we extract fluxes from the SPIRE Photometry maps and combine them with observations from the literature in order to perform an SED analysis of the dust to help further disentangle UV from other heating sources.

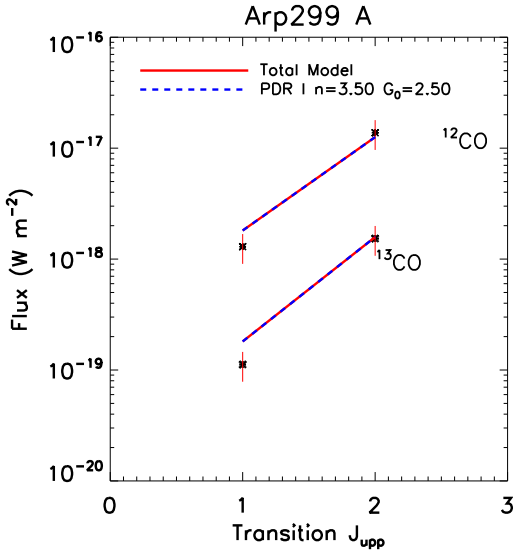


Figure 4.6: Best fit model of ^{13}CO $J<2$ and ^{12}CO $J<2$. The solid line is the total model, the asterisks are the data points with error bars, and the dotted line represents the first ISM phase, represented by a PDR model. The model density and radiation strength are shown in the legend.

4.5.1 The low-excitation phase

Before we blindly fit the full grid of models to our observations, we can constrain the first ISM phase, responsible for the low- J CO lines. Since ^{13}CO is optically thin, the ratio of ^{13}CO to ^{12}CO constrains the optical depth, and in turn the column density. We have observations of ^{13}CO 1-0 and 2-1 from the JCMT, as presented in Section 4.2. We can assume that the ^{13}CO 1-0 and 2-1 lines arise from the same ISM phase that is responsible for the first few transitions of ^{12}CO , and can run the automated fitting routine on the low- J transitions alone. The best fit is displayed in Figure 4.6. Since often, most of the ^{12}CO is in low rotational states, we can help constrain the mass of the whole system by finding the mass of the low-excitation ISM phase. In this phase, we find a mass of $2 \times 10^9 M_{\odot}$ (Eq. 4.4), which represents $\sim 66\%$ of the total molecular gas mass.

4.5.2 Full PDR analysis

Now that we have constrained the first ISM phase, we can include all the available data to constrain the other ISM phases. We will include ^{12}CO observations from PACS including $J=14-13$ through $J=20-19$ to constrain the CO ladder turn-over point, HCN 1-0, 3-2, and 4-3, to constrain the properties of the high density gas, and the SPIRE photometry observations to estimate the dust temperature. With all the available line fluxes, we can first fit the full CO and HCN ladders of Arp 299 A using pure PDR models. In Figure 4.7, we display the ^{12}CO and ^{13}CO

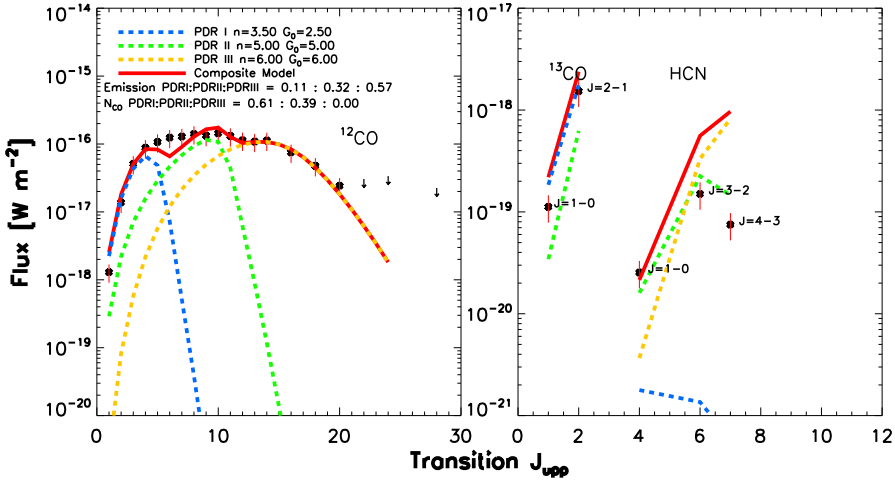


Figure 4.7: Left panel: A χ^2 minimized fit of the CO ladder of Arp 299 A from $J=1-0$ through 24-23. The fit was constrained to three PDR models, displayed in blue, green, and yellow. The black points are the observed CO fluxes and the red line is the total model fit. **Right panel:** The same models as the left panel, but the fits for the ^{13}CO and HCN fluxes. The HCN model lies far above the observed $J=3-2$ and $4-3$ HCN fluxes.

ladders from $J=1-0$ through 28-27 and $J=1-0$ to 2-1 respectively, along with the χ^2 minimized fits. We also calculate the relative contribution of each independent model to the overall CO ladder in terms of luminosity and CO column density.

The parameters of the fits are given in Table 4.4. We have estimated the masses of each ISM phase using the equation from Rosenberg et al. (2014):

$$M_{H_2} = \sum_i^n \frac{\Omega_i N_{H_2,i} A_{beam} m_{H_2}}{M_{\odot}} \quad (4.4)$$

where N_{H_2} is the H_2 column density in cm^{-2} which is consistently calculated in the PDR models, A_{beam} is the beam area in cm^2 , and m_{H_2} is the mass of a hydrogen molecule.

We estimate the relative contributions of column density and emission to the total ^{12}CO ladder. In order to estimate the relative contribution of emission, we use the following equation:

$$C_{em} = \frac{\sum_{i=1}^{13} {}^{12}\text{CO}_{mod,i}}{{}^{12}\text{CO}_{tot}} \quad (4.5)$$

where ${}^{12}\text{CO}_{mod}$ is the summed flux from the modeled CO transitions from $J=1-0$ to $J=13-12$ of a specific PDR model and ${}^{12}\text{CO}_{tot}$ is the total model flux, defined

Component	Density $\log(n_H)$ $\log[\text{cm}^{-3}]$	$\log(G)$ G_0	$\log(N_{CO})$ $\log[\text{cm}^{-2}]$	$\log(N_{H_2})$ $\log[\text{cm}^{-2}]$	Ω^a	C_{em}^b	C_{NCO}^c	$\text{Mass}_{N_{H_2}}^d$ M_\odot
$M_{tot}: 2 \times 10^9 M_\odot$								
PDR I	3.5	2.5	17.1	21.5	1.2	0.11	0.61	2×10^9
PDR II	5.0	5.0	18.2	21.9	0.06	0.32	0.39	3×10^8
PDR III	6.0	6.0	16.7	21.2	0.006	0.57	< 0.01	6×10^6

Table 4.4: Model parameters for the three molecular gas ISM phases using only PDR heating.

^a Ω is the beam filling factor for each ISM phase.

^b C_{em} is the fractional contribution of each ISM phase to the emission, as in Eq. 4.5.

^c C_{NCO} is the fractional contribution of each ISM phase to the column density.

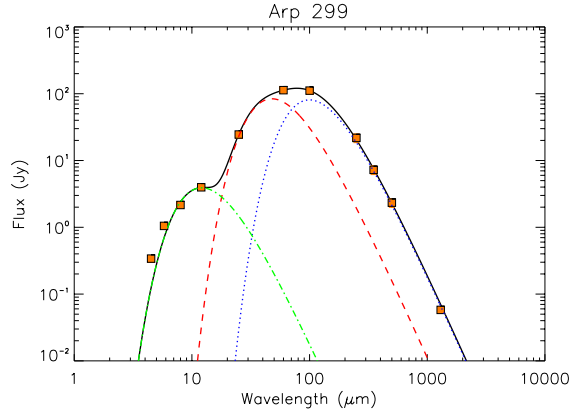
^d $\text{Mass}_{N_{H_2}}$ is the mass of each ISM phase as estimated by the column density using Eq. 4.4.

in Eq. 4.2. We use the same method for calculating the contribution of column density, except we compare the column density of each PDR model to the total column density.

Three pure PDR models fit the ^{12}CO well, although the mid-J lines are not all fully reproduced. The ^{13}CO is also very well reproduced. We find an H_2 mass of $3 \times 10^9 M_\odot$, which matches the mass estimates from the literature, $1.8\text{--}8.6 \times 10^9 M_\odot$ (Sliwa et al. 2012; Sargent et al. 1987; Solomon & Sage 1988). As shown in Rosenberg et al. (2014), HCN is a good tracer of the excitation mechanism since the relative line ratios of various HCN transitions depend on excitation mechanism, and in the pure PDR fit, the models fail to fit any of the HCN transitions. Note that the red line for HCN lies far above the observed J=3-2 and 4-3 transitions. Since we cannot reproduce both the CO and HCN emission with the same best fit model, this suggests that there is an alternative heating mechanism responsible for heating the dense gas, which is traced by the HCN. In order to produce enough CO flux in the high-J transitions, the HCN is overproduced, thus we need a mechanism which selectively heats the high-J CO without heating as much HCN.

In addition, the only way to reproduce the flux of the high-J CO lines with a PDR is with a density of 10^6 cm^{-3} and a radiation flux of $10^6 G_0$, which is an order of magnitude higher than the most extreme PDRs (i.e. Orion Bar) found in the Milky Way. In terms of mass, this ISM phase represents about $\sim 0.2\%$ of the total molecular gas mass of Arp 299 A (Table 4.4). Since UV photons are even more efficient in heating the dust than the gas (unlike X-rays, cosmic rays, and mechanical heating), we expect the same percentage of the dust mass to be heated to high temperatures ($>200 \text{ K}$). Using a combination of three gray bodies, we can fit the SED with a "cool", "warm", and "hot" dust component (see, e.g., Papadopoulos et al. (2010)) aiming to account for the cold cirrus-type dust, the star formation-

Figure 4.8: The dust SED of Arp 299. This is a fit with three gray bodies representing the cold (blue), warm (red) and hot (green) dust components. Observations are plotted with orange squares while the black line is the total SED model fit (Section 4.2).



heated dust, and an AGN-heated dust respectively. We caution the reader on the simplicity of the physics underlying this kind of modeling and especially for the emission at mid-infrared wavelengths where dust is primarily not in thermal equilibrium with the local interstellar radiation field. However this approach provides reasonable estimates for the average dust temperatures and masses for each component. The dust emissivity is a power law, where $\kappa_\nu = \kappa_0^\beta$. We assume a value of $\kappa_0 = 0.192 \text{ m}^2 \text{ kg}^{-1}$ at $350 \mu\text{m}$ (Draine 2003) and $\beta = 2$. The value $\beta=2$ was adopted as the most suitable for global dust emission SEDs (e.g., Dunne & Eales (2001)). It has to be noted though that β varies within galaxies (see, e.g., Tabatabaei et al. (2014)). To find the best fit SED our code minimizes the χ^2 function using the Levenberg-Marquardt algorithm (Bevington & Robinson 1992). Besides the SPIRE data, which were reduced by us, we used the fluxes presented in U et al. (2012). The result of the three component fit is shown in Figure 4.7 (see the figure caption for an explanation of the symbols).

The temperature and mass of each dust component is calculated. We find a temperature of $29.1 \pm 3.5 \text{ K}$ for the "cool" component, $60.6 \pm 4.9 \text{ K}$ for the "warm" component, and $239.4 \pm 22.7 \text{ K}$ for the "hot" component. The dust masses are $1.1 \times 10^8 M_\odot$, $2.9 \times 10^6 M_\odot$, and $141 M_\odot$, respectively. We find that the "hot" dust component contains only $\sim 10^{-6}$ of the total dust mass. This is four orders of magnitude smaller than the 2×10^{-2} of hot dust expected from a PDR with the parameters of PDR III (last column of Table 4.4). This along with the poor reproduction of HCN emission shows that the third ISM phase cannot be heated purely by UV photons.

4.5.3 Additional heating sources

We can explore alternative heating sources to explain the high-J CO and HCN transitions. We consider cosmic ray heating, X-ray heating, and mechanical heating (shocks and turbulence) as alternative heating sources. Cosmic rays can also heat gas in cosmic ray dominated regions (CDRs), which are PDRs with an enhanced cosmic ray ionization rate; we employ a typical model for enhanced cosmic ray ionization rate with $\zeta_{CDR} = 750\zeta_{gal}$, $3.75 \times 10^{-14} \text{ s}^{-1}$. Cosmic rays are able to penetrate into the very centers of molecular clouds, where even X-rays have trouble reaching and are typically produced by supernovae. Similarly, PDRs with additional mechanical heating (mPDRs) are due to turbulence in the ISM and may be driven by supernovae, strong stellar winds, jets, or outflows. We parameterize the strength of the mechanical heating (Γ_{mech}) with α , which represents the fractional contribution of mechanical heating in comparison to the total heating at the surface of a pure PDR (excluding mechanical heating).

At the surface the heating budget is dominated by photoelectric heating. Both the mPDR and CDR models have the same basic radiative transfer and chemistry as the PDR models, with either an enhanced cosmic ray rate or mechanical heating. In the classical PDR models, the far-UV photons often do not penetrate far enough to affect the molecular region. Thus, far-UV heating, cosmic ray heating, and mechanical heating can be varied in such a way that one source might dominate over the other depending on the depth into the cloud. In the case of an enhanced cosmic ray ionization rate (CDRs), we increase the heating rate of the cosmic rays by a factor of 750 compared to the galactic value, used in the classical PDR models. In the case of an added mechanical heating rate (mPDR), we add a new heating term to the heating balance of the classical PDR model, which we vary from 0-100% of the UV heating at the surface of the PDR. We use the names CDR and mPDR for convenience, to refer to PDR models with specific enhanced heating terms, yet both have the same classical PDR model base. On the other hand, X-rays heat gas in regions called X-ray dominated regions (XDRs), where the chemistry is driven by X-ray photons instead of FUV photons (Meijerink & Spaans 2005); the X-ray photons are able to penetrate farther into the cloud without efficiently heating the dust at the same time. These X-rays are mostly produced by active galactic nuclei (AGN) or in areas of extreme massive star formation and the strength of the X-ray radiation field (F_X) is measured in $\text{erg s}^{-1} \text{ cm}^{-2}$. To test which excitation mechanisms are mainly responsible for heating the gas we will fit three cases.

1. two PDRs one (m)CDR
2. two PDRs one XDR

3. two PDRs one mPDR

We hold the first PDR and allow only the second and third ISM phases to vary, since PDR I is well constrained using ^{13}CO (Figure 4.6). In case 1, we use the term (m)CDR since we allow the molecular emission to be fit with either a pure CDR or a CDR with mechanical heating (mCDR). The best fit models are displayed for all three cases in Figure 4.9. We give all model parameters for each case in Table 4.5 and we discuss each case in detail below.

Case 1

In this case, the best fit is two PDRs and one mechanically heated CDR (mCDR) with 25% mechanical heating at the surface. We also tried a fit with one, two, and three pure CDRs. The case of one CDR is the best of those options, yet has the same model parameters as the three PDR fits. This suggests that it is still the UV photons that are heating the gas instead of a strong contribution from the cosmic rays. In addition, in the case of one pure CDR, the HCN is overproduced by an order of magnitude, as in the three PDR fit. Thus, we concentrate on the overall best fit using an enhanced cosmic ray ionization rate and with 25% mechanical heating. This model is able to fit all ^{12}CO transitions within the error bars. However, the second and third ISM phases (green and yellow) produce more HCN luminosity than we observe. The ^{13}CO is also poorly fit, overproducing not only the J=1-0 but also the J=2-1 transition, thus making this an overall poor fit. We suggest that cosmic rays play an unimportant role in heating the molecular gas in Arp 299 A, especially since the model needs 25% mechanical heating in order to fit the high-J CO transitions.

Case 2

The second case that includes X-ray heating is justified by the existence of an AGN in Arp 299 A that could be heating a molecular torus around the AGN. However, HCN is very poorly fit. In order for an XDR to produce the high-J CO lines, it does not produce much emission in the mid-J CO lines. This means that the mid-J CO lines must be produced by a powerful and dense PDR that results in bright HCN emission. Thus, the best fitting XDR model is the one that can reproduce most of the high-J CO lines while producing minimal HCN emission. This points to the fact that XDR chemistry is unlikely to be the cause of the observed high-J CO emission. If it were responsible for the high-J CO emission, the third ISM phase would be the most massive one. The mass of the XDR phase exceeds the total measured molecular mass for the entire system, and thus we rule out X-rays as a significant heating source of the gas.

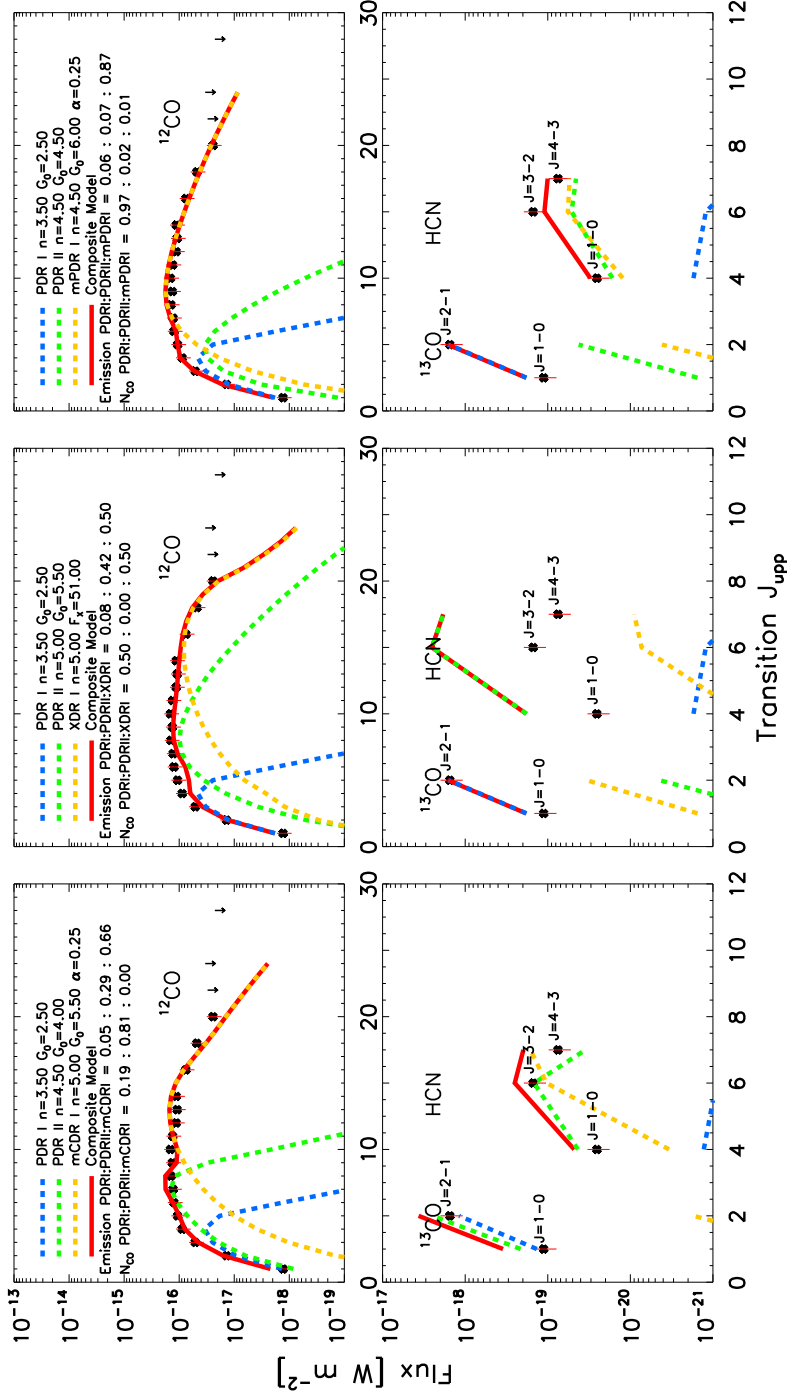


Figure 4.9: ^{12}CO (top), ^{13}CO , and HCN (bottom) excitation ladders of Arp 299 A with the flux of each transition plotted as black asterisks with red error bars. In blue, green and yellow dotted lines we plot the PDR/PDR/mCDR (left), PDR/PDR/mPDR (center), and PDR/PDR/XDR(right) ISM phases with their filling factors. The composite model is plotted with a red solid line. The model H_2 density [$\log \text{cm}^{-3}$], G/G_0 [$\log \text{erg s}^{-1} \text{cm}^{-2}$], and percentage mechanical heating (α) are shown in the legend along with the relative contribution of each phase in terms of emission and column density. For emission, we compared the integrated intensity of each ISM phase to the total modeled CO flux (the red line). For the column density we perform the same calculation except comparing the column density of each phase to the total combined model column density.

Component	Density $\log(n_H)$ $\log[\text{cm}^{-3}]$	$\log(G)$ G_0	$\log(N_{CO})$ $\log[\text{cm}^{-2}]$	$\log(N_{H_2})$ $\log[\text{cm}^{-2}]$	α %	Ω^a	C_{em}^b	C_{NCO}^c	$Mass_{N_{H_2}}^d$ M_\odot
Case 1 $M_{tot}: 3 \times 10^9 M_\odot$									
PDR I	3.5	2.5	17.1	21.5	0	0.9	0.05	0.19	2×10^9
PDR II	4.5	4.0	18.2	21.9	0	0.3	0.29	0.81	1×10^9
mCDR I	5.0	5.5	17.2	21.0	25	0.006	0.66	< 0.01	3×10^6
Case 2 $M_{tot}: 4 \times 10^9 M_\odot$									
PDR I	3.5	2.5	17.1	21.5	0	1.2	0.11	0.50	2×10^9
PDR II	5.0	5.5	14.9	21.2	0	1.2	0.40	0.003	1×10^9
XDR I	5.0	51.0 ^e	19.4	23.4	0	0.006	0.48	0.50	1×10^9
Case 3 $M_{tot}: 3 \times 10^9 M_\odot$									
PDR I	3.5	2.5	17.1	21.5	0	1.2	0.06	0.97	2×10^9
PDR II	4.5	4.5	15.5	21.4	0	0.8	0.07	0.02	1×10^9
mPDR I	4.5	6.0	15.7	19.5	25	0.3	0.87	< 0.01	6×10^6

Table 4.5: Model parameters for the three ISM phases for each of the three cases.^a Ω is the beam filling factor for each ISM phase.^b C_{em} is the fractional contribution of each ISM phase to the emission, as in Eq. 4.5.^c C_{NCO} is the fractional contribution of each ISM phase to the column density.^d $Mass_{N_{H_2}}$ is the mass of each ISM phase as estimated by the column density using Eq. 4.4.^e Units of XDR radiation field (F_X) are $[\text{erg s}^{-1} \text{cm}^{-2}]$.

Case 3

Case 3 represents two PDRs and one mechanically heated PDR. This case is the only case that fits all observed transitions within the error bars. We also attempted to fit the observed transitions with one, two, and three mPDRs, yet in the case of two mPDRs, one of them has negligible mechanical heating, and in the case of three mPDRs there is no reasonable fit. Thus, the situation represents a galaxy in which most of the gas is heated by UV photons, but a small amount of gas is heated almost entirely by mechanical heating. This gas could be in pockets of violent star formation where the stellar winds, jets, and/or supernovae are creating turbulence that efficiently couples to the gas. The heating rate of the mechanical heating is $7.9 \times 10^{-19} \text{ erg s}^{-1} \text{ cm}^{-2}$, which represents $\sim 4\%$ of the total heating, reflecting the fact that in this system the mechanical heating is very localized. We conclude that mechanical heating is the most likely candidate for the additional heating source in Arp 299 A.

This result is similar to what was found in NGC 253 (Rosenberg et al. 2014; Hailey-Dunsheath et al. 2008), where mechanical heating is needed as an additional heating mechanism. However, in NGC 253, the system requires mechanical heating in all three ISM phases to reproduce the extremely bright CO emission. Since Arp 299 A only needs mechanical heating to explain the third, most extreme, ISM phase, this lends itself to isolated and localized mechanical heating deriving from either supernova remnants or extreme star formation regions with powerful winds. The nuclear region of NGC 253 on the other hand, has universally bright CO lines, meaning the mechanical heating must be distributed throughout the galactic nucleus, perhaps coming from the massive molecular outflow (Bolatto et al. 2013; Turner & Ho 1985). In addition, although the far-infrared luminosity in Arp 299 is about an order of magnitude higher than in NGC 253, we see much brighter cooling lines in NGC 253. This is most likely due to a distance effect. With SPIRE's beam size, in NGC 253 we observe only the nuclear region, while in Arp 299 A we observe the nucleus and surrounding disk. Thus the extreme environment of the galactic nucleus is averaged out with the less luminous disk regions in Arp 299.

4.5.4 Molecular gas mass

We can estimate the mass of each molecular gas ISM phase as well as the total molecular gas mass for each case using Equation 4.4. We find a total molecular mass equal to $3 \times 10^9 M_{\odot}$ regardless of excitation mechanism, which is in good agreement with the literature values. In addition, using the dust mass of $1.1 \times 10^8 M_{\odot}$, we find a gas to dust ratio of ~ 30 . The first ISM phase is well constrained in

all cases; the mass is $2 \times 10^9 M_{\odot}$, making it the most massive component in most cases. The second ISM phase is also well constrained with a mass of $1 \times 10^9 M_{\odot}$. The third ISM phases' mass is not as well constrained, yet it is the least massive component in most cases, ranging from $3 - 6 \times 10^6 M_{\odot}$, except in the case of the XDR, where this phase is more massive, $1 \times 10^9 M_{\odot}$.

The fact that the mass is so well constrained underlines the importance of observing even just two ^{13}CO transitions. We also see the strength of including HCN measurements to constrain both the high density ISM phase, and the excitation mechanism. Further, these results agree with those from Rosenberg et al. (2014) that mechanical heating plays an important role in understanding the molecular line emission, even though UV heating is still the most dominant heating source.

4.6 Limitations and usefulness of the ^{12}CO ladder

Herschel SPIRE gave access to the full CO ladder ranging from J=4-3 to J=13-12, in the nearby universe. With Herschel PACS, higher J lines could also be observed. Before Herschel, it was thought that observing the flux of CO transitions greater than J=10 would break the degeneracy between UV excitation and X-ray excitation. However, now that the wealth of observations from the Herschel Space Observatory are available, access to the full CO ladder does not necessarily break this degeneracy. In fact, the information that can be extracted from observations of only ^{12}CO is very limited.

Qualitatively, bright ^{12}CO emission indicates the presence of warm molecular gas. However, without any other information, the source of heating, the amount (mass) of heated gas, and the precise density and temperature cannot be determined. It is possible, however, to extract the turnover point of the ^{12}CO . If the turnover point is in the low to mid-J transitions (from J=1-0 to J=6-5), as seen in Arp 299 B+C, the gas is most likely heated by UV photons in PDRs. If the turnover is higher than that, it can be either an extreme PDR ($n_H > 10^5 \text{ cm}^{-3}$, $G > 10^5 G_0$), X-rays, cosmic rays, or mechanical heating that may be responsible. This is demonstrated fitting a pure PDR model to the high-J CO lines, and is clear in the degeneracy parameter space diagrams shown in Figure 3 by Rosenberg et al. (2014).

For metal-rich extragalactic sources, the ^{12}CO ladder represents all the molecular clouds in the galaxy, spanning a range of physical environments. Therefore, multiple ISM phases are necessary to fit the ladder. These ISM phases represent many clouds with similar physical properties. In addition, with just transitions of ^{12}CO , you can determine distinct density-temperature combinations for each phase. In general, the low-J CO lines are from a lower density, lower tempera-

ture ISM phase, but the density-temperature combination is highly degenerate. The mid-J CO transitions arise from a warm and medium density phase, and the high-J transitions from a high density, high temperature phase.

If multiple transitions of ^{13}CO are added, then the beam averaged optical depth, and thus column density, are constrained. This allows for a better constrained mass estimate. It also helps lessen the temperature-density degeneracy, but does not break it. In order to break this degeneracy, other molecules must be added. For example, HCN, HNC, and HCO^+ are good tracers of density for high density environments. For lower density regimes, [CI] can be a good probe of the gas temperature, yet it is very difficult to interpret, since we cannot disentangle different emitting regions within our beam. To summarize, if bright ^{12}CO emission is observed, there is warm gas. Yet in order to probe the physical parameters of that gas, other molecular information is crucial. Some of these molecules do not always originate from the same spatial location as the ^{12}CO and may be tracing a different gas component altogether. Interpreting ^{12}CO is not trivial and the analysis should be performed with an understanding of the challenges and limitations.

Many Herschel SPIRE CO ladders have been obtained from luminous infrared galaxies, and they all require some additional heating mechanism to explain the high-J CO emission. For example in Arp 220, Rangwala et al. (2011) find that PDRs, XDRs, and CDRs can be ruled out, while the mechanical energy available in this galaxy is sufficient to heat the gas. Similarly, Meijerink et al. (2013) find strong evidence for shock heating in NGC 6240. On the other hand, Spinoglio et al. (2012) and van der Werf et al. (2010a) find in NGC 1068 and Mrk 231 respectively, that it is likely XDR heating responsible for the high excitation CO lines. Although both of these sources have confirmed AGN, the CO ladder fitting was not combined with a dense gas tracer (HCN/HNC/ HCO^+), and thus mechanical heating cannot be directly ruled out. The picture emerging from the SPIRE CO-ladders is that in these extreme star forming galaxies, the gas is rarely heated by only UV photons and that in most cases, the molecular gas is heated through either X-rays or mechanical heating.

4.7 Conclusions

We observed Arp 299 with Herschel PACS and SPIRE in both the spectrometer and photometer mode. The Herschel SPIRE FTS observations had three separate pointings, namely towards Arp 299 A, B and C. The pointings of Arp 299 B and C are overlapping so it is difficult to separate the emission from each nucleus. We extract the line fluxes of the CO transitions, [CI], [NII], and bright H_2O lines for Arp 299 A, B, and C separately. We also measure the continuum fluxes from

SPIRE photometer mode at 250, 350, and 500 μm . With PACS, we detect CO transitions from $J=14-13$ to $20-19$ and upper limits up to $J=28-27$. Using these data, we find:

1. A simple quantitative comparison of the spectra of Arp 299 A with B and C shows that the environment of source A is much more excited, with more warm molecular gas.
2. Using the full range of CO transitions we construct CO excitation ladders for each of the three pointings. Again, the CO ladders reveal a clear disparity between Arp 299 A and B+C; source A displays a flattened ladder, while B+C turns over around $J=5-4$.
3. Since we have high- J ^{12}CO PACS observations along with ^{13}CO and HCN JCMT observations of Arp 299 A, we perform an automated χ^2 minimized fitting routine to fit the CO and HCN ladders with three ISM components. We find a suitable fit for ^{12}CO and ^{13}CO but not for HCN. In addition, the third ISM phase would then be a truly extreme PDR, an order of magnitude more extreme than Orion Bar.
4. We create an infrared SED using values from the literature along with PACS and SPIRE continuum measurements. We fit this SED with three gray bodies and determine the temperature and mass of each dust component (cold, warm, and hot). We do not observe enough hot dust to match the amount of hot dust that would then be produced by the extreme PDR, in the case of a fit by three pure PDRs. Thus, we conclude that the flattening of the CO ladder, and extra excitation of the ^{12}CO in Arp 299 A in comparison to B+C, is due to an additional heating mechanism.
5. We allow the third ISM phase (high density, high excitation) to have additional heating by cosmic rays, mechanical heating, and X-rays. We find mechanical heating to be the most likely additional heating source since it fits all transitions within the errors. As the best fit model requires mechanical heating only in the third component, this suggests that for Arp 299A the mechanical heating is localized, likely to come from supernovae remnants or pockets of intense star formation.
6. We caution the use of ^{12}CO alone as a tracer of the physical conditions of the ISM. We find that ^{12}CO reveals only the presence of warm molecular gas, but that the amount, physical properties, and heating source cannot be determined without observations of other molecules.

Acknowledgments

The authors would like to thank the referee for their fruitful feedback and time spent. The authors gratefully acknowledge financial support under the "DeMoGas" project. The project "DeMoGas" is implemented under the "ARISTELA" Action of the "PERATIONAL PROGRAMME EDUCATION AND LIFELONG LEARNING" and is co-funded by the European Social Fund (ESF) and National Resources. We would like to thank Edward Polehampton for his help preparing the SPIRE observations. SPIRE has been developed by a consortium of institutes led by Cardiff Univ. (UK) and including: Univ. Lethbridge (Canada); NAOC (China); CEA, LAM (France); IFSI, Univ. Padua (Italy); IAC (Spain); Stockholm Observatory (Sweden); Imperial College London, RAL, UCL-MSSL, UKATC, Univ. Sussex (UK); and Caltech, JPL, NHSC, Univ. Colorado (USA). This development has been supported by national funding agencies: CSA (Canada); NAOC (China); CEA, CNES, CNRS (France); ASI (Italy); MCINN (Spain); SNSB (Sweden); STFC, UKSA (UK); and NASA (USA). The Herschel spacecraft was designed, built, tested, and launched under a contract to ESA managed by the Herschel/Planck Project team by an industrial consortium under the overall responsibility of the prime contractor Thales Alenia Space (Cannes), and including Astrium (Friedrichshafen) responsible for the payload module and for system testing at spacecraft level, Thales Alenia Space (Turin) responsible for the service module, and Astrium (Toulouse) responsible for the telescope, with in excess of a hundred subcontractors. HCSS / HSpot / HIPE is a joint development (are joint developments) by the Herschel Science Ground Segment Consortium, consisting of ESA, the NASA Herschel Science Center, and the HIFI, PACS and SPIRE consortia.

5 | [FeII] as a tracer of supernova rate in nearby starburst galaxies

Supernovae play an integral role in the feedback of processed material into the ISM of galaxies making them responsible for much of the chemical enrichment of the universe. The rate of supernovae can also reveal star formation histories. These rates are usually measured through the nonthermal radio continuum luminosity; however, a correlation between near-infrared [FeII] emission and supernova remnants has also been noted. We aim to find a quantitative relationship between the [FeII] at $1.26 \mu\text{m}$ ($[\text{FeII}]_{1.26}$) luminosity and the supernova rate in a sample of 11 nearby starburst galaxy centers. We performed a pixel-pixel analysis of this correlation on SINFONI data cubes. Using $\text{Br}\gamma$ equivalent width and luminosity as the only observational inputs into the Starburst 99 model, we derived the supernova rate at each pixel and have thus created maps of supernova rates. We then compared these morphologically and quantitatively to the $[\text{FeII}]_{1.26}$ luminosity. We have found that a strong linear and morphological correlation exists between supernova rate and $[\text{FeII}]_{1.26}$ on a pixel-to-pixel basis. This relation is valid for normal star-forming galaxies but breaks down for extreme ultraluminous galaxies. The supernova rates derived from the Starburst 99 model are in good agreement with the radio derived supernova rates, which underlines the strength of using [FeII] emission as a tracer of supernova rate. With the strong correlation found in this sample of galaxies, we conclude that $[\text{FeII}]_{1.26}$ emission can generally be used to derive accurate supernova rates on either a pixel-pixel or integrated galactic basis.¹

M. J. F. Rosenberg, P. P. van der Werf, and F. P. Israel
A&A **540**, A116

¹Coauthors contributed helpful discussion and comments about text and figures.

5.1 Introduction

Supernova rates (SNrates) are typically estimated by the integrated nonthermal radio continuum emission from their remnants (Condon 1992, and references therein). The connection between radio continuum emission and SNrate comes from the tight infrared–radio relation that is usually interpreted to be a natural consequence of (massive) star formation and stellar evolution (Condon 1992, and references therein). Observations of nearby starburst galaxies show many compact radio sources, generally attributed to supernova remnants (SNR). Condon & Yin (1990) use observations of SNR in our own galaxy to establish a relation between the nonthermal radio continuum and SNrate. Huang et al. (1994) find a similar relation using observations of compact radio sources in M82.

In addition, near-infrared (NIR) observations of SNR often show strong [FeII] emission line flux at 1.257 and 1.644 μm coincident with the radio peak (Graham et al. 1987, 1990; Oliva et al. 1989, 1990). In interstellar space, iron atoms are typically locked in dust grains. However, shock fronts associated with SNRs cause efficient grain destruction through thermal sputtering. This releases the iron into the gas phase where it is singly ionized by the interstellar radiation field. In the extended post-shock region, [FeII] is excited by electron collisions (Mouri et al. 2000), making it a strong diagnostic line for tracing shocks. Since [FeII] is commonly associated with SNRs, the [FeII]/Br γ line intensity ratio is often used to estimate the abundance of SNRs relative to current star formation. The Shull & Draine (1987) shock models of [FeII]/H β imply an [FeII]/Br γ ratio of 20–70 (Moorwood & Oliva 1988), which is in good agreement with SNR observations (Graham et al. 1987; Moorwood et al. 1988). Since the [FeII] emission lifetime of an SNR is approximately 10^4 years (Oliva et al. 1989), the [FeII] luminosity should also be a strong tracer of the SNrate. Qualitatively, the connection between [FeII] emission and supernova activity is supported by a wealth of galactic and extragalactic NIR spectroscopy (Moorwood et al. 1988; Greenhouse et al. 1991; Vanzi & Rieke 1997) and high-resolution imaging (Forbes et al. 1993; Greenhouse et al. 1997; Alonso-Herrero et al. 2000), which both demonstrate that [FeII] emission often coincides with known radio SNRs and may indeed provide at least a relative measure of SNrate.

However, the quantitative connection between NIR [FeII] emission and supernovae has proved to be more complex, so a better understanding of the underlying physics is necessary. Radio continuum and [FeII] emission do not always correspond, even in a specific SNR. For instance, Greenhouse et al. (1997) find that there is little correlation between the radio continuum and [FeII] line emission in radio-loud SNRs in M82 and suggest that the SNR emission char-

acteristics change as a function of age. In addition, Alonso-Herrero et al. (2003) obtained high-resolution HST [FeII] images of M82 and NGC 253 and find compact [FeII] emission in only 30-50% of radio all SNRs. They note that up to 73-78% of the [FeII] flux is actually diffuse emission and does not originate in the discrete radio SNR, which makes it more difficult to interpret the connection between SNR and [FeII] emission. Vermaas & van der Werf (in preparation) argue that the absence of [PII] line emission at $1.19 \mu\text{m}$ implies that [FeII] emission is the outcome of grain destruction by strong shocks. This diagnostic allows the determination of the excitation mechanism of [FeII]. Vermaas & van der Werf (in preparation) find in M83 that, although the [FeII] is diffuse, the distinct lack of [PII] indicates that this emission is nevertheless the consequence of grain destruction by evolved SNRs that have lost their individual identities.

Van der Werf et al. (1993), Calzetti (1997) and Vanzi & Rieke (1997) have attempted to correlate SNrates to [FeII] emission by finding a relationship between the nonthermal radio continuum and [FeII] flux and using a conversion factor to derive an SNrate. Van der Werf et al. (1993) uses 6 cm radio fluxes of NGC 6240 from Eales et al. (1990) to estimate SNrates with the conversion factor from Condon & Yin (1990), which was based on galactic SNR observations. Calzetti (1997) adapted the relation from Van der Werf et al. (1993) to $[\text{FeII}]_{1.26}$. Vanzi & Rieke (1997) demonstrated that in blue dwarf galaxies, all of the [FeII] emission is plausibly accounted for by SNRs and presented a relationship between [FeII] luminosity and SNrates based on the M82 calibration. They also found a relationship between [FeII] and age, assuming that most of the [FeII] derives from SNRs.

Thus far, there has been little agreement between the radio continuum and [FeII] line emission in terms of determining SNrates. However, such a relationship is desirable because it allows us to use relatively straightforward NIR [FeII] observations to estimate SNrates whenever individual radio SNRs cannot be resolved. In this paper, we will show that a well determined relationship between [FeII] and SNrate exists, and explore and constrain it in a sample of eleven central regions of nearby starburst galaxies.

First, we will briefly introduce the galaxies in our sample in Section 5.2 and outline the observational parameters in Section 5.3. The results are discussed in Section 5.4, which also displays the spectra, $\text{Br}\gamma$, [FeII], and H_2 line-maps and continuum maps. In Section 5.5 we explain the methods used in the analysis, and in Section 5.6 we present our analysis of the [FeII]-SNrate connection. Section 5.7 explores the dependency of our results on the star formation history of the galaxy and Section 5.8 compares the SNrates derived from the Starburst 99 model to the more classical radio continuum derived SNrates. Finally, our conclusions are highlighted in Section 5.9.

Galaxy	RA ^a J2000	DEC ^a J2000	Morph. ^b J2000	Activity ^c	Dist. ^d [Mpc]	cz ^e [km s ⁻¹]	i ^f [°]	log L _{FIR} ^g [L _⊙]
NGC 3628	11h20m17.0s	+13d35m23s	Sb pec edge-on	HII LINER	12.8	847±2	79.29	10.14
NGC 4536	12h34m27.0s	+02d11m17s	SAB(rs)bc	HII Sbrst	15.4	1802±3	58.9	10.17
NGC 1792	05h05m14.4s	-37d58m51s	SA(rs)bc	HII	13.2	1210±5	62.78	10.22
NGC 1084	02h45m59.9s	-07d34m42s	SA(s)c	HII	16.6	1409±4	46	10.42
NGC 1808	05h07m42.3s	-37d30m47s	(R)SAB(s)a	HII	12.3	1001±4	83.87	10.55
NGC 520	01h24m35.1s	+03d47m33s	pec	Merger Sbrst	30.5	2162±4	77.49	10.81
NGC 7552	23h16m10.8s	-42d35m05s	(R')SB(s)ab	HII LINER	22.5	1611±6	23.65	11.03
NGC 7632	23h22m00.9s	-42d28m50s	(R')SB(s)0 ⁰	HII	19.3	1535±15	82.44	11.43 ^h
NGC 1614	04h33m59.8s	-08d34m44s	SB(s)c pec	Sbrst	64.2	4778±6	41.79	11.43
NGC 6240	16h52m58.9s	+02d24m03s	S0-a	LINER	108.8	7242±45	73.0	11.73
Arp 220	15h34m57.1s	+23d30m11s	Sd	LINER Sy2	82.9	5420±6	57	12.50

Table 5.1: Summary of galaxy parameters.^a Coordinates of galactic nucleus from NED.^b NED^c Corwin et al. (1994)^d NED Hubble Flow Distance (Virgo + GA + Shapley where $H_0 = 73.0 \pm 5$ km/sec/Mpc) for NGC 520, NGC 7552, NGC 1614, NGC 6240 and Arp 220, metric distances for the rest.^e Heliocentric radial velocity (cz) from radio measurement from Prugniel et al. (1998) except for NGC 7632 which is from optical measurements.^f Inclination measured from Prugniel et al. (1998)^g L_{FIR} from Sanders et al. (2003)^h L_{IR} for NGC 7632 from Yuan et al. (2010)

5.2 Sample

We have selected eleven bright nearby starburst galaxies at distances ranging from 10-100 Mpc (see Table 5.1). All are spiral galaxies with types ranging from S0a to Sd, with the exception of NGC 520, which is a merging galaxy. Two of the galaxies in our sample are seen edge-on, NGC 520 and NGC 3628. Far-infrared luminosities range from $1.4 \times 10^{10} L_{\odot}$ to $3.2 \times 10^{12} L_{\odot}$, where Arp 220 with $L > 10^{12} L_{\odot}$ must be classified as an ultra luminous infrared galaxy (ULIRG), and NGC 6240, NGC 1614 and NGC 7552, all with $L > 10^{11} L_{\odot}$ are luminous infrared galaxies (LIRGs). Our sample does not contain galaxies with a dominant active nucleus, but it does have four low ionization nuclear emission line region (LINER) galaxies and one weak Seyfert 2 (Sy2) nucleus.

5.2.1 NGC 3628

NGC 3628 is a nearby (~ 12.8 Mpc) HII LINER galaxy. It is of morphological type Sb pec and is seen edge-on. Although this galaxy's nucleus is dominated by a central starburst, it may also be host to a small AGN (González-Martín et al. 2006; Roberts et al. 2001). NGC 3628 is a member of the Leo triplet, a group of 3 closely interacting galaxies. Observations of the HI disk reveal a very disturbed

distribution, pointing to the interaction between NGC 3628 and its nearby companion NGC 3627 (Rots 1978; Haynes et al. 1979). Radio observations show an extended radio core of 350×60 pc with a predominately nonthermal spectrum (Hummel 1980; Condon et al. 1982; Reuter et al. 1991). Its inner kiloparsec is dominated by a significant concentration of molecular gas (Israel 2009).

5.2.2 NGC 4536

NGC 4536 is a late type HII/Starburst galaxy that shows [Ne V] line emission, which may indicate that the nucleus harbors a weak AGN (Hughes et al. 2005). Previous observations indicate vigorous star formation in the central nuclear region, shown through Br γ emission (Puxley et al. 1988). The diffuse radio emission with three central peaks (Vila et al. 1990; Laine et al. 2006) may indicate that this occurs in a ring around the nucleus. There are two ultraluminous X-ray sources, one of which is located in the core of the galaxy and possibly associated with the weak AGN (Liu & Bregman 2005).

5.2.3 NGC 1792

NGC 1792 is in a strongly interacting galaxy group with the dominant galaxy NGC 1808. NGC 1792 has surprisingly high luminosities, comparable to those of its more massive partner NGC 1808, at many different wavelengths (Dahlem et al. 1994). Upon closer inspection, Dahlem et al. (1994) found a strongly asymmetric star formation distribution caused by the external trigger of gravitational interactions with NGC 1808.

5.2.4 NGC 1084

NGC 1084 is a HII driven Sa(s)c galaxy located ~ 16.6 Mpc away. More recently, this galaxy has been classified as an Sbc and Sb based on its B and H band images, respectively (Eskridge et al. 2002). The H band image reveals a bright nucleus with an elongated bulge. Many weakly defined spiral arms were detected along with many bright knots. NGC 1084 was mapped at 1.49 GHz by Condon (1987), who detected a strong continuum source to the south of the nucleus. Ramya et al. (2007) derived a star formation rate of $2.8 M_{\odot} \text{ yr}^{-1}$ along with chaotic star formation that is not necessarily confined to the spiral arms. The northern and southern regions of the galaxy have different star formation rates and typical ages. The north is characterized by a series of short bursts happening intermittently over the past 40 Myr, possibly due to an interaction with a gas rich galaxy (Ramya et al. 2007).

The southern half of the galaxy is home to much younger stars, < 4 Myr (Ramya et al. 2007).

5.2.5 NGC 1808

NGC 1808 is the most massive member of a small group of galaxies. The galactic center has a superwind, compact radio sources, and a molecular ring (Kotilainen et al. 1996). Veron-Cetty & Veron (1985) first suspected that NGC 1808 has a faint Seyfert nucleus. This has since been refuted by many (Forbes et al. 1992; Phillips 1993; Krabbe et al. 1994), yet there is recent hard X-ray evidence to support the Seyfert nucleus (Awaki & Koyama 1993).

5.2.6 NGC 520

Using long slit optical photometry and near-infrared imaging, Stanford & Balcells (1990) uncovered two separate nuclei in NGC 520, establishing this as a galaxy in the process of merging. Stanford & Balcells (1991) went on to determine that NGC 520 is most likely the result of a galaxy collision of a gas rich and a gas poor galaxy that happened $\sim 3 \times 10^8$ years ago. A thick dust lane at PA=95° completely obscures the primary nucleus at optical wavelengths, but the secondary nucleus is visible to the northwest of the primary. There are strong plumes of ionised gas, thought to represent a bipolar outflow away from the starburst dominated nucleus (Norman et al. 1996).

5.2.7 NGC 7552

NGC 7552 is a LIRG HII galaxy and host to a weak LINER. This galaxy has a starburst ring surrounding the nucleus. It does not appear to be overly disturbed, which suggests a slow bar mediated star formation evolution. Due to the quiescent nature of the nucleus, NGC 7552 provides a near perfect environment to study the bar and starburst ring around it. In addition to the bar, there are two dominant spiral arms and two weaker rings at radii of 1.9 and 3.4 kpc (Feinstein et al. 1990). Forbes et al. (1994b) found an inner ring with a radius of 1 kpc in the radio, which is not visible in the NIR continuum but is visible in NIR color maps and Br γ emission. The dominant circumnuclear ring is at a distance of 850 pc from the center of the nucleus and the spiral arms provide a flow of molecular gas into this region (Schinnerer et al. 1997).

5.2.8 NGC 7632

NGC 7632 is a member of a loose galaxy group, containing multiple galaxies. This is a ring galaxy, which is observed to be distorted and bent towards the other group members (Arp 1981). The interacting galaxies located south of the NGC 7632 also appear strongly distorted with much absorbing material (Arp 1981).

5.2.9 NGC 1614

NGC 1614 is a SB(s)c peculiar LIRG with both LINER and starburst activity. Although only one NIR peak has been observed, Neff et al. (1990) considered the tidal tails or plumes to be evidence that NGC 1614 is the result of a merger of at least two galaxies. A central nucleus of 45 pc is surrounded by a 600 pc diameter ring of current star formation (Alonso-Herrero et al. 2001). The Br γ emission reveals a double peaked morphology (Kotilainen et al. 2001), in agreement with the radio continuum (Condon et al. 1982). Further studies of NGC 1614 by Olsson et al. (2010) found the molecular gas distribution double peaked at R = 300 pc with an additional weaker peak in the center of the nucleus. A radio continuum ring is also found at R = 300 pc which is triple peaked, each consistent with the brightness temperature of SNR. Olsson et al. (2010) concludes that the LINER spectrum is due to shocks associated with supernovae and therefore most likely caused by star formation and not AGN activity.

5.2.10 NGC 6240

NGC 6240 just falls short of being a traditional ULIRG with a luminosity of $L_{IR} = 10^{12} L_{\odot}$ but otherwise has all the characteristics of the class. The extended tidal tails seen in the optical indicate a merger. NGC 6240 hosts a double nucleus separated by $1.5'' \pm 0.1''$ as seen in ground based observations in the optical (Schulz et al. 1993) and near-infrared (Doyon et al. 1994), yet a separation of $2'' \pm 0.15''$ as measured in [FeII] $_{1.64}$ μm (Van der Werf et al. 1993) and radio observations (Carral et al. 1990; Eales et al. 1990; Beswick et al. 2001). The high infrared luminosity is partially due to the powerful nuclear starburst and partially to an AGN continuum (Genzel et al. 1998).

5.2.11 Arp 220

The ULIRG Arp 220 emits 99% of its bolometric luminosity in the infrared (Soifer et al. 1984; Emerson et al. 1984). Arp 220 is a very gas rich galaxy, with the highest density component in the nucleus, with a molecular gas density up to $\sim 10^{-8} \text{cm}^{-3}$ (Rangwala et al. 2011). This high IR luminosity and intense starburst activity

points to a merger, supported by the existence of two nuclei, separated by $\sim 1''$ (Scoville et al. 1997). Arp 220 has an extremely high extinction, with estimates running from $A_v \sim 50$ to 1000 (Sturm et al. 1996; Downes & Solomon 1998). Smith et al. (1998) resolve the radio nucleus of Arp 220 and find many radio point sources, which they identify as SNRs. They deduce a star formation rate of 50-100 $M_\odot \text{ yr}^{-1}$ and a corresponding SNrate of 1.75-3.5 yr^{-1} .

5.3 Observations

Observations of the sample galaxies were made with the Spectrograph for INtegral Field Observations in the Near-Infrared (SINFONI) at the VLT. SINFONI provides spatial and spectral data in the form of data cubes in J, H, and K bands. The SINFONI instrument is mounted at the Cassegrain focus of the Unit Telescope 4 at the Very Large Telescope (VLT).

We took observations in all three J, H, and K bands using a spatial pixel scale of $0.25''$ corresponding to a field of view of $8'' \times 8''$ and a spectral resolution of 2000, 3000 and 4000 respectively, between October, 2006 and March, 2007. All science observations were taken in the ABA'nodding mode (300s of object 300s of sky 300s of object), where A' is slightly offset from A. The object exposures are averaged during the reconstruction of the data cube.

We extracted additional observations from the SINFONI archive (<http://archive.eso.org/wdb/wdb/eso/sinfoni/form>). These observations include five galaxies, Arp 220, NGC 1614, NGC 1808, NGC 6240 and NGC 7552. As selection criteria we required the galaxies to be bright and nearby, and to have archival observations in the $0.25''$ spatial resolution mode in all three bands and 300s integration times.

We used the standard reduction techniques of the SINFONI pipeline on all observations. including corrections for flat field, dark current, nonlinearity of pixels, distortion, and wavelength calibration. We obtained the flux calibration and atmospheric corrections from observations of a standard star. Finally, we calibrated the continuum fluxes to match the published 2MASS observations in the same aperture, and we determined a ``flux correction factor'' for each galaxy in each observed band, and we applied these correction factors to the line intensities as well.

5.4 Results

5.4.1 Spectra

We show the spectra of each galaxy center integrated over a high signal-to-noise region in the J (Figure 5.1), H (Figure 5.2) and K bands (Figure 5.3). The actual spatial area over which the spectra were integrated is overplotted in the K band images in Figure 5.4 and 5.5. We have focused on non-nuclear regions to illustrate the spectral signature of the extended emission. The dominant emission lines in each band are marked with dotted lines, notably $[\text{FeII}]_{1.26}$ and $\text{Pa}\beta$ in the J band, $\text{FeII}_{1.64}$ in the H band and $\text{Br}\gamma$, $\text{HeI}_{2.06}$, and multiple H_2 lines in the K band.

5.4.2 Continuum and Linemaps

The SINFONI datacubes allow us to construct J, H and K continuum maps as well as linemaps for each of the emission lines detected in these bands. These emission lines provide important diagnostics to trace specific physical processes. The $\text{Pa}\beta$ ($1.282 \mu\text{m}$) and $\text{Br}\gamma$ ($2.166 \mu\text{m}$) HI lines trace massive, young star formation. The $[\text{FeII}]$ emission lines, which emit most strongly at 1.257 and $1.644 \mu\text{m}$, are commonly used as tracers of strong shocks associated with supernova remnants, nuclear winds, or jets. There is also a wealth of ro-vibrational H_2 lines throughout the H, and K bands, the brightest of which occur at rest wavelengths of $2.122 \mu\text{m}$ (1-0 S(1)), $2.248 \mu\text{m}$ (2-1 S(1)), and $2.034 \mu\text{m}$ (1-0 S(2)). H_2 can be excited by UV fluorescence from massive stars, or thermally by shocks from supernovae or stellar winds. The relative intensities of the various H_2 lines indicates which of these physical processes is exciting the gas.

In Figure 5.4 and Figure 5.5 we present the K band continuum, $\text{Br}\gamma$, $[\text{FeII}]_{1.26}$ and $\text{H}_{2,2.12}$ line maps for each of the galaxies in our sample. The continuum maps were created by finding the average continuum level at each pixel, excluding any emission lines. The linemaps were created using QFitsView and DPUSER's evaluated velocity map function "evalvelmap", developed by the Max Planck Institute for Extraterrestrial Physics and available at <http://www.mpe.mpg.de/ott/QFitsView/>. This function fits a gaussian profile to the emission line at each pixel.

The first galaxy in Figure 5.4 is the edge-on NGC 3628, which has a strong central dust lane running from east to west. This is best seen by comparing the $\text{Br}\gamma$ and $[\text{FeII}]$ maps. Since K-band $\text{Br}\gamma$ emission is at a longer wavelength, it is less prone to extinction and the morphology resembles that of the K band continuum, with an additional emission peak at the western edge of the galaxy. The J-band $[\text{FeII}]$ emission is at a shorter wavelength and is more affected by the dust lane. It shows an asymmetric hour glass morphology, with the brightest regions above the

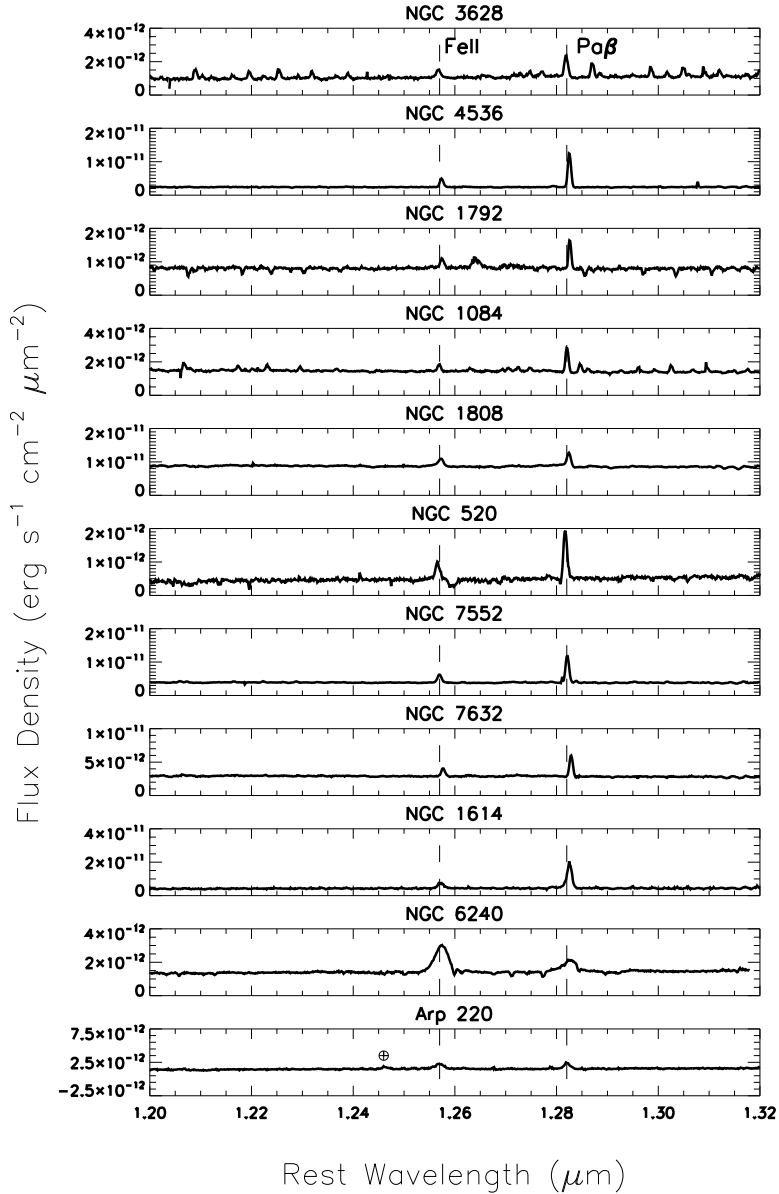


Figure 5.1: Spatially integrated rest frame spectra from the nucleus of each galaxy in the J band. The spatial area used in the integration is shown in Figure 5.4 and 5.5 by a black rectangle. Each spectrum is integrated over an 8x8 pixel area. $[\text{FeII}]_{1.26}$ and $\text{Pa}\beta$ emission lines are denoted by dashed lines and marked along the top of the figure. The broad feature near $1.25 \mu\text{m}$ in the Arp 220 spectra is an atmospheric artifact along with the narrow absorption features in NGC 520, and the numerous broad peaks between $1.2\text{-}1.24$ and $1.29\text{-}1.32 \mu\text{m}$ in the NGC 3628, NGC 1792 and NGC 1084 spectra.

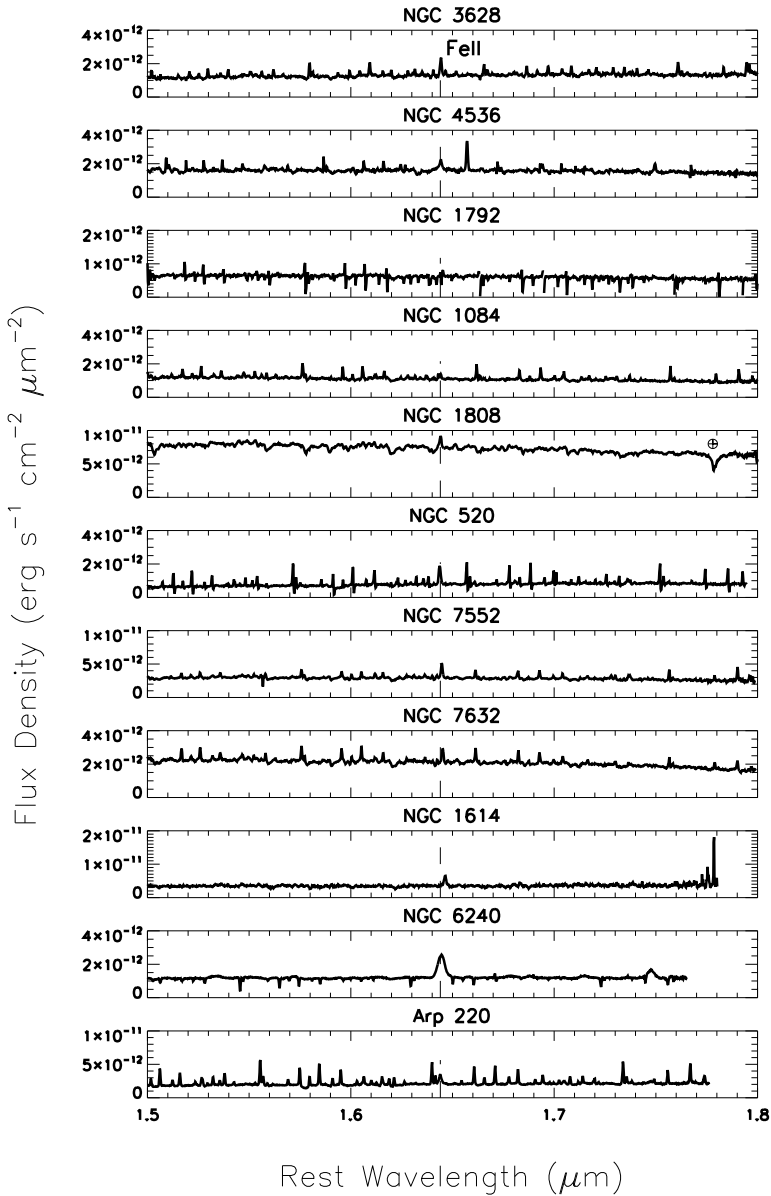


Figure 5.2: Spatially integrated rest frame spectra from the nucleus of each galaxy in the H band. The spatial area used in the integration is shown in Figure 5.4 and 5.5 by a black rectangle. Each spectrum is integrated over an 8x8 pixel area. The $[\text{FeII}]_{1.64}$ emission line is denoted by a dashed line and marked along the top of the figure. Several spectra are degraded by residual atmospheric OH features.

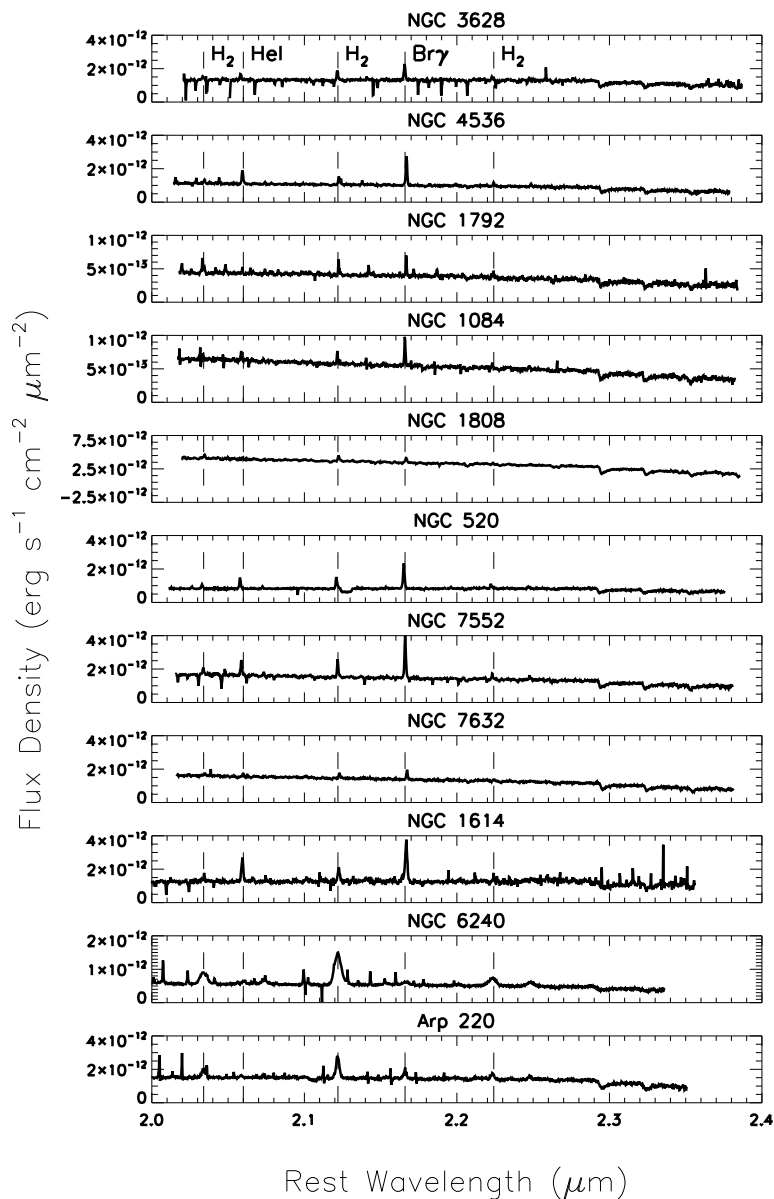


Figure 5.3: Spatially integrated rest frame spectra from each galaxy in the K band. The spatial area used in the integration is shown in Figure 5.4 and 5.5 by a black rectangle. Each spectrum is integrated over an 8x8 pixel area. $\text{Br}\gamma$, H_2 , and $\text{HeI}_{2.06}$ emission lines are denoted by dashed lines and marked along the top of the figure. Residual atmospheric contamination is present in the form of narrow peaks in the spectra of NGC 1614 and Arp 220 and as sharp absorption features in the spectra of NGC 3628 and NGC 7552.

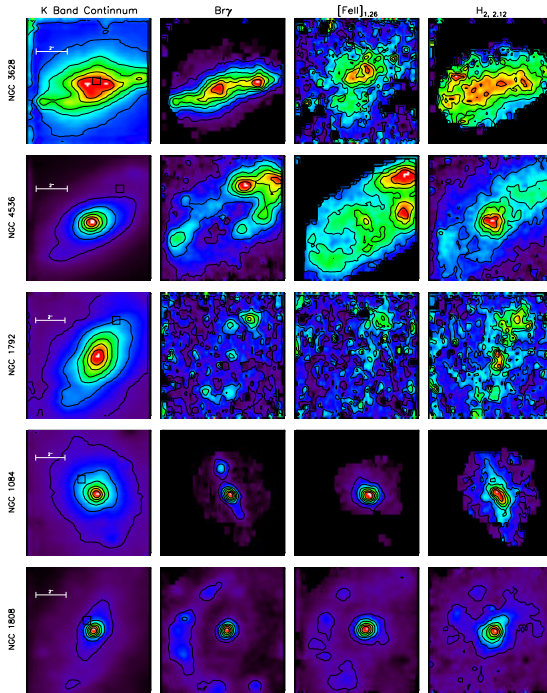


Figure 5.4: K band continuum map, $\text{Br}\gamma$, $[\text{FeII}]_{1.26}$, and $\text{H}_{2,2.12}$ line maps of NGC 7632, NGC 3628, NGC 4536, NGC 1792, and NGC 1084. The pixel scale is given by the $2''$ scale bar in the K band column. The black rectangle marks the areas over which the spectra in Figures 5.1, 5.2 and 5.3 were integrated. In all figures, north is up.

K band nucleus. The H_2 emission is similar to the $\text{Br}\gamma$ emission, but it has more diffuse morphology with strong emission throughout the very central region.

NGC 4536 reveals a star forming ring best seen in $\text{Br}\gamma$ and $[\text{FeII}]$ emission. The H_2 emission is concentrated at the K band continuum peak, with extended diffuse emission throughout the ring. Both $\text{Br}\gamma$ and $[\text{FeII}]$ peak in the northwest corner of the galaxy but their peaks do not coincide.

NGC 1792 has a K-band continuum morphology similar to that of NGC 4536, but the line emission is much weaker in this galaxy. The low signal-to-noise ratios prevent us from identifying any real structure. However, in the $\text{Br}\gamma$ map a small peak occurs at the K band continuum maximum, with structures suggesting spiral arms emanating from the nucleus. Although both H_2 and $[\text{FeII}]$ emission peaks at the end of these "arms", the actual $[\text{FeII}]$ fluxes hardly exceed the noise level. The H_2 has a higher signal-to-noise than the other emission lines and there are distinct H_2 peaks emission in the nuclear region.

In NGC 1084, all three emission lines appear to peak on the K-band continuum maximum. The $\text{Br}\gamma$ and H_2 maps show a somewhat similar distribution, with extended diffuse emission along the major axis line, and a weak secondary peak to the north. The $[\text{FeII}]$ map shows a single central maximum surrounded by weak

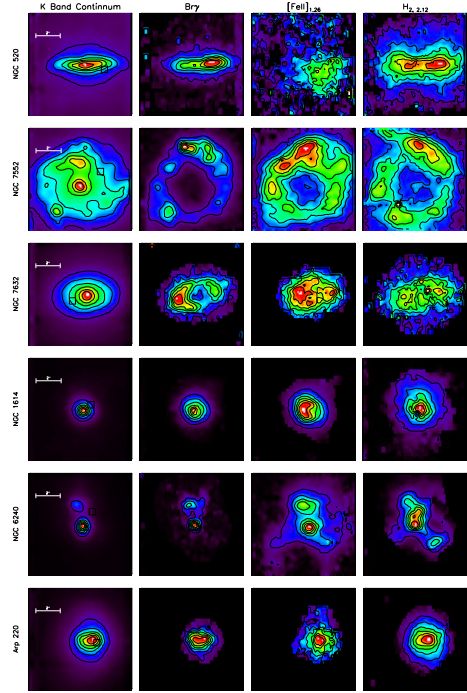


Figure 5.5: K band continuum map, $\text{Br}\gamma$, $[\text{FeII}]_{1.26}$, and $\text{H}_{2,2.12}$ line maps of NGC 1808, NGC 520, NGC 7552, NGC 1614, NGC 6240 and Arp 220. The pixel scale is given by the 2'' scale bar in the K band column. The black rectangle represents the area over which the spectra in Figures 5.1, 5.2 and 5.3 were integrated. In all figures, north is up.

diffuse emission.

NGC 1808 also has a star-formation ring, weakly seen in both the $\text{Br}\gamma$ and $[\text{FeII}]$ maps and a few local maxima also seen in the H_2 map. The ring appears to be very asymmetric, with relative bright fluxes at the eastern edge and almost no emission from the western edge. The H_2 emission is distributed more symmetrically around the K band peak.

In Figure 5.5, we first examine NGC 520, another nearly edge-on galaxy that also hosts a dense dust lane running east to west. The $\text{Br}\gamma$ morphology is very asymmetric, peaking to the west of the K-band continuum maximum. The H_2 emission peaks at the same location as the $\text{Br}\gamma$, but has a secondary peak east of the K-band center. The $[\text{FeII}]$ emission suffers from extinction by the dust lane and only weak $[\text{FeII}]$ emission is seen to the southwest of the galaxy mid plane.

NGC 7552 is a face-on galaxy with a very clear star-formation ring around the nucleus. The $\text{Br}\gamma$ emission shows a pronounced minimum in the center, but clear individual maxima in the ring. Unlike Forbes et al. (1994a), who found the H_2 morphology to match that of the K band continuum, we find the distributions of the H_2 and the $\text{Br}\gamma$ emission to be very similar, with an arm or bar-like structure extending from the northern $\text{Br}\gamma$ peaks. The $[\text{FeII}]$ emission is different: it

shows roughly the same ring-like shape, but with emission peaks in very different positions.

NGC 7632 reveals an asymmetric ring in $\text{Br}\gamma$ emission. The emission is much stronger on the east side of the galaxy in both $\text{Br}\gamma$ and $[\text{FeII}]$ emission. The east side is in the direction of the other group members (Arp 1981). The distortion and asymmetry is most likely evidence of the tidal interaction with its partner galaxies.

NGC 1614 has a very compact and radially symmetric morphology in the K band, $\text{Br}\gamma$ and H_2 emission lines. However, the $[\text{FeII}]$ emission shows a crescent morphology around the nucleus.

The double nucleus of NGC 6240 is evident in the K band continuum and the $\text{Br}\gamma$ line images. Less clearly, the double nucleus also shows up in the H_2 and $[\text{FeII}]$ images that reveal a more complex morphology. In all images, strongest emission coincides with southern nucleus.

Arp 220 is another compact galaxy that appears fairly symmetric in the K band and all the emission line maps. The peak is slightly off center towards the western side of the galaxy and there are two separate peaks in the $[\text{FeII}]$ emission.

5.5 Methods

To further study the correlation between $[\text{FeII}]$ emission and SNrate, we have performed a pixel by pixel analysis. We evaluated the continuum flux, emission line strength and equivalent width at each pixel in the SINFONI datacubes in order to gain insight into the variation of physical properties (such as ages and excitation mechanisms) across each galactic nucleus. We first corrected the linemaps for extinction, and used the $\text{Br}\gamma$ equivalent widths as an input into Starburst 99 to calculate SNrates. These could then be correlated with extinction corrected $[\text{FeII}]$ luminosities.

5.5.1 Extinction correction

In order to study the intrinsic emission line strengths, it is necessary to determine the degree to which dust obscures each nucleus. We accomplish this by identifying emission lines with fixed intrinsic intensity ratios, and comparing the observed to the intrinsic line ratio. In our NIR database, the best line pair to use is $\text{Pa}\beta$ (H 5-3) and $\text{Br}\gamma$ (H 7-4), which has a ratio of 5.88 (Hummer & Storey 1987) over a wide range of physical conditions. Extinction is also probed by the $[\text{FeII}]_{1.26}/[\text{FeII}]_{1.64}$ ratio, in which both $[\text{FeII}]$ lines originate in the same upper level with an intrinsic ratio of 1.36 (Nussbaumer & Storey 1988). For completeness sake, we calculated both line ratios and compared the extinction maps. There is little disparity

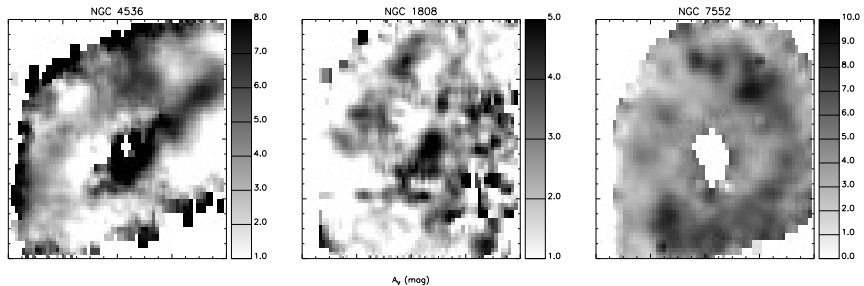


Figure 5.6: Extinction maps of NGC 4536, NGC 1808 and NGC 7552. The color scales are displayed to the right of each map, the values represent A_V measured in magnitudes.

in morphology between the [FeII] derived and HI derived extinction maps. It is clear, however, that the [FeII] lines are of limited use, as the spectral baseline they define is small and provides relatively little differential extinction. More importantly, the [FeII] lines have lower signal-to-noise ratios than the J and K lines, the [FeII]_{1.64} being particularly bad in this respect as it is degraded by residual atmospheric OH contamination in many of our observations. As a result, meaningful extinction maps based on the [FeII] line ratio could only be derived over limited areas for a minority of the galaxies. Thus, the extinctions derived from the Pa β /Br γ ratio should be the more reliable and will be used to complete the following analysis.

We calculated the extinction at each pixel and created an extinction map revealing the regions most effected by dust. Extinction maps for three example galaxies are shown in Figure 5.6. Table 5.2 lists the averaged visual extinction (A_V) over the observed field of view for both line ratios. The Table also includes the integrated, extinction corrected Br γ , Pa β , and [FeII] line fluxes. The maps were integrated over the full field of view but were filtered for low signal-to-noise pixels and pixels with linewidths either too narrow or too broad. The visual extinction A_V is determined assuming using the near-infrared extinction law $A_\lambda \propto \lambda^{-1.8}$ (Martin & Whittet 1990). The disparity between the extinctions derived from the Fe and H lines mostly reflects the poor quality of the former, as discussed above. In the case of NGC 1792, the little line emission observed has a very low signal-to-noise ratio (cf. Figure 5.4), negatively affecting the accuracy of any A_V measurement, hence also the accuracy of the extinction corrected [FeII] and Br γ fluxes. In NGC 6240, the extremely low Br γ flux makes it difficult to accurately determine the extinction on a pixel by pixel basis.

In order to obtain the best possible result, we constructed extinction corrected [FeII]_{1.26} and Br γ line maps using pixel-by-pixel extinctions derived from the

Galaxy	Pa β	Br γ	[FeII] _{1.26}	[FeII] _{1.64}	A _v _{Brγ} ^a
NGC 3628	0.7	1.4	1.4	0.6	20.3
NGC 4536	12.7	3.5	3.4	4.5	3.9
NGC 1792	1.3	0.3	0.1	--	2.9
NGC 1084	1.0	0.3	0.3	0.5	3.0
NGC 1808	18.3	4.4	9.2	8.0	2.7
NGC 520	1.2	1.3	1.2	0.3	15.3
NGC 7552	20.7	6.8	6.3	8.1	5.3
NGC 7632	1.8	0.5	0.5	0.8	3.9
NGC 1614	13.8	3.5	3.1	3.7	3.3
NGC 6240	3.3	0.6	8.5	8.7	15.6
Arp 220	0.4	0.5	0.7	--	15.4

Table 5.2: Un-extinction corrected Br γ , Pa β , [FeII]_{1.26}, and [FeII]_{1.64} fluxes with the A_v derived by the Pa β /Br γ intrinsic line ratio. All measurements are listed in units of 10¹⁴ erg s⁻¹ cm⁻² with a 10% error, which is the estimated calibration uncertainty. NGC 1792 has a 20% error due to the low signal to noise of this observation.

^a A_v is determined assuming using the near-infrared extinction law $A_\lambda \propto \lambda^{-1.8}$ (Martin & Whittet 1990). Although the measured A_v is very high in some galaxies, the extinction measured in the NIR wavelength range is significantly less.

Pa β /Br γ line ratio only. We also constructed pixel-by-pixel maps of the Br γ equivalent width directly from the observed Br γ ; these are therefore independent of the assumed extinction. The Br γ equivalent width and the Br γ luminosity thus determined are the *only* observational inputs used in the calculation of SNrates from the Starburst 99 model, described in detail in Section 5.5.2 below.

5.5.2 Calculating SNrate

Starburst 99 (from here on referred to as SB99) is a tool that models spectrophotometric properties of star-forming galaxies (Leitherer et al. 1999) such as spectral energy distributions (SEDs), luminosities, equivalent widths, supernova rates and colors. This includes predictions of the variations in these properties as a function of starburst age. The models have been calculated for 5 different metallicities ($Z = 0.04, 0.02, 0.008, 0.004, 0.001$) and 3 different initial mass functions (IMF). In addition, the two extreme star-formation modes are considered: the *continuous* mode in which star formation proceeds continuously at a constant rate, and the *instantaneous* mode where it has the form of a delta function starburst.

In our analysis, we assumed a near solar metallicity ($Z = 0.02$), a Salpeter IMF ($\alpha = 2.35, M_{low} = 1M_\odot, M_{up} = 100M_\odot$) and an instantaneous star formation

mode. In the case of an instantaneous starburst, the model normalizes the burst to an initial starburst mass of $10^6 M_{\odot}$. We calculated the average age of the population dominating the emission in each pixel from the observed $\text{Br}\gamma$ equivalent width ($\text{EW}(\text{Br}\gamma)$), which is independent of this normalization. SB99 provides the expected SNrate as a function of the age thus determined. Due to the normalization of $10^6 M_{\odot}$, the SNrate must be appropriately scaled by comparing the SB99 age dependent prediction of ionizing photon flux ($N(\text{H}^{\circ})$) to the observed ionizing photon flux, which in turn scales with $\text{Br}\gamma$ luminosity. This comparison yields a scaling factor that is directly proportional to the initial mass and initial star formation rate. This allowed us to determine the actual SNrates based on the true initial conditions of the region represented in each pixel.

5.6 Analysis

In this section, we use the observed linemaps and the SB99 results to do a detailed analysis of each galaxy in order to better understand the complex relationship between $[\text{FeII}]$ emission and SNrate. First, we present the age and SNrate estimates for each galaxy. Then we will provide both a qualitative and quantitative comparison of the SNrates and the $[\text{FeII}]$ luminosity.

5.6.1 Age and SNrate

Table 5.3 lists the $\text{Br}\gamma$ equivalent widths as well as the average age and integrated SNrate using the SB99 instantaneous burst model for each galaxy. Although the analysis was done on a pixel-to-pixel basis, the values given in Table 5.3 are either averaged (in the case of age and equivalent width) or integrated (in the case of the SNrate) over the galaxy.

5.6.2 Qualitative correlation

To illustrate the morphological relation between the $[\text{FeII}]$ emission and the SNrate, we show a side-by-side comparison of the K-band continuum, the extinction-corrected $\text{Br}\gamma$ flux, the extinction corrected $[\text{FeII}]_{1.26}$ flux, and the derived SNrate in Figure 5.7 for the galaxies NGC 4536, NGC 1808, and NGC 7552, which have the highest quality observations. A visual comparison of the morphologies in the four different maps of each galaxy shows that the SNrate map most closely resembles that of the $[\text{FeII}]$ emission.

For instance, in NGC 4536 there is a bright knot of $\text{Br}\gamma$ emission directly north of the nucleus with secondary emission peaks to the northwest and southeast of the galaxy. The $[\text{FeII}]$ emission is concentrated on the galaxy nucleus with a long plume

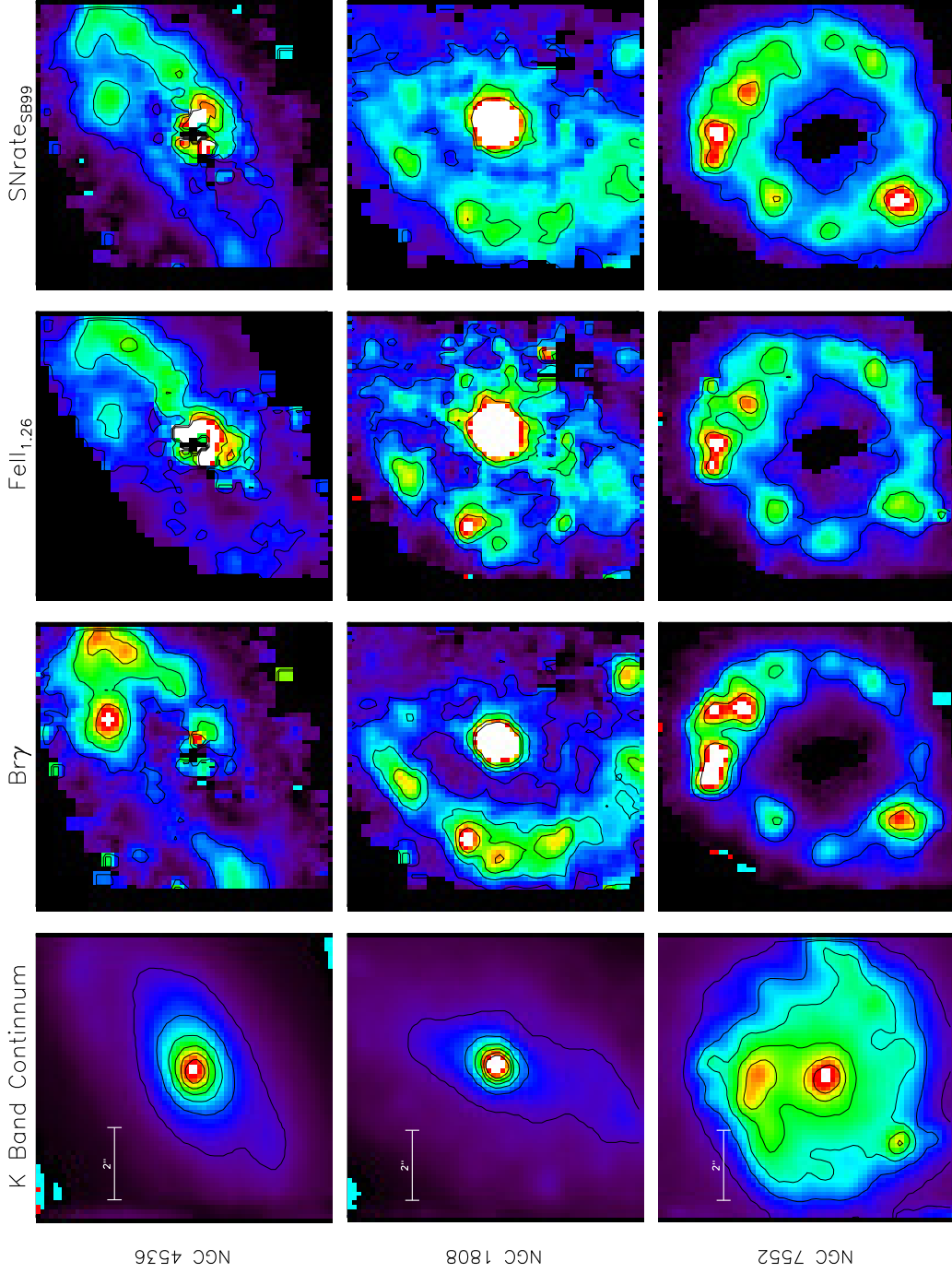


Figure 5.7: A comparison between the K-band continuum, Br γ line map, [FeII]_{1.26} line map, and the SNrate morphologies for NGC 4536, NGC 1808, and NGC 7552. The black discontinuities represent areas that have been filtered due to low signal-to-noise values in the line or extinction maps. The white pixels represent the highest flux regions.

Table 5.3: Average equivalent width of Br γ and the SB99 derived average ages and integrated SNrates using the instantaneous starburst model.

Galaxy	EW(Br γ) Å	Age _{inst} (Myr)	SNrate _{inst} yr ⁻¹
NGC 7632	5.9	7.0	0.03
NGC 3628	7.5	6.9	0.01
NGC 4536	10.6	6.7	0.3
NGC 1792	4.1	7.9	0.007
NGC 1084	4.8	7.3	0.009
NGC 1808	7.2	6.9	0.06
NGC 520	11.7	6.6	0.3
NGC 7552	13.7	6.7	0.3
NGC 7632	5.9	7.0	0.03
NGC 1614	22.9	6.4	0.9
NGC 6240	3.6	7.7	3.6
Arp 220	8.0	6.8	0.7

of emission (perhaps an inner spiral arm) extending from the nucleus towards the northwest. A small knot of faint [FeII] emission coincides with the Br γ peak. Mimicking the [FeII] emission, the SNrate peaks at the center and also shows an arm extending towards the northwest. The SNrate exhibits a slight increase at the Br γ peak, but on the whole more closely resembles the morphology of [FeII] emission.

The starburst ring surrounding the bright nucleus of NGC 1808 shows up clearly in Br γ . The ring contains individual bright knots of Br γ emission. The ring is much less prominent in [FeII] emission. The SNrate map shows a ring structure more clear than in the [FeII] map but it is quite diffuse and lacks the contrast that the Br γ knots provide. The SNrate map also shows diffuse extended structure around the nucleus, similar to the [FeII] emission but distinct from the Br γ map in which the compact nucleus is much more isolated.

Finally, the face-on spiral, NGC 7552, also reveals its starburst ring in Br γ , with little emission at the nucleus. In the northern part of the ring we find three major Br γ knots, two slightly northwest of the nucleus and one elongated knot directly north of the nucleus. Comparison shows that only one of the two northwestern Br γ knots is discernible in [FeII] emission. We also see that the morphology in the elongated knot differs in the two maps. Focusing on the SNrate morphology, the northern emission knots resemble the relative flux and morphologies of the [FeII] emission much more closely than the Br γ emission. Specifically, the top northwestern knot is also missing in SNrate map and the elongated northern Br γ

peak is resolved to two peaks, resembling the relative flux ratios seen in [FeII].

All comparisons show that, at least qualitatively, the SNrate maps resemble the [FeII] maps much more than those of the Br γ emission on a pixel by pixel basis. Once again we emphasize that the *only* observational input into the SNrate calculation is the Br γ luminosity and EW(Br γ); the [FeII] flux is never used. As the SNrate nevertheless correlates better with the [FeII] than with the Br γ emission, we conclude that this strongly supports [FeII] as a robust tracer of SNrate.

5.6.3 Quantitative correlation

Now that we have established that a qualitative correlation exists between [FeII] emission and SNrates, it is important to verify to what extent this relationship holds up quantitatively. To do this, we compare in Figure 5.8 for each galaxy the [FeII]_{1.26} luminosity and the SNrate derived from Br γ pixel-by-pixel. The linemaps were not additionally filtered, with the exception of NGC 6240 which was filtered to eliminate pixels where the Br γ flux is insufficient to determine the true extinction. We normalized both the SNrate and the [FeII] luminosity to values per square parsec so that each pixel represents the same physical area. We performed a least squares regression in log space on the combined points from all sample galaxies except NGC 1792 because of its poor signal-to-noise data. The combined linear regression is indicated by a solid black line in Figure 5.8; it takes the analytical form:

$$\log \frac{\nu_{SNrate}}{yr^{-1}pc^{-2}} = (1.01 \pm 0.2) * \log \frac{[FeII]_{1.26}}{ergs^{-1}pc^{-2}} - 41.17 \pm 0.9 \quad (5.1)$$

The errors represent the standard deviation of the slopes and intercepts of the individual galaxies, thus representing the variation between individual galaxies' fits. This is an intrinsic error, corresponding to the variations in properties among the galaxies and not derived from the quality of the observation. To investigate the strength of the relationship on a global basis, we have plotted , excluding NGC 1792, the integrated SNrate plotted against the integrated [FeII] luminosity for each galaxy, again with the best fit regression line. Errors in the extinction are a potentially significant source of uncertainty in the derived relationship. The dashed lines at either side of this best fit in Figure 5.9 mark the regression lines we would find if the extinction magnitudes were overestimated respectively underestimated by factors of two. It is obvious from the Figure that our result is essentially unaffected by this uncertainty. The best fit for the global values is given by:

$$\log \frac{\nu_{SNrate}}{yr^{-1}pc^{-2}} = (0.89 \pm 0.2) * \log \frac{[FeII]_{1.26}}{ergs^{-1}pc^{-2}} - 36.19 \pm 0.9 \quad (5.2)$$

Thus, the averaged and the integrated SNrate - [FeII] luminosity relation are identical within the errors. Both procedures yield a power law with a slope of nearly unity. The relation is linear well within the errors.

An important source of uncertainty in the SNrate calculation is caused by observational errors in the Br γ , [FeII] and K band continuum intensities. These observational errors are dominated by the uncertainty in the calibration, which is of the order of 10% of the flux in all cases except NGC 1792, where the errors are dominated by noise, estimated to be about 20% of the flux. The uncertainties in the derived SNrate are the same as those in Br γ flux, i.e. about 10%. However, the observational errors are not the dominant source of uncertainty. This is the systematic error introduced by the choice of the starburst model. Because we use SB99, our choices are limited to two star-formation models only, instantaneous and continuous. In the next section, we discuss the effects of the choice of the burst model on the relation between SNrate and [FeII] luminosity.

5.7 Dependency on burst model

So far, we have based our analysis on the assumption that star formation in the sample galaxies is best represented by an instantaneous burst. The other extreme case also modeled by SB99 is the continuous star-formation scenario. It is unlikely that either of these extreme cases is a true representation of the situation in the galaxies considered; we suspect that reality is somewhere in between and better described by one or more star bursts extended in time. We cannot determine the actual star formation history of the sample, but the SB99 model allows us to constrain the validity of our determination of SNrate/[FeII] luminosity relation by performing the same analysis this time assuming a continuous star-formation mode. The result is shown in (Figure 5.10) as a plot of the [FeII] luminosity versus the SNrate for the combined pixels of all sample galaxies. In this Figure, the black dots represent the SNrates assuming an instantaneous burst (as in Figure 5.8) and the red points represent the same pixels where the SNrate is calculated assuming continuous star formation.

From Figure 5.10 it is clear that also in continuous star-formation mode, the SNrate is still closely related to the [FeII] luminosity. However, in this case, the relation is no longer linear as the best fit slope is 1.20. We also note that in this situation, a given [FeII] luminosity also implies an SNrate roughly an order of magnitude higher than in the instantaneous burst model.

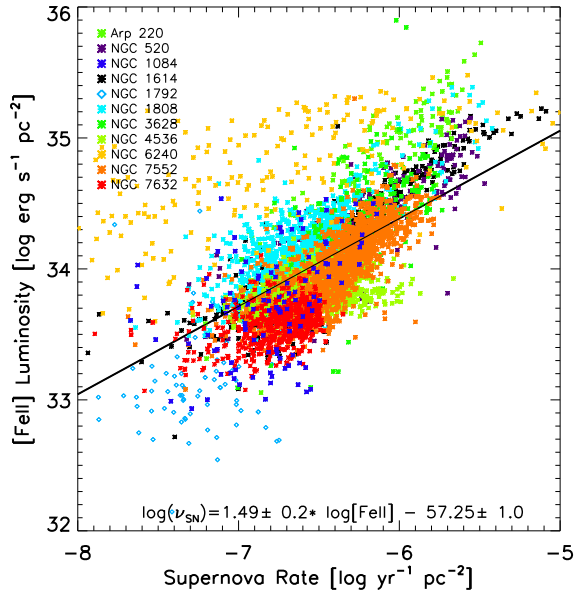


Figure 5.8: A pixel-pixel plot of SNrate, as derived from SB99, compared to [FeII] luminosity. Each galaxy is represented with a different color and the values are normalized to a square parsec. The black line represents the best fit power law excluding NGC 1792, which is represented by diamonds.

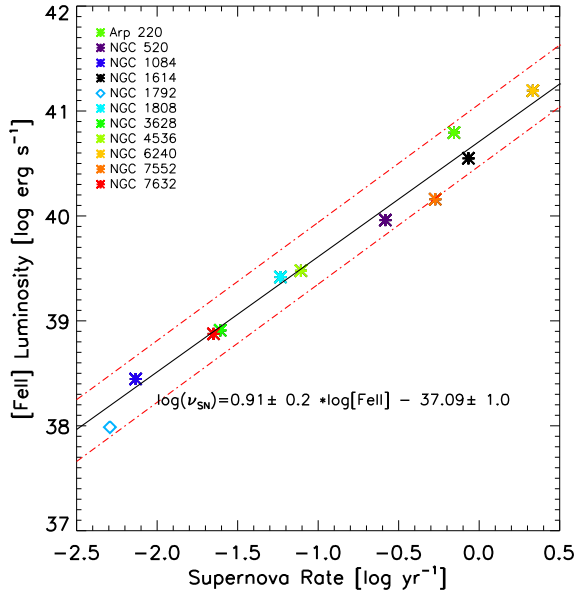


Figure 5.9: Integrated SNrate plotted against integrated [FeII] luminosity over the field of view. The black line is the least squares regression line, excluding NGC 1792. The red dotted lines represent the least squares regression line if the magnitude of extinction was overestimated respectively underestimated by a factor of two in optical depth.

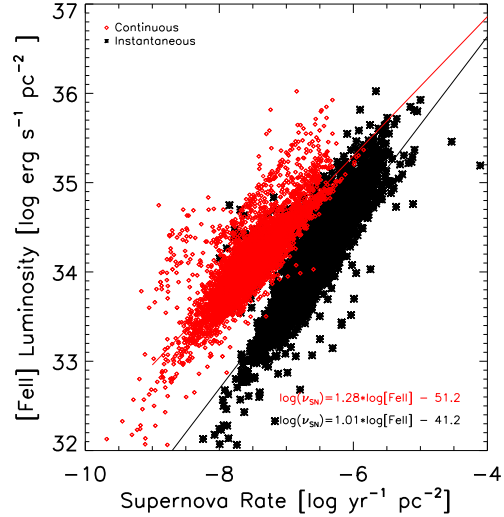


Figure 5.10: Pixel-pixel comparison of SNrate to [FeII] luminosity. The black points represent the pixel values for all the galaxies using the instantaneous burst model, while the red points represent the same pixels using the continuous burst model.

5.8 Comparison to Radio SNrate

Which mode best represents our sample? Radio continuum emission is the classical tracer of SNrate, and radio flux densities can be used to obtain an independent estimate of the SNrate for comparison to the SNrates derived with the SB99 models. We apply the equation given by Huang et al. (1994), which relates nonthermal radio luminosity and SNrate, to VLA observations. There are no VLA archived observation of NGC 7632 and this galaxy is excluded from the comparison. A similar situation applies to NGC 7552, but here we could use the ATCA 4.8 GHz map instead. For the nearest extended galaxies, we matched the radio integration area to that of SINFONI. For the more distant NGC 1614, NGC 6240, and Arp 220, we used NED VLA 1.4 GHz integrated flux densities since these galaxies are compact enough that the entire galaxy is encompassed in the SINFONI field of view. In Figure 5.11 we compare the radio SNrates thus derived to the SB99 instantaneous and continuous SNrates.

For all galaxies, except NGC 1792, NGC 4536, NGC 6240 and Arp 220, the radio SNrate closely matches those given by the SB99 instantaneous burst model. As noted before, the NIR emission linemaps of NGC 1792 are too noisy to be reliable. However, NGC 4536 is a nearly face-on galaxy with relatively low extinction and high signal-to-noise spectra, and the NIR data should be reliable. Thus, NGC 4536 is undergoing star formation that is closer to instantaneous but extended in time. Arp 220 and NGC 6240 have radio SNrates even higher than the SB99

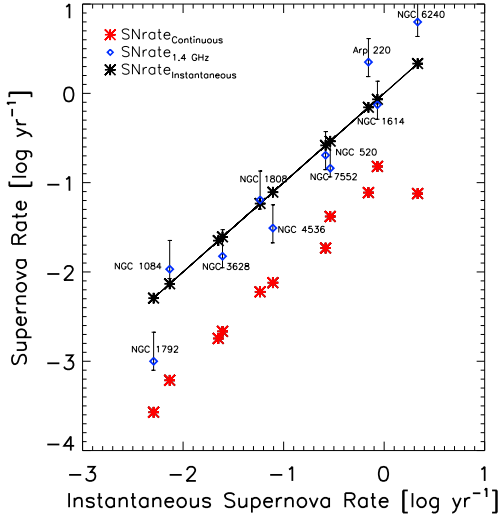


Figure 5.11: Comparison of the SB99 instantaneous SNrate (x-axis) to the radio SNrate (blue diamond), the SB99 continuous SNrate (red asterisk) and for comparison the SB99 instantaneous SNrate (black asterisk).

instantaneous SNrates. Also, in Figure 5.8, the points for these galaxies lie systematically above the best fit line, with a similar slope to the rest of the galaxies. This offset can be explained by either an excess of [FeII] emission or a deficiency of $\text{Br}\gamma$ emission, since these are the two observables that are used to scale SNrate and [FeII] luminosity. In the case of $\text{Br}\gamma$ deficiency, the $\text{Br}\gamma$ emission could be selectively suppressed by dust absorption of Lyman continuum photons in these very dense systems. However, in NGC 6240 and Arp 220, it is tempting to speculate that this excess is caused by merger related shocks that are over exciting the [FeII] in addition to the SNRs. Evidence for large scale shocks in NGC 6240 comes from the prominent wings on the H_2 1-0 S(1) line which trace the shocked superwind (Van der Werf et al. 1993; Engel et al. 2010). The [FeII] emission is morphologically similar to the H_2 , indicating that the [FeII] also traces the superwind. These powerful merger (U)LIRGs may demonstrate a limit to the validity of the direct relationship between SNrate and [FeII] luminosity. In addition, determining an accurate extinction in (U)LIRGs presents a challenge. The under or over estimation of extinction leads to inaccurate [FeII] luminosities as well as $\text{Br}\gamma$ luminosities used to scale the SNrate. However, the offset between the (U)LIRGs and the other galaxies is minor. They share a common slope and appear to be offset only in [FeII] emission. The validity of this relationship in the case of (U)LIRGs can only be established by studying a larger sample of these galaxies. In any case, it appears that the majority of (modest) starburst galaxies is well represented by the assumption of a (nearly) instantaneous burst of star formation. In addition,

the very good agreement between SNrates derived from the radio continuum, and from NIR data provides added confidence in the diagnostic strength of [FeII] as a tracer of SNrate.

5.9 Conclusion

Using SINFONI observations of 11 nearby galaxies, we have performed a pixel-by-pixel analysis of the correlation between [FeII]_{1.26} emission and independently derived SNrates. We measured accurate Br γ , Pa β , [FeII]_{1.26}, [FeII]_{1.64}, and H_{2,2.12} line fluxes. We determined Br γ equivalent widths which were used as input into the SB99 model to find the starburst age in each pixel. In the SB99 model, this defines an SNrate, normalized to an initial mass of $10^6 M_{\odot}$, which we scaled with the observed Br γ luminosity to find the actual SNrate in each pixel.

The comparison of the [FeII]_{1.26} luminosity to the SNrate (derived only from Br γ equivalent width and luminosity) reveals a nearly linear correlation, where the error represents the spread of intrinsic properties over our sample of galaxies.

$$\log \frac{\nu SNrate}{yr^{-1}pc^{-2}} = 1.01 \pm 0.2 * \log \frac{[FeII]_{1.26}}{ergs^{-1}pc^{-2}} - 41.17 \pm 0.9$$

This relationship is valid both on a pixel-pixel basis and for the integrated galaxy. For the integrated [FeII] luminosity and SNrate, the fit is remarkably tight with very little spread. However, to correctly determine the absolute SNrates, it is still critical to determine whether star formation has occurred in a (nearly) instantaneous burst, or has proceeded in a continuous fashion. SNrates derived from radio continuum observations may be used to distinguish these scenarios. Most of the modest starburst galaxies in our sample are best fitted assuming instantaneous star formation. However, we find that the relationship breaks down for (U)LIRGs in our sample.

From the strong correlations found in this sample of galaxies, we confidently conclude that [FeII]_{1.26} emission line strengths are quantitatively correlated with SNrates and can be used to derive these rates either locally or globally. This use of [FeII] as a robust tracer of SNrate provides us with a very useful diagnostic tool. It is particularly important as it allows determination of SNrates from NIR observations of distant galaxies, where individual SNRs can not be resolved.

6 | The Herschel Comprehensive (U)LIRG Emission Survey (HerCULES)

(Ultra) Luminous Infrared Galaxies ((U)LIRGs) are objects characterized by their extreme infrared (8-1000 μm) luminosities ($L_{LIRG} > 10^{11} L_{\odot}$ and $L_{ULIRG} > 10^{12} L_{\odot}$). The Herschel Comprehensive ULIRG Emission Survey (HerCULES; PI van der Werf) presents a representative flux-limited sample of 29 (U)LIRGs that spans the full luminosity range of these objects ($10^{11} \leq L_{\odot} < 10^{13}$). With the *Herschel Space Observatory*, we observe [CII] 157 μm , [OI] 63 μm , and [OI] 145 μm line emission with PACS, CO J=4-3 through J=13-12, [CI] 370 μm , and [CI] 609 μm with SPIRE, and low-J CO transitions with ground-based telescopes. The CO ladders of the sample are separated into three classes based on their excitation level. In approximately 50% of the galaxies, the [OI] 63 μm emission line is self absorbed. Comparing the CO excitation to the IRAS 60/100 μm ratio and to far infrared luminosity, we find that the CO excitation is more correlated to the far infrared colors. We present cooling budgets for the galaxies and find fine-structure line flux deficits in the [CII], [SiII], [OI], and [CI] lines in the objects with the highest far IR fluxes, but do not observe this for CO. In order to study the heating of the molecular gas, we present a combination of three diagnostic quantities to help determine the dominant heating source. Using the CO excitation, the CO J=1-0 linewidth, and the AGN contribution, we conclude that galaxies with large CO linewidths always have high-excitation CO ladders, and often low AGN contributions, suggesting that mechanical heating is important. ¹

M. J. F. Rosenberg, P. P. van der Werf *et. al*
ApJ (submitted)

¹Contribution from coauthors included helpful suggestions and comments on the text.

6.1 Introduction

(Ultra) Luminous Infrared Galaxies ((U)LIRGs) in the local universe are remarkable galaxies exhibiting an extremely high infrared luminosity, $L_{8-1000\mu\text{m}} > 10^{11}L_{\odot}$ for LIRGs and $L_{8-1000\mu\text{m}} > 10^{12}L_{\odot}$ for ULIRGs. The first galaxy identified as a luminous infrared galaxy was NGC 6240 (Zasov & Karachentsev 1979), and many more followed with observations from the InfraRed Astronomical Satellite (IRAS), which was launched in 1983 (Houck et al. 1985). After the discovery that these objects all contain massive amounts of molecular gas (Sanders et al. 1988a; Veilleux et al. 2002), detailed studies of the spectroscopic cooling lines were carried out with the *Infrared Space Observatory* (ISO; Malhotra et al. (1997); Luhman et al. (1998); Helou et al. (2001); Malhotra et al. (2001); Luhman et al. (2003); Abel et al. (2009)), ground based observations of [CI] (Gerin & Phillips 1998, 2000), *Spitzer* Space Telescope (Armus et al. 2009; Díaz-Santos et al. 2011; Stierwalt et al. 2013) and the *Herschel* Space Observatory (Graciá-Carpio et al. 2011; Díaz-Santos et al. 2013; Farrah et al. 2013; Lu et al. 2014; Díaz-Santos et al. 2014). In the local universe ULIRGs are rare (Soifer & Neugebauer 1991), but at higher redshifts ($z > 1$) they represent most of the cosmic infrared background and are the dominant source of star formation up to $z=2$ (Caputi et al. 2007; Magnelli et al. 2011; Berta et al. 2011). Locally, these objects are hosts to intense starbursts, and/or active galactic nuclei (AGN), and often are part of a merging galaxy group (Armus et al. 1987; Sanders et al. 1988b; Barnes & Hernquist 1992; Sanders & Mirabel 1996; Veilleux et al. 2002; Lonsdale et al. 2006). Regardless of the various heating processes available, however, the luminosity of most (U)LIRGs seem to be energetically driven by starbursts (Genzel et al. 1998; Downes & Solomon 1998; Veilleux et al. 1999, 2002; Gao & Solomon 2004; Veilleux et al. 2009). (U)LIRGs are also thought to represent the transitional phase in evolution from a starburst galaxy to elliptical/lenticular galaxies (Sanders et al. 1988b; Genzel et al. 2001; Tacconi et al. 2002; Rothberg & Fischer 2010; Rothberg et al. 2013), and thus must quench their star formation during this period. In fact, some evidence for this was found in the discovery of massive molecular outflows with the *Herschel* Space Observatory (Fischer et al. 2010; Sturm et al. 2011; Spoon et al. 2013; Veilleux et al. 2013; González-Alfonso et al. 2014) as well as as by ground-based telescopes (e.g., Feruglio et al. 2010; Weiß et al. 2012).

Since (U)LIRGs offer a unique insight into this transitional phase from star-forming to quiescent galaxies, understanding which mechanisms are affecting the star-forming gas is crucial. Many studies of the star forming gas in (U)LIRGs have been made since its universal presence in (U)LIRGs was determined (Sanders et al. 1991; Sanders & Mirabel 1996; Solomon et al. 1997). In general, gas is heated

by either radiation (i.e. UV photons, X-ray photons), energetic particles (cosmic rays) or mechanical processes (i.e. turbulence, stellar winds, outflows, supernovae). The interplay between these heating sources can account for the extreme environments found in (U)LIRGs, in comparison to less intense star forming environments (Aalto et al. 1991, 1995a). The high amount of energy injected into the gas in these galaxies is displayed by emission lines that serve as a coolant along with infrared dust emission. The emission lines responsible for most of the gas cooling are the [CII] line at $157 \mu\text{m}$ (${}^2P_{3/2} - {}^2P_{1/2}$), the [OI] line at $63 \mu\text{m}$ (${}^3P_1 - {}^3P_2$), and CO (rotational transitions). The *Herschel Space Observatory* has, for the first time, provided astronomers with simultaneous access to these important far infrared cooling lines and the CO rotational ladder (CO ladder) in (U)LIRGs. Using the multiple rotational transitions of CO from $J=1-0$ through $J=13-12$, the density, temperature, column density, and mass (with the addition of ${}^{13}\text{CO}$) can be estimated (eg. Rangwala et al. 2011; Spinoglio et al. 2012; Rigopoulou et al. 2013; Papadopoulos et al. 2014). In some cases, it is possible to even discern specifically the heating mechanism (Loenen et al. 2008; Hailey-Dunsheath et al. 2008; van der Werf et al. 2010b; Meijerink et al. 2013; Lu et al. 2014; Rosenberg et al. 2014; Pereira-Santaella et al. 2014). In this paper, we introduce a representative sample of (U)LIRGs spanning the luminosity range from $10^{11} \leq L_{\odot} < 10^{13}$. In Section 6.2, we present observations from the *Herschel*/SPIRE and *Herschel*/PACS spectrometers, which include [CII], [OI] $63\mu\text{m}$, [OI] $145\mu\text{m}$, CO ($4 \leq J_{\text{upp}} \leq 13$), and [CI] $370 \mu\text{m}$ and $609 \mu\text{m}$. In this paper we focus on the main neutral gas cooling lines. We therefore do not analyze the [NII] lines, which arise in ionized gas, or the fainter molecular lines which do not affect the thermal balance. Specifically, we do not discuss H_2O since in the cases where these lines are bright, they are radiatively excited (González-Alfonso et al. 2010; van der Werf et al. 2011; Yang et al. 2013) and do not remove kinetic energy from the gas and thus do not contribute to the cooling. We show spectra for three sample galaxies that represent three different classes of excitation, and the CO ladders for the full sample in Section 6.3. Using the full sample, in Section 6.4 we analyze the gas excitation, cooling budget of the sample, and a diagram for determining additional heating mechanisms for the gas. Our conclusions are presented in Section 6.5.

6.2 Observations

6.2.1 The HerCULES sample

The sample was chosen from the IRAS Revised Bright Galaxy Sample (RBGS), which contains all 629 extragalactic sources with IRAS $60 \mu\text{m}$ flux density $S_{60} >$

5.24 Jy in the (IRAS-covered) sky at Galactic latitudes $|b| > 5$ (Sanders et al. 2003). From the IRAS RBGS we select a sub-sample applying limits both in S_{60} and L_{IR} : at luminosities $L_{\text{IR}} > 10^{12} L_{\odot}$ (ULIRGs), all sources with $S_{60} > 11.65$ Jy are included, while at luminosities $10^{11} L_{\odot} < L_{\text{IR}} < 10^{12} L_{\odot}$ (LIRGs), sources with $S_{60} > 16.4$ Jy are included. From this flux-limited and statistically complete parent sample of 32 targets, we removed three LIRGs for which no ground-based CO data are available. The resulting representative flux-limited sample consists of 21 LIRGs and 8 ULIRGs. The sample covers a factor of 32 in L_{IR} and contains a range of objects including starburst galaxies, AGNs, and composite sources, and covering also a range of IRAS 60/100 micron ratios. The full list of included galaxies and their respective properties can be found in Table 6.1. The infrared luminosity is from Sanders et al. (2003) and the luminosity distance is from Armus et al. (2009) using the cosmological parameters $H_0=70 \text{ km s}^{-1} \text{ Mpc}^{-1}$, $\Omega_{\Lambda}=0.72$, and $\Omega_{\text{matter}}=0.28$.

In order to obtain a comprehensive view of the CO emission and the cooling budget of these galaxies, we proposed *Herschel*/SPIRE spectroscopy (for the CO ladder) and *Herschel*/PACS spectroscopy (for the [CII] and [OI] fine structure lines) of the entire sample. This project was approved as a Key Project on the Herschel Space Observatory, under the name Herschel Comprehensive (U)LIRG Emission Survey (HerCULES - P.I. Van der Werf). Key elements of HerCULES are:

- a representative flux-limited sample of local LIRGs and ULIRGs, where NGC 4418, NGC 1068, and Arp 220 are not formally part of the HerCULES sample;
- comprehensive coverage of the SPIRE spectral range at the highest spectral resolution mode (covering the CO ladder, [CI] and [NII] fine structure lines, and any other bright features such as H₂O lines);
- comprehensive coverage of the key fine-structure cooling lines [CII] and [OI] with PACS observations;
- integration times were scaled based on the IRAS 60 μm flux density, such that the S/N ratio (at a fixed observing wavelength) would be approximately constant over the sample, except where this would lead to excessively long integration times (in which case maximum integration time of 4 hours was adopted).

6.2.2 Herschel/SPIRE observations

Spectra were obtained with the Spectral and Photometric Imaging Receiver and Fourier-Transform Spectrometer (SPIRE-FTS, Griffin et al. 2010b) on board the *Herschel Space Observatory* (Pilbratt et al. 2010b) for the full HerCULES sample. The observations were carried out in staring mode with the galaxy nucleus on the central pixel of the detector array. The high spectral resolution mode was used with a resolution of 1.2 GHz over both observing bands. The low frequency focal plane array (Long Wavelength Spectrometer Array, SLW) covers $\nu=447-989$ GHz ($\lambda=671-303 \mu\text{m}$) and the high frequency focal plane array (Short Wavelength Spectrometer Array, SSW) covers $\nu=958-1545$ GHz ($\lambda=313-194 \mu\text{m}$), and together they include the CO $J = 4 - 3$ to CO $J = 13 - 12$ lines. Details about the galaxy type and observation ID can be seen in Table 6.1. We have included observations from other programs to help realize the complete flux-limited sample. The references for these observations are also in Table 6.1.

The data were reduced using version 9.0 of the Herschel Interactive Processing Environment (HIPE). Initial processing steps included timeline deglitching, linearity correction, clipping of saturated points, time-domain phase correction, and interferogram baseline subtraction. After a second deglitching step and interferogram phase correction, the interferograms were Fourier transformed, and the thermal emission from instrument and telescope was removed from the resulting spectra. The averaged spectra were flux calibrated as point sources using the calibration tree associated with HIPE 9.0. Following these steps a "dark" spectrum was subtracted, to remove any residual emission from the telescope and the instrument. Since the emission of most of our sources is contained entirely in the central pixel of the detector arrays, a "dark" spectrum was constructed by spectrally smoothing a combination of several off-axis pixels. For extended targets, where the off-axis pixels contain emission, the dark was obtained from a deep blank-sky observation obtained on the same observing day.

For all extended sources (Arp 299, ESO 173-G015, MGC+12--02--001, Mrk 331, NGC 1068, NGC 1365, NGC 2146, NGC 3256, NGC 5135, and NGC 7771), an aperture correction is necessary to compensate for the wavelength dependent beam size (Makiwa et al. 2013). In order to correct for the extended nature of these sources, we employ HIPE's semiExtendedCorrector tool (SECT). This tool 'derives' an intrinsic source size by iterating over different source sizes until it finds one that provides a good match in the overlap range near 1000 GHz, and is further discussed in Wu et al. (2013). We set the Gaussian reference beam to $42''$, the largest SPIRE beam size. The beam size corrected flux values for the 6 extended sources are listed in Table 6.2, along with the unextended sources. There are three targets in the sample that have multiple pointings; Arp 299, NGC 1365,

and NGC 2146. In order to compare these targets with the PACS observations, we choose only the nuclear pointings for these sources. In the case of Arp 299, we use only the pointing for Arp 299 A. For NGC 1365 we take the average of the northeast and southwest pointings and for NGC 2146, we use only the nuclear pointing.

We note that the error in the extended source flux correction could be significant due to the assumptions. Namely we assume that the high-J CO transitions are distributed in the same way as the low-J CO lines. If high-J CO transitions are only coming from a centralized compact region, we are overestimating their flux with our beam correction method. For this reason, we apply an additional 15% error to the extended galaxies.

CO and [CI] line fluxes were extracted using FTFinder, a program specifically created to extract line fluxes from Fourier transform spectrographs, and are listed in Table 6.2. This is an interactive data language (IDL) based graphical user interface, that allows the user to fit lines, choose line profiles, fix any line parameter, and extract the flux. We define a polynomial baseline to fit the continuum for the SLW and SSW separately and derive the integrated line intensities from baseline subtracted spectra with a simultaneous line fit of all CO, [CI], [NII] and other bright lines in the spectrum. We use a Gaussian line profile with a fixed full width half maximum (FWHM), based on the line width of the CO 1-0 transition. We adopt an error of 16% for the non-extended galaxy fluxes, which encompasses our dominant sources of error, $\sim 10\%$ for the flux extraction and baseline definition and 6% for the absolute calibration uncertainty for staring-mode SPIRE FTS observations (Swinyard et al. 2014). For the case of extended sources, we adopt an additional $\sim 15\%$ error from the beam size corrections, making the total error $\sim 30\%$ for the 5 extended sources.

6.2.3 Herschel/PACS observations

We have obtained observations of the [OI] $63 \mu\text{m}$ ([OI]₆₃), [OI] $145 \mu\text{m}$ ([OI]₁₄₅), and [CII] $157 \mu\text{m}$ emission lines with the Integral Field Spectrometer of the Photodetector Array Camera and Spectrometer (PACS, Poglitsch et al. 2010b) on board *Herschel Space Observatory* for every object in the HerCULES sample. The data presented here were obtained as part of the Herschel program KPOT_pvanderw_1 (PI: P. van der Werf), complemented by observations from other programs. The observations and program IDs of the [CII] and [OI] lines are listed in Table 6.1.

The data were downloaded from the Herschel Science Archive and processed using HIPE v11.0. Standard processing steps including timeline deglitching, application of the Relative Spectral Response Function and detector flat fielding, and

Object	L_{IR} $\log(L_{\odot})$	z	D_L [Mpc]	Δv_{FWHM} [km s $^{-1}$]	Type	Lines	OBSID	Program
Arp 193	11.67	0.02330	110	400	SB,L	[OI] $_{63}$, [OI] $_{145}$, [CII] $_{145}$	1342197801	KPOT_pvanderw_1
Arp 220	12.0	0.01813	77	504	SB,AGN	194 – 671 μ m [OI] $_{63}$, [OI] $_{145}$ [CII] $_{145}$	1342209853 1342191304 1342191306	KPOT_pvanderw_1 KPGT_esturm_1 KPGT_esturm_1K
Arp 299 A IC 694	11.88	0.01030	50.7	325	SB,AGN	194 – 671 μ m [OI] $_{63}$ [OI] $_{145}$ [CII] $_{145}$	1342190674 1342199421 1342232602 1342208906	KPGT_cwils01_1 KPGT_esturm_1 OT1_shalleyd_1 KPGT_esturm_1
ESO 173--G015	11.34	0.00974	34	200	SB	194 – 671 μ m [OI] $_{63}$, [OI] $_{145}$, [CII] $_{145}$	1342199248 1342190368	KPOT_pvanderw_1 KPOT_pvanderw_1
IRAS13242--5713	11.10	0.01078	41.2	350	SB	194 – 671 μ m [OI] $_{63}$, [OI] $_{145}$, [CII] $_{145}$	1342202268 1342212227	KPOT_pvanderw_1 KPOT_pvanderw_1
ESO 320--G030	11.10	0.01078	41.2	350	SB	194 – 671 μ m [OI] $_{63}$, [OI] $_{145}$, [CII] $_{145}$	1342210861 1342212532	KPOT_pvanderw_1 KPOT_pvanderw_1
IRAS11506--3851 IC 1623	11.65	0.02007	85.5	250	SB,AGN	[OI] $_{63}$, [OI] $_{145}$, [CII] $_{145}$	1342212314	KPOT_pvanderw_1
IC 4687/6	11.55	0.01735	81.9	230	SB	194 – 671 μ m [OI] $_{63}$ [CII] $_{145}$	1342239740 1342239739	OT1_larnus_1 OT1_larnus_1
IRAS F17207--0014	12.39	0.04281	198	620	SB,L	194 – 671 μ m [OI] $_{63}$	1342192993 1342229692	KPOT_pvanderw_1 KPGT_esturm_1
IRAS F05189--2524	12.02	0.04256	187	300	QSO	[OI] $_{145}$, [CII] $_{145}$	1342229693 1342192829	KPGT_esturm_1 KPOT_pvanderw_1
IRAS F18293--3413	11.81	0.01817	86	270	SB	194 – 671 μ m [OI] $_{63}$, [OI] $_{145}$, [CII] $_{145}$	1342192829 1342192830	KPGT_esturm_1 KPOT_pvanderw_1
IRAS13120--5453	12.26	0.03076	144	400	Sy2,SB	[OI] $_{63}$ [OI] $_{145}$, [CII] $_{145}$	1342214628 1342214629	KPGT_esturm_1 KPGT_esturm_1
MGC+12--02--001	11.44	0.01570	69.8	200	SB	194 – 671 μ m [OI] $_{63}$, [OI] $_{145}$, [CII] $_{145}$	1342212342 1342193211	KPOT_pvanderw_1 KPOT_pvanderw_1
Mrk 231	12.51	0.04217	192	200	QSO	194 – 671 μ m [OI] $_{63}$	1342213377 1342189280	KPOT_pvanderw_1 KPGT_esturm_1
Mrk 273	12.14	0.03736	173	520	SB,Sy2	[OI] $_{145}$, [CII] $_{145}$	1342186811 1342210493	SDP_esturm_3 KPOT_pvanderw_1
Mrk 331	11.41	0.01790	79.3	215	SB	194 – 671 μ m [OI] $_{63}$, [OI] $_{145}$, [CII] $_{145}$	1342207801 1342207802	KPGT_esturm_1 KPGT_esturm_1
NGC 34	11.44	0.01962	84.1	330	SB	194 – 671 μ m [OI] $_{63}$, [OI] $_{145}$, [CII] $_{145}$	1342209850 1342197840	KPOT_pvanderw_1 KPOT_pvanderw_1
NGC 1068	11.30	0.003793	15.9	300	AGN,SB	194 – 671 μ m [OI] $_{63}$, [OI] $_{145}$, [CII] $_{145}$	1342212316 1342199416	KPOT_pvanderw_1 KPOT_pvanderw_1
NGC 1365	11.00	0.00546	17.9	250	Sy1,SB	194 – 671 μ m [OI] $_{63}$	1342199253 1342191153	KPOT_pvanderw_1 KPGT_esturm_1
NGC 1614	11.60	0.01594	67.8	220	SB	[OI] $_{63}$, [OI] $_{145}$, [CII] $_{145}$	1342191154 1342213445	KPGT_esturm_1 KPGT_cwils01_1
NGC 2146	11.07	0.00298	17.5	250	SB	194 – 671 μ m [OI] $_{63}$, [OI] $_{145}$, [CII] $_{145}$	1342191295 1342191294	KPGT_esturm_1 KPGT_esturm_1
NGC 2623	11.54	0.01851	84.1	400	SB,AGN	194 – 671 μ m [OI] $_{63}$, [OI] $_{145}$, [CII] $_{145}$	1342204020 1342190367	KPOT_pvanderw_1 KPOT_pvanderw_1
NGC 3256	11.56	0.00935	38.9	230	SB	194 – 671 μ m [OI] $_{63}$	1342192831 1342193210	KPOT_pvanderw_1 KPOT_pvanderw_1
NGC 4418	11.19	0.007268	36.5	163	Sy2	194 – 671 μ m [OI] $_{63}$, [OI] $_{145}$, [CII] $_{145}$	1342204025 1342219553	KPOT_pvanderw_1 KPOT_pvanderw_1
NGC 5135	11.17	0.01369	60.9	150	Sy2,SB	[OI] $_{63}$	1342210383 1342210384	KPGT_esturm_1 KPGT_esturm_1
NGC 6240	11.85	0.02448	116	500	SB,AGN	194 – 671 μ m [OI] $_{63}$, [OI] $_{145}$, [CII] $_{145}$	1342201201 1342187780	KPOT_pvanderw_1 KPGT_esturm_1
NGC 7469	11.59	0.01632	70.8	300	Sy1,SB	[OI] $_{145}$, [CII] $_{145}$	1342210830 1342210848	KPGT_esturm_1 KPGT_esturm_1
NGC 7552	11.03	0.00537	23.5	180	SB	194 – 671 μ m [OI] $_{63}$	1342190371 1342212344	KPOT_pvanderw_1 KPOT_pvanderw_1
NGC 7771	11.34	0.01427	61.2	250	SB	[OI] $_{63}$, [OI] $_{145}$, [CII] $_{145}$	1342216622 1342216623	KPGT_esturm_1 KPGT_esturm_1
Zw 049.057 CGCG 049-057	11.27	0.01300	65.4	200	SB	194 – 671 μ m [OI] $_{63}$, [OI] $_{145}$, [CII] $_{145}$	1342214831 1342187847	KPOT_pvanderw_1 KPGT_esturm_1
							1342211171	KPGT_esturm_1
							1342199252	KPOT_pvanderw_1
							1342210400	KPGT_esturm_1
							1342210399	KPGT_esturm_1
							1342198428	KPOT_pvanderw_1
							1342197839	KPOT_pvanderw_1
							1342212317	KPOT_pvanderw_1
							1342190374	KPOT_pvanderw_1
							194 – 671 μ m	KPOT_pvanderw_1

Table 6.1: Sample properties.

SB=Starburst, L=LINER, AGN=Active Galaxy Nucleus, Sy1=Seyfert 1, Sy2=Seyfert 2, QSO=Quasi-Stellar Object, Object name, infrared luminosity, redshift, luminosity distance, line width of CO J=1-0, galaxy type, lines observed, observation ID, and program name are listed for the full HerCULES sample. Classifications are based on optical and X-ray observations. The infrared luminosity (Sanders et al. 2003) and the luminosity distance (Armus et al. 2009) use the cosmological parameters $H_0=70$ km s $^{-1}$ Mpc, $\Omega_{vacuum}=0.72$, and $\Omega_{matter}=0.28$.

subtraction of the on and off chop positions, gridding along the spectral axis, and combination of the nod positions. With the exception of Arp 299, the objects are all centered on the $9''.4$ central spaxel of the 5 by 5 PACS array, observed in staring mode. The fluxes are extracted from the central spaxel, using the `extractSpaxel-Spectrum` routine, and referenced to a point source. We use the `pointSourceLoss-Correction` routine to capture any additional flux that may not be captured in the central spaxel. Finally, SPLAT as part of the STARLINK software package was used to subtract the baseline from each observation, and isolate the desired lines, in the case of PACS range spectroscopy.

Arp 299 was observed in the mapping mode. The integrated flux for Arp 299 A (presented in this paper) was calculated by summing the flux within a $25''$ aperture centered on the source.

6.3 Results

6.3.1 Spectra and line fluxes

All SPIRE CO and [CI] line fluxes are listed in Table 6.2. We present three examples of galaxy spectra obtained with SPIRE in the top panels of Figure 6.1, 6.2, and 6.3 for NGC 7552, Mrk 331, and IRAS F17207--0014, respectively. It is important to note that the baseline ripple seen in the SPIRE FTS spectra is due to both the sinc profile of the strong CO transitions and the noise. Since in this paper we only discuss the neutral gas cooling, we do not present fluxes of [NII] (which originates in ionized gas) or the molecular lines other than CO, which are irrelevant to the total neutral gas cooling. A comprehensive set of fluxes will be presented in Van der Werf et al. (in prep).

In order to extract the line parameters from the PACS observations, we first integrate over the baseline subtracted spectrum and then we fit a Gaussian profile to the baseline subtracted flux. In some sources, the [OI]₆₃ line shows a double-peaked profile, where the flux at the central wavelength is diminished, which could indicate Keplerian rotation. However, if this were the case, then we would expect a similar profile in the [OI] 145 μm line and possibly the other fine structure lines as well, which is not seen. The spectral resolution of PACS at 145 μm is more than sufficient to resolve the $\sim 0.2 \mu\text{m}$ separation between the two peaks in the [OI]₆₃ profile. Therefore, we conclude that this double-peaked profile is due to absorption in the center of the profile by colder foreground gas. We note that [OI]₆₃ absorption is due to O in the ground state while absorption at 145 μm requires O to be at a state having an energy of 226 K above the ground state. Therefore, in cool or moderate density gas the [OI]₁₄₅ line will not show an absorption feature, even

if the $[\text{OI}]_{63}$ line does. This same effect has been noted in Arp 220, which shows the $[\text{OI}]_{63}$ in full absorption (González-Alfonso et al. 2012). In the case of NGC 4418 and Zw 049.057, the $[\text{OI}]_{63}$ line has an inverse P Cygni profile, suggesting that the absorbing foreground gas is flowing into the nuclear region. The three example galaxies for which the spectra are shown in Figures 1-3 display different behavior in the $[\text{OI}]_{63}$ μm line. In NGC 7552, a face-on starburst galaxy, the profile remains Gaussian, while in Mrk 331, a late-stage merger, there is a strong dip in the middle of the profile. IRAS F17207--0014 is known for being one of the coolest ULIRGs, here absorption dominates the $[\text{OI}]_{63}$ emission. For the $[\text{OI}]_{63}$ profiles that show an absorption feature, we fit the Gaussian only to the wings of the emission profile and state the flux in parentheses. the Gaussian-fit flux, is only valid if the true line profile is Gaussian. However, we suggest this is a more robust estimate of the true integrated flux of the $[\text{OI}]_{63}$ line emerging from the warm nuclear region, since in many cases, the absorption dominates the profile. We note that using a Gaussian profile to extrapolate the line flux requires an assumption of the location of the line center, which may not be accurate, especially in the case of IRAS F17207--0014. We have tested the relations presented in the rest of this paper with both the integrated flux and the Gaussian fit, and find it does not strongly affect the results. Both the observed line fluxes and the gaussian-fit line fluxes, stated in the parenthesis, are also presented in Table 6.2. In the bottom row of the spectra in Figures 6.1, 6.2, and 6.3, the PACS line profiles of the three sample galaxies are presented (NGC 7552, Mrk 331, IRAS F17207--0014).

6.3.2 Classification of CO ladders

In Figure 6.4, we present the CO ladders of the full HerCULES sample. We have collected the available ground based observations of CO J=1-0, 2-1, and 3-2, whose fluxes and references are listed in Table 6.3. Where necessary we have converted the ground-based measurements to the cosmology adopted here. In order to compare these CO ladders directly, we have normalized the ladders by the integrated CO flux summed from J=5-4 through J=13-12, to focus on the relative behavior of the higher-J transitions since we do not have CO J=1-0 data for all sources. We excluded the J=4-3 transition since at $z > 0.03$ the rest frequency of the J=4-3 transition falls short of the SPIRE coverage, even when it is within the spectral coverage, the signal to noise is often too low to detect the transition. The CO ladders are separated into three classes based on the parameter α , where:

$$\alpha = \frac{L_{\text{CO}_{J=12-11}} + L_{\text{CO}_{J=13-12}}}{L_{\text{CO}_{J=5-4}} + L_{\text{CO}_{J=6-5}}}. \quad (6.1)$$

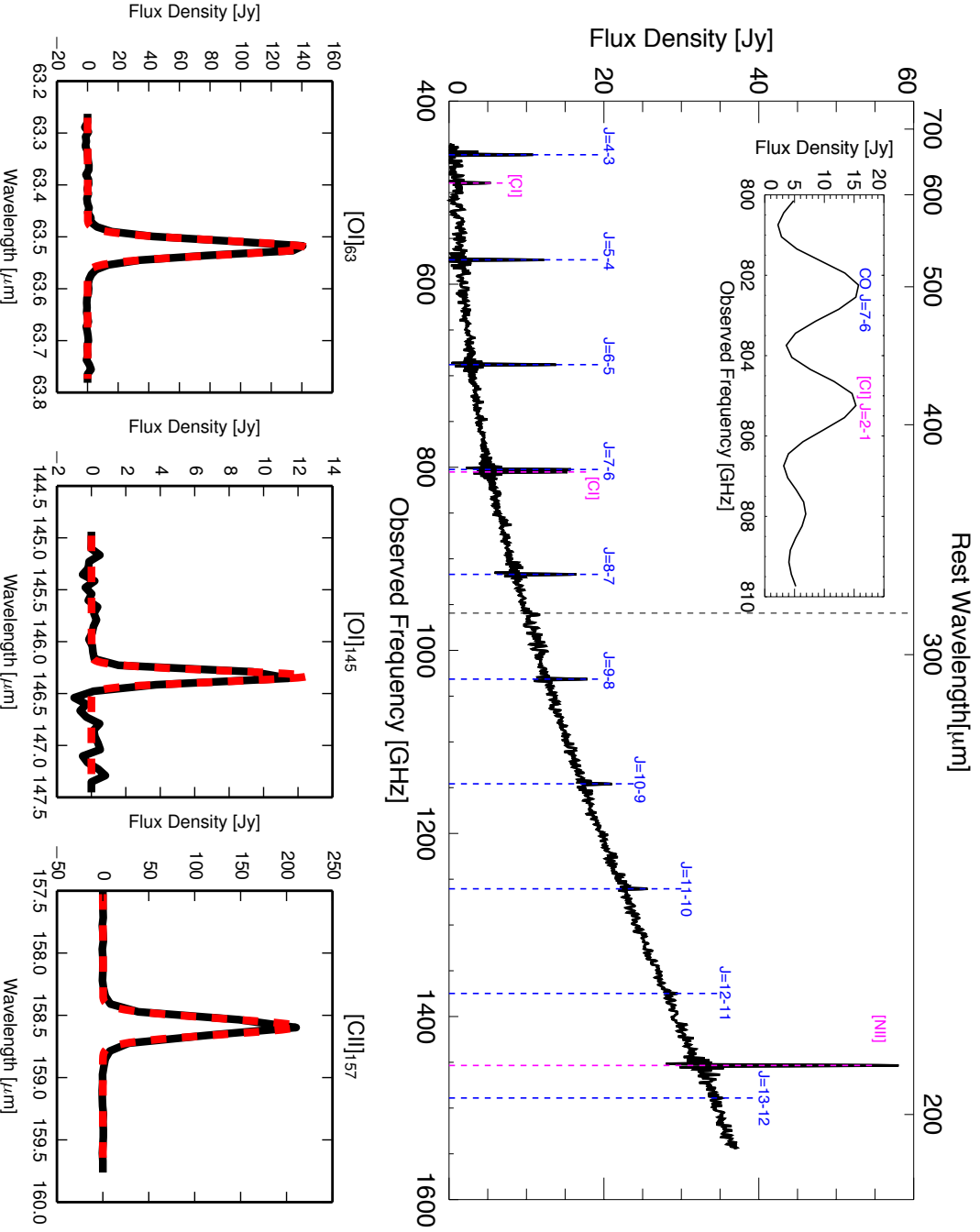


Figure 6.1: Top: Herschel SPIRE spectra for NGC 7552 in observed frequency. CO lines are indicated in blue and fine structure lines in pink. The vertical black dashed line near 920 GHz separates the SLW and SSW arrays. The inset shows a magnified version of the CO J=7-6 and [OI]₃₇₀ transitions. Bottom: Herschel PACS observations of [OII]₆₃, [OII]₁₄₅, and [CII]₁₅₇ presented in black, with Gaussian fits in red.

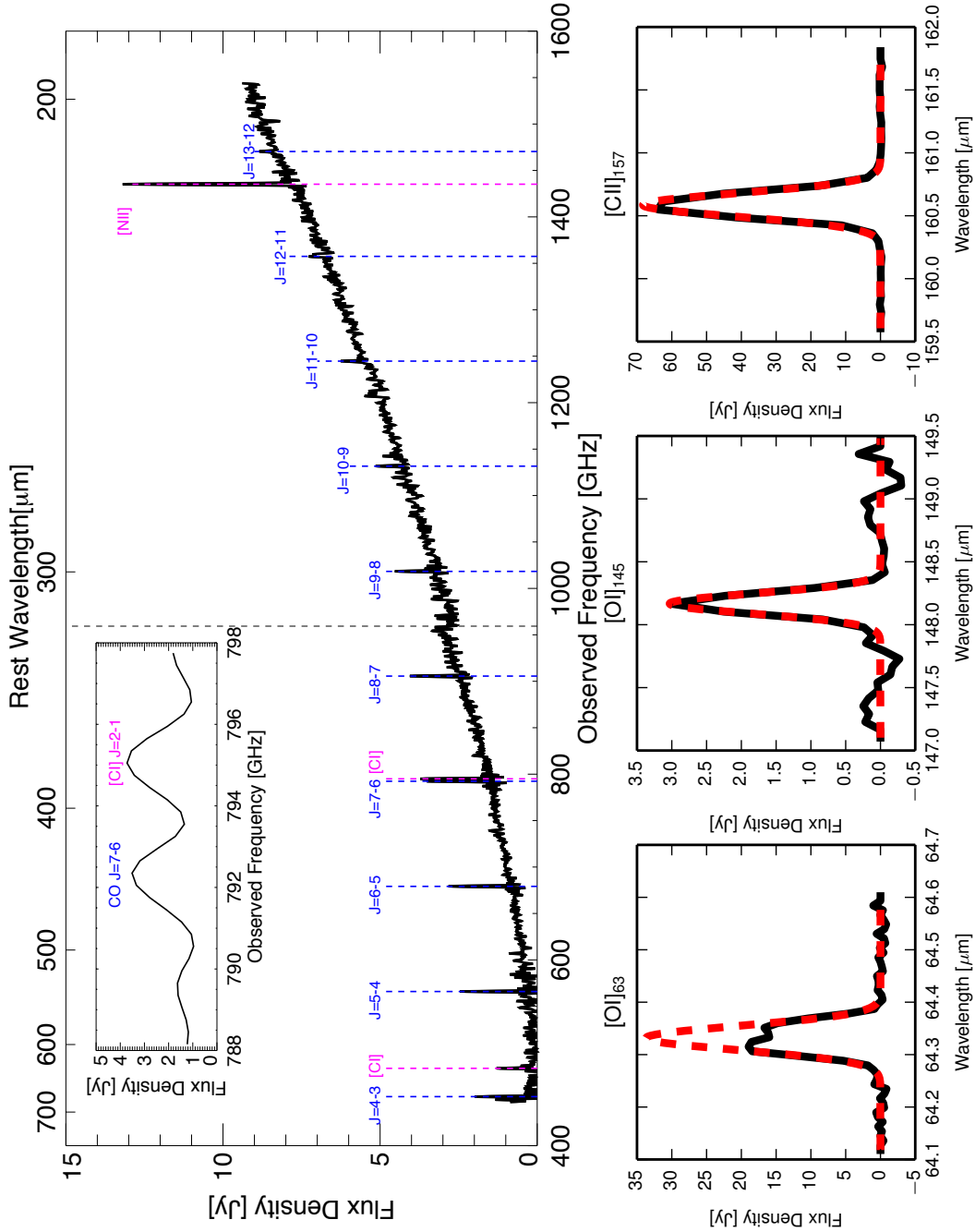


Figure 6.2: Top: Herschel SPIRE spectra for Mrk 331 in observed frequency. CO lines are indicated in blue and fine structure lines in pink. The vertical black dashed line near 920 GHz separates the SLW and SSW arrays. The inset shows a magnified version of the CO J=7-6 and [CII]₃₇₀ transitions. Bottom: Herschel PACS observations of [OII]₆₃, [OII]₁₄₅, and [CII]₁₅₇ presented in black, with Gaussian fits in red.

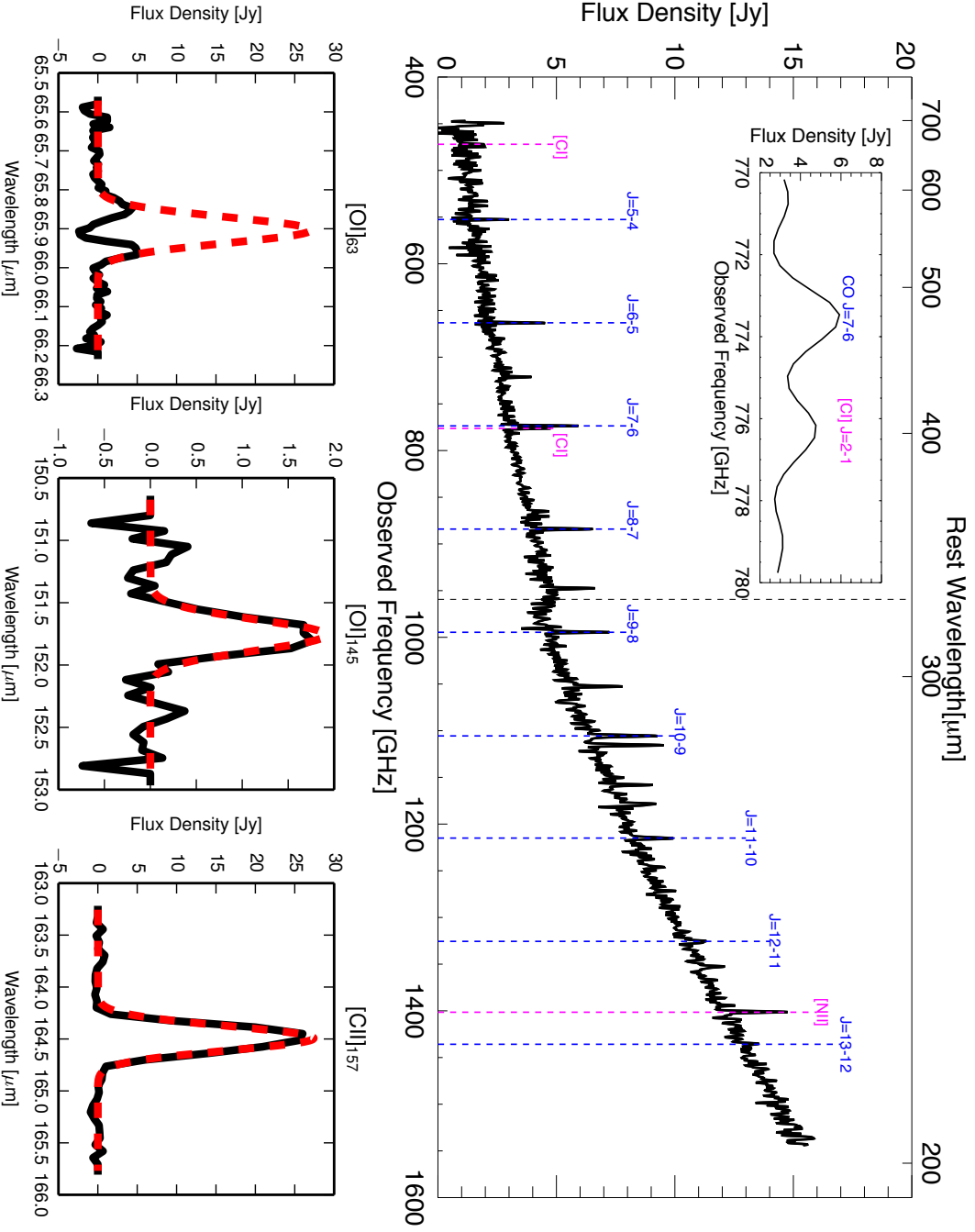


Figure 6.3: Top: Herschel SPIRE spectra for IRAS F17207-0014 in observed frequency. CO lines are indicated in blue and fine structure lines in pink. The vertical black dashed line near 920 GHz separates the SLW and SSW arrays. The inset shows a magnified version of the CO J=7-6 and [CII]₃₇₀ transitions. Bottom: Herschel PACS observations of [OIII]₆₃, [OII]₁₄₅, and [CII]₁₅₇ presented in black, with Gaussian fits in red.

Object	J=4-3	J=5-4	J=6-5	J=7-6	J=8-7	J=9-8	J=10-9	J=11-10	J=12-11	J=13-12	[CII] ₁₆₀₉	[CII] ₁₅₇₀	[OI] ₁₆₃	[OI] ₁₄₅	[CII]
Arp 193	3.00	2.87	3.52	3.46	3.05	2.61	2.27	1.87	1.01	1.11	1.64	3.71	1.21(2.23) ^b	0.12(0.13)	1.52(1.54)
Arp 220	6.89	8.81	11.95	13.17	14.07	12.79	8.98	9.67	5.29	6.01	2.95	7.43	-5.80(-5.97) ^c	-0.03(0.15)	1.16(1.07)
Arp 299	5.36	6.93	8.61	10.54	12.10	11.73	12.77	10.42	11.48	11.59	3.47	11.49	5.90(5.93)	0.58(0.57)	9.13(9.02)
ESO 173-G015	6.32	8.85	9.18	10.06	9.76	10.99	10.85	11.25	8.03	6.93	4.49	8.35	1.48(1.73) ^a	0.22(0.21)	2.53(2.51)
ESO 320--G030	4.30	4.56	5.09	4.50	3.57	4.08	2.78	2.56	2.21	1.44	1.84	2.34	0.77(2.87) ^a	0.06(0.06)	1.63(1.66)
IC 1623	4.44	4.48	3.28	2.75	1.83	0.84	0.31	0.39	1.14	--	2.41	3.62	0.87(1.29) ^a	0.08(0.08)	2.26(2.27)
IC 4687	1.67	1.87	1.96	1.54	1.14	0.53	0.71	--	0.42	--	--	1.66	1.40(1.44)	--	2.69(2.68)
IRAS F17207--0014	--	1.78	3.47	4.42	5.13	3.38	2.75	4.05	2.75	2.06	1.22	2.48	0.19(1.57) ^a	0.06(0.08)	0.87(0.89)
IRAS F05189--2524	--	1.96	2.38	2.61	2.83	0.90	1.35	1.25	1.32	0.81	0.46	1.50	0.10(0.15)	0.01(0.01)	0.17(0.15)
IRAS F18293--3413	5.73	7.01	7.05	6.16	4.47	3.26	2.02	1.51	1.05	1.18	4.39	6.16	2.56(4.95) ^a	0.23(0.24)	4.82(4.89)
IRAS 13120-5453	--	4.99	5.87	6.71	6.44	4.21	5.75	4.21	3.16	2.51	2.54	5.39	1.09(1.57) ^a	0.08(0.10)	1.33(1.34)
MGC+12--02--001	3.22	3.67	3.34	2.74	2.26	2.04	1.45	1.84	0.49	0.72	1.11	2.64	1.60(1.60)	0.10(0.11)	2.08(2.06)
Mrk 231	--	1.88	2.26	2.45	2.61	1.85	2.38	2.61	1.97	1.65	0.45	1.39	0.14(0.17)	0.03(0.03)	0.39(0.38)
Mrk 273	--	1.77	2.47	2.76	3.03	2.86	2.68	1.99	1.69	1.79	5.15	1.68	0.39(0.69) ^a	0.07(0.07)	0.74(0.73)
Mrk 331	2.60	2.52	2.68	2.32	2.18	1.94	1.21	1.37	0.70	0.91	1.48	2.61	1.00(1.41) ^a	0.09(0.08)	1.82(1.84)
NGC 34	--	1.97	2.13	2.43	2.90	2.80	1.55	2.39	1.63	1.23	1.19	1.06	0.67(0.82) ^a	0.07(0.07)	0.71(0.72)
NGC 1068	25.24	24.27	24.27	24.63	25.31	18.00	16.52	16.27	14.24	8.37	5.70(4.88)	0.27(0.27)	3.09(2.96)	--	4.33(4.29)
NGC 1365	20.10	23.28	22.49	20.62	17.92	11.87	8.08	7.05	4.24	--	10.19	17.37	1.37(1.40)	0.11(0.12)	4.33(4.29)
NGC 1614	2.11	3.44	3.22	3.31	3.18	2.81	2.23	1.42	0.84	0.55	1.29	2.58	2.24(2.29)	0.19(0.19)	2.46(2.36)
NGC 2146	8.42	11.27	12.86	13.15	11.39	9.89	8.06	5.88	3.41	5.56	2.86	11.69	2.78(2.74)	0.43(0.43)	7.65(7.60)
NGC 2623	2.01	2.07	2.47	2.82	3.32	2.79	3.12	3.02	1.74	2.20	0.93	2.42	0.40(0.71) ^a	0.08(0.08)	0.60(0.61)
NGC 3256	8.90	11.44	12.95	12.63	10.65	9.31	7.50	5.96	4.37	4.24	3.41	11.20	5.11(5.16)	0.36(0.35)	5.53(5.47)
NGC 4418	2.47	2.78	3.56	4.14	5.20	5.25	5.88	6.43	5.85	6.19	1.83	1.08	-0.07(-0.13) ^b	--	0.14(0.14)
NGC 5135	2.66	4.12	4.06	3.13	2.36	2.28	1.32	1.52	0.92	0.41	4.08	6.17	1.18(1.14)	0.09(0.09)	1.60(1.54)
NGC 6240	9.57	11.13	13.38	16.53	18.08	16.51	13.92	13.20	12.45	9.80	3.03	9.11	6.25(5.99)	0.50(0.46)	3.74(3.57)
NGC 7469	2.69	4.46	4.34	3.45	2.91	2.88	1.78	1.82	1.15	1.05	2.31	4.41	1.72(1.77)	0.16(0.15)	2.04(2.02)
NGC 7552	12.59	12.50	13.32	12.14	10.73	7.40	4.25	4.62	2.16	1.83	5.43	1.83	3.90(3.76)	0.23(0.23)	4.20(4.09)
NGC 7771	3.70	4.95	4.65	4.41	2.29	2.09	0.99	2.68	0.15	0.85	3.20	6.67	0.60(0.95) ^a	--	1.64(1.68)
Zw 049.057	--	1.90	2.57	2.89	2.42	2.50	1.24	1.51	0.84	0.94	1.12	1.21	0.06(0.07) ^b	0.02(0.02)	0.35(0.35)

Table 6.2: The SPIRE and PACS integrated line intensities. ^a Profile shows a partial absorption feature.

^b Profile shows inverse P-cygni profile.

^c Profile is in full absorption.

The integrated fluxes of CO, [CI], [OI], and [CII]. Flux errors are 16% for all galaxies that are not extended. For the extended galaxies Arp 299, ESO 173-G015, NGC 1365, NGC 2146, and NGC 3256, the CO transitions are denoted with just their J number (e.g. 4-3). The [CI] and CO transitions are observed with *Herschel*/SPIRE and are in units of $10^{-17} \text{ W m}^{-2}$, while the [OI] and [CII] lines are observed with *Herschel*/PACS and are in units of $10^{-15} \text{ W m}^{-2}$. For the PACS observations, the number in parenthesis is the flux of the best fit gaussian profile. The fluxes characterized by a '-' indicate that we did not detect these lines above the noise. Negative numbers are lines that appear in absorption (Arp 220) or with complex profiles, such as inverse P-cygni profiles (NGC 4418 and Zw 049.057).

Object	J=1-0	Beam FWHM (")	Reference	J=2-1	Beam FWHM (")	Reference	J=3-2	Beam FWHM (")	Reference
Arp 193	0.73	22"	P12	6.37	14"	P12	13.55	11"	P12
Arp 220	1.58	22"	P12	8.49	14"	P12	41.53	11"	P12
Arp 299	2.23	22"	P12	--	--	--	49.66	11"	P12
ESO 173--G015	--	--	--	--	--	--	--	--	--
ESO 320--G030	0.68	48"	M90	--	--	--	--	--	--
IC 1623	2.60	22"	P12	17.11	52"	I04	37.5	11"	P12
IC 4687/6	0.42	48"	A07	2.65	23"	A07	--	--	--
IRAS F17207--0014	0.59	22"	P12	5.06	14"	P12	13.22	11"	P12
IRAS F05189--2524	0.18	22"	P12	0.96	14"	P12	2.83	11"	P12
IRAS F18293--3413	2.23	55"	G04	--	--	--	--	--	--
IRAS13120--5453	--	--	--	--	--	--	--	--	--
MGC+12--02--001	--	--	--	--	--	--	--	--	--
Mrk 231	0.32	22"	P12	2.32	14"	P12	6.27	11"	P12
Mrk 273	0.30	22"	P12	2.00	14"	P12	5.35	11"	P12
Mrk 331	1.27	55"	G04	--	--	--	--	--	--
NGC 34	0.74	48"	H98	3.06	23"	H98	--	--	--
NGC 1068	10.82	22"	P12	86.37	14"	P12	196.05	11"	P12
NGC 1365	13.16	55"	G04	18.70	23"	H98	53.90	14"	I14
NGC 1614	0.79	21"	G04	1.54	22"	K13	--	--	--
NGC 2146	9.53	21"	G04	6.91	12.5"	B93	84.46	21"	M99
NGC 2623	0.61	22"	P12	2.01	14"	P12	6.94	11"	P12
NGC 3256	3.30	44"	A95	53.00	22"	A95	--	--	--
NGC 4418	0.50	22"	P12	--	--	--	11.37	11"	P12
NGC 5135	1.45	22"	P12	9.35	14"	P12	22.25	11"	P12
NGC 6240	1.21	22"	P12	11.17	14"	P12	36.00	11"	P12
NGC 7469	1.12	22"	P12	6.72	14"	P12	18.12	11"	P12
NGC 7552	3.10	48"	C92	21.00	22"	A95	26.00	15"	I14
NGC 7771	1.33	55"	S91	--	--	--	10.12	23"	N05
Zw 049.057	0.45	22"	P12	4.58	14"	P12	8.06	11"	P12

Table 6.3: Ground based CO integrated fluxes from the literature. All units are in 10^{-18} W m^{-2} .

References are as follows: A95=Aalto et al. (1995b), A07= Albrecht et al. (2007), G04= Gao & Solomon (2004), H89= Heckman et al. (1989), I04= Iono et al. (2004), I14=Israel, F.P., 2014 A&A to be submitted, K13= König et al. (2013), M90= Mirabel et al. (1990), M99= Mauersberger et al. (1999), N05= Narayanan et al. (2005), P12= Papadopoulos et al. (2012), and references therein, S91= König et al. (2013).

and $L_{CO} = 4\pi D_L^2 F_{CO}$, with F_{CO} in $[W m^{-2}]$ (Table 6.2) and D_L^2 in $[m]$ (listed in Table 6.1). Here we use two transitions of both the mid- and high-J CO transitions to help prevent noise or a non-detection of one of these lines from dominating α . We define the three classes as:

- Class I: $\alpha < 0.34$
- Class II: $0.34 < \alpha < 0.66$
- Class III: $\alpha > 0.66$

The definition of the classes is quantitatively arbitrary, but chosen to reflect similarities in the spectral line energy distributions, which is illustrated in Figure 6.4. We have linearly interpolated the fluxes for those transitions where we do not have observations. In the case that we do not observe any of the low-J transitions, we do not plot any low-J fluxes. The parameter α is based on the ratio of two high-J CO lines to two mid-J CO lines, which essentially defines the drop-off slope of the CO ladder from J=5-4. Thus, the steepest drop-offs are in Class I, while the flattest ladders are in Class III. Class II consists of objects that peak around J=6-5, but do not fall off as steeply as those of Class I. Our three example galaxies were selected to fit into these categories, with NGC 7552 as a Class I, Mrk 331 as a Class II, and IRAS F170207-0014 as a Class III object.

We note that the CO ladders for many Class II and III objects have been published. In the case of all of these sources, heating mechanisms besides UV heating are required to explain the high-J CO emission, when also considering additional constraints. Arp 220 (Rangwala et al. 2011), Arp 299 (Rosenberg et al. in press), NGC 253 (Rosenberg et al. 2014), and NGC 6240 (Meijerink et al. 2013) require mechanical heating to reproduce the high-J CO lines, while Mrk 231 (van der Werf et al. 2010a) and NGC 1068 (Spinoglio et al. 2012) require X-rays to directly heat the gas in order to reproduce the observed molecular emission. This trend suggests that when dealing with highly excited CO ladders, such as in Class II and especially Class III objects, there is an additional heating mechanism necessary to explain the observed molecular emission. We will explore this issue for the full sample in the next section.

6.4 Analysis

We will combine our PACS and SPIRE observations of all the major neutral gas cooling lines ([OI], [CI], [CII], and CO), with ancillary data obtained as part of The Great Observatories All-Sky LIRG Survey (GOALS) (Armus et al. 2009), including the major PDR coolant [SiII] at $34.8\mu m$. We will not be dealing with any

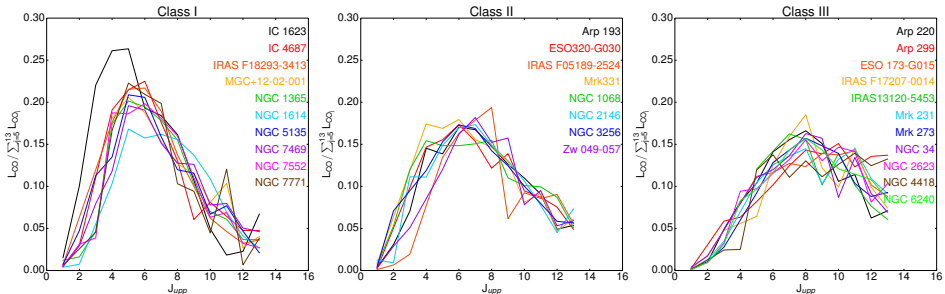


Figure 6.4: CO spectral line energy distributions for the full HerCULES sample divided into three classes. Class I (left panel) includes galaxies with $\alpha < 0.34$, Class II (center panel) is where $0.34 < \alpha < 0.66$, and Class III (right panel) is where $0.66 > \alpha$, α is defined in Eq. 6.1 in Section 6.3.2. Where we do not have line transitions, we have linearly interpolated between the neighboring transitions. If we lack all three ground based transitions, we do not plot any low-J fluxes.

ionized gas coolants such as [NII], [OIII]. We use the IRAS definition of the far infrared flux (FIR) as $\text{FIR} = 1.26 \times 10^{-14} (2.58 S_{60\mu\text{m}} + S_{100\mu\text{m}}) [\text{W m}^{-2}]$, where S_ν is in units of Jansky [Jy] (Helou et al. 1985). We then use the luminosity distances (D_L), from Armus et al. (2009), to define the far infrared luminosity (L_{FIR}), making our calculations directly comparable to Stierwalt et al. (2013). When we refer to the CO flux, we use the sum of the line fluxes from CO J=4-3 through J=13-12.

6.4.1 Warm gas tracers

In the local universe, the ratio of IRAS 60/100 μm flux densities correlates with infrared luminosity (e.g., Dale et al. 2001). It is of interest to determine whether the IRAS 60/100 μm ratio or L_{FIR} correlates better with the degree of CO excitation, as parametrized by α . Since α represents the slope of the CO ladder above J=5, it traces the relative brightness of high-J lines in comparison to mid-J lines, allowing a rough estimate of overall CO excitation. When α is small, the CO excitation is low and the CO SLED is declining from mid-J to high-J transitions and when α is large, the CO SLED is flattened and the excitation is high, indicating significant emission by warm and dense molecular gas. We compare the $S_{60\mu\text{m}}/S_{100\mu\text{m}}$ ratio from Sanders et al. (2003) and the L_{FIR} to the molecular gas excitation (α). In the left panel of Figure 6.5 the excitation (α) is plotted as a function of $S_{60\mu\text{m}}/S_{100\mu\text{m}}$, where each circular point is a galaxy in our sample. The best-fit power law is shown with a red dashed line. In the right panel, a similar correlation between L_{FIR} and α is shown, with the best-fit power law plotted with a red dashed line. We see

that although both panels show a positive trend, the correlation found with the $S_{60\mu m}/S_{100\mu m}$ ratio is tighter than that seen with the L_{FIR} . The molecular gas excitation to infrared color relation has a correlation coefficient of an $r=0.67$, while the excitation to L_{FIR} relation has a correlation coefficient of an $r=0.38$. Although the excitation to infrared color relationship is significantly correlated, there are three outliers (shown in red in the left panel of Figure 6.5), IC 1623, IC 4687, and NGC 1614. We also select the three farthest outliers, based on the Euclidean distance, in the α to L_{FIR} relation (IC 1623, IC 4678, and IRAS F18293--3413), also plotted as red points in the right panel. To test the strength of the correlations, we refit a power law excluding the three outliers in each plot, which are marked in red. The new best-fit is plotted as the blue solid line in Figure 6.5. Although the exclusion of these points does not result in a significant change in the best fit in either case, it does improve the correlation coefficients, resulting in a correlation coefficient of an $r=0.74$ for the molecular gas excitation to infrared color correlation, and an $r=0.56$ for the molecular gas excitation to L_{FIR} relation. Physically, this suggests that the presence of warm, dense molecular gas, is correlated with the presence of warm dust. It is, however, important to note that, once removing the outliers, the correlation between α and L_{FIR} is also significant, with a 1.6% probability of this relation being spurious. Further, since the IRAS 60/100 μm ratio is shown to correlate with L_{FIR} , these two quantities are likely related by underlying variables, making this correlation difficult to interpret. We note however that Lu et al. (2014) compared specific CO line transitions normalized by FIR and the IRAS 60/100 μm flux ratio. They find that as the CO gas becomes warmer, the 60/100 μm ratio also increases, which is in agreement with our results. Similarly, Díaz-Santos et al. (2013) show that the [CII] deficit is also better correlated to the IRAS 60/100 μm ratio than to the L_{FIR} .

6.4.2 Cooling budget

We can calculate the neutral gas cooling budget in each galaxy by summing the luminosities of the [OI], [CI], [SiII], [CII], and CO lines, since these are the main neutral gas coolants in the mid- and far-infrared regime. We take the [SiII] fluxes from Inami et al. (2013), which were observed with the *Spitzer* IRS instrument in the long wavelength, high resolution mode. In Figure 6.6, we present the percentage of cooling contributed by each emission line as a function of L_{FIR} . The percentage cooling for each species is calculated by comparing the luminosity of a species to the total summed luminosity of the [OI], [CI], [SiII], [CII], and CO lines. We exclude three galaxies based on their [OI]₆₃ profiles, Arp 220 that is fully in absorption, and NGC 4418 and Zw 049.057, which are both heavily absorbed and show inverse P-Cygni profiles (González-Alfonso et al. 2012). For

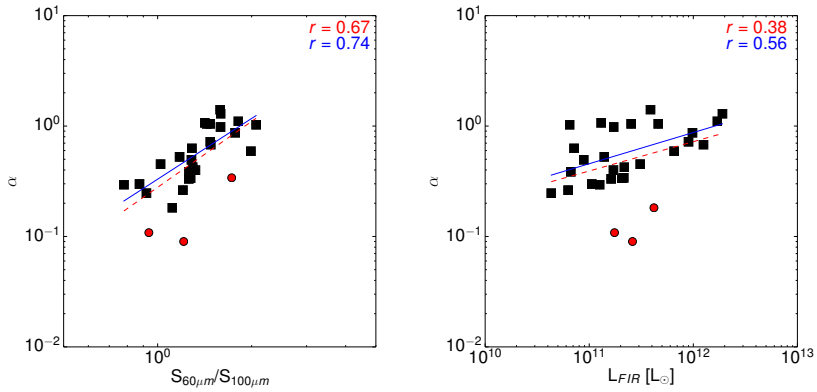


Figure 6.5: Left panel: The gas excitation (α , for a definition see Section 6.3.2) plotted against the IRAS infrared color ($S_{60\mu\text{m}}/S_{100\mu\text{m}}$), each square is a galaxy in our sample. The dashed line and top r value represents the least squares fit and correlation coefficient (r) for the full sample. The three circles represent the the most extreme outliers (largest Euclidean distance value) in the relation (IC 1623, IC 4678, and NGC 1614). The solid line and the bottom r value represent the best fit and correlation coefficient for the sample excluding the three most extreme outliers. Right panel: The same as the left panel but the gas excitation is plotted against the L_{FIR} , calculated in Section 6.4. The three outliers in this case are IC 1623, IC 4678, and IRAS F18293–3413.

each galaxy, the percent of cooling contributed by $[\text{C I}]_{609}$ and $[\text{C I}]_{370}$ is plotted as a yellow circle, $\text{CO } J=4-3$ through $J=13-12$ in red, $[\text{S i II}]$ in blue, and the combined cooling of $[\text{O I}]_{63\mu\text{m}}$, $[\text{O I}]_{145\mu\text{m}}$, and $[\text{C II}]$ is plotted in green. In the bottom panel of Figure 6.6, we separate the cooling contributions of $[\text{O I}]$ and $[\text{C II}]$. The solid lines show the mean percent-cooling for each emitting species. For example, the neutral atomic carbon is responsible for no more than 2% of the total cooling with an average cooling contribution of 1.5%, while CO contributes a mean of 10.8%, and $[\text{S i II}]$ contributes 24.2%. There are two galaxies with exceedingly high CO cooling percentages, namely IRAS F05189--2524 and Mrk 231, the two strongest AGN in the sample. Very high CO cooling percentages have also been noted in the massive Galactic star forming region W3 with 32% total gas cooling (Kramer et al. 2004), and even higher percentages in DR21 (Jakob et al. 2007). In both cases, the high CO percentage is attributed to self absorption of the $[\text{O I}]_{63}$ line, yet we calculate our fluxes both with the Gaussian and observed $[\text{O I}]_{63}$ line fluxes and see little change. The most efficient coolants are $[\text{O I}]$ and $[\text{C II}]$, which together provide a mean of 63.7% of the total gas cooling budget. Separating their cooling contributions, $[\text{C II}]$ provides a mean cooling percentage of 33.6% and $[\text{O I}]$ cools a mean of 30.1% of the gas. The mean cooling percentages and their standard deviations are shown in Table 6.4. Inspection of Figure 6.6 shows that the outliers are randomly distributed, and there is no clear trend of outliers as a function of L_{FIR} .

Table 6.4: Mean and standard deviation of percent cooling contribution.

Line	Mean	Std. Dev.
$[\text{C II}] + [\text{O I}]_{63+145}$	63.7	14.3
$[\text{C II}]$	33.6	9.1
$[\text{O I}]_{63+145}$	30.1	11.8
$[\text{S i II}]$	24.2	9.9
$\sum_{j=4}^{13} \text{CO}_j$	10.8	10.0
$\sum_{j=1}^2 [\text{C I}]_j$	1.5	0.9

It is interesting to note how constant each cooling range is as a function of L_{FIR} . It is a well known phenomenon that as far infrared luminosity increases, an apparent $[\text{C II}]$ deficit is observed in the local Universe (Malhotra et al. 2001; Luhman et al. 2003; Díaz-Santos et al. 2013), in terms of the $[\text{C II}]/\text{FIR}$ ratio. In addition, Graciá-Carpio et al. (2011) find a fine-structure line deficit in $[\text{N II}]$ and $[\text{O I}]$ as well. One corollary to this fine-structure line deficit is that other (molecular) coolants could become more efficient at higher L_{FIR} . However, as shown in Figure 6.6, the relative efficiencies of each coolant remain mostly constant. In or-

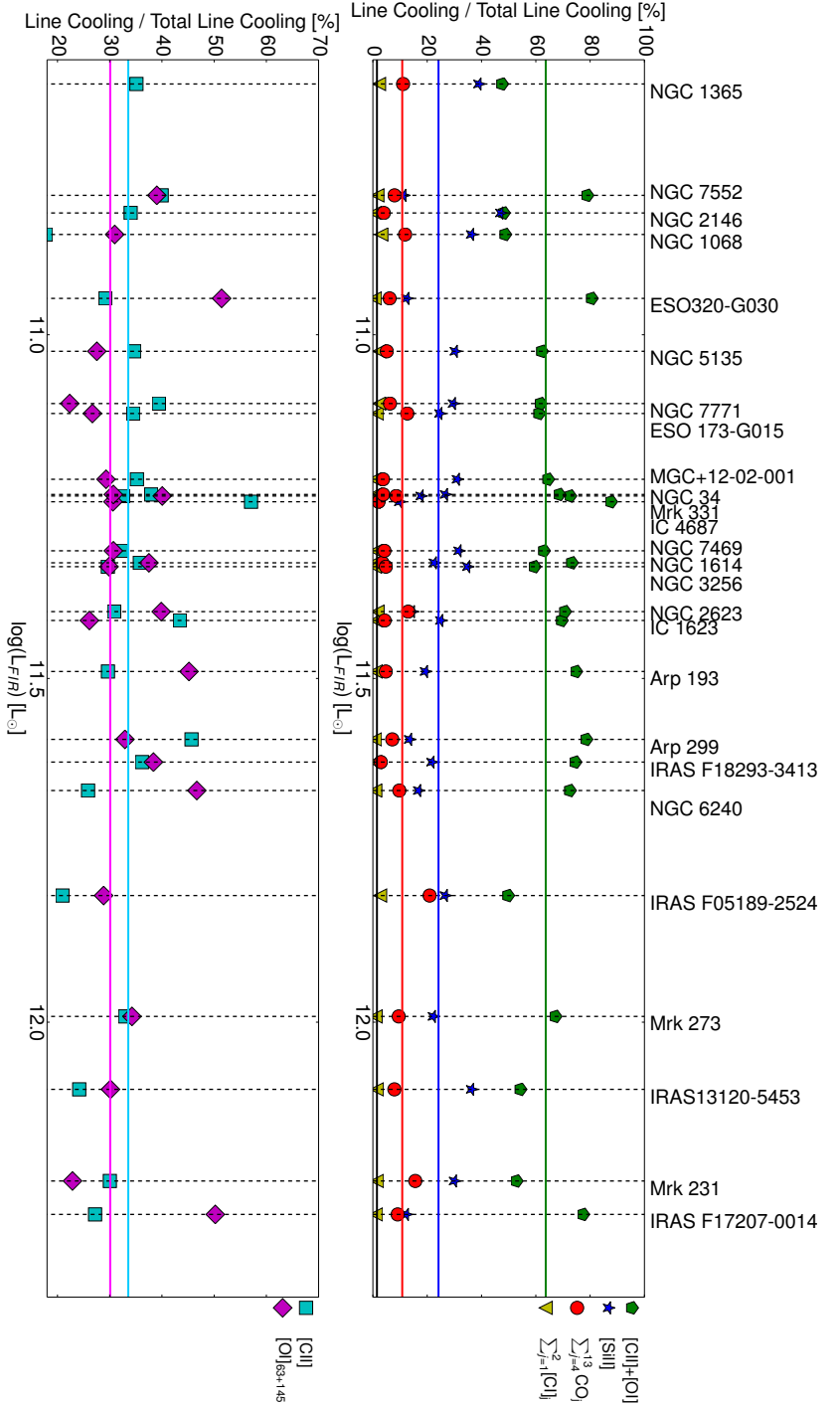


Figure 6.6: Top: Percentage of line cooling of the total gas cooling from each observed species as a function of L_{FIR} . Given are absolute, not cumulative percentages. The yellow triangles are the percentage of cooling from [CII]₆₀₉ and [CII]₃₇₀, the red circles are the cooling from CO ($4 \leq J_{\text{upper}} \leq 13$), the blue stars are the cooling from [SIII], and the green pentagons are from [OI]₃₊₁₄₅+ [CII]. The colored lines represent the mean cooling percentages for each coolant. We exclude galaxies that show [OI] in absorption (Arp 220), or show a complex line profile (NGC 4418 and Zw 049.057). **Bottom:** Same as top but separating the cooling contributions of [CII] (cyan squares) and [OI]₃₊₁₄₅ (magenta diamonds).

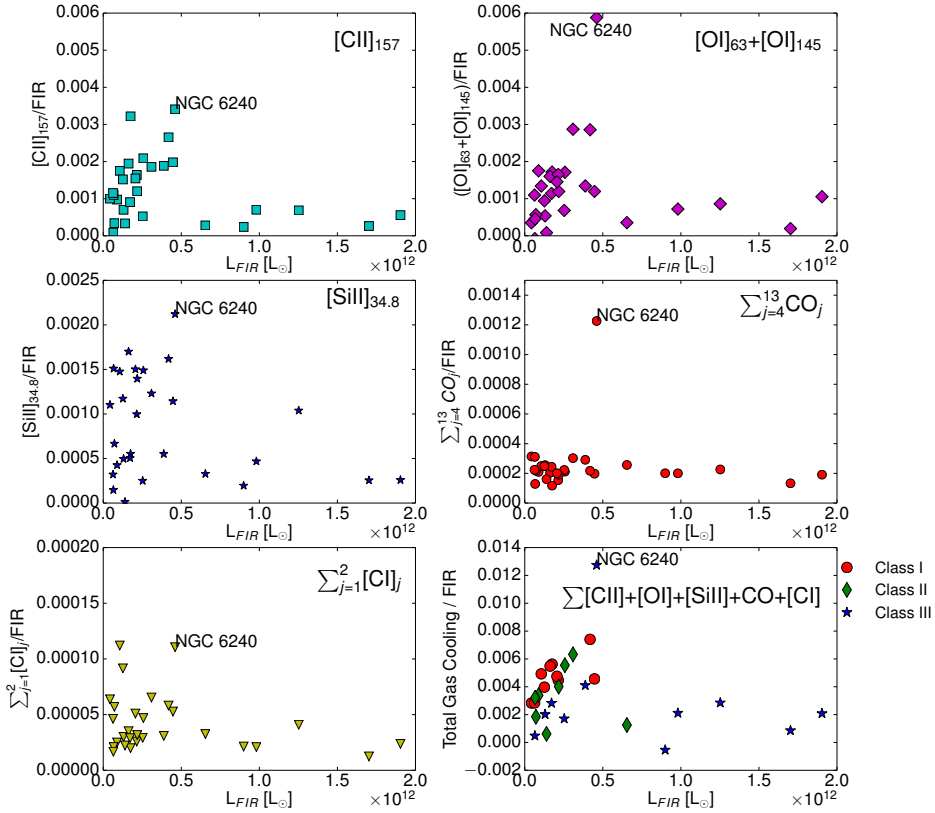


Figure 6.7: The ratio of line fluxes to far infrared flux (FIR) plotted as a function of far infrared luminosity (L_{FIR}) (both defined in Section 6.4) for [CII] (top left), [OI] (top right), [SIII] (middle left), CO (middle right), [CI] (bottom left), and the total cooling (bottom right). The L_{FIR} of each source was calculated using the method described in Section 6.4 and follows the definition of Helou et al. (1988). The [OI] flux is derived from the sum of [OI]₆₃ and [OI]₁₄₅, the CO flux is the sum of line transitions from J=4-3 to J=13-12, and the [CI] flux is the sum of [CI]₆₀₉ and [CI]₃₇₀. The total cooling refers to the total neutral gas cooling and includes all aforementioned fluxes. We exclude Arp 220, NGC 4418, and Zw 049.057 from the [OI] and total deficit plots, since we only observe these lines in full or partial absorption and can thus not get a flux estimate.

der to better understand this phenomenon, we plot the [CII] deficit ([CII] to FIR ratio), as a function of L_{FIR} in the top left corner of Figure 6.7. For comparison, we plot the same ratios but for the [OI]₆₃₊₁₄₅, [SiII], CO, and [CI] lines, where the CO lines encompass all transitions $4 \leq J_{\text{upper}} \leq 13$ and [CI] is the sum of both [CI]₆₀₉ and [CI]₃₇₀. We see a clear deficit in [CII], agreeing with the observations from Díaz-Santos et al. (2013). Since our sample spans a smaller luminosity range than Díaz-Santos et al. (2013), our deficit only spans a factor of 2 in the [CII]/FIR ratio, while in the GOALS sample, it spans an order of magnitude. Thus, we plot the deficit in linear space and see clearly that the only points with a high [CII]/FIR ratio are those of lower L_{FIR} . We see a similar trend in [SiII] and [CI], where the latter has also been observed from ground based observatories (Gerin & Phillips 1998, 2000). The [OI] shows a tentative line deficit, which becomes clear when we include galaxies of higher IR luminosities Graciá-Carpio et al. (2011). Although we find evidence of line deficits in [CII], [OI], [SiII], and [CI], this deficit is not observed in CO, which shows a particularly flat distribution over L_{FIR} , further strengthening the results from Lu et al. (2014). In all panels, NGC 6240 is an extreme outlier, as was also noted in Lu et al. (2014).

The difference between the molecular and fine structure emission can be understood in terms of heating mechanisms. The fine structure lines are originating from regions that are heavily affected by UV photons, at the edges of PDRs. As shown in the PDR models from Kaufman et al. (1999), as the radiation field and density increase, the fine structure line emission is expected to weaken compared to the far infrared flux. However, this does not apply for the molecular gas (CO), where we see no line deficit. This result may not be surprising since CO traces the molecular gas deeper in molecular clouds, where the UV field is significantly attenuated. We can test the gas versus dust cooling efficiency by plotting the ratio of the total gas cooling to the far infrared flux as a function of L_{FIR} , which is shown in the bottom right panel of Figure 6.7. Here, it is clear that the trend is decreasing in a very similar manner to that of the fine structure lines. Therefore, we can say that the fine structure line deficit is actually a gas cooling deficit in comparison to the FIR flux that is a result of UV heating becoming a more efficient coolant of dust in exceedingly extreme environments. It is critical to note that the fine structure line fluxes are not decreasing in absolute flux, but their relative contribution in comparison to the warm dust (measured with the FIR flux) is decreasing, due to the warm dust becoming increasingly efficient at a faster rate than the gas coolants.

However, if the neutral gas cooling efficiency is decreasing, and we observe a line deficit in all species except for CO, then we would expect the percentage of CO cooling to increase slightly as a function of L_{FIR} , to compensate for the decreasing fine structure line cooling efficiency. We do see a slight increase in the percentage

of CO cooling, but the trend is tentative and within the general scatter of the other CO cooling percentages. In addition, the galaxies with high L_{FIR} have flatter CO ladders, meaning there is non-negligible flux in high-J ($J > 13$) transitions, that we do not account for in our cooling budget. This missed high-J flux would increase the CO cooling percentage, and could make the CO cooling budget increase for higher luminosity sources. Since we only have four galaxies in our sample within the range that we would expect to see an elevated CO cooling percentage, we would need to increase our sample size in the high luminosity regime to determine if this trend is real.

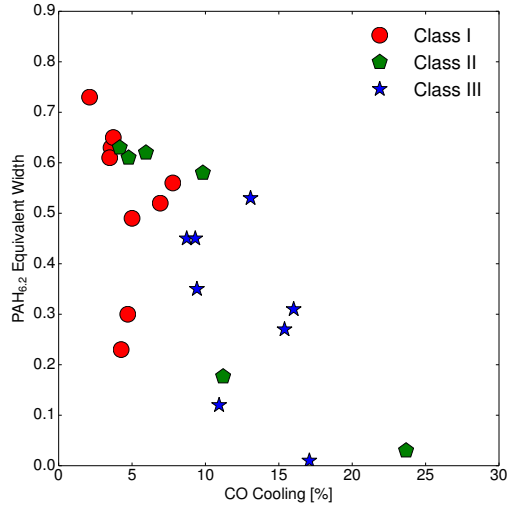
These results have several implications. Firstly, it is unlikely that the [CII] line deficit could be caused by high dust opacities at $158 \mu\text{m}$, since the line deficit is also observed in lines of much longer wavelengths, notably the [CI] line. Similarly, the line deficits are not likely caused by the line being optically thick, since the deficit is also observed in the optically thin [CI] lines, which agrees with the results of Díaz-Santos et al. (2013). A likely explanation is star formation dominated by ultracompact HII regions, which would suppress all fine-structure lines due to an increase of dust competition for UV photons. This is further supported by the fact that the total gas cooling ($[\text{CII}]+[\text{OI}]+\text{CO}+[\text{CI}]$) decreases as a function of L_{FIR} , meaning that dust becomes an even more efficient coolant as the infrared luminosity increases. Since high- z galaxies often have high L_{FIR} , this would place them in the high density regime, which would further drive star formation, since the star formation rate is proportional to the amount of dense gas (e.g., Gao & Solomon 2004).

The lack of a strong CO-line deficit shows that the bulk of the molecular gas heating is not affected by the mechanism suppressing the fine structure lines. This is interesting, since in a UV-photon heated environment, suppressing the UV field implies a reduced heating rate, and therefore also a lack of warm molecular gas might be expected. We also note that the integrated CO luminosity, that represents 10s of percent of the total gas cooling, is much more than what is predicted by any pure PDR model, which give a CO cooling fraction of at most a few percent of the total gas cooling (e.g., Meijerink et al. 2011). This result suggests that the CO luminosity may be powered by a different heating mechanism, which does not lead to dissociation or ionization.

6.4.3 Heating Mechanisms

The CO molecule can be heated indirectly through the photoelectric effect by ultraviolet (UV) photons, or by fast electrons from directly ionized H and H_2 by X-rays, cosmic rays (Meijerink & Spaans 2005), or mechanical processes, which includes shocks and turbulence. X-rays heat gas by ionizing H and H_2 directly,

Figure 6.8: The PAH 6.2 μm equivalent width from the Spitzer IRS (Stierwalt et al. 2013) as a function of percentage of CO cooling, as calculated in Section 6.4.2. Each galaxy is shape-coded by class, a circle is Class I, a pentagon is Class II, and a star is Class III. In addition, we exclude Arp 220, NGC 4418, and Zw 049.057 since their [O I] profiles are fully in absorption or show a complex line profile, making our CO cooling percentage inaccurate. Finally, we exclude NGC 1365 since it is extended and we do not capture all of the CO emission in one SPIRE pointing, affecting the accuracy of our CO cooling percentage.



and these fast electrons then thermalize the molecular gas with an efficiency of 10%. UV photons ionize PAHs and dust grains, and the resulting free electrons heat the molecular gas with a net efficiency of 1-3%. In addition, the chemistry in an XDR is driven by X-ray photons instead of FUV photons that are able to penetrate further into the cloud without efficiently heating the dust at the same time. These X-rays are mostly produced by active galactic nuclei (AGN) or in areas of extreme massive star formation. Cosmic rays can also heat the gas by penetrating into cloud centers, similarly to X-rays, and are typically produced by supernovae. Mechanical heating is another efficient source of gas heating. This is commonly attributed to turbulence in the ISM, which may be driven by supernovae, strong stellar winds, jets, galaxy mergers, cloud-cloud shocks, shear in the gaseous disk, or outflows.

To investigate the main mechanism heating the molecular gas, we use another diagnostic molecule, namely polycyclic aromatic hydrocarbons (PAHs). PAHs are carbonaceous, nanometer sized macromolecules that contain 50-100 carbon atoms with an abundance of 10^{-7} per hydrogen atom (Tielens 2008b). The absorption of one far-UV photon is enough to heat the PAH molecule to a high temperature and will cause this molecule to emit in the characteristic bands at 3.3, 6.2, 7.7, 8.6, and 11.2 μm (Tielens 2008b, and references therein). Because PAHs are only fluorescently excited, and are easily destroyed by more energetic radiation, they are ideal tracers of UV heating. Thus, we can use the equivalent width of the 6.2 μm feature from the *Spitzer* Space Telescope (Stierwalt et al. 2013), as

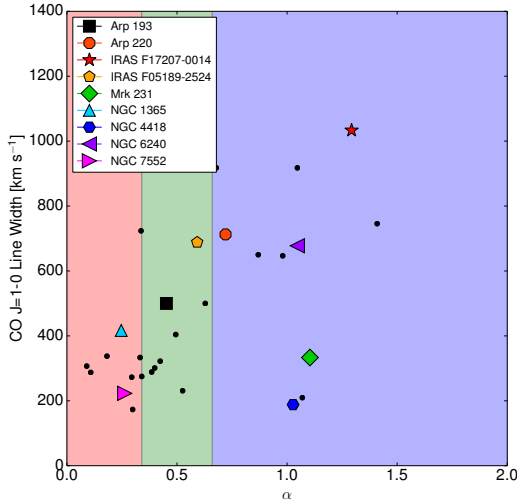


Figure 6.9: CO J=1-0 linewidth (FWHM) in km s^{-1} plotted against α (Eq. 6.1). The different classes are highlighted with different background colors, red is Class I, green is Class II, blue is Class III. Most sample galaxies are plotted with black dots, but some of those specifically mentioned in the discussion are highlighted. This also includes the three targets addressed in Figures 1-3.

a proxy for the UV energy density. In Figure 6.8, we compare the PAH equivalent width to the percentage of the total gas cooling done by CO, as calculated in Section 6.4.2. Class I objects have the steepest decreasing CO SLED, high PAH equivalent widths (EW), and low percentages of CO cooling. On the other hand, Class II and Class III objects with high percentages of CO cooling have low PAH equivalent widths. We note that the two objects with very low PAH equivalent widths are the most AGN-dominated objects in our sample (Mrk 231 and IRAS F05189--2524), where PAH destruction by X-rays and nuclear hot dust combine to strongly lower the PAH equivalent width. The high CO cooling fractions of these objects can likewise be attributed to energy input by the AGN (through X-ray heating or mechanical energy input from an AGN-driven outflow). These trends reinforce the idea that in objects with the high CO cooling fraction, the CO is efficiently excited by something besides UV photons.

We now compare our α parameter with the CO J=1-0 linewidth for the sources in our sample (Figure 6.9). We correct the linewidth for inclination such that all galaxies are effectively turned edge on using the K-band axis ratio from 2MASS, with the exception of Arp 220 and NGC 6240. For Arp 220 we used the inclination derived by Scoville et al. (1997) using arcsecond imaging of CO J=1-0 and for NGC 6240 we used the inclination derived by Engel et al. (2010) using sub-arcsecond near-infrared imaging. The range of Class I objects is highlighted with a red, Class II with a green, and Class III with a blue background.

The linewidths are dominated by rotation, and therefore depend mostly on

the mass in the nuclear regions of our targeted galaxies. Merging and interaction, molecular outflows, and random motions may all play a role in increasing the linewidths, but are not expected to dominate the linewidths of our target sources. Therefore, Figure 6.9 shows that higher levels of excitation occur in more massive host galaxies, assuming the velocities are attributed to regular rotation. However, the inclination-corrected linewidths also correlate with the amount of mechanical energy that is available in the molecular gas component associated with the galaxy nucleus. If the fraction of mechanical energy that is converted into heating the molecular gas was constant, then the high linewidth galaxies in Figure 6.9 could be attributed to mechanical heating. However, establishing this result would require a detailed study of the velocity fields of the molecular gas in all of our targets. Since such data is not available, all we suggest is that the linewidth provides an estimate of the available reservoir of mechanical energy, but we remain agnostic as to the extent that this reservoir is actually tapped.

Inspecting Figure 6.9 with these considerations in mind, the fact that low-excitation galaxies all have the smallest linewidths, while high-excitation galaxies have a range of linewidths has an attractive physical interpretation. In high excitation galaxies with high linewidths, mechanical energy input is a viable source of excitation, while in high excitation galaxies with low linewidths, radiative energy input may be more important. Indeed, in Fig. 10, the lowest linewidths among high excitation galaxies are found in Mrk 231 and NGC 4418 (an exposed and an obscured AGN, respectively).

Class I and II objects with low linewidths are likely dominated by UV heating, since their CO ladders turn around somewhere before $J=7-6$. For comparison, we have highlighted the position of our three example galaxies, NGC 7552 (Class I), Mrk 331 (Class II), and IRAS F1207-0014 (Class III), as well as some of the more famous galaxies in our sample. The major merger galaxies NGC 6240 and Arp 220 have high α values and linewidths around 650 km/s. On the other hand, the strongest AGN in our sample, Mrk 231, lies in the low linewidth region of Class III, suggesting that its gas is radiatively heated, likely by X-rays from the AGN. This confirms the results of van der Werf et al. (2010a), where they find the high- J CO excitation to be caused by an XDR. The other two galaxies with AGN contribution are NGC 1068 and IRAS F05189--2524, both of which are Class II objects that lie in the low linewidth region, suggesting that they are also radiatively excited. However, since both of these objects lie in Class II (albeit on the border between Class II and III), it is unclear whether their excitation is from UV, higher energy photons, or cosmic rays. Both NGC 1068 and IRAS F05189--2524 have also been studied in detail by Spinoglio et al. (2012) and Pereira-Santaella et al. (2014) respectively. For NGC 1068, Spinoglio et al. (2012) and Garcia-Burillo

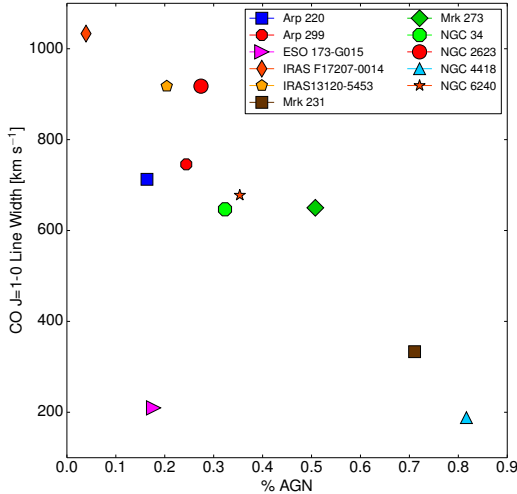


Figure 6.10: The AGN contribution of the bolometric luminosity compared to the CO J=1-0 inclination corrected linewidth for Class III galaxies along with the Class II template galaxies presented in Figure 6.9.

et al. (2014) find that indeed, the excitation is due to either XDRs (in the circumnuclear disk) or PDRs (in the star-forming ring), which agree with our results. In IRAS F05189--2524, Pereira-Santaella et al. (2014) find that there is a large contribution from mechanical heating in this source, as traced by a shallow H₂ temperature distribution, yet they cannot rule out the AGN as an important heating source for the molecular gas.

In order to examine this method vis-a-vis the role of AGNs and to determine additional heating sources, and to check if there are any underlying biases in the J=1-0 linewidth, we can compare the inclination corrected linewidths with the percentage AGN contribution for each galaxy. The AGN contribution can be estimated using both the 15/30 μm flux density ratio (f_{15}/f_{30}) and the [NeV]/[NeII] ratio along with the prescriptions from Veilleux et al. (2009). We take the f_{15}/f_{30} ratio from Stierwalt et al. (2013) and the [NeV]/[NeII] ratio from Inami et al. (2013). We average the results of the AGN contribution from both methods and find average AGN contributions ranging from 0-95% of the bolometric luminosity. For the high excitation sources (Class II and Class III), we use the average AGN contribution in combination with the inclination corrected linewidth to separate mechanical heating from AGN heating. In Figure 6.10, we plot the AGN contribution on the x-axis and the inclination corrected CO J=1-0 linewidth along the y-axis. This scatter plot shows that for our high-excitation galaxies, very high linewidths are not associated with high AGN contributions and conversely the galaxies with high AGN contributions do not display high linewidths.

For example, we can compare Arp 220 and Mrk 231. Both galaxies have high α values, but Arp 220 has a high linewidth and a low AGN contribution, while Mrk 231 has a low linewidth and a high AGN contribution. Comparing NGC 6240 and Arp 220 reveals that although both have high linewidths and α values, NGC 6240 also has a high AGN contribution. This suggests that both the AGN and mechanical processes are contributing to heating the gas in NGC 6240.

It is difficult to conclude anything definitive about objects that show average or typical values of α or linewidths. It is also important to note that although there is a non-negligible contribution of heating from mechanical processes or the AGN in Class III galaxies, the gas is still mostly heated through UV heating processes. We caution the use of any two of these diagnostics alone, since for example, a Class III object with a low linewidth may still be mechanically heated by small-scale turbulence that would not produce an observable line broadening effect. In this case, the AGN contribution would be low, but the α would be high, discounting AGN heating. Using all three parameters simultaneously renders a qualitative estimate of which additional processes are exciting the warmest molecular gas.

6.5 Conclusion

We report the initial results of the Herschel Open Time Key Project Herschel Comprehensive (U)LIRG Survey (HerCULES). Both *Herschel*/SPIRE spectra and *Herschel*/PACS [OI]63, [OI]145 and [CII] line profiles of a sample of 29 galaxies spanning an order of magnitude of infrared luminosity were analyzed. Our main results are summarized below:

- Luminous galaxies can be separated into three classes based on the parameter α , which we define as the ratio of the high-J to mid-J CO transitions.

$$\alpha = L_{CO_{J=12-11}} + L_{CO_{J=13-12}}/L_{CO_{J=5-4}} + L_{CO_{J=6-5}}$$

Class I ($\alpha < 0.34$) is characterized with a CO SLED peak around J=5 and a steep decline towards higher J transitions. Class II ($0.34 < \alpha < 0.66$) has a CO SLED peak around J=7-6 and a shallower decline towards higher J transitions. Class III ($\alpha > 0.66$) show very flat CO ladders. We present the spectra of three example galaxies for each of these three categories.

- We find that molecular gas excitation (approximated by α) is well correlated with the infrared color (as traced by S_{60}/S_{100}), and not as well correlated with the L_{FIR} .
- The cooling budgets of the galaxies are presented. We find that the percentage of cooling from each species ([CI], CO, [CII], [SiII], and [OI]) appears

to be constant over the full range of L_{FIR} . There is indication of a slight increase in the percentage of CO cooling at higher L_{FIR} .

- We detect [CII], [SiII], and [CI] deficits (i.e., the [CII]/FIR ratio decreases with L_{FIR}), and also a weak [OI] deficit for the high luminosity galaxies. On the other hand, we observe no CO deficit, the CO/FIR ratio is very constant for all L_{FIR} . Thus, the fine structure line deficits reflect a decrease in the total gas heating efficiency with increasing L_{FIR} . The fact that we observe a deficit in all fine structure lines but not in the molecular gas suggests that the mechanism responsible for heating the [CII], [OI], [SiII], and [CI], is not the same mechanism responsible for heating the CO. The CO may instead be affected by a heating mechanism that is immune to this deficit.
- Using the PAH 6.2 μm equivalent width as a proxy for the importance of massive star formation and therefore UV excitation, we find that when the cooling efficiency of CO is high, the amount of UV heating is low. This again indicates that CO is more efficiently heated by another mechanism.
- We suggest a qualitative schematic based on α , the CO J=1-0 linewidth, and the AGN contribution, that helps indicate which additional mechanism, if any, is heating the gas. Class I galaxies with a low α ($\alpha < 0.34$) do not require any heating in addition to UV-heating to explain the observations. Class III galaxies with high linewidths and low AGN contributions probably require mechanical, in addition to UV heating. Class III galaxies with narrow linewidths and large AGN contributions are experiencing excitation from harder radiation (X-rays or cosmic rays). Class III objects with wide linewidths and high AGN contributions are composite galaxies that are being heated by both mechanical processes and the AGN. For the objects that have median α , linewidth, or AGN contribution values, such as many Class II objects, it is not possible to discriminate which heating mechanisms are affecting the gas without additional information.

6.6 Acknowledgments

We would like to thank Edward Polehampton for his help reducing the SPIRE observations. SPIRE has been developed by a consortium of institutes led by Cardiff Univ. (UK) and including: Univ. Lethbridge (Canada); NAOC (China); CEA, LAM (France); IFSI, Univ. Padua (Italy); IAC (Spain); Stockholm Observatory (Sweden); Imperial College London, RAL, UCL-MSSL, UKATC, Univ. Sussex (UK); and Caltech, JPL, NHSC, Univ. Colorado (USA). This development has been supported by national funding

agencies: CSA (Canada); NAOJ (China); CEA, CNES, CNRS (France); ASI (Italy); MCINN (Spain); SNSB (Sweden); STFC, UKSA (UK); and NASA (USA).

7 | Outlook

In this thesis, I have studied the extreme environment of galaxy centers by understanding the conditions of the molecular gas, that act as the fuel for star formation. The fundamentals of star formation can be understood as a balance between the available molecular gas supply and feedback processes. By observing transitions of molecular and atomic species, we have determined the mechanisms that are heating the gas, the gas density, radiation environment, and mass. We first focus on an isolated typical starburst galaxy, NGC 253. We use various near- and mid-infrared diagnostic emission lines to determine whether the H_2 gas is being fluorescently or shock excited. Then, since the near-infrared H_2 lines represent only the hottest molecular gas at the very edge of clouds, we study the CO in NGC 253 to see which mechanism is exciting the bulk of the molecular gas. In both cases, we find about 30% of the molecular gas must be heated by mechanical processes. This means that the other 70% of the gas is being heated by UV photons, thus UV heating remains the dominant heating mechanism. However, unlike the previous idea that UV heating is the only important mechanism for heating the gas, we find that we cannot explain the atomic and molecular emission without including mechanical heating. In general, this suggests that PDR models employing only UV heating can account for the bulk of the molecular gas mass, but when discussing the most excited molecular gas, it is necessary to include mechanical processes.

We then expand the study to a more luminous interacting galaxy group, Arp 299, in order to test which mechanisms are dominant in a more complex and extreme environment. Arp 299 is an ongoing merger, one nucleus harbors an AGN and one nucleus harbors a powerful starburst. We find that the AGN nucleus also requires mechanical heating, and although it harbors an AGN, there is no significant heating contribution from X-rays. On the other hand, the starburst nucleus is purely radiatively excited. Finally, we use a statistically complete sample of (U)LIRGs to study the gas excitation on a larger luminosity scale. We present a diagnostic diagram that attempts to separate heating mechanisms based on the ro-

tational CO transitions, the linewidth of the CO J=1-0 line, and the contribution of the AGN to the total bolometric luminosity. Again, the results of this sample suggest that in any galaxy with an excited CO ladder, an additional heating source is required to explain the high-J CO emission (the flattened CO ladder). In many cases, the additional source is mechanical heating, yet in the case of strong AGNs, X-ray heating can become an important heating source. By using a combination of diagnostics, it is possible to discern what additional heating is needed. It is important to keep in mind that although additional heating is necessary, it still only represents a minority of the gas heating, the majority of gas is heated through UV processes.

7.1 Heating Mechanisms

The overarching question of this thesis is what is heating the molecular, star-forming gas in the extreme environments of starburst nuclei. We know that in these regions we are potentially dealing with a multitude of excitation mechanisms: UV radiation, X-ray radiation, cosmic rays, turbulence, outflows, shocks, etc. We also know that all of these *can* play a role in heating molecular gas. The new results from *Herschel* have found that in most starburst and (U)LIRG systems, UV heating alone is not enough to excite the gas. Although the ^{12}CO emission can be fit by many emission models, even pure PDR models with only UV heating, the inclusion of additional constraints from other molecules or dust emission strongly suggest UV heating is not the sole mechanism. This begs the question: which other mechanisms are responsible for the highly excited molecular gas? Is it always the same mechanism, or does it simply depend on the type of galaxy? From the studies in this thesis, it appears that mechanical heating is the only mechanism that can account for the emission of all the observed molecules, even in Arp 299 A which has a confirmed AGN. Similarly NGC 1068, NGC 6240, and Arp 220 which each harbor AGN, all show signs of mechanical heating. Mrk 231 is the strongest AGN in the HerCULES sample, and although it has a very high ($\sim 70\%$) AGN contribution to the bolometric luminosity, the molecular gas is better fit using mechanically heated models than XDR models. In the case of confirmed AGN, why don't the X-rays play a larger role in heating the gas? One possibility is that they are heating the gas, but only a small amount that is directly surrounding the AGN. The physical beam size for Arp 299 A is 8.7 kpc, thus we are taking the beam-averaged emission from the entire region, and the small area around the AGN is likely averaged out. Schleicher et al. (2010) estimate the influence sphere of an XDR region surrounding a $10^7 M_{\odot}$ black hole using the cross section of helium and hydrogen. They find the XDR to be effective up to 100 pc, yet since they only use the

helium and hydrogen cross sections, we expect this number to be even smaller if other molecules are considered. In addition, radiative processes including UV, X-ray, and cosmic ray heating all decrease in intensity as a function of r^{-2} from the emitting source, where mechanical heating can permeate the ISM without being absorbed. Therefore, it would require the spatial resolution of ALMA to truly resolve the XDR heated region around the AGN. An ALMA observation of HCN and HNC in the nucleus of an AGN would allow for the determination of XDR and PDR heating.

Similarly to X-rays, cosmic rays do not appear to be a dominant heating source. Even with a cosmic ray ionization rate of 1000 times the Milky Way value, the cosmic rays contribute less than 1% of the total gas heating at $A_V=5$. This is due to the fact that the cosmic ray heating rate is determined only by the ionization rate and the volume density of H_2 (Tielens & Hollenbach 1985). Therefore, the heating rate of cosmic rays stays constant once the H is all converted into H_2 . Only in the case of pure UV heating (no mechanical component) would the cosmic rays eventually dominate the heating, since the UV flux drops off quickly as the column density increases. If mechanical heating was included, it would continue to dominate the cosmic ray heating, since the mechanical heating is not affected by cloud depth. Thus, cosmic ray heating could play a role in heating the very cores of high column density clouds in regions free of mechanical heating. However, using the observed ^{12}CO to ^{13}CO ratio, we determine the column density of the average observed molecular clouds to be around $A_V=5$. In a cloud this small, the surface heating of the PDR is still strong, meaning the cloud is not deep enough for cosmic rays to dominate over UV heating. We expect a cloud of $A_V > 15$, with an enhanced cosmic ray ionization rate and no mechanical heating to be dominated by cosmic ray heating. Yet in the extreme environments of (U)LIRGs, mechanical heating is often required, thus always overpowering the effect of cosmic rays.

Although additional heating is necessary to explain the observed emission, UV heating is still the dominant heating source. Even in the case of NGC 253, where all ISM phases require mechanical heating, UV heating represents 75% of the total gas heating. It is interesting to discover which mechanism is responsible for heating the highest excitation gas, yet it is still the UV heating that is the dominant mechanism. This suggests that it is the star-formation itself that is driving the excitation of the molecular gas, and perhaps also driving the source of the mechanical heating. Figure 7.1 is a scheme of when specific heating mechanisms are applicable, their sources, and to what extent they are able to heat the gas.

	Source	Location	Size
PDR	Star formation Far UV photons	Edge of molecular clouds Galaxy disks	$A_V < 5$
XDR	AGN Starbursts Soft X-rays	Galaxy nuclei Starbursts	$r < 100$ pc
CDR	Supernovae Supernova Remnants (SNR)	Around SNR Starbursts	$A_V > 30$
Mechanical Heating	Shocks Mergers Outflows Turbulence Stellar winds	Galaxy centers Starbursts Everywhere?	$A_V > 3$

Figure 7.1: Schematic view of the dominant molecular gas heating mechanisms; UV heating (PDR), X-ray heating (XDR), cosmic ray heating (CDR), and mechanical heating. The first column presents the source of the heating, the second column outlines the location that this heating takes place, and the third column shows the size of the affected region.

7.2 Mechanical Heating

Since mechanical heating is required to explain the observed molecular emission, it is crucial to understand empirically what this actually means. The way mechanical heating is added to the models is by including a constant additional heating term into the thermal balance equations. This heating term is calculated as some percentage of the UV heating at the surface of the PDR, the lowest amount being 0.1% of the initial UV heating. The inclusion of mechanical heating has the attractive benefit of being able to explain the emission of many molecules including ^{12}CO , ^{13}CO , HCN, and HNC thus far. As discussed in the introduction, in all current emission models (PDR and XDR), the biggest difficulty is that models cannot reproduce the bright [CI] observed in galaxies. It is still unknown if mechanical heating models solve the [CI] under-production problem, yet this could be a strong piece of evidence in support of mechanical heating.

One critical restriction to what we call 'mechanical heating' is that we implement it more honestly as simply additional heating. We apply a heating plateau evenly throughout the PDR, and it seems to account for all the previous problems. We add no underlying physics, and to that end, have no specific shock or turbulence driven chemistry. Including actual mechanical processes to create mechanical heating is currently being implemented in models (Kazandjian et al. in prep.), but is still in the experimental phase. The physical interpretation of this additional heating is that it is mechanical, since it can increase the temperature of the gas while not affecting the chemistry. However, it could be equally possible that there is another element that we are missing, that is causing our PDRs to consistently underestimate the amount of heating available. One other possibility is that PDRs have an inherent pressure gradient, where the high density molecules are at the highest pressures and the atoms are at lower pressures. This gradient, along with the power of the ionization source, would cause this PDR to continually evaporate. This turbulent motion of evaporation could also account for the additional heating needed to reproduce the emission (Joblin & Tielens 2013).

Since we have not yet identified the source of mechanical heating, we cannot know if the simple approach of an additional heating term is a reasonable approximation. If the source of the mechanical heating is some widespread turbulence, then this approximation is not unreasonable. However, if it is shocks that are heating the gas, a much more in depth treatment of the chemistry is required. Again, using ALMA's spatial resolution, we can probe the areas where mechanical heating is dominant. If it is important equally throughout the whole galaxy center, then the current approximation is useful. If we see isolated regions of strongly mechanically heated gas, then we must treat this modeling more carefully.

7.3 Modeling ^{12}CO

As discussed at the end of Chapter 4, ^{12}CO is a very poor diagnostic molecule. It is bright, has many observable transitions, and is the second most abundant molecule in the Universe. However, it does not yield much quantitative information, only the proof that there is molecular gas present and some general indications about temperatures. By using models to recreate observations, we are essentially attempting reverse engineering the emission, even though the process is not directly reversible. For example, given a PDR with a specific density, temperature, and column density, there is only one possible solution for the molecular emission. But if we have only the molecular emission, and attempt to measure the density, temperature, and column density, there are multiple solutions that yield the same observed outcome. Therefore, it is critical for astronomers to understand the limitations of coming to quantitative conclusions from observations of ^{12}CO . Without isotopes such as ^{13}CO and C^{18}O to constrain column density, an accurate gas mass is unachievable. In addition, without the inclusion of specific tracer molecules to constrain density, such as (but not limited to) HCN, HNC, and HCO^+ , the mid- and high- excitation components are not constrained. Even when using these tracers, it is important to keep in mind that their chemistry is not always straight forward. For example, HCO^+ has a very complex abundance pattern that is highly dependent on column density (Meijerink et al. 2011). Many chemical models do not incorporate this complexity into their models. In general, it is also important to keep in mind that there are still large variations within PDR models themselves. During the conference 'Exciting CO in the Local and High-Redshift Universe' (Leiden, Netherlands 2012), all available PDR codes were tested, to determine the differences and try to create a benchmark to promote uniformity among the codes. Even at the end of this conference, different models produce CO ladders that vary greatly in the high-J regime, especially for high density PDRs.

The future study of molecular gas in extreme environments must be attacked from three different angles simultaneously. Firstly, observations will allow astronomers to formulate new questions about the gas emission, excitation, and chemistry. Secondly, the emission process needs to be studied further so that models are in agreement. Thirdly, the models need to be advanced, taken to two and three dimensions, and to implement mechanical heating using underlying physical mechanisms and shock chemistry. Future observations must focus on spatially resolving the complex chemistry of galaxy centers. For example, Takano et al. (2014) have already shown the strength of ALMA imaging in the center of NGC 1068, where the high HCO^+ to HCN ratio surrounding the AGN shows the direct affect of X-ray heating. In a similar manner, ALMA or other interferometer sub-millimeter arrays can

study mechanical heating, by using high spatial resolution maps of characteristic line ratios to determine if mechanical heating is isolated around shock sources, or more widespread through the galaxy center. In order to interpret the chemical ratios observed, it is critical to have emission models that agree with one another. Currently, the disparity in the models is due to poorly known chemical reaction rates, heating and cooling rates, and H_2 formation rates, among other factors. The differences in the models are most pronounced when dealing with high radiation fluxes, which are the most relevant models for galactic center environments. Thus, studying these rates will allow a realistic benchmark for all of the emission models. In the meantime, implementing mechanical heating in a physically and chemically accurate way is the next major step for emission models. Since mechanical heating involves kinematics, it is a logical next step to use two or three dimensional models to determine where the mechanical heating is strongest and how it permeates the ISM.

In summary, it is very difficult to measure the physical properties of molecular gas from observing the emission. Both the degeneracy inherent in reverse engineering emission and the inconsistency of the models themselves, make the task of probing the properties of the ISM extremely difficult. The inclusion of multiple molecular species along with the continued efforts to benchmark the PDR models are both necessary to improve our ability to use molecular emission as a diagnostic of the physical properties in the extreme environments of (U)LIRG and starburst nuclei. However, in-depth studies of the molecular ISM are just entering their golden age. The *Herschel Space Observatory* has completed its mission, and all observations are available on the *Herschel Science Archive*. The archive provides a wealth of unexplored data for nearby star forming galaxies. The *Herschel/PACS* instrument provides observations of the strongest gas cooling lines ([CII] and [OI]), while the *Herschel/SPIRE* instrument gives access to the full CO rotational ladder from $J=4-3$ to $J=13-12$. Together, we can begin to understand star formation in deeply obscured galactic nuclei. In addition, the Atacama Large Millimeter Array (ALMA) has begun science operations. This impressive interferometer will not only give a ground-based observation tool for the molecular lines, but allow for unprecedented spatial resolution. Instead of observing an entire galaxy as with *Herschel*, ALMA can resolve specific star forming regions within galaxy centers, which will greatly increase our understanding of star formation in these intense star-forming systems. ALMA will fuel the improvement of the current model and observational limitations and drive astronomers towards a uniform understanding of the star-forming gas in luminous galaxy centers.

Bibliography

- Aalto, S., Booth, R. S., Black, J. H., & Johansson, L. E. B. 1995a, *A&A*, 300, 369
Aalto, S., Booth, R. S., Black, J. H., & Johansson, L. E. B. 1995b, *A&A*, 300, 369
Aalto, S., Johansson, L. E. B., Booth, R. S., & Black, J. H. 1991, *A&A*, 249, 323
Aalto, S., Radford, S. J. E., Scoville, N. Z., & Sargent, A. I. 1997, *ApJL*, 475, L107
Abel, N. P., Dudley, C., Fischer, J., Satyapal, S., & van Hoof, P. A. M. 2009, *ApJ*, 701, 1147
Acero, F., Aharonian, F., Akhperjanian, A. G., et al. 2009, *Science*, 326, 1080
Albrecht, M., Krügel, E., & Chini, R. 2007, *A&A*, 462, 575
Alonso-Herrero, A., Engelbracht, C. W., Rieke, M. J., Rieke, G. H., & Quillen, A. C. 2001, *ApJ*, 546, 952
Alonso-Herrero, A., Rieke, G. H., Colina, L., et al. 2009, *ApJ*, 697, 660
Alonso-Herrero, A., Rieke, G. H., Rieke, M. J., & Kelly, D. M. 2003, *AJ*, 125, 1210
Alonso-Herrero, A., Rieke, G. H., Rieke, M. J., & Scoville, N. Z. 2000, *ApJ*, 532, 845
Armus, L., Heckman, T., & Miley, G. 1987, *AJ*, 94, 831
Armus, L., Mazzarella, J. M., Evans, A. S., et al. 2009, *PASP*, 121, 559
Arp, H. 1981, *ApJS*, 46, 75
Awaki, H. & Koyama, K. 1993, *Advances in Space Research*, 13, 221
Bakes, E. L. O. & Tielens, A. G. G. M. 1994, *ApJ*, 427, 822
Ballo, L., Braitto, V., Della Ceca, R., et al. 2004, *ApJ*, 600, 634
Barnes, J. E. & Hernquist, L. 1992, *ARA&A*, 30, 705
Bendo, G. J., Wilson, C. D., Pohlen, M., et al. 2010, *A&A*, 518, L65
Berta, S., Magnelli, B., Nordon, R., et al. 2011, *A&A*, 532, A49
Beswick, R. J., Pedlar, A., Mundell, C. G., & Gallimore, J. F. 2001, *MNRAS*, 325, 151
Bevington, P. R. & Robinson, D. K. 1992, *Data reduction and error analysis for the physical sciences*
Black, J. H. & van Dishoeck, E. F. 1987, *ApJ*, 322, 412
Blitz, L. & Shu, F. H. 1980, *ApJ*, 238, 148
Bolatto, A. D., Warren, S. R., Leroy, A. K., et al. 2013, *Nature*, 499, 450
Bradford, C. M., Nikola, T., Stacey, G. J., et al. 2003, *ApJ*, 586, 891
Calzetti, D. 1997, *AJ*, 113, 162
Cappellari, M. & Copin, Y. 2003, *MNRAS*, 342, 345
Cappellari, M. & Emsellem, E. 2004, *PASP*, 116, 138
Caputi, K. I., Lagache, G., Yan, L., et al. 2007, *ApJ*, 660, 97

- Carral, P., Hollenbach, D. J., Lord, S. D., et al. 1994, *ApJ*, 423, 223
- Carral, P., Turner, J. L., & Ho, P. T. P. 1990, *ApJ*, 362, 434
- Condon, J. J. 1987, *ApJS*, 65, 485
- Condon, J. J. 1992, *ARA&A*, 30, 575
- Condon, J. J., Condon, M. A., Gisler, G., & Puschell, J. J. 1982, *ApJ*, 252, 102
- Condon, J. J. & Yin, Q. F. 1990, *ApJ*, 357, 97
- Corwin, Jr., H. G., Buta, R. J., & de Vaucouleurs, G. 1994, *AJ*, 108, 2128
- Dahlem, M., Bomans, D. J., & Will, J. 1994, *ApJ*, 432, 590
- Dale, D. A., Helou, G., Contursi, A., Silbermann, N. A., & Kolhatkar, S. 2001, *ApJ*, 549, 215
- Davidge, T. J. & Pritchett, C. J. 1990, *AJ*, 100, 102
- de Jong, T., Dalgarno, A., & Chu, S.-I. 1975, *ApJ*, 199, 69
- Della Ceca, R., Ballo, L., Tavecchio, F., et al. 2002, *ApJL*, 581, L9
- Demoulin, M. H. & Burbidge, E. M. 1970, *ApJ*, 159, 799
- Díaz-Santos, T., Armus, L., Charmandaris, V., et al. 2014, *ApJ*, 788, L17
- Díaz-Santos, T., Armus, L., Charmandaris, V., et al. 2013, *ApJ*, 774, 68
- Díaz-Santos, T., Charmandaris, V., Armus, L., et al. 2011, *ApJ*, 741, 32
- Dickman, R. L. 1975, *ApJ*, 202, 50
- Downes, D. & Solomon, P. M. 1998, *ApJ*, 507, 615
- Doyon, R., Wells, M., Wright, G. S., et al. 1994, *ApJ*, 437, L23
- Draine, B. T. 2003, *ARA&A*, 41, 241
- Draine, B. T. 2011, *Physics of the Interstellar and Intergalactic Medium*
- Draine, B. T. & Li, A. 2007, *ApJ*, 657, 810
- Dunne, L. & Eales, S. A. 2001, *MNRAS*, 327, 697
- Eales, S. A., Becklin, E. E., Hodapp, K.-W., Simons, D. A., & Wynn-Williams, C. G. 1990, *ApJ*, 365, 478
- Emerson, J. P., Clegg, P. E., Gee, G., et al. 1984, *Nature*, 311, 237
- Engel, H., Davies, R. I., Genzel, R., et al. 2010, *A&A*, 524, A56
- Engelbracht, C. W., Kundurthy, P., Gordon, K. D., et al. 2006, *ApJ*, 642, L127
- Engelbracht, C. W., Rieke, M. J., Rieke, G. H., Kelly, D. M., & Achtermann, J. M. 1998, *ApJ*, 505, 639
- Eskridge, P. B., Frogel, J. A., Pogge, R. W., et al. 2002, *ApJS*, 143, 73
- Fabbiano, G. & Trinchieri, G. 1984, *ApJ*, 286, 491
- Falgarone, E. & Phillips, T. G. 1990, *ApJ*, 359, 344
- Farrah, D., Lebouteiller, V., Spoon, H. W. W., et al. 2013, *ApJ*, 776, 38
- Feinstein, C., Mendez, M., Vega, I., & Forte, J. C. 1990, *A&A*, 239, 90
- Fernández-Ontiveros, J. A., Prieto, M. A., & Acosta-Pulido, J. A. 2009, *MNRAS*, 392, L16
- Feruglio, C., Maiolino, R., Piconcelli, E., et al. 2010, *A&A*, 518, L155
- Fischer, J., Sturm, E., González-Alfonso, E., et al. 2010, *A&A*, 518, L41
- Forbes, D. A., Boisson, C., & Ward, M. J. 1992, *MNRAS*, 259, 293
- Forbes, D. A., Kotilainen, J. K., & Moorwood, A. F. M. 1994a, *ApJ*, 433, L13
- Forbes, D. A., Norris, R. P., Williger, G. M., & Smith, R. C. 1994b, *AJ*, 107, 984
- Forbes, D. A., Polehampton, E., Stevens, I. R., Brodie, J. P., & Ward, M. J. 2000, *MN-*

- RAS, 312, 689
- Forbes, D. A., Ward, M. J., & Depoy, D. L. 1991, *ApJ*, 380, L63
- Forbes, D. A., Ward, M. J., Rotaciuc, V., et al. 1993, *ApJ*, 406, L11
- Gao, Y. & Solomon, P. M. 2004, *ApJS*, 152, 63
- García-Burillo, S., Combes, F., Usero, A., et al. 2014, ArXiv e-prints
- García-Burillo, S., Martín-Pintado, J., Fuente, A., & Neri, R. 2000, *A&A*, 355, 499
- Genzel, R. & Cesarsky, C. J. 2000, *ARA&A*, 38, 761
- Genzel, R., Lutz, D., Sturm, E., et al. 1998, *ApJ*, 498, 579
- Genzel, R., Tacconi, L. J., Rigopoulou, D., Lutz, D., & Tecza, M. 2001, *ApJ*, 563, 527
- Gerin, M. & Phillips, T. G. 1998, *ApJ*, 509, L17
- Gerin, M. & Phillips, T. G. 2000, *ApJ*, 537, 644
- Glassgold, A. E., Galli, D., & Padovani, M. 2012, *ApJ*, 756, 157
- Glassgold, A. E. & Langer, W. D. 1973, *ApJ*, 186, 859
- Goldreich, P. & Scoville, N. 1976, *ApJ*, 205, 144
- Goldsmith, P. F. & Langer, W. D. 1978, *ApJ*, 222, 881
- González-Alfonso, E., Fischer, J., Graciá-Carpio, J., et al. 2014, *A&A*, 561, A27
- González-Alfonso, E., Fischer, J., Graciá-Carpio, J., et al. 2012, *A&A*, 541, A4
- González-Alfonso, E., Fischer, J., Isaak, K., et al. 2010, *A&A*, 518, L43
- González-Martín, O., Masegosa, J., Márquez, I., Guerrero, M. A., & Dultzin-Hacyan, D. 2006, *A&A*, 460, 45
- Graciá-Carpio, J., Sturm, E., Hailey-Dunsheath, S., et al. 2011, *ApJ*, 728, L7
- Graham, J. R., Wright, G. S., & Longmore, A. J. 1987, *ApJ*, 313, 847
- Graham, J. R., Wright, G. S., & Longmore, A. J. 1990, *ApJ*, 352, 172
- Greenhouse, M. A., Satyapal, S., Woodward, C. E., et al. 1997, *ApJ*, 485, 438
- Greenhouse, M. A., Woodward, C. E., Thronson, Jr., H. A., et al. 1991, *ApJ*, 383, 164
- Griffin, M. J., Abergel, A., Abreu, A., et al. 2010a, *A&A*, 518, L3
- Griffin, M. J., Abergel, A., Abreu, A., et al. 2010b, *A&A*, 518, L3
- Grimm, H.-J., Gilfanov, M., & Sunyaev, R. 2003, *MNRAS*, 339, 793
- Hailey-Dunsheath, S., Nikola, T., Stacey, G. J., et al. 2008, *ApJ*, 689, L109
- Hailey-Dunsheath, S., Sturm, E., Fischer, J., et al. 2012, *ApJ*, 755, 57
- Harrison, A., Henkel, C., & Russell, A. 1999, *MNRAS*, 303, 157
- Harrison, A., Puxley, P., Russell, A., & Brand, P. 1998, *MNRAS*, 297, 624
- Haynes, M. P., Giovanelli, R., & Roberts, M. S. 1979, *ApJ*, 229, 83
- Heckman, T. M., Blitz, L., Wilson, A. S., Armus, L., & Miley, G. K. 1989, *ApJ*, 342, 735
- Helou, G., Khan, I. R., Malek, L., & Boehmer, L. 1988, *ApJS*, 68, 151
- Helou, G., Malhotra, S., Hollenbach, D. J., Dale, D. A., & Contursi, A. 2001, *ApJ*, 548, L73
- Helou, G., Soifer, B. T., & Rowan-Robinson, M. 1985, *ApJ*, 298, L7
- Henkel, C., Asiri, H., Ao, Y., et al. 2014, *A&A*, 565, A3
- Henkel, C., Baan, W. A., & Mauersberger, R. 1991, *A&Ar*, 3, 47
- Henkel, C., Peck, A. B., Tarchi, A., et al. 2005, *A&A*, 436, 75
- Hollenbach, D. J. & Tielens, A. G. G. M. 1999, *Reviews of Modern Physics*, 71, 173
- Houck, J. R., Schneider, D. P., Danielson, G. E., et al. 1985, *ApJ*, 290, L5
- Houghton, S., Whiteoak, J. B., Koribalski, B., et al. 1997, *A&A*, 325, 923

- Huang, Z. P., Thuan, T. X., Chevalier, R. A., Condon, J. J., & Yin, Q. F. 1994, *ApJ*, 424, 114
- Hughes, M. A., Axon, D., Atkinson, J., et al. 2005, *AJ*, 130, 73
- Hummel, E. 1980, *A&AS*, 41, 151
- Hummer, D. G. & Storey, P. J. 1987, *MNRAS*, 224, 801
- Imanishi, M. & Nakanishi, K. 2006, *PASJ*, 58, 813
- Inami, H., Armus, L., Charmandaris, V., et al. 2013, *ApJ*, 777, 156
- Indriolo, N. & McCall, B. J. 2012, *ApJ*, 745, 91
- Iono, D., Ho, P. T. P., Yun, M. S., et al. 2004, *ApJ*, 616, L63
- Israel, F. P. 2009, *A&A*, 506, 689
- Israel, F. P. & Baas, F. 2002, *A&A*, 383, 82
- Israel, F. P., Hawarden, T. G., Wade, R., Geballe, T. R., & van Dishoeck, E. F. 1989, *MNRAS*, 236, 89
- Israel, F. P., White, G. J., & Baas, F. 1995, *A&A*, 302, 343
- Jakob, H., Kramer, C., Simon, R., et al. 2007, *A&A*, 461, 999
- Joblin, C. & Tielens, A. G. G. M. 2013, in , C+ as an astronomical tool
- Jones, A. P., Tielens, A. G. G. M., Hollenbach, D. J., & McKee, C. F. 1994, *ApJ*, 433, 797
- Kaufman, M. J., Wolfire, M. G., Hollenbach, D. J., & Luhman, M. L. 1999, *ApJ*, 527, 795
- Kazandjian, M. V., Meijerink, R., Pelupessy, I., Israel, F. P., & Spaans, M. 2012, *A&A*, 542, A65
- Kazandjian, M. V., Meijerink, R., Pelupessy, I., Israel, F. P., & Spaans, M. 2014, *ArXiv e-prints*
- Knudsen, K. K., Walter, F., Weiss, A., et al. 2007, *ApJ*, 666, 156
- König, S., Aalto, S., Müller, S., Beswick, R. J., & Gallagher, J. S. 2013, *A&A*, 553, A72
- Kornei, K. A. & McCrady, N. 2009, *ApJ*, 697, 1180
- Kotilainen, J. K., Forbes, D. A., Moorwood, A. F. M., Van der Werf, P. P., & Ward, M. J. 1996, *A&A*, 313, 771
- Kotilainen, J. K., Reunanen, J., Laine, S., & Ryder, S. D. 2001, *A&A*, 366, 439
- Krabbe, A., Sternberg, A., & Genzel, R. 1994, *ApJ*, 425, 72
- Kramer, C., Jakob, H., Mookerjee, B., et al. 2004, *A&A*, 424, 887
- Laine, S., Kotilainen, J. K., Reunanen, J., Ryder, S. D., & Beck, R. 2006, *AJ*, 131, 701
- Leitherer, C., Schaerer, D., Goldader, J. D., et al. 1999, *ApJS*, 123, 3
- Lepp, S. & Dalgarno, A. 1996, *A&A*, 306, L21
- Liu, J. & Bregman, J. N. 2005, *ApJS*, 157, 59
- Loenen, A. F., Spaans, M., Baan, W. A., & Meijerink, R. 2008, *A&A*, 488, L5
- Lonsdale, C. J., Farrah, D., & Smith, H. E. 2006, *Ultraluminous Infrared Galaxies*, ed. J. W. Mason, 285
- Lu, N., Zhao, Y., Xu, C. K., et al. 2014, *ApJ*, 787, L23
- Luhman, M. L., Jaffe, D. T., Keller, L. D., & Pak, S. 1994, *ApJ*, 436, L185
- Luhman, M. L., Satyapal, S., Fischer, J., et al. 1998, *ApJ*, 504, L11
- Luhman, M. L., Satyapal, S., Fischer, J., et al. 2003, *ApJ*, 594, 758
- Magnelli, B., Elbaz, D., Chary, R. R., et al. 2011, *A&A*, 528, A35

- Makiwa, G., Naylor, D. A., Ferlet, M., et al. 2013, *Appl. Opt.*, 52, 3864
- Malhotra, S., Helou, G., Stacey, G., et al. 1997, *ApJ*, 491, L27
- Malhotra, S., Kaufman, M. J., Hollenbach, D., et al. 2001, *ApJ*, 561, 766
- Maloney, P. R., Hollenbach, D. J., & Tielens, A. G. G. M. 1996, *ApJ*, 466, 561
- Martin, P. G. & Whittet, D. C. B. 1990, *ApJ*, 357, 113
- Martín, S., Martín-Pintado, J., & Mauersberger, R. 2009a, *ApJ*, 694, 610
- Martín, S., Martín-Pintado, J., Mauersberger, R., Henkel, C., & García-Burillo, S. 2005, *ApJ*, 620, 210
- Martín, S., Martín-Pintado, J., & Viti, S. 2009b, *ApJ*, 706, 1323
- Martín, S., Mauersberger, R., Martín-Pintado, J., Henkel, C., & García-Burillo, S. 2006, *ApJs*, 164, 450
- Martin-Pintado, J., Bachiller, R., & Fuente, A. 1992, *A&A*, 254, 315
- Mattioda, A. L., Allamandola, L. J., & Hudgins, D. M. 2005, *ApJ*, 629, 1183
- Mauersberger, R., Henkel, C., Walsh, W., & Schulz, A. 1999, *A&A*, 341, 256
- Mauersberger, R., Henkel, C., Wielebinski, R., Wiklind, T., & Reuter, H.-P. 1996, *A&A*, 305, 421
- McCarthy, P. J., van Breugel, W., & Heckman, T. 1987, *AJ*, 93, 264
- Meijerink, R., Kristensen, L. E., Weiß, A., et al. 2013, *ApJL*, 762, L16
- Meijerink, R. & Spaans, M. 2005, *A&A*, 436, 397
- Meijerink, R., Spaans, M., & Israel, F. P. 2006, *ApJL*, 650, L103
- Meijerink, R., Spaans, M., & Israel, F. P. 2007, *A&A*, 461, 793
- Meijerink, R., Spaans, M., Loenen, A. F., & van der Werf, P. P. 2011, *A&A*, 525, A119
- Mirabel, I. F., Booth, R. S., Johansson, L. E. B., Garay, G., & Sanders, D. B. 1990, *A&A*, 236, 327
- Moorwood, A. F. M. & Oliva, E. 1988, *A&A*, 203, 278
- Moorwood, A. F. M., Oliva, E., & Danziger, I. J. 1988, in *IAU Colloq. 101: Supernova Remnants and the Interstellar Medium*, ed. R. S. Roger & T. L. Landecker, 391--+
- Mouri, H., Kawara, K., & Taniguchi, Y. 2000, *ApJ*, 528, 186
- Müller-Sánchez, F., González-Martín, O., Fernández-Ontiveros, J. A., Acosta-Pulido, J. A., & Prieto, M. A. 2010, *ApJ*, 716, 1166
- Narayanan, D., Groppi, C. E., Kulesa, C. A., & Walker, C. K. 2005, *ApJ*, 630, 269
- Neff, S. G., Hutchings, J. B., Standord, S. A., & Unger, S. W. 1990, *AJ*, 99, 1088
- Nikola, T., Stacey, G. J., Brisbin, D., et al. 2011, *ApJ*, 742, 88
- Norman, C. A., Bowen, D. V., Heckman, T., Blades, C., & Danly, L. 1996, *ApJ*, 472, 73
- Norman, C. A. & Ferrara, A. 1996, *ApJ*, 467, 280
- Nussbaumer, H. & Storey, P. J. 1988, *A&A*, 193, 327
- Oliva, E., Moorwood, A. F. M., & Danziger, I. J. 1989, *A&A*, 214, 307
- Oliva, E., Moorwood, A. F. M., & Danziger, I. J. 1990, *A&A*, 240, 453
- Olsson, E., Aalto, S., Thomasson, M., & Beswick, R. 2010, *A&A*, 513, A11+
- Ott, S. 2010, in *Astronomical Society of the Pacific Conference Series*, Vol. 434, *Astronomical Data Analysis Software and Systems XIX*, ed. Y. Mizumoto, K.-I. Morita, & M. Ohishi, 139
- Paglionie, T. A. D., Jackson, J. M., & Ishizuki, S. 1997, *ApJ*, 484, 656
- Paglionie, T. A. D., Tosaki, T., & Jackson, J. M. 1995, *ApJL*, 454, L117

- Papadopoulos, P. P., van der Werf, P., Isaak, K., & Xilouris, E. M. 2010, *ApJ*, 715, 775
- Papadopoulos, P. P., van der Werf, P. P., Xilouris, E. M., et al. 2012, *MNRAS*, 426, 2601
- Papadopoulos, P. P., Zhang, Z.-Y., Xilouris, E. M., et al. 2014, ArXiv e-prints
- Pereira-Santaella, M., Spinoglio, L., van der Werf, P. P., & Piqueras López, J. 2014, ArXiv e-prints
- Pérez-Torres, M. A., Alberdi, A., Romero-Cañizales, C., & Bondi, M. 2010, *A&A*, 519, L5
- Phillips, A. C. 1993, *AJ*, 105, 486
- Pietsch, W., Vogler, A., Klein, U., & Zinnecker, H. 2000, *A&A*, 360, 24
- Pilbratt, G. L., Riedinger, J. R., Passvogel, T., et al. 2010a, *A&A*, 518, L1
- Pilbratt, G. L., Riedinger, J. R., Passvogel, T., et al. 2010b, *A&A*, 518, L1
- Poglitsch, A., Waelkens, C., Geis, N., et al. 2010a, *A&A*, 518, L2
- Poglitsch, A., Waelkens, C., Geis, N., et al. 2010b, *A&A*, 518, L2
- Prada, F., Machado, A., Canzian, B., et al. 1996, *ApJ*, 458, 537
- Prugniel, P., Zasov, A., Busarello, G., & Simien, F. 1998, *A&AS*, 127, 117
- Puxley, P. J., Hawarden, T. G., & Mountain, C. M. 1988, *MNRAS*, 234, 29P
- Ramya, S., Sahu, D. K., & Prabhu, T. P. 2007, *MNRAS*, 381, 511
- Rangwala, N., Maloney, P. R., Glenn, J., et al. 2011, *ApJ*, 743, 94
- Rekola, R., Richer, M. G., McCall, M. L., et al. 2005, *MNRAS*, 361, 330
- Reuter, H., Krause, M., Wielebinski, R., & Lesch, H. 1991, *A&A*, 248, 12
- Rieke, G. H., Lebofsky, M. J., Thompson, R. I., Low, F. J., & Tokunaga, A. T. 1980, *ApJ*, 238, 24
- Rieke, G. H., Lebofsky, M. J., & Walker, C. E. 1988, *ApJ*, 325, 679
- Rigopoulou, D., Hurley, P. D., Swinyard, B. M., et al. 2013, *MNRAS*, 434, 2051
- Roberts, T. P., Schurch, N. J., & Warwick, R. S. 2001, *MNRAS*, 324, 737
- Rosenberg, M. J. F., Kazandjian, M. V., van der Werf, P. P., et al. 2014, *A&A*, 564, A126
- Rosenberg, M. J. F., van der Werf, P. P., & Israel, F. P. 2012, *A&A*, 540, A116
- Rosenberg, M. J. F., van der Werf, P. P., & Israel, F. P. 2013, *A&A*, 550, A12
- Rothberg, B. & Fischer, J. 2010, *ApJ*, 712, 318
- Rothberg, B., Fischer, J., Rodrigues, M., & Sanders, D. B. 2013, *ApJ*, 767, 72
- Rots, A. H. 1978, *AJ*, 83, 219
- Sakamoto, K., Mao, R.-Q., Matsushita, S., et al. 2011, *ApJ*, 735, 19
- Sanders, D. B., Mazzarella, J. M., Kim, D.-C., Surace, J. A., & Soifer, B. T. 2003, *AJ*, 126, 1607
- Sanders, D. B. & Mirabel, I. F. 1996, *ARA&A*, 34, 749
- Sanders, D. B., Scoville, N. Z., & Soifer, B. T. 1991, *ApJ*, 370, 158
- Sanders, D. B., Soifer, B. T., Elias, J. H., et al. 1988a, *ApJ*, 325, 74
- Sanders, D. B., Soifer, B. T., Elias, J. H., Neugebauer, G., & Matthews, K. 1988b, *ApJ*, 328, L35
- Sargent, A. & Scoville, N. 1991, *ApJL*, 366, L1
- Sargent, A. I., Sanders, D. B., Scoville, N. Z., & Soifer, B. T. 1987, *ApJL*, 312, L35
- Schinnerer, E., Eckart, A., Quirrenbach, A., et al. 1997, *ApJ*, 488, 174
- Schleicher, D. R. G., Spaans, M., & Klessen, R. S. 2010, *A&A*, 513, A7
- Schulz, H., Fried, J. W., Röser, S., & Keel, W. C. 1993, *A&A*, 277, 416

- Scoville, N. Z., Soifer, B. T., Neugebauer, G., et al. 1985, *ApJ*, 289, 129
- Scoville, N. Z., Yun, M. S., & Bryant, P. M. 1997, *ApJ*, 484, 702
- Shull, J. M. & Draine, B. T. 1987, in *Astrophysics and Space Science Library*, Vol. 134, Interstellar Processes, ed. D. J. Hollenbach & H. A. Thronson Jr., 283--319
- Shull, J. M. & Hollenbach, D. J. 1978, *ApJ*, 220, 525
- Sliwa, K., Wilson, C. D., Petitpas, G. R., et al. 2012, *ApJ*, 753, 46
- Smith, H. E., Lonsdale, C. J., Lonsdale, C. J., & Diamond, P. J. 1998, *ApJ*, 493, L17
- Sobolev, V. V. 1960, Moving envelopes of stars
- Soifer, B. T. & Neugebauer, G. 1991, *AJ*, 101, 354
- Soifer, B. T., Neugebauer, G., Helou, G., et al. 1984, *ApJ*, 283, L1
- Solomon, P. M., Downes, D., Radford, S. J. E., & Barrett, J. W. 1997, *ApJ*, 478, 144
- Solomon, P. M. & Sage, L. J. 1988, *ApJ*, 334, 613
- Spinoglio, L., Pereira-Santaella, M., Busquet, G., et al. 2012, *ApJ*, 758, 108
- Spoon, H. W. W., Farrah, D., Lebouteiller, V., et al. 2013, *ApJ*, 775, 127
- Stanford, S. A. & Balcells, M. 1990, *ApJ*, 355, 59
- Stanford, S. A. & Balcells, M. 1991, *ApJ*, 370, 118
- Sternberg, A. & Dalgarno, A. 1989, *ApJ*, 338, 197
- Stierwalt, S., Armus, L., Surace, J. A., et al. 2013, *ApJS*, 206, 1
- Sturm, E., González-Alfonso, E., Veilleux, S., et al. 2011, *ApJ*, 733, L16
- Sturm, E., Lutz, D., Genzel, R., et al. 1996, *A&A*, 315, L133
- Swinyard, B. M., Polehampton, E. T., Hopwood, R., et al. 2014, ArXiv e-prints
- Tabatabaei, F. S., Braine, J., Xilouris, E. M., et al. 2014, *A&A*, 561, A95
- Tacconi, L. J., Genzel, R., Lutz, D., et al. 2002, *ApJ*, 580, 73
- Takano, S., Nakajima, T., Kohno, K., et al. 2014, ArXiv e-prints
- Tarchi, A., Castangia, P., Henkel, C., & Menten, K. M. 2007, *New A Rev.*, 51, 67
- Tielens, A. G. G. M. 2005, *The Physics and Chemistry of the Interstellar Medium*
- Tielens, A. G. G. M. 2008a, *ARA&A*, 46, 289
- Tielens, A. G. G. M. 2008b, *ARA&A*, 46, 289
- Tielens, A. G. G. M. & Hollenbach, D. 1985, *ApJ*, 291, 722
- Tinsley, B. M. & Larson, R. B. 1978, *ApJ*, 221, 554
- Turner, J. L. & Ho, P. T. P. 1985, *ApJL*, 299, L77
- U, V., Sanders, D. B., Mazzarella, J. M., et al. 2012, *ApJs*, 203, 9
- Ulrich, M.-H. 1978, *ApJ*, 219, 424
- Ulvestad, J. S. & Antonucci, R. R. J. 1997, *ApJ*, 488, 621
- van der Tak, F. F. S., Black, J. H., Schöier, F. L., Jansen, D. J., & van Dishoeck, E. F. 2007, *A&A*, 468, 627
- van der Werf, P. P., Berciano Alba, A., Spaans, M., et al. 2011, *ApJ*, 741, L38
- Van der Werf, P. P., Genzel, R., Krabbe, A., et al. 1993, *ApJ*, 405, 522
- van der Werf, P. P., Isaak, K. G., Meijerink, R., et al. 2010a, *A&A*, 518, L42
- van der Werf, P. P., Isaak, K. G., Meijerink, R., et al. 2010b, *A&A*, 518, L42
- van Dishoeck, E. F. & Black, J. H. 1986, *ApJs*, 62, 109
- van Dishoeck, E. F. & Black, J. H. 1988, *ApJ*, 334, 771
- Vanzi, L. & Rieke, G. H. 1997, *ApJ*, 479, 694
- Veilleux, S., Kim, D.-C., & Sanders, D. B. 1999, *ApJ*, 522, 113

- Veilleux, S., Kim, D.-C., & Sanders, D. B. 2002, *ApJS*, 143, 315
- Veilleux, S., Meléndez, M., Sturm, E., et al. 2013, *ApJ*, 776, 27
- Veilleux, S., Rupke, D. S. N., Kim, D.-C., et al. 2009, *ApJS*, 182, 628
- Veron-Cetty, M. & Veron, P. 1985, *A&A*, 145, 425
- Vila, M. B., Pedlar, A., Davies, R. D., Hummel, E., & Axon, D. J. 1990, *MNRAS*, 242, 379
- Watson, A. M., Gallagher, III, J. S., Holtzman, J. A., et al. 1996, *AJ*, 112, 534
- Weaver, K. A., Heckman, T. M., Strickland, D. K., & Dahlem, M. 2002, *ApJL*, 576, L19
- Weiß, A., Kovács, A., Güsten, R., et al. 2008, *A&A*, 490, 77
- Weiß, A., Walter, F., Downes, D., et al. 2012, *ApJ*, 753, 102
- Westmoquette, M. S., Smith, L. J., & Gallagher, III, J. S. 2011, *MNRAS*, 414, 3719
- Wilson, C. D., Petitpas, G. R., Iono, D., et al. 2008, *ApJS*, 178, 189
- Wolniewicz, L., Simbotin, I., & Dalgarno, A. 1998, *ApJS*, 115, 293
- Wu, R., Polehampton, E. T., Etxaluze, M., et al. 2013, *A&A*, 556, A116
- Wynn-Williams, C. G., Hodapp, K.-W., Joseph, R. D., et al. 1991, *ApJ*, 377, 426
- Yang, C., Gao, Y., Omont, A., et al. 2013, *ApJ*, 771, L24
- Yuan, T.-T., Kewley, L. J., & Sanders, D. B. 2010, *ApJ*, 709, 884
- Zasov, A. V. & Karachentsev, I. D. 1979, *Soviet Astronomy Letters*, 5, 126
- Zezas, A., Ward, M. J., & Murray, S. S. 2003, *ApJL*, 594, L31

Nederlandse Samenvatting

Het belang van stervorming

Sterren zijn de allerbelangrijkste objecten in het Universum. Elk sterrenstelsel heeft honderden miljoenen sterren, en deze sterren bepalen elk aspect van deze sterrenstelsels op elke schaal. Een enkele ster kan worden gezien als een fabriek waar de simpelste elementen omgezet worden in de bouwstenen voor leven. Op een grotere schaal verhitten de reuzensterren hun omgeving met hun licht, zijn ze de oorzaak voor stervorming, en komt er enorm veel energie vrij bij hun dood tijdens een supernova explosie. Om deze redenen is het van fundamenteel belang om te begrijpen hoe sterren ontstaan en wat deze formatie reguleert.

Sterren ontstaan in regionen met koud, compact gas en stof die we moleculaire wolken noemen. De sterrenvormingscyclus begint met het ontstaan van sterren uit het gas en stof in deze wolken. De sterren verbranden dit materiaal vervolgens tijdens hun leven en geven de rest terug aan de ruimte als ze sterven. Het is deze cyclische aard van het sterrenvormingsproces die ervoor zorgt dat sterren en hun omgeving zo een sterke band met elkaar hebben.

In sommige omgevingen zorgt de sterrenvormingscyclus voor een sterrenuitbarsting waarbij sterren tussen 10-1000 keer sneller vormen dan normaal. In dit proefschrift bestudeer ik enkel de sterrenstelsels die een dergelijke sterrenuitbarsting ondergaan. Hiernaast focus ik ook op een unieke soort van de sterrenvormingscyclus die zich voordoet in het midden van sterrenstelsels. In die regionen is de sterrenvormingscyclus niet geïsoleerd, maar wordt het beïnvloed door wat er nog meer gebeurt in het centrum van een sterrenstelsel. Hierdoor is het proces nog heviger.

De extreme omgeving in het centrum van sterrenstelsels

In het centrum van ons sterrenstelsel, de Melkweg, ligt een zwart gat dat even zwaar is al vier miljoen Zonnen. In tegenstelling tot ons zwarte gat zijn veel andere zwarte gaten zogenaamd *actief*. Een actief zwart gat is een zwart gat dat in massa toeneemt door samenvoeging met steeds meer materiaal. Terwijl het materiaal in het zwarte gat valt wordt het tegelijkertijd rondgeslingerd met enorme snelheden en wordt het extreem heet. Hierbij straalt het hoge doses energie uit. Deze straling is slechts één van de componenten die de omgeving in het centrum van sterrenstelsels zo extreem maakt.

Naast de zwarte gaten vindt er in het centrum van een sterrenstelsel ook veel stervorming plaats. Zoals boven al is aangegeven zorgt stervorming in de vorm van de extreem snelle sterrenuitbarstingen ervoor dat de omgeving wordt overspoeld met straling, vooral wanneer sterren sterven. Een sterrenuitbarsting kan ook voor sterke winden zorgen die door de ruimte waaien en welke hun directe omgeving compleet hervormen. Tot slot kan er ook *mechanische verhitting* plaatsvinden in grote hoeveelheden. Deze brede en alomvattende term kan worden gebruikt voor alles wat het gas en stof beroerd, zoals turbulentie of schokgolven. Mechanische verhitting vernietigt stof en roert het materiaal, waardoor het verhit en verstoord raakt.

Samen zijn de zwarte gaten en de mechanische verhittingsprocessen zeer gewelddadig en genereren ze een sterke *outflow* van materiaal, waarbij het materiaal uit het centrum van het sterrenstelsel en in de ruimte wordt geslingerd. Zodra al het materiaal voor stervorming uit het sterrenstelsel is geslingerd spreken we van een dood sterrenstelsel, omdat het immers geen nieuwe sterren meer kan vormen. In afbeelding 7.3 zien we links hoe het sterrenstelsel M82 er uit ziet als we er met onze eigen ogen naar zouden kijken, in het optische spectrum. Echter, moleculen die verantwoordelijk zijn voor stervorming zijn niet zichtbaar in dit spectrum, maar zijn alleen waarneembaar in het infrarood. Zodra we een andere telescoop gebruiken die ook het infrarode spectrum observeert (zoals rechts in afbeelding 7.3) kunnen we de enorme hoeveelheid stervormend gas en stof zien die uit het centrum van het sterrenstelsel wordt geslingerd.

Om dit proces van de sterfte van sterrenstelsels te bestuderen (ook wel het doven van stervorming genoemd) moeten we het samenspel tussen de sterren, het zwarte gat en de turbulentie en schokgolven in de centra van *extreme starburst galaxies* onderzoeken.

Mijn proefschrift

Dit proefschrift is gebaseerd op observaties die gemaakt zijn met de *Herschel*



Figuur 7.2: Links: het uitbraak-sterrenstelsel M82 zoals we die met onze ogen zien in het waarneembare spectrum. Rechts: hetzelfde sterrenstelsel geobserveerd in een spectrum met infrarood. Het rode gas en stof dat uit het centrum van M82 vloeit is stervormend materiaal.

Space Observatory. Met *Herschel* observeer ik stervormend materiaal in het centrum van extreme *starburst* sterrenstelsels. Ik maak hierbij gebruik van een combinatie van observaties en modellen om te begrijpen welke processen (sterren, actieve zwarte gaten, of mechanische verhitting) van invloed zijn op het stervormend materiaal. Om te beginnen heb ik wat bekend staat als een 'archetypische' *starburst* sterrenstelsel, NGC 253, onderzocht. Dit sterrenstelsel is ideaal aangezien het relatief dichtbij staat en het zeer helder is. Hierdoor is het al door veel mensen bestudeerd en is er al veel over bekend. Allereerst is er met behulp van een telescoop vanaf de grond het heetste stervormende gas dat het dichtst bij de sterren staat bestudeerd. Hieruit kon ik vaststellen dat dit gas voornamelijk werd verhit door de sterren zelf. Toch werd 20% van het heetste gas eigenlijk verhit door schokgolven (hoofdstuk 2). Daarna observeerde ik het koudere stervormende gas dat verder van de sterren in de gaswolken ligt. Hierbij presenteer ik een nieuwe methode waarbij ik veel verschillende moleculen gebruik (in plaats van één molecuul, zoals voorheen gebruikelijk was) om vast te stellen welk proces het stervormende gas beïnvloed. Hoewel het koude gas op een compleet andere plek ligt dan het warme gas is het verrassend gelijkwaardige resultaat waarneembaar waarbij het merendeel van het gas wordt verhit door de sterren, maar waarvan 20% alsnog door de schokgolven wordt verhit (hoofdstuk 3). Dit was een onverwacht resultaat gezien het feit dat eerder werd aangenomen dat het gas enkel en alleen door de sterren werd verhit, en in zijn geheel niet door schokgolven. Maar aan de hand van mijn observaties bleek het niet mogelijk te zijn om te verklaren wat er gebeurde *zonder* de 20% van verhitting aan schokgolven toe te schrijven.

Omdat dit resultaat onverwacht was ging ik door met mijn onderzoek, en richtte ik mij op een nog extremer sterrenstelsel, Arp 299. Arp 299 is eigenlijk een stelsel van verschillende botsende sterrenstelsels met drie stervormende centra. De eerste, Arp 299 A is een *starburst* sterrenstelsel met ook een actief zwart gat in het midden. Arp 299B is daarentegen enkel een *starburst*sterrenstelsel, en Arp 299 C is de regio waar de twee stelsels elkaar raken en waar minder intense stervorming plaatsvindt. Dit gehele sterrenstelsel biedt een unieke kans om het stervormende materiaal te bestuderen op drie verschillende locaties, elk met een eigen omgeving die nét iets anders is van die van de andere, maar die nog wel in hetzelfde sterrenstelsel te vinden is. Wederom heb ik het koudere gas bestudeerd met dezelfde methode die ik ontwikkeld heb in hoofdstuk 3. We kunnen zien dat in het geval van Arp 299 B en C enkel de sterren invloed hebben op het gas, terwijl Arp 299 A we wederom mechanische verhitting nodig hebben om de verhitting te verklaren (hoofdstuk 4). Dit resultaat was ook verrassend aangezien Arp 299 A een actief zwart gat bevat. Toch konden de observaties niet verklaard worden door de aanwezigheid van een zwart gat, maar moest er wel sprake zijn van mechanische verhitting. Dit betekent niet dat er geen actief zwart gat aanwezig is in Arp 299 A, maar nog belangrijker, dat het zwarte gat geen invloed uitoefent op het gas. Het toont ook aan dat mechanische verhitting een krachtig en efficiënt proces is.

Zoals eerder vermeld kan mechanische verhitting door veel zaken veroorzaakt worden. Eén grote bron van mechanische verhitting zou de dood van een ster kunnen zijn. Als een ster groot is in massa zal deze exploderen als een supernova als hij sterft. Dit betekent dat hij eerst implodeert om vervolgens een enorme explosie te veroorzaken. Maar mechanische verhitting kan ook worden veroorzaakt door processen die niet gerelateerd zijn aan sterren, zoals de botsing tussen twee sterrenstelsels. Daarom biedt hoofdstuk 5 een manier om te meten hoeveel supernovae er elk jaar plaats vinden. Hiermee kunnen we beter begrijpen of de mechanische energie aan de sterren is gerelateerd of dat dit komt door een extern proces. Tot slot heb ik, door te bouwen op de eerdere gedetailleerde studies naar de uitbarststerrenstelsels, een verzameling van bijna 30 sterrenstelsels geobserveerd. Net als in de geïsoleerde gevallen van NGC 253 en Arp 299 zien we dat het stervormende gas vaak wordt beïnvloed door mechanische verhitting. Echter, in het geval van uitermate extreme zwarte gaten zien we dat deze zwarte gaten ook het stervormende gas, zei het in mindere mate, beïnvloeden. In alle gevallen blijven sterren de dominante en heersende bron van energie en hitte, hoewel zowel zwarte gaten als mechanische verhitting vaak nodig zijn om de observaties te verklaren.

Executive Summary

Dedicated to Dr. Michael N. Rosenberg

The importance of star formation

Stars are the single most important objects in the Universe. Each galaxy has hundreds of billions of stars, and these stars govern aspects of the galaxy from the smallest to the largest scales. A single star can be thought of as a factory; converting simple elements into the building blocks of life. On larger scales, the light from giant stars can heat their surrounding environments, trigger further star formation, and in death, release enormous amounts of energy in a supernova explosion. Thus, it is fundamentally important to understand how stars form and what regulates that formation.

Stars arise from regions of cool, dense gas and dust that are called molecular clouds. The star formation cycle begins with stars forming from gas and dust. The stars then burn this material throughout their lifetime and return it back into space when they die. The cyclical nature of star formation is what allows stars to interact so strongly with their environments.

In some environments, the star forming cycle results in a starburst, where stars are formed anywhere from 10-1000 times faster than normal. In this thesis, I exclusively study galaxies that are undergoing a starburst. In addition to studying starburst galaxies, I focus on a unique type of star formation cycle that occurs in galaxy centers. There, the star formation cycle is not isolated, but influenced by everything that is happening in the center of a galaxy, making it even more extreme.

The extreme environment of galaxy centers

The center of our galaxy, the Milky Way, harbors a black hole that weighs the same as 4 million Suns. Unlike the black hole in the Milky Way, many black holes

are considered *active*. An active black hole is one that is gaining mass by accreting more and more material. As this material falls into the black hole, it gets spun around at extremely fast speeds and becomes extremely hot, emitting high energy radiation. This radiation is only one of the components that makes the environment of galaxy centers so extreme.

In addition to black holes, some galaxy centers are also undergoing star formation. The most extreme mode of star formation, a starburst, will flood the galaxy center with radiation. When these stars die, they emit even more extreme radiation. A starburst can also create strong winds that blow through space and can completely reshape their surrounding environment.

Aside from black holes and radiation, in galaxy centers there can be large amounts of what is referred to as *mechanical processes*. This is a blanket term that refers to anything that stirs up the gas and dust, such as turbulence or shock waves. Shock waves are similar to what you see (and hear) when a plane passes the sound barrier. Turbulence, on the other hand, is a very disturbed and chaotic motion of gas, and is the same thing that causes 'turbulence' on plane. Mechanical processes destroy dust and stir the material, so it becomes heated and disturbed.

Working together, these processes are extremely violent and create powerful outflows that eject star-forming gas and dust from the galaxy center out into space. If all the star-forming material is removed from the center, we consider that galaxy to be dead, because it can no longer form stars. Looking at Figure 7.3, on the left we see what this galaxy (M82) would look like to our own eyes, in the visible wavelength range. However, star-forming molecules cannot be seen in the visible, but can be observed in the infrared wavelength range. If we use a different telescope to observe this same galaxy in the infrared wavelength (as in the right panel), we discover a huge amount of star-forming gas and dust being expelled from the galaxy center.

In order to study this process of galaxies dying (referred to as star-formation quenching), we must investigate the interplay between the stars, the central black hole, and the turbulence and shockwaves in the centers of extreme starburst galaxies.

My Thesis

This thesis bases its findings on observations made with *Herschel Space Observatory*. With *Herschel*, I observe star-forming material in the centers of extreme starburst galaxies. Using a combination of observations and models, I study which process (stars, active black holes, shocks) are acting on the star-forming material.

First, we focus on what is considered an 'archetypal' starburst galaxy, NGC 253.



Figure 7.3: Left: The starburst galaxy M82, as seen by our own eyes, in the visible wavelength range. Right: The same galaxy (M82) observed in the infrared wavelength range. The red gas and dust flowing out from the center of M82 is star-forming material.

This galaxy is ideal since it is relatively close by and very bright, so many people have observed the galaxy before, and much is already known about it. Using a large ground based telescope (called the Very Large Telescope, VLT), we studied the hottest star-forming gas, which is located closest to the stars. We determined that this gas is being heated mostly by the stars themselves, although 20% of the hottest gas is actually being heated by shocks (Chapter 2). We then shift focus to the cooler star-forming gas, that is further away from the stars inside of gas clouds. We present a new method to use many different molecules, instead of one molecule, which was historically used, to determine which process is affecting the star-forming gas. Although the cool gas is in a location very different from that of the hot gas, we find the surprisingly similar result that most of the gas is being heated by the stars, but 20% of this gas must be heated by shocks (Chapter 3). This is an unexpected result since it was thought previously that the gas was heated only by the stars, and not so much by shocks. Yet it was impossible to explain the observations without including 20% heating by shocks.

Since this result was not expected, we continued our study with an even more extreme galaxy, Arp 299. Arp 299 is actually a system of colliding galaxies, with three centers of star formation. The first, Arp 299 A, is a starburst but also harbors an active black hole in its center. Arp 299 B on the other hand is a pure starburst, and Arp 299 C is a region where the two galaxy disks collided and began less intense star formation. This galaxy provides a unique opportunity to study the star forming material in three different locations, each with a slightly different environment, but all within the same galaxy. Again, we study the cooler gas inside the

star-forming clouds and use the same method developed in Chapter 3. We find that in the case of Arp 299 B and C, it is only the stars that are affecting the gas, while in Arp 299 A, again we require mechanical heating (Chapter 4). This result was also surprising. Despite the presence of an active black hole in Arp 299 A, our observations could not be explained by this, but required mechanical heating. This finding does not imply that there is no active black hole in Arp 299 A, but more importantly, that the black hole is not affecting (heating) the gas. It also shows that mechanical heating is a powerful and efficient process.

As previously mentioned, mechanical processes encompass any thing that stirs up gas and dust. One large source of heating from mechanical processes can be from the death of a star. If a star is very large, it will supernova when it dies, which means it will collapse in on itself and result in an enormous explosion. However, mechanical heating can also come from non-star-related processes, such as a galaxy-galaxy collision. Thus, in Chapter 5, we present a way to measure how many supernovae happen each year in the galaxy. This can help us understand whether or not the mechanical energy is still related to stars, or if it is an external process.

Finally, building on our detailed studies of specific starburst galaxies, we observe a large sample of about 30 of these galaxies. Similarly to the isolated cases of NGC 253 and Arp 299, we find that the star forming gas is often affected by mechanical heating. However, in the case of very extreme active black holes, they can also affect the star forming gas to a small degree. In all cases, stars remain the dominant source of energy and heat, although both active black holes and mechanical heating are often required to explain the observations.

List of publications

Refereed Publications

1. Rosenberg, M. J. F., Meijerink, R., Israel, F. P., et al. 2014, A&A (accepted), arXiv:1407.2055
2. Rosenberg, M. J. F., Berné, O., & Boersma, C. 2014, A&A, 566, L4
3. Rosenberg, M. J. F., Kazandjian, M. V., van der Werf, P. P., et al. 2014, A&A, 564, A126
4. Rosenberg, M. J. F., van der Werf, P. P., & Israel, F. P. 2013, IAU Symposium, 292, 295
5. Rosenberg, M. J. F., van der Werf, P. P., & Israel, F. P. 2013, A&A, 550, A12
6. Rosenberg, M. J. F., van der Werf, P. P., & Israel, F. P. 2012, A&A, 540, A116
7. Rosenberg, M. J. F., Berné, O., Boersma, C., Allamandola, L. J., & Tielens, A. G. G. M. 2011, A&A, 532, A128
8. M. V. Kazandjian, I. Pelupessy, R. Meijerink, F. P. Israel, **M. J. F. Rosenberg**, & M. Spaans 2014, A&A (submitted)
9. Brandl, B. R., Martín-Hernández, N. L., Schaerer, D., **Rosenberg, M.**, & van der Werf, P. P. 2012, A&A, 543, A61

Conference Proceedings & Other

1. Rosenberg, M., Russo, P., Bladon, G., & Christensen, L. L. 2013, IAU Themes, "Why is Astronomy Important?"
2. Rosenberg, M. J. F., van der Werf, P. P., & Israel, F. P. 2013, IAU Symposium, 292, 295
3. Rosenberg, M. J. F., van der Werf, P. P., & Israel, F. P. 2012, Journal of Physics Conference Series, 372, 012068

Curriculum Vitae

I was born on April 14th, 1987 in Palo Alto, California, in the United States of America. I completed elementary school just south of San Francisco, and consequently moved up to beautiful wine country, and to the small town of Kenwood. Through both curricular and extracurricular activities, my love and passion for astronomy and human space flight grew. I graduated from Maria Carrillo High School in 2005, with Summa Cum Laude.

Next, I attended University of California Los Angeles into the Astrophysics degree program. There I completed two research projects in addition to two summer programs at the NASA Academy. I graduated with a Bachelors of Science in Astrophysics in 2009, with highest departmental honors and the Charles Goeffrey Hilton award for student of the year.

My next step was to begin a Master's in Space Studies at the International Space University in Strasbourg, France. My Master's research project was completed at Leiden Observatory with Prof. dr. Alexander Tielens on Polycyclic Aromatic Hydrocarbons (PAHs) in a reflection nebula. I graduated from the program with a Master in Science in Space Studies in 2010.

In the fall of 2010, I began my PhD work in Sterrewacht Leiden (Leiden Observatory) under the supervision of Prof. dr. Frank Israel and Prof. dr. Paul van der Werf. My thesis work has focused on excitation mechanisms of gas in the interstellar medium, specifically focusing on observations with *Herschel* Space Observatory and the Spectrograph for INtegral Field Observations in the Near Infrared instrument (SINFONI) on the Very Large Telescope (VLT). During my PhD, I presented my work at international conferences in the Netherlands, France, Austria, Germany, the United State, and China.

In the fall of 2014, I will begin a Master of Science in Space Physiology and Health, with the intention of switching research fields to study and prevent the effects of space on the human body.

Acknowledgements

Receiving a doctorate in astronomy is something that I have been working towards for multiple decades and could not have been achieved without the love and support of friends, mentors, and family.

First, I would like to thank the people who made this all possible, my parents. Mom and Dad, thank you so much for supporting me, both financially and emotionally through my (many) years of education. I thank you for being understanding of my choice to pursue an academic career, and especially one in the Netherlands. I realize it is not ideal to have a daughter living 5,500 miles away. That being said, I can't believe how incredibly lucky I am to have parents that are both willing and able to come visit me and travel the world together. The memories we have made here will last a lifetime. I love you both so much! Brother, although you didn't make it to visit me until my graduation itself, thank you so much for being there for me as my paranymph. Growing up together was not always the easiest, but we managed to get through it, and I love you all the more for it. Aunt Di & Uncle Michael, you have been such a large part of my life, and I really appreciate all your love and support. Every step of my journey, you've been there for me. Thank you for opening your home and your hearts to me, I am so lucky to have a two sets of parents. Glenner, to my cuz with the travel bug, I've loved getting to see the world with you and am honored that you have taken the time to come see me and be a part of my life throughout the years. Grandpa Jim & Gram, thanks for always staying in touch and even coming to visit me in Paris, it was so fun to show you a bit of my European life. Papa & Grandma Paulette, thank you so much for sending messages, postcards, and packages, I always feel loved. Papa, you have inspired me to study science and engineering (as well as play basketball!), thanks for being so supportive.

In high school, I had two especially influential teachers. The first was Mr. Salkovics, who taught me AP Physics. Mr. Salkovics, thank you for encouraging me to always be curious about physics and to continue asking questions. The second was Ms. Devlin, who taught me English. Ms. Devlin, although I do not

study English, I use the lessons you taught me on a daily basis. Moreover, you instilled a confidence in my writing skills that I never had. I appreciate both of you very much and think about how you influenced my accomplishments often.

Similarly, at UCLA I had two Professors that truly impacted my success. Professor Ghez, thank you for not only teaching us in an enthusiastic and transparent manner, but for taking the time out of your busy schedule to offer us an honors class on presentation skills. It gave me the competitive edge in my future work as an astronomer. Professor Turner, I very much enjoyed all of your lectures, you taught in an incredibly logical manner, I feel like I could still pass one of your exams! In addition, thank you for being a mentor, having a strong female role undoubtedly influenced my decision to do a PhD.

I would like to thank everyone at the Sterrewacht for fostering an open and active scientific community, the department is like no other. I would like to thank the members of the ISM group for including me in their discussions. A special thanks to Bram and Sebastiaan for always being available to discuss puzzling results, even though they were extragalactic. I would like to thank Xander Tielens, I appreciate your mentorship, both scientifically and about my career path. Olivier, I've had a really great time working with you over the past few years. You have continually inspired me to be excited by astronomy. Ryan, thanks so much for all of your advice over the years. I really appreciate your selfless willingness to help and encourage me, especially with fellowship applications. Finally, thank you to my supervisors Paul and Frank for many years of scientific discussions and guidance.

A big thanks to all the Bear Balls Brewery supporters at the observatory that have been there from the beginning, Monica, Bernard, Henriette, Alex (north and south), Marco, Matteo, Mattia, Irene, Jesse, Nienke, Tiffany, Tom, Mason, Mart, Paul, and of course Yuval. Monica, we had some very fun time at conferences over the years, keep up the Insanity. Irene, thanks for always being so happy and positive, I know it hasn't been the easiest few years, but you always have a smile and I really appreciate that. Mattia, I still remember our first years here, exploring the Netherlands, being the only single people in the entire observatory (oh how things change). Thanks for maintaining our friendship throughout the years, you've been a great source of support and friendship. Matteo, you were my first friend here. Moving to a new country, with a new language, and surprisingly terrible weather, you were always there to help with the culture shock, or at least to complain along side me. Thanks for all the coffees, borrels, and advice along the way. I wish you all the best in your future, and hope to see you in the US soon! To my officemates Gilles and Jesse, thanks for everything! You guys were both always willing to help, whether it be with Dutch translations or coding problems. I'm lucky to have as great of officemates as you.

To my non-sterrewacht friends, Tiffany, Tom, Leanne, Miguel, Mark, Olga, Karimu, Gorana, René, Graeme, Mason, Allison, Alex (S/W), Yuval, and Mart, thank you for being my surrogate family. Living so far from home was difficult, but any time I got down, you were there to pick me up. I have shared so many great memories with all of you, there is most definitely not enough space to remind you of all the great times, but please know that you have left a mark and I look forward to maintaining our friendships for years to come, preferably when you visit me in London or California. Alex South, thanks for all the talks, I've had a really great time getting to know you and thanks for always being up for anything! Mason and Allison (and Alex West), although it's really only been a year, we've made some really great memories, keep it real in Leiden, I leave it in your hands!

Yuv, you helped me build my life here. You made our affectionately dilapidated house into a home, we started a brewery, and we built a real community around it. I've loved becoming better and better friends over the years. Thanks for your support and your effort in maintaining our friendship, especially since I hate Skype.

Mart, thank you for being my rock. Thank you for all the small things, making me dinner when I worked late, fixing my bike, and encouraging me when I needed it most. I've had an amazing time with you over the past years and will always remember our time in Leiden with a smile.

Tiffany, you have been on this journey with me since 2006. You have been my classmate, roommate, colleague, travel mate, co-borrel organizer, partner in crime, tour director, but most of all, friend. Thank you for always being there for me. I will miss our morning coffees, discussing work, life, family etc. Having someone from 'home' was so comforting, I am extremely lucky to have had you here throughout the past 4 years. You're an incredible scientist and an even better friend, I look forward to many many more adventures in the future. Much love.